REALIZING A MID-INFRARED OPTICALLY PUMPED MOLECULAR GAS LASER
INSIDE HOLLOW-CORE PHOTONIC CRYSTAL FIBER

by

ANDREW MICHAEL JONES

B.S., Kansas State University, 2006

AN ABSTRACT OF A DISSERTATION

submitted in partial fulfillment of the requirements for the degree

DOCTOR OF PHILOSOPHY

Department of Physics
College of Arts and Sciences

KANSAS STATE UNIVERSITY
Manhattan, Kansas

2012

Report Documentation Page		*Form Approved* *OMB No. 0704-0188*

Public reporting burden for the collection of information is estimated to average 1 hour per response, including the time for reviewing instructions, searching existing data sources, gathering and maintaining the data needed, and completing and reviewing the collection of information. Send comments regarding this burden estimate or any other aspect of this collection of information, including suggestions for reducing this burden, to Washington Headquarters Services, Directorate for Information Operations and Reports, 1215 Jefferson Davis Highway, Suite 1204, Arlington VA 22202-4302. Respondents should be aware that notwithstanding any other provision of law, no person shall be subject to a penalty for failing to comply with a collection of information if it does not display a currently valid OMB control number.

1. REPORT DATE **2012**	2. REPORT TYPE	3. DATES COVERED **00-00-2012 to 00-00-2012**
4. TITLE AND SUBTITLE **Realizing A Mid-Infrared Optically Pumped Molecular Gas Laser Inside Hollow-Core Photonic Crystal Fiber**		5a. CONTRACT NUMBER
		5b. GRANT NUMBER
		5c. PROGRAM ELEMENT NUMBER
6. AUTHOR(S)		5d. PROJECT NUMBER
		5e. TASK NUMBER
		5f. WORK UNIT NUMBER
7. PERFORMING ORGANIZATION NAME(S) AND ADDRESS(ES) **Kansas State University,Manhattan,KS,66506**		8. PERFORMING ORGANIZATION REPORT NUMBER
9. SPONSORING/MONITORING AGENCY NAME(S) AND ADDRESS(ES)		10. SPONSOR/MONITOR'S ACRONYM(S)
		11. SPONSOR/MONITOR'S REPORT NUMBER(S)
12. DISTRIBUTION/AVAILABILITY STATEMENT **Approved for public release; distribution unlimited**		
13. SUPPLEMENTARY NOTES		

14. ABSTRACT

This research has focused on the development, demonstration, and characterization of a new type of laser based on optically-pumped gases contained within hollow optical fibers. These novel lasers are appealing for a variety of applications including frequency metrology in the midinfrared,free-space communications and imaging, and defense applications. Furthermore,because of the hollow core fibers used, this technology may provide the means to surpass the theoretical limits of output power available from high power solid-core fiber laser systems. Gasfilled hollow-core fiber lasers based on population inversion from acetylene ($12C_2H_2$) and hydrogen cyanide (HCN) gas contained within the core of a kagome-structured hollow-core photonic crystal fiber have now been demonstrated. The gases are optically pumped via first order rotational-vibrational overtones near 1.5 μm using 1-ns duration pulses from a home-built optical parametric amplifier. Narrow-band laser emission peaks in the 3-μm region corresponding to the $\Delta J = ?1$ dipole allowed rotational transitions between the pumped vibrational overtone modes and the fundamental C-H stretching modes have been observed in both molecules. High gain resulting from tight confinement of the pump and laser light together with the active gas permits these lasers to operate in a single pass configuration, without the use of any external resonator structure. Studies of the generated mid-infrared pulse energy, threshold energy, and slope efficiency as functions of the launched pump pulse energy and gas pressure have been performed and show an optimum condition where the maximum laser pulse energy is achieved for a given fiber length. The laser pulse shape and the laser-to-pump pulse delay have been observed to change with varying pump pulse energy and gas pressure, resulting from the necessary population inversion being created in the gases at a specific fiber length dependent on the launched pulse energy. Work is on going to demonstrate the first continuous wave version of the laser which may be used to produce a single coherent output from many mutually incoherent pump sources.

15. SUBJECT TERMS

16. SECURITY CLASSIFICATION OF:			17. LIMITATION OF ABSTRACT	18. NUMBER OF PAGES	19a. NAME OF RESPONSIBLE PERSON
a. REPORT **unclassified**	b. ABSTRACT **unclassified**	c. THIS PAGE **unclassified**	**Same as Report (SAR)**	**190**	

Abstract

This research has focused on the development, demonstration, and characterization of a new type of laser based on optically-pumped gases contained within hollow optical fibers. These novel lasers are appealing for a variety of applications including frequency metrology in the mid-infrared, free-space communications and imaging, and defense applications. Furthermore, because of the hollow core fibers used, this technology may provide the means to surpass the theoretical limits of output power available from high power solid-core fiber laser systems. Gas-filled hollow-core fiber lasers based on population inversion from acetylene ($^{12}C_2H_2$) and hydrogen cyanide (HCN) gas contained within the core of a kagome-structured hollow-core photonic crystal fiber have now been demonstrated. The gases are optically pumped via first order rotational-vibrational overtones near 1.5 µm using 1-ns duration pulses from a home-built optical parametric amplifier. Narrow-band laser emission peaks in the 3-µm region corresponding to the $\Delta J = \pm 1$ dipole allowed rotational transitions between the pumped vibrational overtone modes and the fundamental C-H stretching modes have been observed in both molecules. High gain resulting from tight confinement of the pump and laser light together with the active gas permits these lasers to operate in a single pass configuration, without the use of any external resonator structure. Studies of the generated mid-infrared pulse energy, threshold energy, and slope efficiency as functions of the launched pump pulse energy and gas pressure have been performed and show an optimum condition where the maximum laser pulse energy is achieved for a given fiber length. The laser pulse shape and the laser-to-pump pulse delay have been observed to change with varying pump pulse energy and gas pressure, resulting from the necessary population inversion being created in the gases at a specific fiber length dependent on the launched pulse energy. Work is on going to demonstrate the first continuous wave version of the laser which may be used to produce a single coherent output from many mutually incoherent pump sources.

REALIZING A MID-INFRARED OPTICALLY PUMPED MOLECULAR GAS LASER
INSIDE HOLLOW-CORE PHOTONIC CRYSTAL FIBER

by

ANDREW MICHAEL JONES

B.S., Kansas State University, 2006

A DISSERTATION

submitted in partial fulfillment of the requirements for the degree

DOCTOR OF PHILOSOPHY

Department of Physics
College of Arts and Sciences

KANSAS STATE UNIVERSITY
Manhattan, Kansas

2012

Approved by:

Major Professor
Dr. Kristan L. Corwin

Copyright

ANDREW MICHAEL JONES

2012

Table of Contents

List of Figures

xiii

List of Tables

Acknowledgements

I would like to thank Dr. Yingying Wang, Dr. Coralie Fourcade Dutin, Dr. François Couny, and Dr. Fetah Benabid, head of the Gas-Phase Photonics Materials research group at the University of Bath for providing the hollow-core photonic crystal fibers that are central to this work.

I would like to thank Professor Wolfgang Rudolph for his generous support while working on the initial demonstrations of the laser in his laboratory at the University of New Mexico. Additionally, I would like to thank Dr. Vasudevan Nampoothiri for useful discussions and indispensable technical expertise in the lab during the initial laser demonstrations, whose helpful attitude and tireless dedication contributed directly to the project's success.

I would like to thank my advisor Professor Kristan Corwin for all of her terrific support and guidance, who I feel truly fortunate and honored to have worked with and gotten to know these past six years. I would like to thank Professor Brian Washburn for valuable training as well, who generously provided me with laboratory space for this experimental work at Kansas State University.

Finally, I would like to acknowledge my friends, colleagues, and fellow graduate students who have provided invaluable support in the form of helpful discussions, moral support, and much need sanity checks through social interaction. A special thanks to my lab mates past and present that I am very glad to know and have worked with: Rajesh Kadel, Shun Wu, Chenchen Wang, Dr. Jinkang Lim, Dr. Kevin Knabe, Dr. Rajesh Thapa, Dr. Karl Tillman, and Dr. William Hageman.

Dedication

This work is dedicated to my family, whose love and support has kept me going throughout my graduate career: to my mother, Sheila, and father, Michael, who have always provided me encouragement throughout my life, to my wonderful wife, Ashley, who has shared in the joy and endured the pain with me throughout these past six years and who has stood with me steadfast through it all, and to my son, Solomon, whose smiling face always brings me joy. Thank you so much, and I love you all.

Chapter 1 - Introduction and Motivation

1.1 Introduction

Mid-infrared (mid-IR) laser sources operating at wavelengths from 3 – 12 μm have become increasingly popular. A primary reason for this popularity stems from the fact that this retina-safe region of the spectrum contains several windows of high atmospheric transmission which is desirable in a variety of applications such as remote sensing, space-based terrestrial imaging, free space communications, and range finding. Additionally, the fundamental rotational-vibrational transitions of many molecules including hazardous pollutants and greenhouse gases like NO and NO_2, CO and CO_2, N_2O, and CH_4 correspond to mid-IR wavelengths [1]. The transition strengths of these fundamental transitions are generally orders of magnitude stronger than corresponding overtone transitions that lie at shorter wavelengths within the near infrared or visible regions of the spectrum. Mid-IR sources are then a natural choice for applications involving trace gas detection and molecular fingerprinting such as breath analysis and stand-off explosives detection.

While there exists a strong desire to capitalize on and explore these interesting applications unique to mid-IR wavelengths, the source technology in this spectral region is somewhat limited. Color center lasers like those based on lithium defects in KCl and RbCl crystals have been used to generate tunable emissions at wavelengths from 2.3 to 3.65 μm at continuous-wave (CW) powers up to ~ 1 W [2, 3]. However, the color centers in these crystals are susceptible to diffusion and clustering effects which degrade the overall laser performance [4]. To mitigate these effects, the crystals often must be cooled to cryogenic temperatures. This tends to limit the usefulness of these lasers, confining them to relatively well controlled environments and making them unsuitable for use in many applications requiring field operation.

Semiconductor lasers made of IV-VI materials including lead-salt compounds have been demonstrated to produce mid-IR emissions in the region from below 3 μm to beyond 20 μm [5]. Additionally, spectral tuning on the order of 100 nm of the emission wavelength has been demonstrated from these lasers in external cavity configurations [3]. These monolithic solid state devices use current injection to drive the recombination of electrons and holes across a material band gap just like their near IR and visible semiconductor laser counterparts. The band gaps for these IV-VI materials are less than 0.5 eV [5], allowing them to produce light at

1

wavelengths in the mid-IR. Unfortunately, these materials are relatively soft and exhibit poor mechanical strength and poor thermal stability [5, 6]. Furthermore, these lasers are typically operated at near cryogenic temperatures, and while CW output powers of ~ 0.5 W have now been demonstrated, typical output powers remain fairly low at the milliwatt level [3, 6].

A particularly clever approach to developing mid-IR semiconductor lasers comes in the form of quantum cascade lasers (QCLs). These lasers use mature semiconductor materials like GaAs and InP to fabricate pn-junctions that incorporate energy well structures to effectively produce a reduced band gap device [7]. QCLs have emerged as promising mid-IR sources, with commercial sources now capable of producing watt-level output powers and broad wavelength tuning (e.g. ± 1.2 μm around 11.2 μm [8]). QCLs have even been integrated with photonic crystal resonator structures [9]. QCLs do suffer from a few drawbacks. While broader spectral coverage has been demonstrated, they typically operate from 4-10 μm [7]. Furthermore, they continue to have thermal management challenges and can become multi-mode at high powers [10]. Additionally, the structures that determine the bad gap are relatively complex, making fabrication of the devices relatively complicated and expensive.

Nonlinear wavelength conversion has also proved itself a very useful means of producing mid-IR emissions. Optical parametric oscillators can be used to generate tunable, narrow-band, watt-level CW powers at wavelengths reaching beyond 6 μm [3, 11], and have achieved pump-to-idler optical-to-optical efficiencies in excess of 30% for mid-IR wavelengths [11]. Furthermore, difference frequency generation can be used to extend the range of generated wavelengths to ~ 28 μm [12]. While these sources are incredibly versatile, the total cost of the nonlinear crystals, pump sources, and cavity mirrors typically makes these sources relatively expensive in addition to often being somewhat complex to setup, maintain, and operate.

Optically pumped gas lasers (OPGLs) offer an attractive means of generating mid-IR light. Efficient excitation of the gas can be accomplished using a narrow-band pump laser which is resonant with a particular transition in the gas-phase medium. These lasers can be pumped in the near-infrared to produce mid-IR emissions [13-16]. Compared to solid state laser media, gases have attractive properties including high damage thresholds, the possibility of heat dissipation through gas circulation, relatively large gain cross-sections, and emission frequencies that span from the near to far-infrared. Many OPGLs have been demonstrated, from the earliest CH_3F [17], CO_2 [18], and OCS [19], to alkali vapor [20], CO [13, 14], HBr [15], C_2H_2 and HCN

2

[16]. Some of these OPGLs can be pumped via rotational-vibrational (ro-vibrational) overtones at wavelengths within the telecommunication bands where commercial pump sources (like erbium-doped fiber lasers and amplifiers) are well established and readily available.

OPGLs based on alkali vapors such as rubidium and cesium can be quite efficient, with demonstrated slope efficiencies in excess of 50% for both systems [21, 22]. Furthermore, a total optical-to-optical efficiency of 63% has been demonstrated [22]. However, the emission wavelengths from these lasers only span from 671 – 894 nm and do not come close to reaching into the mid-IR. Fundamental ro-vibrational transitions in molecular gases provide a means to generate longer wavelength emissions. Early work with HBr gas cells pumped via a second-order ro-vibrational overtone at 1.3 μm has demonstrated lasing at ~ 4 μm with conversion efficiencies of ~ 25% [15]. More recently cascade lasing in HBr at wavelengths near 4 μm suggests that conversion efficiencies exceeding 50% are possible [23]. The main disadvantage that has limited widespread use of OPGLs and gas lasers in general and prevented their integration into many practical optical systems is the bulky, fragile packaging necessary to achieve long optical path lengths and extract appreciable laser output due to the dilute nature of gas media.

The problem of weak interaction between light and gas has been solved by employing gas-filled hollow-core photonic crystal fibers (HC-PCFs). HC-PCF [24] consists of a hollow, air-filled core surrounded by cladding structure which is comprised of a periodic array of smaller air holes. Unlike glass capillaries, these hollow microstructured optical fibers can be used to confine gas and light together to areas on the order of $100 \ \mu m^2$ over distances of tens of meters [25] with optical attenuations as low as 1.2 dB/km [26]. HC-PCF is also much less susceptible to bending losses. Furthermore, HC-PCFs can be spliced to solid-core fibers to create hermetically sealed all-fiber gas cells [27]. These fiber cells can be made more compact and robust than conventional gas cells and should lend themselves well to integration with other devices. A variety of nonlinear optical phenomena [28] have been demonstrated using gas-filled HC-PCFs including electromagnetically induced transparency (EIT), saturated absorption spectroscopy (SAS), solitonic pulse compression, and the development of a Raman laser [29] and a multi-octave spanning Raman frequency comb [30], both of which rely on stimulated Raman scattering in hydrogen gas to spectrally shift pump power to the Stokes and AntiStokes wavelengths.

The focus of this work has been to utilize HC-PCF to eliminate the bulky and cumbersome packaging typical of OPGLs while capitalizing on the enhanced interaction of light and gas provided by these fibers to create a mid-IR source that combines the best of gas and fiber laser technologies. We have now developed, demonstrated, and begun to patent a new class of OPGLs based on population inversion in gas-filled HC-PCF [31]. Gases are confined within kagome-structured HC-PCFs [32] whose transmission spans several octaves, providing guidance at both the near IR pump and mid-IR laser wavelengths. OPGLs in fiber waveguides offer many advantages over traditional gas laser geometries and have fantastic potential to provide a simple, compact, and robust means of generating mid-IR light. Lasers of this type have now been demonstrated to produce light near $3 - 3.2 \, \mu m$ when pumped at $1.5 \, \mu m$ [33, 34], offering a potentially robust, efficient, and compact means of producing step-tunable eye-safe mid-IR radiation well suited to a multitude of applications. Additionally, gas-filled HC-PCF lasers offer a means to outperform comparable solid-core fiber laser systems in terms of maximum achievable output powers/pulse energies. This comes from the fact that the maximum output from cladding-pumped single mode fiber lasers is limited at long fiber lengths by the onset of nonlinear processes, namely stimulated Brillouin scattering in the case of narrow-band laser emissions [35]. The nonlinear processes limiting the performance of solid-core fiber laser systems primarily result from interactions of light with the host material in the fiber's core and not the active dopants. By using gas-filled HC-PCF we effectively remove the all material but the active gas from the high intensity region in the central region of the fiber's core. The low overlap of the guided light with the HC-PCF's glass structure together with a higher threshold for the onset of nonlinear effects in the dilute gas lead us to expect that the maximum achievable power from an HC-PCF laser should be an order of magnitude or more higher than that of a comparable solid-state fiber laser system.

1.2 Thesis Outline

The primary focus of the research described here is the development and characterization of optically pumped gas-filled hollow-core fiber lasers based on population inversion which produce light at mid-infrared (mid-IR) wavelengths. In addition to this primary goal, an effort was made to try to develop gas-filled hollow-core fiber lasers that could be pumped and made to

lase at similar wavelengths in the near infrared with high efficiency. Such lasers might be scaled to high power because they could be pumped with multiple mutually incoherent pump lasers, or coherently combined to create the next generation of high power fiber lasers.

Chapter 2 focuses on the molecular physics associated with the C_2H_2 and HCN molecules we use in the laser system. A quantitative description of the energies associated with the rotational and vibrational motions of these molecules is presented as energies and motions will be used later to describe the particular states of the molecular laser systems.

Chapter 3 introduces the optical parametric amplifier (OPA) and optical parametric oscillator (OPO) used as the pump sources to demonstrate mid-IR lasing from gas-filled hollow-core fibers. The concepts of a nonlinear response and three-wave mixing in particular are discussed. The nonlinear processes produced through three-wave mixing are described, with a particular focus on parametric amplification. The parametric amplifier designed and constructed here at Kansas State University is discussed in detail, including results from the modeling which helped guide the component selection.

Chapter 4 describes the special microstructured hollow-core photonic crystal fibers (HC-PCFs) used to contain the molecular gases and guide the pump light together with the generated laser light. The structure and guidance characteristics of both photonic band gap fiber (PBGF) and kagome-structured HC-PCF are discussed. Measurements of the mid-IR fiber loss for several kagome fibers of various dimensions are presented, including a relatively new type of kagome fiber with a hypocycloid-shaped silica core-cladding interface. The measured mid-IR mode profile is shown for one of these hypocycloidal kagome fibers. The OPA discussed in Chapter 3 is reconfigured and used as a broadly tunable source of mid-IR light for the fiber loss measurements, and as such some discussion of the operation and performance of the reconfigured OPA is presented.

Chapter 5 describes initial results from the first gas-filled hollow-core fiber lasers demonstrated. Both an OPO and an OPA were used to pump C_2H_2 (acetylene) gas molecules contained within ~ 1-m lengths of 23-µm pitch single-cell defect kagome-structured HC-PCFs with ~ 20 dB/m loss in the mid-IR near the laser wavelengths. Measurements of the generated ~ 3-µm wavelength laser pulse energy, spectrum, and pump-to-laser pulse delay are presented, along with some general predictions for a model based on coupled rate equations. Initial measurements from an HCN-filled hollow-core fiber laser are also presented. The procedure for

5

turning the raw measurement data from oscilloscope traces into the generated laser pulse energy and the absorbed pump pulse energy is presented in detail.

Chapter 6 focuses on the most recent and most efficient OPA-pumped mid-IR gas-filled hollow-core fiber laser results achieved using a 7-cell defect kagome-structured HC-PCF exhibiting a loss of only ~ 5 dB/m near the laser wavelengths. Again, measurements of the generated ~ 3-μm wavelength laser pulse energy, spectrum, and pump-to-laser pulse delay are presented, along with some general predictions from the model based on coupled rate equations and some discussion of the how the model predictions compare with the measured data.

Chapter 7 discusses the various attempts to realize a small quantum defect laser that is both pumped and made to lase at near infrared wavelengths. Several laser configurations are explored which rely on a CW or long-pulse (pulse durations on the order of tens of nanoseconds or more) pump source and optical cavities resonant at the laser wavelengths. Resonators based on both polarization and dichroic optics are described.

Chapter 8 provides a summary of this thesis work, and discusses some of the unresolved issues pertaining to various aspects of this research. These remaining questions lead to the proposal of additional experimental work in gas-filled hollow-core fiber lasers, and some discussion of this future work is presented.

Chapter 2 - Molecular Physics of C_2H_2 and HCN

2.1 Introduction

The mid-IR gas-filled fiber lasers demonstrated in this thesis rely on population inversions in molecular gases to create gain down the length of the fibers. The molecules are excited from the ground state via first-order vibrational overtone transitions in the near infrared and lase on transitions from this pumped state to fundamental vibrational states. Central to the concept of this laser is an understanding of the fundamental modes and energies associated with the rotational and vibrational motions of molecules. This is introduced in the following section.

2.2 Molecular Energy States

Molecules are comprised of two or more atoms which are bound to one another through electrostatic forces between the positively charged atomic nuclei and the electrons of the combined atomic systems. Stable molecules remain so, because the total energy of the combined system is lower than the energy of a partially or totally separated system of atoms. Just like the atoms they are built from, molecules possess discrete energy levels associated with the particular configuration of their electrons. Additionally, molecules have the ability to vibrate and rotate. As we are particularly interested in using rotational-vibrational transitions to create lasers, we will focus on these motions and assume in all future discussions that the molecules being discussed are in the electronic ground state unless explicitly stated otherwise.

Basic vibrational and rotational motions are illustrated in Fig. 2.1 for a simple diatomic molecule. The spring shown connecting the two nuclei is symbolic, as the vibrations of the nuclei can to a reasonable approximation be assumed to follow the motions of simple harmonic oscillators about their equilibrium positions. However, the harmonic motion takes place within a set of normal coordinates of the molecular system which in general are not simply one set of coordinates describing the relative nuclear displacements, but instead are linear combinations of these displacement positions.
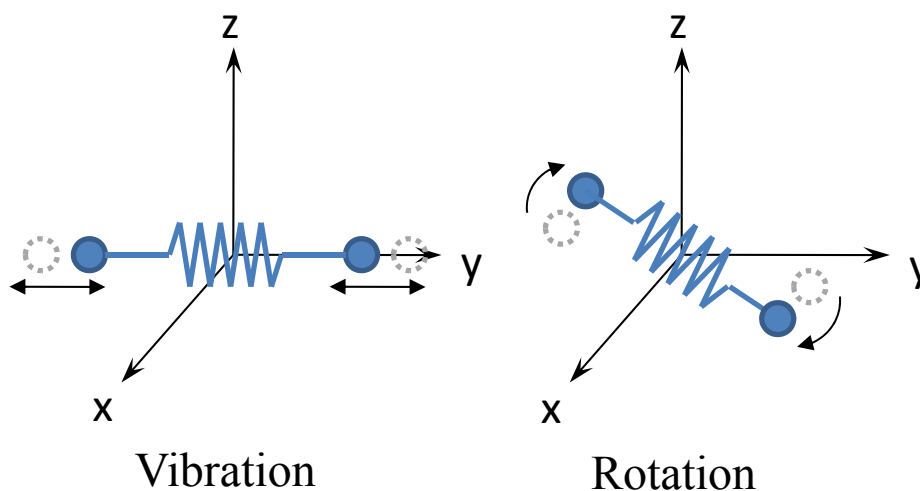
Figure 2.1 Diagram illustrating basic vibrational and rotational motions of a diatomic molecule.

The vibrational frequencies and the corresponding vibrational eigenvectors (called normal modes) are determined by assuming that the nuclei will respond as simple harmonic oscillators to small perturbations in their equilibrium positions. The process of solving for the normal frequencies and normal modes is described in detail in reference [36].

The total energy associated with v_i quanta of vibration of a single simple harmonic oscillator oscillating at a frequency v_i is given by [36],

$$E_{vib,i}(v_i) = hv_i\left(v_i + \frac{1}{2}\right), \qquad v_i = 0, 1, 2, \ldots \qquad 2.1$$

where h is Planck's constant. The total vibrational energy from all the oscillating vibrational normal modes is then just the sum of the individual vibrational energies in each mode and is given by [36],

$$E_{vib}(v_1, v_2, \ldots, v_n) = hv_1\left(v_1 + \frac{1}{2}\right) + hv_2\left(v_2 + \frac{1}{2}\right) + \cdots + hv_n\left(v_n + \frac{1}{2}\right) \qquad 2.2$$

The normal modes of vibration for the C_2H_2 molecular are shown in Fig 2.2a while the normal modes for the HCN molecule are shown in Fig. 2.2b. The energies associated with the

normal modes of the molecules are shown together in Table 2.1. While both molecules are linear, only acetylene is linear and symmetric.
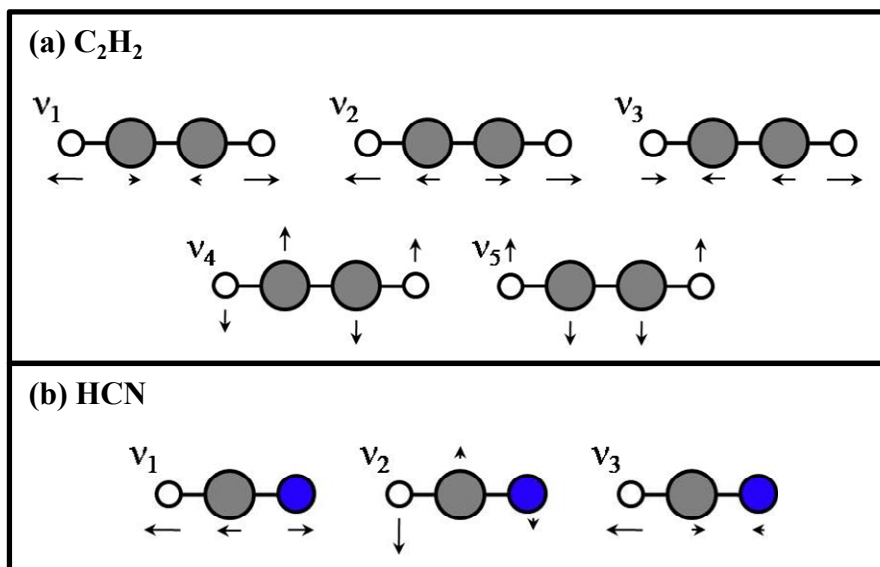
Figure 2.2 The normal modes of C_2H_2 and HCN [36]. The small white-filled circles represent hydrogen atoms; the larger, gray-filled circles represent carbon atoms, and the medium sized blue-filled circles represent nitrogen atoms. The relative motions of the atoms comprising the molecules are indicated by the black arrows (not to scale) above or below each atom. The label $v_1 - v_5$, corresponding to each normal mode, is shown at the upper left of the molecules.

Acetylene is seen to have three stretching modes and two bending modes for a total of five vibrational normal modes. The v_1 and v_3 modes correspond to the symmetric and antisymmetric C – H stretch; the v_2 mode corresponds to the C – C symmetric stretch; and the v_4 and v_5 modes correspond to the symmetric and antisymmetric C – H bends. The two stretching modes are doubly degenerate as two orthogonal bending modes could be created simply by rotating the molecule 90° about the internuclear axis.

Similarly, HCN is seen to have two stretching modes and one bending mode which is doubly degenerate. The v_1 mode corresponds to the C – N stretch; the v_2 mode corresponds to C – H bend; and the v_3 mode corresponds the C – H stretch. Unlike acetylene, none of the

normal modes of HCN have a definite symmetry. This directly related to the fact that all three of the atoms comprising the linear molecular have different masses.

Table 2.1 Frequencies of vibrational normal modes of acetylene [37] and HCN [38].

Vibrational Normal Mode[*]	Frequency in $^{12}C_2H_2$ (cm^{-1})	Frequency in $H^{12}C^{14}N$ (cm^{-1})
v_1	3397.12	2096.85
v_2	1981.80	711.98
v_3	3316.86	3311.48
v_4	608.73	–
v_5	729.08	–

[*]The motions corresponding to each mode designation are shown in Fig. 2.2 and follow the convention used in reference [36].

The energies associated with the rotational motion of linear molecules in their electronic ground states are equal to those of a simple rotator (the angular momentum of electrons about the internuclear axis is zero for all known linear polyatomic molecules in the ground state [36]). Depending on the symmetry of the configuration, for molecules in an excited electronic state the rotational problem may need to be analyzed as a standard symmetric top, specifically including the moments of inertia of the electrons. The rotational energy of a linear molecule without any vibrational angular momentum is then given by [36],

$$E_{rot}(J) = hcB_V J(J+1) - hcD_V J^2 (J+1)^2, \qquad J = 0, 1, 2, ... \qquad 2.3$$

where c is the speed of light B_V and D_V are rotational constants specific to the molecule (the subscript "V" indicates that these constants do have a slight vibrational state dependence) and related to the moment of inertia about an axis in the plane perpendicular to the internuclear axis and containing the center of mass, and J is the rotational quantum number. The magnitude of the angular momentum of the rotating molecule, |**J**|, is given in terms of the rotational quantum number by,

$$|\mathbf{J}| = \frac{h}{2\pi}\sqrt{J(J+1)} \qquad\qquad 2.4$$

The first term in Eq. 2.3 is exactly the energy of rigid rotator where the rotational constant B is related to the moment of inertia, I_B, by,

$$B = \frac{h}{8\pi^2 c I_B} \qquad\qquad 2.5$$

The second term in Eq. 2.3 is generally much smaller than the first term and accounts for the apparent centrifugal force which causes the internuclear distance between molecules to increase with increasing angular momentum.

A molecule initially occupying a particular vibrational and rotational state can make a transition to other states by absorbing or emitting a light. However, there are certain restrictions regarding what states molecules can transition between. The rules governing simultaneous rotational-vibrational transitions are generally the same as those governing transitions between states having the same type of molecular motion.

The selection rule for transitions between vibrational states are identical to those of a one-dimensional simple harmonic oscillator [39], namely,

$$\Delta v_i = \pm 1 \qquad\qquad 2.6$$

For molecules which have more than one normal mode, the total vibrational wavefunction for the system of independent harmonic oscillators is written as the product of the individual harmonic oscillator wavefunctions. Therefore, there is the additional stipulation that no more than one vibrational transition may occur at a time, forbidding simultaneously transitions in the other normal modes, *i.e.*,

$$\Delta v_{j \neq i} = 0 \qquad\qquad 2.7$$

Molecules can absorb or emit light during a vibrational transition only if the dipole moment changes during the transition. Transitions satisfying this condition are said to be infrared active

11

(named such because many of these transitions interact with light at infrared wavelengths). Fundamental transitions (transitions which abide by the rules given in Eqs. 2.6 and 2.7) can only occur for vibrational modes associated with a non-zero dipole moment.

The rules given above are strictly true for molecular vibrations which act like ideal independent simple harmonic oscillators. However, real molecules do not strictly behave as ideal harmonic oscillators, but instead can show some anharmonicities. This non-ideal behavior loosens the restrictions dictated by Eqs. 2.6 and 2.7, and allows additional transitions in which Δv_i can change by multiple quanta and simultaneous transitions within different vibrational modes are permitted. These transitions are referred to as overtone transitions, and in general they are much weaker than the fundamental transitions which obey Eqs. 2.6 and 2.7.

For pure rotational transitions (no accompanying change in the vibrational state of the molecule) the molecule must have a permanent dipole moment and the selection rule is,

$$\Delta J = \pm 1 \, . \tag{2.8}$$

This results from the parity and the orthogonality of the spherical harmonics which are the rotational state eigenfunctions. For simultaneous rotational-vibrational transitions, $\Delta J = 0$ is also permitted when the vibrational angular momentum, l, of either the initial or final state is non-zero [36]. Transitions between rotational levels are labeled P(J'), Q(J') or R(J'), corresponding to a change in rotational angular momentum of $\Delta J = -1$, 0, or 1, respectively, as determined from the state with the lower total energy, having $J = J'$. As the R-branch transitions correspond to $\Delta J = +1$, they always occur at higher energies than the P-branch transitions, and thus always absorb or emit light at shorter wavelengths than P-branch transitions. This can be seen directly from the $v_1 + v_3$ rotational-vibrational overtone absorption spectrum of acetylene shown in Fig. 2.3. No Q-branch transitions are observed since there is no angular momentum associated with either the v_1 or v_3 vibrational modes.
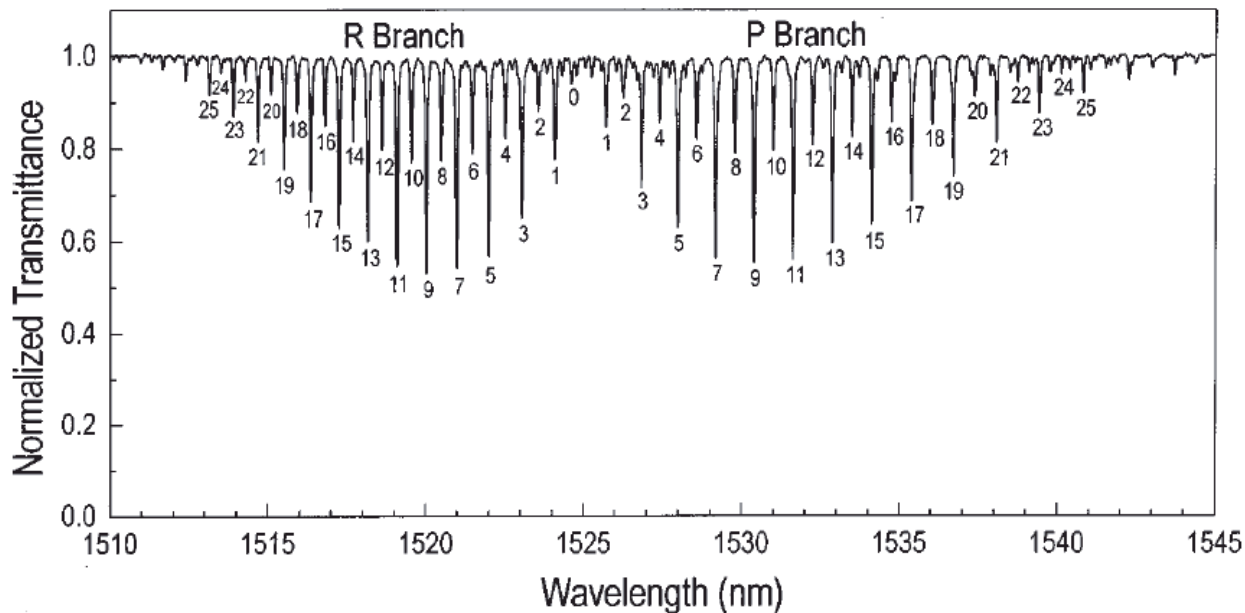
Figure 2.3 Absorption spectrum of $^{12}C_2H_2$ molecules contained in a 5-cm long gas cell showing the R and P-branch transitions between the vibrational ground state and the $v_1 + v_3$ vibrational state. Reproduced from Reference [40].

One interesting feature seen in this absorption spectrum is the difference in absorption strength of transitions between initial rotational states with even J as compared to those with odd J. The underlying cause for this has deep roots and is a direct consequence of the symmetry requirements of the total multi-particle wavefunction under exchange of identical nuclei.

The total wavefunction, ψ_{tot}, describing the multi-particle polyatomic molecular system can be written to a good approximation as a product wavefunction of the constituent translation, electronic, vibrational, rotational, and nuclear wavefunctions given by [41],

$$\psi_{tot} = \psi_{trans}\psi_{elec}\psi_{vib}\psi_{rot}\psi_{nuc} \qquad 2.9$$

The total wavefunction is required to be either symmetric or antisymmetric when any two identical particles are exchanged. For a molecule with one or more pairs of identical fermions (such as the spin-1/2 hydrogen nuclei), the total wavefunction must be antisymmetric overall (this symmetry condition for fermions is referred to as the Pauli exclusion principal). The operation of exchanging identical nuclei is most conveniently thought of in two steps, where all

13

of the particles (electrons and nuclei) are first inverted through the origin of symmetry, and then just the electrons are inverted back again. Let us examine the effect of these processes on each of the individual wavefunctions.

The translational wavefunction only depends on the position of the molecule's center of mass, and since the center of inversion symmetry always occurs at the center of mass, inversion about this point will have no effect on the translational wavefunction. Additionally, the ground state electronic and vibrational wavefunctions are both symmetric with respect to inversion of both the electrons and the nuclei [41]. This just leaves the rotational and nuclear wavefunctions to produce the overall antisymmetric wavefunction required.

The rotational wavefunctions are the eigenfunctions of the simple rotator, which are the spherical harmonics, $Y_J^{m_J}(\theta, \varphi)$ [39]. Under inversion of the nuclei, $\theta \to \pi - \theta$ and $\varphi \to \varphi + \pi$. This does nothing to the parity of spherical harmonics with even J but flips the parity of the harmonics with odd J [41]. Therefore, to keep an overall antisymmetric wavefunction, the nuclear wavefunction must be antisymmetric for even J rotational states and symmetric for odd J rotational states. The nuclear spin states available for the two coupled $I = 1/2$ hydrogen nuclei are the three symmetric triplet states ($I = 1$) and the one antisymmetric singlet state ($I = 0$) [39]. It is this 3 fold increase in the number of states available for odd J rotation states resulting from the nuclear triplet states ($I = 1$) required to maintain an overall antisymmetric wavefunction that produces the enhanced absorption on the odd J rotational lines shown in Fig. 2.3.

All of this energy level information is put to use when we consider an ensemble of N_{tot} molecules in thermal equilibrium at a temperature T. The overall population at thermal equilibrium follows a Boltzmann distribution, and the population in any particular state is given by,

$$N(V, J; I) = N_{tot} \frac{(2I + 1)(2J + 1)e^{-(E_{vib}(V) + E_{rot}(J))/k_B T}}{\sum_{V'} \sum_{J'} (2I' + 1)(2J' + 1)e^{-(E_{vib}(V') + E_{rot}(J'))/k_B T}} \qquad 2.10$$

where V represents the set of vibrational quantum numbers for the state, J is the rotational state, I is the total nuclear spin (required for symmetric molecules like acetylene) which is determined by the vibrational and rotational state symmetries, and E_{vib} and E_{rot} are the vibrational and rotational energies given by Eqs. 2.2 and 2.3, respectively. The double sum in the denominator

is the partition function which acts to normalize the distribution such that the sum of all the molecules in all states is equal to N_{tot}.

Chapter 3 - Nonlinear Wavelength Conversion

3.1 Introduction

A source of energetic and tunable 1.5-μm wavelength pulses is desired to use as the pump source to optically excite the molecules used in the gas-filled HC-PCF lasers. Optical parametric amplifiers (OPAs) and optical parametric oscillators (OPOs) offer a convenient solution. Both of these devises rely on the nonlinear optical response of an optically transparent material system to generate new spectral components from the incident light. The process employed in both cases is a three-wave mixing process referred to as optical parametric amplification [42].

Three-wave mixing is a second-order nonlinearity ($\chi^{(2)}$ process) involving three distinct fields [42]. Figure 3.1 illustrates several of these processes. The subscripts p, s, and i denote the pump, signal, and idler frequencies which are designated according to the convention $\omega_p > \omega_s > \omega_i$. From the expressions for the frequency of the generated fields shown in each process it is clear that all of these processes conserve photon energy. Difference frequency generation is a method sometimes employed to generate frequency components at long wavelengths coherently from two shorter frequency sources. The process of parametric amplification is seen from the figure to essentially be stimulated difference frequency generation. Degenerate sum frequency generation, in which the two input fields have the same frequency, is the process of second harmonic generation, which can be exceedingly efficient and is a very simple means of shifting light from easy to generate wavelengths in the near-IR into the visible or ultraviolet.
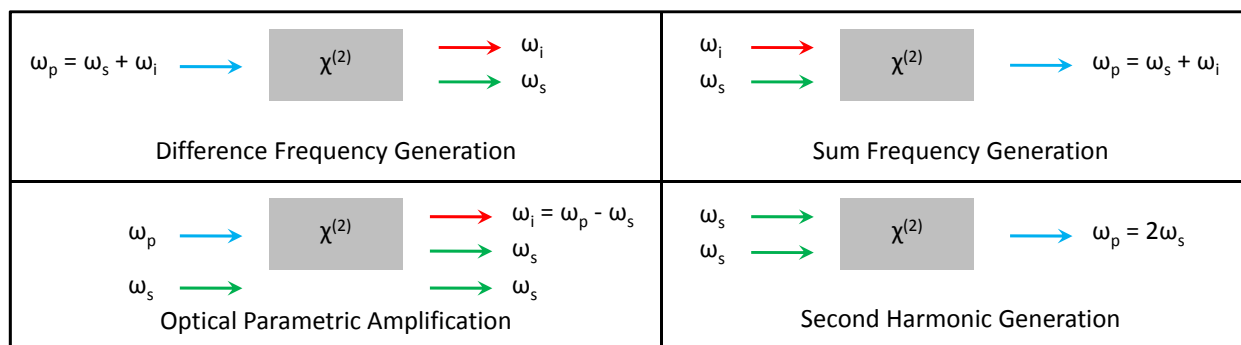
Figure 3.1 Schematic of various three-wave mixing processes including sum and difference frequency generation, optical parametric amplification, and second harmonic generation.

Most of these processes look schematically identical: two optical fields enter the medium, and one new field exits. It is the phase matching condition which determines if a particular process will be favored. Phase matching comes directly from conservation of momentum and essentially requires that sum of the wavevectors corresponding to the incident fields for a given process equal the sum of the wavevectors of the fields produced [42]. The magnitude of the wavevector, k, of a particular optical field of frequency ω is given by,

$$k = \frac{n\omega}{c} = \frac{2\pi n}{\lambda} \qquad\qquad 3.1$$

where n is the index of refraction of the nonlinear optical material for the optical field having a vacuum wavelength λ.

The phase matching is typically expressed in terms of the phase mismatch, Δk, which is equal to zero for perfect phase matching [42]. The phase matching condition that must be satisfied for parametric amplification is given by [42],

$$\boldsymbol{k}_p = \boldsymbol{k}_s + \boldsymbol{k}_i \qquad\qquad 3.2$$

or in terms of the magnitude of the phase mismatch by,

$$\Delta k = k_s + k_i - k_p \qquad\qquad 3.3\text{a}$$
$$\Delta k = \left[n(\omega_s)\omega_s + n(\omega_i)\omega_i - n(\omega_p)\omega_p \right]/c \qquad\qquad 3.3\text{b}$$

Many of the materials that have strong nonlinear responses also exhibit normal dispersion, *i.e.* $n(\omega_p) > n(\omega_s) > n(\omega_i)$, which makes satisfying the phase matching condition nontrivial [42]. Fortunately, many of the nonlinear crystals typically used are birefringent, allowing the index of refraction for the lower frequency signal and/or idler to be greater than the index of the higher frequency pump, *i.e.* $n(\omega_s) > n(\omega_p) > n(\omega_i)$ or $n(\omega_s) > n(\omega_i) > n(\omega_p)$. This permits the right-hand side of Eq. 3.3b to equal zero for certain pump, signal, and idler frequencies which are said to be phase matched. There are two categories of birefringent phase matching: type I and type II. Type I phase matching refers to the case where the signal and idler

17

fields share the same polarization, while the case where the signal and idler fields are orthogonally polarized is refer to as type II phase matching [42].

The strength of the nonlinear response of the medium to the driving fields depends on the polarizations of all the fields involved. If either type I or type II phase matching is employed, by design two of the three fields involved will always be orthogonally polarized. Birefringent phase matching can then never be used to generate fields co-polarized with the pump field. This would be particularly detrimental for materials like $LiNbO_3$ that have a very large effective nonlinearity when the polarizations of the incident and generated fields are all parallel. Luckily, quasi-phase-matching techniques have been developed to create engineered materials which can phase match pump, signal, and idler wavelengths all polarized in the same direction, in order to take advantage of the large nonlinearity afforded by this configuration [42].

3.2 Optical Parametric Oscillators and Amplifiers

3.2.1 Optical Parametric Amplification

A schematic of the OPA used to pump the gas-filled fiber lasers is shown in Fig. 3.2. The OPA is comprised of three basic components: 1) a high energy pump source, 2) a low energy signal source, and 3) a nonlinear crystal used to transfer energy from one to the other.

The pump source used is a diode-pumped single mode passively Q-switched Nd:YAG laser. Q-switching is a technique used to generate long duration (typically ~ 100 ps or longer), high energy laser pulses by controlling the feedback from the optical cavity to the gain medium (the degree of loss in the cavity can be quantified by a parameter called the "quality factor", or simply the Q factor). Passive Q-switching employs a saturable absorber inside of the laser resonator. The saturable absorber is typically made of either a doped glass or crystal (like Cr:YAG) or a semiconductor material. The saturable absorber functions by preferentially absorbing more low intensity light than high intensity light. In this way the saturable absorbed acts like an intensity dependent switch, only providing optical feedback to the gain material after a certain amplified spontaneous emission (ASE) intensity threshold has been reached. Once the threshold has been reached, the saturable absorber becomes saturated and allows low loss feedback from the cavity to the gain medium. The energy stored in the population inversion inside of the gain medium is then rapidly extracted, producing a high energy pulse.

The particular Nd:YAG laser used in the OPA produces 1064-nm wavelength pulses ~ 1 ns in duration with energies of ~ 3 mJ. The spectral bandwidth of the pulses is ~ 1 GHz. The pulse repetition rate can be varied from ~ 1 – 100 Hz, and is typically triggered at 30 Hz using TTL pulses from a Stanford Research Systems delay generator. This particular repetition rate was seen to be the highest possible without compromising the pulse energy stability. At repetition rates higher than 30 Hz, random spiking in the pulse energy from the laser has been observed.

At the heart of the OPA is a 50-mm long magnesium oxide doped congruently grown periodically poled lithium niobate (MgO:PPLN) crystal. Inside of this crystal 1064-nm wavelength, ~ 100-μJ energy pulses roughly 1-ns in duration from the Nd:YAG pump laser are mixed with narrow linewidth CW light from either a tunable fiber laser or an extended-cavity tunable diode laser. A variable attenuator comprised of a half-wave plate and a polarizing beam
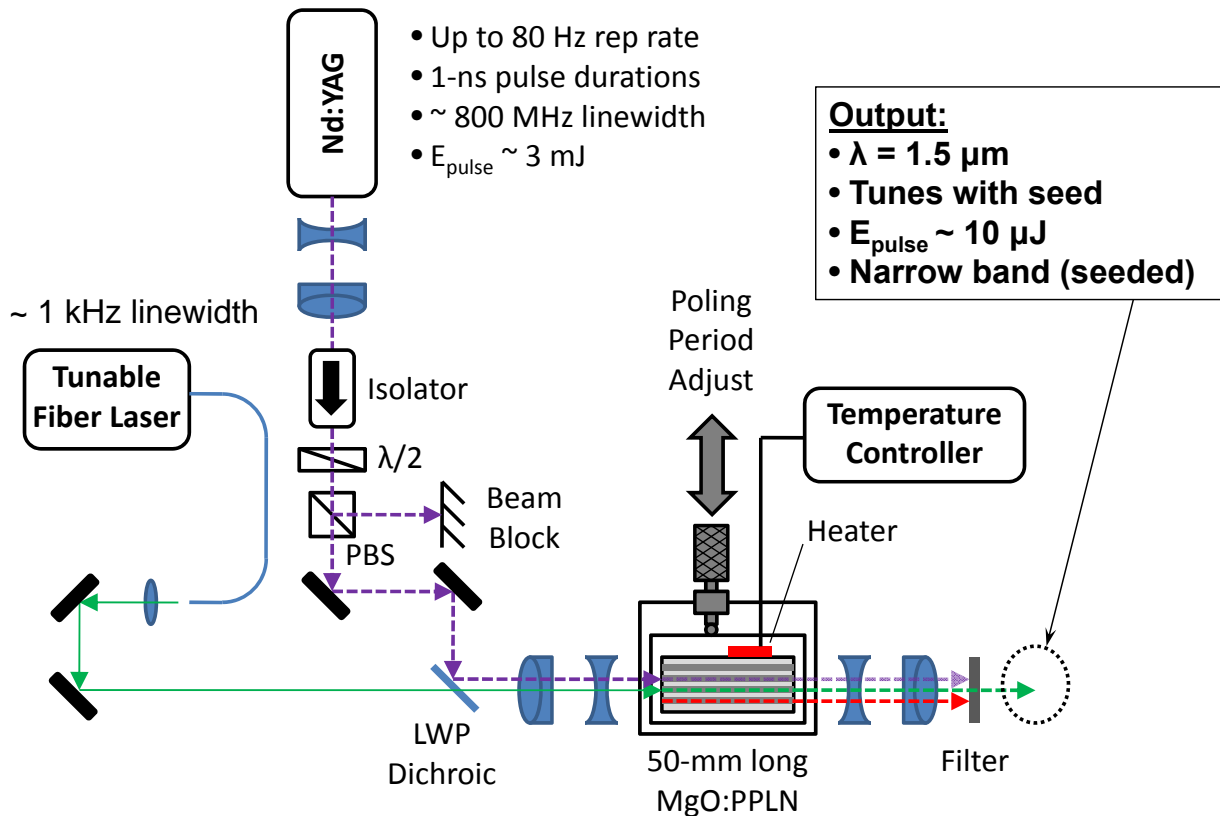
Figure 3.2 Setup for the OPA used as the source of tunable 1.5-μm wavelength pulses to pump the gas-filled HC-PCF lasers.

19

splitter is used to adjust the pump pulse energy incident on the MgO:PPLN crystal. The damage threshold for the crystal is > 500 µJ for nanosecond duration, 1-µm wavelength pulses. The nonlinear process essentially shifts energy from the high-power 1-µm wavelength pulses into moderate energy, tunable 1.5-µm wavelength signal pulses. As the source of this energy transfer is difference frequency generation, conservation of energy requires that a moderate energy ~ 3-µm wavelength idler pulse also be generated. The wavelength of the OPA output tunes with that of the CW signal.

Pump pulses are combined together with the signal light using a dichroic mirror which reflects the short wavelength pump pulses while transmitting the longer wavelength signal light. The signal collimating lens and the telescope just after the Nd:YAG are configured to produce collimated beams with roughly the same beam waist. The telescope before the nonlinear crystal is needed to shrink the beam size down to within the full aperture of the crystal. The MgO:PPLN crystal has a minimum full aperture of 800 µm, so the beam waist must be less than this.

The beam waist was measured by attaching a razor blade to a translation stage and incrementally moving the blade into the beam while measuring the total pulse energy transmitted past the blade from the unblocked portion of the beam. Assuming that the spatial intensity profile of the beam has a Gaussian shape with a $1/e^2$ beam waist w, the CW power or pulse energy transmitted past the razor in the unblocked portion of the beam, P, is related to the total pulse energy, P_{tot}, by,

$$P(x) = \frac{1}{2} P_{tot} \cdot \left[1 + \text{Erf}\left(\frac{x - x_0}{w}\right)\right]$$ 3.4

where x is the relative position of the razor to the center position x_0 of the Gaussian beam, and the error function "Erf" is given by,

$$\text{Erf}(z) = \frac{2}{\sqrt{\pi}} \int_0^z e^{-z'^2} dz'$$ 3.5

Data from a knife edge measurement of the signal beam just after the MgO:PPLN crystal is shown in Fig. 3.3. The Gaussian fit to the data is quite good and gives a $1/e^2$ beam waist of

335 μm, or a beam diameter or 670 μm. The distance over which a Gaussian beam will be collimated is equal to twice the Rayleigh range of the beam. The Rayleigh range is defined as the propagation distance that a Gaussian beam of initial minimum waist, w_0, will travel before the waist increases by a factor of $\sqrt{2}$ (causing the area of the beam to double) [43]. The Rayleigh range is given by,

$$z_R = \frac{\pi w_0^2}{\lambda}$$

3.6

where λ is the wavelength of the light. So assuming that the beam waist measured after the MgO:PPLN crystal is the minimum beam waist, the beam will only be collimated for about 25 cm. It is for this reason that a second telescope is placed after the crystal to expand the beam, so that the larger beam can remain collimated for several meters while being transported to the laser setup.
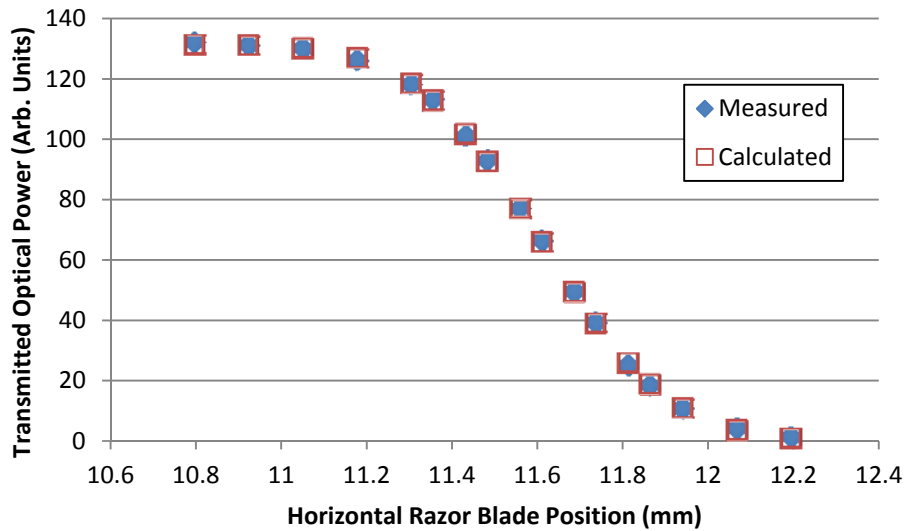
Figure 3.3 The power in the unobstructed signal beam as a function of knife edge position measured just after the MgO:PPLN. The measured data is shown in blue. The red data points are fit to the measured data using Eq. 3.4 which assumes a Gaussian beam profile.

In order for the signal wavelength to be amplified, it must satisfy the phase matching condition imposed by conservation of momentum in the crystal. For a first-order quasi-phase-matched crystal, the phase mismatch condition for optical parametric amplification can be written as [42],

$$\Delta k_{QPM} = k_p - k_s - k_i - \frac{2\pi}{\Lambda} \qquad\qquad 3.7$$

where Λ is the poling period of the quasi-phase-matched material. The grating period is defined as twice the distance over which the nonlinear coupling coefficient is made to change sign. For our first-order quasi-phase-matched MgO:PPLN crystal, the optimum grating period can be calculated by setting the phase mismatch in Eq. 3.7 equal to zero and solving for the grating period giving,

$$\Lambda = \frac{2\pi}{k_p + k_s - k_i}. \qquad\qquad 3.8$$

The MgO:PPLN contains four separate grating periods with Λ equal to 30.0, 30.5, 31.0, and 31.5 μm. Since the wavelength from the Nd:YAG pump is fixed, these separate grating periods alone only allow four different sets of signal and idler wavelengths to be quasi-phase-matched with the pump. However, the indices of refraction of the crystal at the different wavelengths is dependent on temperature such that by tuning the temperature nearly all wavelengths between ~ 1.5 and 1.8 μm (corresponding to idler wavelengths of ~ 2.6 to 3.6 μm) can be quasi-phase-matched.

Inverting both sides of Equation 3.8 and using Eq. 3.1 to rewrite the wavevectors in terms of the wavelengths gives,

$$\frac{1}{\Lambda(T)} = \frac{n_e(\lambda_p, T)}{\lambda_p} - \frac{n_e(\lambda_s, T)}{\lambda_s} - \frac{n_e(\lambda_i, T)}{\lambda_i}, \qquad\qquad 3.9$$

where now the poling period is temperature dependent to account for thermal expansion of the crystal, and $n_e(\lambda, T)$ is the wavelength and temperature dependent index of refraction of the

crystal for light polarized along the extraordinary axis. The index of refraction for MgO:PPLN can be computed from the following Sellmeier equation taken from reference [44],

$$n_e^2(\lambda, T) = a_1 + b_1 f(T) + \frac{a_2 + b_2 f(T)}{\lambda^2 - a_3^2} + \frac{a_4 + b_3 f(T)}{\lambda^2 - a_5^2} - a_6 \lambda^2, \qquad 3.10$$

where λ is in units of micrometers, the coefficients a_i and b_i are given in Table 3.1, and the function $f(T)$ is given by [44],

$$f(T) = (T - 24.5)(T + 570.82), \qquad 3.11$$

where T is the crystal temperature in degrees centigrade. The poling periods are typically transferred to these crystals through lithographic techniques in a clean room environment at a temperature of 19 °C [44]. The temperature dependent poling period, $\Lambda(T)$, is then given in

Table 3.1 Sellmeier coefficients for the temperature-dependent extraordinary index of refraction of MgO doped congruently grown LiNbO$_3$ given by Eq. 3.10 (from reference [44]).

Coefficient	Numerical Value
a_1	5.319725
a_2	0.09147285
a_3	0.3165008
a_4	100.2028
a_5	11.37639
a_6	0.01497046
b_1	4.753469×10^{-7}
b_2	3.310965×10^{-8}
b_3	2.760513×10^{-5}

terms of the poling period created from the lithographic process, Λ_0, by [44],

$$\Lambda(T) = \Lambda_0[1 + \alpha(T - 19) + \beta(T - 19)^2],$$ 3.12

where T is again the temperature of the crystal in degrees centigrade, and $\alpha = 1.53 \times 10^{-5}$ °C^{-1} and $\beta = 5.3 \times 10^{-5}$ °C^{-2} are the thermal expansion coefficients for undoped congruently grown LiNbO$_3$ [44, 45].

The temperature-dependent phase matching curves for the MgO:PPLN crystal are calculated by solving Eq. 3.9 numerically for temperature at specific wavelengths. The pump wavelength is determined by the Nd:YAG pump laser and is measured to be 1063.81 ± 0.05 nm. The signal wavelength can then be varied during the calculation and the corresponding idler wavelength resulting from energy conservation is computed as,

$$\lambda_i = \left(\frac{1}{\lambda_p} - \frac{1}{\lambda_s}\right)^{-1}$$ 3.13

Figure 3.4 shows the phase matching curves calculated for the four different poling periods using the Mathematica code given in Appendix A. Along with the calculated curves, two data points corresponding to the idler wavelengths measured at two temperatures on the 31.0-μm poling period are shown. The idler pulses were generated from the OPA without any externally applied signal light (quantum noise takes the place of the signal light that would otherwise stimulate the parametric amplification process). The linewidth of the idler pulses measured is therefore fairly broad at ~ 10 nm (FWHM). Error bars corresponding to this linewidth have been placed on the data points, but fall within the data symbols themselves. The measured wavelengths are only 6 nm longer than those calculated from the phase matching curve. This is a great result, as we can calculate the quasi-phase-matched wavelength of the generated idler (and signal) pulses with reasonable accuracy from the crystal's poling period, Λ_0, and temperature. This is necessary to determine the wavelength of the idler pulses from the unseeded OPA which is used to measure the mid-IR fiber losses from various HC-PCFs as is discussed in detail in Chapter 4.

Predictions for the generated signal pulse energy were made prior to purchasing the Nd:YAG pump laser and the MgO:PPLN crystal, in order to ensure that the OPA would be appropriate for use pumping the gas-filled fiber lasers we are interested in developing and characterizing. The OPA's performance was estimated by numerically integrating the coupled wave equations for CW plain waves using the Mathematica code shown in Appendix B. The coupled wave equations are taken from Ref [46] and are given by,

$$\frac{dA_p}{dz} = \frac{2i\omega_p d_{QPM}(z)}{n_e(\omega_p)} A_s A_i e^{-i\Delta k \cdot z} \qquad\qquad 3.14a$$

$$\frac{dA_s}{dz} = \frac{2i\omega_s d_{QPM}(z)}{n_e(\omega_s)} A_p A_i^* e^{i\Delta k \cdot z} \qquad\qquad 3.14b$$

$$\frac{dA_i}{dz} = \frac{2i\omega_i d_{QPM}(z)}{n_e(\omega_i)} A_p A_s^* e^{i\Delta k \cdot z} \qquad\qquad 3.14c$$

where the effective nonlinearity of the first-order quasi-phase-matched MgO:PPLN crystal, d_{QPM}, varies with linear distance, z, through the crystal and is given by,

$$d_{QPM}(z) = \frac{2}{\pi} d_{eff} \text{Sign} \left[\text{Sin}\left(\frac{2\pi z}{\Lambda}\right) \right] \qquad\qquad 3.9$$

The strength of the nonlinear response is quantified by d_{eff}, which for LiNbO$_3$ with all fields polarized along the crystal's optical axis is equal to 27 V/pm [46]. For comparison, the largest d_{eff} that can be achieved in LiNbO$_3$ using birefringent phase matching is only about one-sixth as large.

The "sign" function is used to return either $+ 1$ or $- 1$ depending on the sign of its argument. The particular argument is a sine function that changes sign from positive to negative or negative to positive every time z advances by a distance $\Lambda/2$. This causes the sign of the derivatives of the signal and idler fields to flip just as the accumulated phase mismatch advances
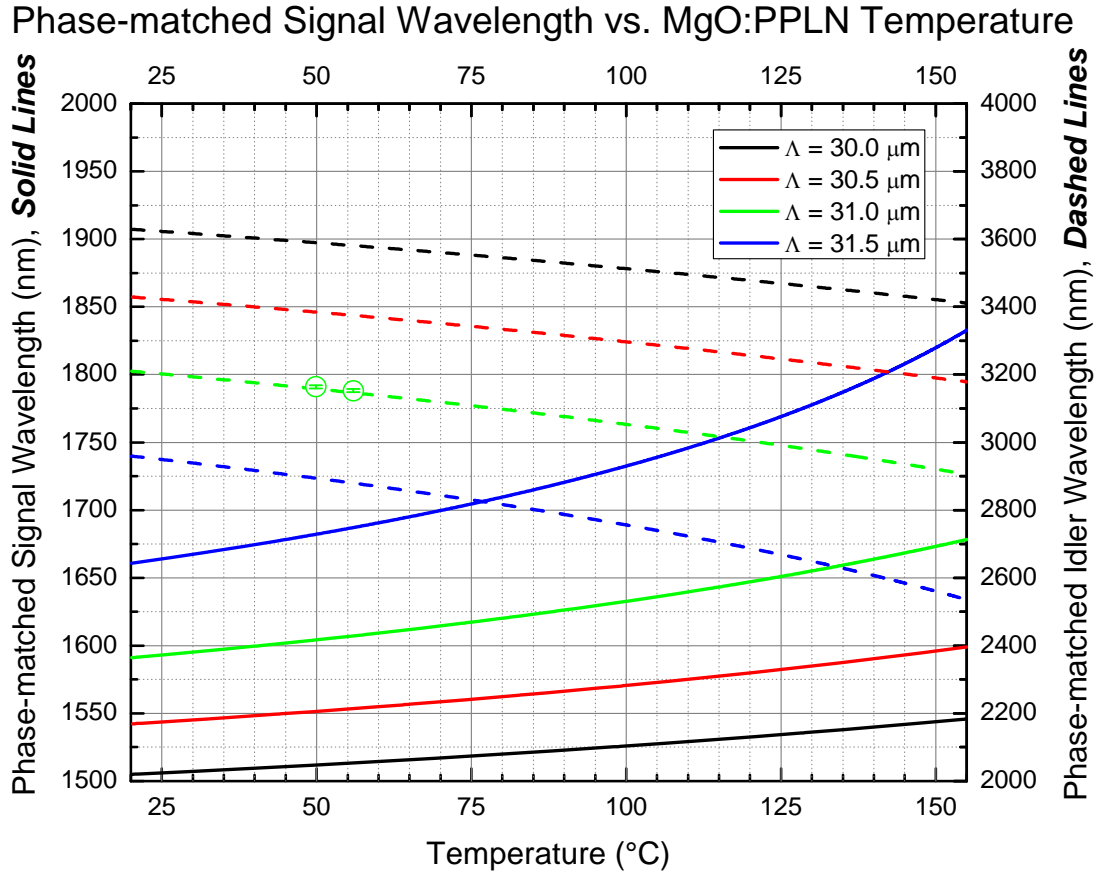
Figure 3.4 Quasi-phase-matched signal and idler wavelengths from a MgO:PPLN crystal as a function of crystal temperature and poling period. The two idler wavelengths measured near 50 °C using the 31.0 µm poling period are just 6-nm longer than the calculated values.

by a value of π, effectively keeping the overall sign of the derivatives of all of the fields unchanged and allowing the signal and idler fields to grow monotonically while propagating through the crystal.

Estimates from the CW calculation were compared with results from a more sophisticated program designed to simulate nonlinear mixing processes called SNLO (free to download from AS-Photonics) that can handle both CW and pulsed inputs directly. Both models assumed 500-µm diameter flat-top beams in a 50-mm long periodically PPLN crystal with ideal quasi-phase-matching, *i.e.* the grating period is given by Eq. 3.8. The pump and signal light in both models are taken to be at wavelengths of 1064 and 1533 nm, respectively. The CW model is run using the pump power corresponding to the peak power from a 300-µJ energy pulse with a Gaussian temporal profile for a range of durations between 5 and 100 ns. The signal powers used range

between 5 and 100 mW. The pump pulse energy and pulse duration were input directly into the SNLO program along with the CW signal power. Figure 3.5 shows the predicted signal pulse energy produced from the OPA as a function of the pump pulse duration for several incident CW signal powers calculated by numerically integrating Eqs. 3.8a-c along the length of the 50-mm long crystal (dashed lines) and calculated using the SNLO program (solid lines).
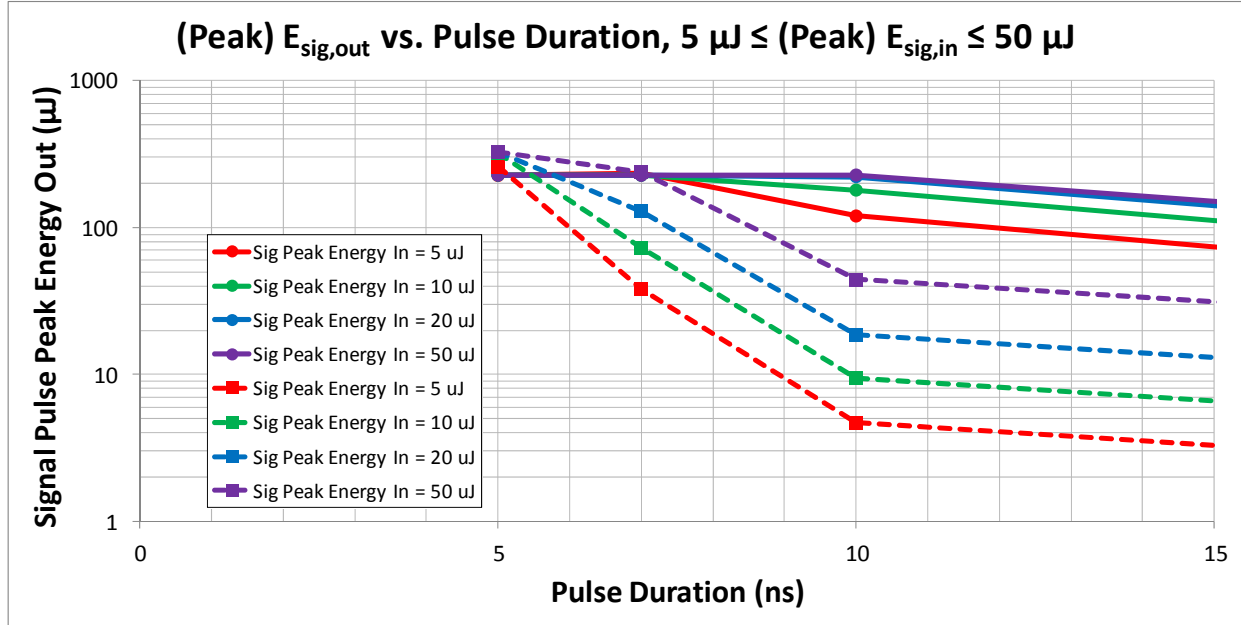
Figure 3.5 Predicted signal pulse energies produced from the OPA calculated by numerically integrating Eqs. 3.8a-c (dashed lines) and using the SNLO program (solid lines) for various CW input signal powers. The nonlinear material is assumed to be a 50-mm long PPLN crystal with ideal quasi-phase-matching.

The calculation results are seen to agree reasonable well for the short pump pulse durations, and both methods predict that the amplified signal pulse energies will be ~ 100 µJ at short pump pulse durations. The numerical integration code actually calculates the CW output signal power and not the output signal pulse energy directly. To convert the signal power to the signal energy, the calculated CW signal power is multiplied by the pulse duration of the pump. These calculations guided our procurement of the 1-ns duration Nd:YAG pump laser and the 50-mm long MgO:PPLN crystal.

3.2.2 Optical Parametric Oscillation

Optical parametric oscillation is a special case of optical parametric amplification where the nonlinear medium is placed inside an optical resonator which provides the optical feedback responsible for stimulating the amplification process. The optical cavity is often configured in a ring, as the phase matching condition is typically satisfied for light propagating in only one direction through the nonlinear medium. The cavity is typically resonant at the shorter signal wavelength, but can be resonant at either the signal or idler wavelength (singly resonant OPO) or both (doubly resonant OPO) [42].

A schematic of a singly resonant OPO in a ring cavity configuration is shown in Fig. 3.6. OPOs are an attractive alternative to OPAs for a number of reasons. OPOs offer broad wavelength tuning without the need for multiple or broadly tunable signal or idler sources. Wavelength tuning is accomplished by adjusting the phase matching condition of the nonlinear crystal, typically by angle or temperature tuning a birefringent crystal. OPOs also tend to be more efficient, as much larger circulating field strengths can easily be achieved within a resonator [42].
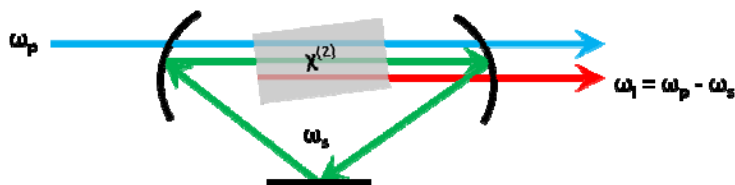
Figure 3.6 Singly resonant optical parametric oscillator employing a ring cavity resonant at the signal wavelength for optical feedback and angle tuning to achieve phase matching.

A commercial OPO was used to pump the first gas-filled HC-PCF laser demonstrated. The OPO produced tunable 1.5-µm wavelength pulses roughly 10 ns in duration with pulse energies up to ~ 10 mJ. The spectral bandwidth of the pulses was ~ 3.5 GHz. While this OPO worked well enough to pump the first ever demonstration of a gas-filled fiber laser based on population inversion, issues with beam quality and frequency instability ultimately limited the usefulness of this particular pump source for gathering precise quantitative data. It was these issues that helped inspire the decision to build the OPA described in the preceding section.

Chapter 4 - Hollow-Core Photonic Crystal Fibers

4.1 Introduction

The first HC-PCF was fabricated in 1999 by researchers at the University of Bath [24]. HC-PCFs generally consist of a hollow, air-filled core surrounded by a periodic microstructured array of smaller holes. The fibers are fabricated in a stack and draw technique where silica tubes are arranged by hand to give the desired structures, fused together, then heated and pulled using vertical draw towers, typically several meters tall [47]. To keep the very delicate structures from collapsing due to surface tension forces, different core and cladding regions in the fibers are often pressured using a gas flow [47].

There are generally two classes of HC-PCFs: photonic band gap fibers (PBGF) and kagome-structured fibers. As the name suggests, PBGF employs a band gap to guide light in its hollow core. Essentially, the cladding structure of the PBGF creates wavelength regions where no photonic states are permitted to exist within the cladding. Therefore, light within this wavelength region is confined to the cladding defect, *i.e.* the hollow core, where it can propagate with low loss [24]. Unfortunately, while narrow-band guidance near 3 μm has been demonstrated in PBGF [48], generally speaking the spectral width of the band gap region is limited to less than the octave we require for our gas-filled fiber lasers [49].

Kagome-structure HC-PCFs on the other hand have been demonstrated to guide multiple octaves with low loss [30]. Kagome HC-PCF [25] guides via a mechanism akin to Von Neumann and Wigner states [50] allowing core and cladding modes to coexist at a given wavelength essentially without coupling to each other (in stark contrast to the PBGF mechanism where low-loss core guidance relies on the existence of regions devoid of cladding states). This salient feature of kagome-structured HC-PCF permits ultra-broad, multi-octave spanning spectral guidance [25], with reasonably low loss (< 1 dB/m) across a broad spectrum. Just recently, kagome fibers with a hypocycloidal core surround have been demonstrated to push the minimum fiber loss of these broadband kagome fibers even lower [51]. Additionally, it has been demonstrated that these fibers can be spliced to solid-core fibers, creating compact, robust sealed gas cells [27]. These self-contained cells could readily be integrated into a wide variety of devices.

29

However, because these fibers are made from fused silica and are typically optimized for performance at visible and near infrared wavelengths, most existing kagome fibers exhibit relatively large loss at mid-IR wavelengths, *e.g.* ~ 20 dB/m at 3.16 μm [33]. Using finite element analysis software like JCMwave to optimize the fiber loss profile, kagome fibers exhibiting low loss regions in both the near and mid-IR can be designed which should be suitable for use in gas-filled fiber lasers operating in the mid-IR. Calculating the fiber loss for these microstructured fibers is computationally intensive and time consuming. Instead collaborators at the University of Bath have gone with a coarser, much quicker approach where empirical rules are used to scale existing designs to create fibers with the desired loss profiles. These fiber designs of varying pitch and strut thicknesses are then sent to us at Kansas State University and characterized via cut-back measurements to map out the fiber loss characteristics at mid-IR wavelengths. The spectral loss data is then provided to our collaborators so that they can continue to tailor the fiber designs to reduce the mid-IR fiber loss and to hopefully extend the guidance to longer wavelengths.

4.2 Measurements of Mid-Infrared Fiber Loss in Hollow Fibers

As we are interested in using gas-filled HC-PCFs to create mid-IR laser sources, it is important to have a quantitative idea of the fibers' loss characteristics in the mid-IR spectral region. After fabrication, collaborators at the University of Bath performed in-house characterizations of the fiber loss using a simple and straightforward cut-back technique.

This technique consists of coupling light from a white light source into one end of a relatively long (~ 10 m or more, typically) length of the fiber under test. Light transmitted through the other end of the fiber is coupled into a commercial optical spectrum analyzer (OSA), where the optical power is spectrally resolved. A length of the fiber is then carefully cut and removed, so as not to disturb the end of the test fiber that is coupled to the light source. The length of fiber that is removed is carefully measured, and the spectrum of the light now being transmitted through the end of the fiber is again measured using the OSA. By comparing the spectra before and after a section of the fiber was cut, the loss through the cut section of fiber can be calculated for all the wavelengths measured. Furthermore, by knowing the exact length of

fiber that was cut, the loss per unit length can be determined. It is this length independent fiber loss that we use to make comparisons between different fibers.

Unfortunately, owing to the combination of the white light source and the commercial OSA used, these quick and convenient loss characterizations of the HC-PCFs are limited to wavelengths within the visible and near infrared ($\sim 500 - 1800$ nm) regions of the spectrum. However, by using an appropriate source and detector the same cut-back technique can be employed to measure fiber losses at mid-IR wavelengths.

Long-wavelength idler pulses from the optical parametric amplifier (OPA) discussed in section 3.2 are used as the tunable mid-IR source. The center-wavelength of the idler pulses can be tuned roughly 1000 nm, from $\sim 2.6 - 3.6$ μm, as is indicated by the tuning curves for the MgO:PPLN crystal shown in Fig. 3.4. This is accomplished by changing the phase-matching condition of the crystal via the optical poling period and crystal temperature. In contrast to how the OPA is run to amplify signal light at ~ 1.5 μm, no seed light is used to generate the idler light described here. Instead, we rely on quantum noise (fluctuations in the average number-density of photons present at the beginning of the crystal) to provide the initial stimulus for down converting pump photons into signal and idler photons in the crystal. While the initial production of signal and idler photons relies on this spontaneous down conversion process, once signal and idler photons are present their numbers increase rapidly as they stimulate the process along the length of the crystal, leading to large pulse energies at the signal and idler wavelengths.

The quantum noise that begins the process is white, meaning fluctuations in the average photon number density per mode are equally probable for all photon wavelengths. This means the pulse bandwidth will no longer be as narrow as when the OPA is seeded with CW signal light (as now we are essentially seeding with white light). The bandwidth is instead limited by the phase-matching condition imposed by the 50-mm long MgO:PPLN nonlinear crystal.

A spectrum of the idler pulses from the unseeded OPA, pumped using 150-μJ energy pulses at a wavelength of 1064 nm, is shown in Fig. 4.1. The spectral bandwidth of the pulse is seen to be about 10 nm. Therefore a $\pm$ 5-nm wavelength error will be assumed for the wavelengths where spectral losses are measured.

A schematic of the setup used to perform cut-back measurements on HC-PCFs at mid-IR wavelengths is shown in Fig. 4.2. An AR-coated germanium filter is used to filter out the pump and signal light from the mid-IR idler pulses produced by the unseeded OPA. A small portion

(a few percent) of the idler pulse energy is then split off from the main beam and sent to a room-temperature HgCdTe detector using a CaF_2 window oriented at ~ 45° to the incident beam. The majority of the idler pulse energy is coupled into one end of the HC-PCF under test using a CaF_2 lens. The other end of the HC-PCF is then positioned directly in front of a thermoelectric cooler (TEC) cooled HgCdTe photodetector, allowing the mid-IR light transmitted through the fiber to be observed with high sensitivity. Measuring the relative pulse energy before and after the fiber allows us to employ a balanced detection scheme, in which we can use the ratio of the two detector signals to produce a signal that is insensitive to fluctuations in the pulse energy emitted from the OPA.
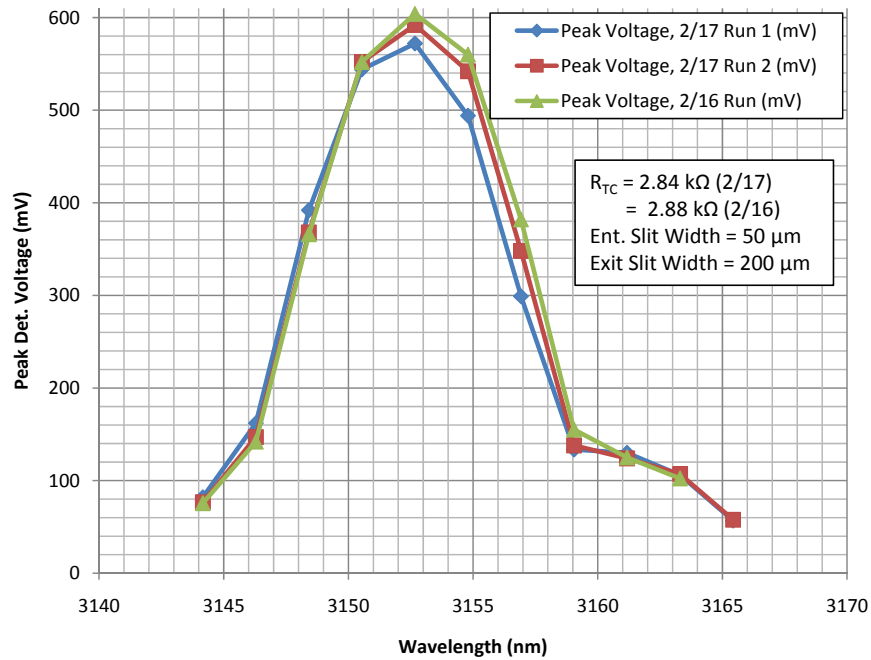
Figure 4.1 Spectrum of the idler-wavelength pulses emitted from the unseeded OPA. The spectral bandwidth in the 3-μm wavelength region is ~ 10 nm (FWHM).

The ends of the test fiber must be prepared prior to coupling any light through the fiber. Because these specialty fibers typically use a tough acrylic buffer instead of a softer polymer buffer, a razor blade is used to strip the buffer from the fiber cladding. This is done by holding the razor blade firmly against the buffer and then pulling the blade toward the fiber's end. This is done three or four times, rotating the fiber after each time to remove the buffer from all sides

of the fiber. With the buffer removed, the stripped region of the fiber is wiped with a dry lint-free optical tissue in preparation for cleaving. Precision fiber cleavers meant for standard fibers usually cannot be used, as these HC-PCFs have variable and nonstandard cladding diameters. Instead, flexible fiber optic field cleavers like those made by FIS or FITEL work quite well. Hand scoring with a ceramic tile or diamond tipped scoring tool has also been used to achieve uniform flat cleaves. After cleaving, the fiber ends are placed in a fiber splicer so that the cleaves can be inspected. If the cleaves are uniform and flat, the fiber is placed in the measurement setup. If not, the cleaving and inspection procedure is repeated until the fiber ends look satisfactory.
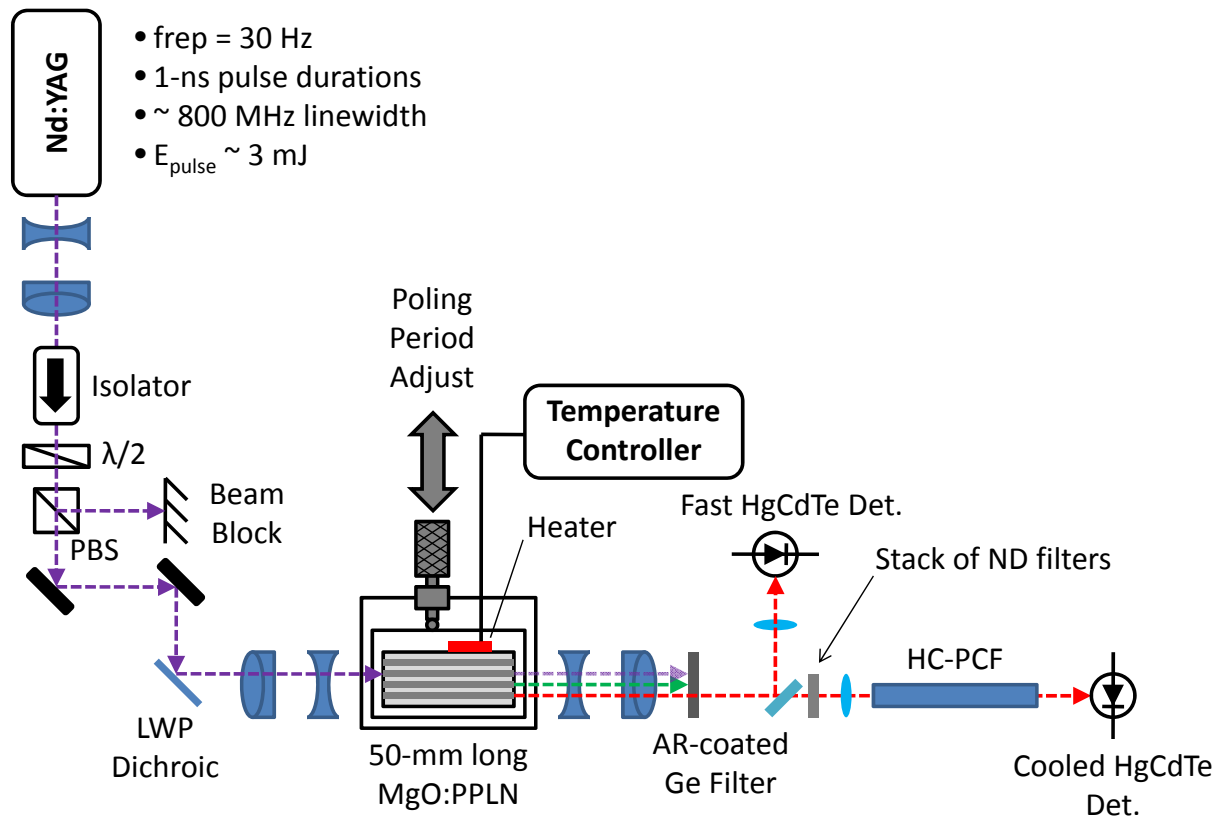
Figure 4.2 Setup used to perform cut-back measurements on HC-PCFs at mid-IR wavelengths. Idler pulses transmitted through the fiber are observed using a high-sensitivity TEC-cooled HgCdTe photodetector. The signal measured after the fiber is used in conjunction with the signal measured from the room-temperature HgCdTe detector before the fiber to remove effects from fluctuations in the idler pulse energies from the OPA.

With the fiber ends cleaved and free of any debris, the ends are securely supported using grooved fiber clamps. Mid-IR light is then coupled through the fiber. A 5-axis fiber stage is used to adjust the position of the fiber end relative to the CaF_2 focusing lens in order to optimize the OPA-to-fiber coupling.

The center wavelength of the idler pulses can be set to any wavelength within the ~ 2.6 – 3.6 μm tuning range of the OPA. While measuring the fiber loss continuously across this entire wavelength region is highly desirable, it is not very practical owing to the very long measurement times associated with tuning the OPA wavelengths. The largest factor impacting the measurement time is the speed at which the crystal temperature can be tuned. To ensure that the 50-mm long MgO:PPLN crystal is not thermally shocked, the crystal's temperature is not increased or decreased faster than 10 °C/minute. Furthermore, it can take several minutes for the crystal temperature to stabilize after the desired temperature is initially reached.

In lieu of a continuous scan, fiber losses are measured at 20 different wavelengths corresponding to 5 crystal temperatures between 35 and 145 °C and 4 different crystal poling periods from 30.0 to 31.5 μm, spaced by 0.5 μm. Table 4.1 shows the wavelengths that are typically measured along with the corresponding crystal temperature and poling period. The wavelength produced at a specific crystal temperature and poling period is calculated directly by solving the phase matching equation for the MgO:PPLN crystal given by Eq. 3.9 using the Mathematica code shown in Appendix A (the phase matched signal and idler wavelengths are plotted in Fig. 3.4).

The fiber loss measurement procedure begins by setting the crystal temperature and allowing it to stabilize. The temperature is adjusted using a DC power supply connected to two flexible silicon heaters which are attached to the aluminum crystal mount. The crystal temperature is shown on a digital read out connected to a resistance temperature detector (RTD) which thermally contacts the top of the crystal mount.

While the temperature is stabilizing, the crystal poling period and fiber end position are optimized. The optimum position of the crystal is determined by maximizing the signal amplitude from the room-temperature HgCdTe detector just before the fiber. Once the crystal position is optimized, the fiber end position is adjusted via the 5-axis fiber stage to maximize the signal amplitude from the TEC-cooled HgCdTe photodetector after the fiber. This

Table 4.1 Summary of the wavelengths (in ascending order) used in HC-PCF loss measurements along with the corresponding unseeded OPA crystal configuration required.

Wavelength (µm)	MgO:PPLN Crystal Temperature (°C)	MgO:PPLN Crystal Poling Period (µm)	Wavelength Cont.	MgO:PPLN Crystal Temperature Cont.	MgO:PPLN Crystal Poling Period Cont.
2.585	145.0	31.5	3.202	145.0	30.5
2.669	125.0	31.5	3.246	125.0	30.5
2.756	100.0	31.5	3.297	100.0	30.5
2.844	70.0	31.5	3.351	70.0	30.5
2.928	35.0	31.5	3.407	35.0	30.5
2.936	145.0	31.0	3.431	145.0	30.0
2.991	125.0	31.0	3.469	125.0	30.0
3.053	100.0	31.0	3.513	100.0	30.0
3.119	70.0	31.0	3.560	70.0	30.0
3.185	35.0	31.0	3.610	35.0	30.0

photodetector includes a built in amplifier to increase its sensitivity, allowing us to measure the loss through ~ 1-m long fibers that have very large attenuations (~ 100 dB/m). To ensure the photodetector does not saturate, combinations of reflective nickel-coated fused silica neutral density filters are used to attenuate the mid-IR light just before the CaF_2 lens used to couple the light into the fiber.

Selecting the appropriate combination of filters is very important and somewhat time intensive. To avoid having to perform and rely on filter calibrations for every filter (~ 10 total) at 20 different wavelengths, the same filters are used for signal measurements made both before and after the fiber is cut. This also precludes signal variations that may arise from coupling changes into the fiber occurring as a result of different filter combinations (which would not be accounted for simply by measuring the individual filters' transmissions).

The filter values are carefully chosen so that the amount of light transmitted through the fiber is high enough to create a voltage signal that can be clearly observed above the photodetector's noise floor, but not so high that once a length of the fiber is cut, the resulting

voltage signal would saturate the detector, requiring the use of additional filters. For our particular detection system, filter values are chosen to keep the signal amplitude observed from the TEC-cooled HgCdTe photodetector between 10 and 20 mV. The detector saturates at output voltages above ~ 1 V. The maximum total loss that can be measured using this dynamic range is ~ 20 dB. However, because we can choose to cut as little fiber as we like, fiber losses of ~ 100 dB/m can easily be measured simply by using a short initial length of fiber and cutting ~ 20 cm or less at a time.

Occasionally the amount of light transmitted through the fiber is too high after a length of the fiber is cut, and the photodetector will begin to show saturation indicated by clipping of the voltage near the peak of the signal from the transmitted pulse. When this happens another filter is added to the set of filters already present in front of the fiber, so that the signal measured after the fiber is no longer saturated. This now unsaturated photodetector signal measured after the fiber is used to calibrate one additional filter, by measuring how the signal amplitude changes with and without this one additional filter as measured on the photodetector after the fiber. Once the calibration is complete, the extra uncalibrated filter is removed, and the additional calibrated filter is left in place along with the set of filters that was used in the measurement before the fiber was cut.

With the temperature stabilized, the crystal position optimized, and the filter values set, the voltage signals from the photodetectors before and after the fiber are measured, and the 100-pulse average of the ratio of the transmitted pulse signal amplitude to the incident pulse signal amplitude is computed by the Tektronics CSA7404 oscilloscope. For a given fiber length, this measurement is repeated for all 4 poling periods and all 5 crystal temperatures. To compute the fiber loss, a signal must be measured through at least two different fiber lengths and the signals compared. Typically two complete cut-back measurements are performed on the test fiber, which requires signals to be measured through three different fiber lengths. By measuring the loss from multiple cut-back measurements, a quantitative estimate can be made of the error associated with the measured fiber losses.

A simplified schematic of the two cut-back measurement process is shown in Fig. 4.3. Signal S_A corresponds to the ratio of the transmitted to incident voltage amplitudes measured using the initial, uncut length of fiber. Signal S_B corresponds to the same ratio measured after cutting a length of fiber, ΔL_{AB}, with the same neutral density filters present before the fiber's

input as were used when measuring S_A. This constitutes one complete cut-back. Now without changing the fiber length, signal $S_{B'}$ is measured using additional filters before the fiber's input in order to decrease the voltage amplitude measured on the photodetector after the fiber to within the $10 - 20$ mV range as was done prior to measuring S_A before the fiber was first cut. With the new filter values still in place, another length of fiber, ΔL_{BC}, is removed, and the resulting signal, $S_{C'}$, is measured. If no additional filters are needed after measuring S_B, then this single measurement value is used for comparison with S_A and $S_{C'}$ (where the prime is not really necessary in this case as the same filters are used for all three fiber lengths).
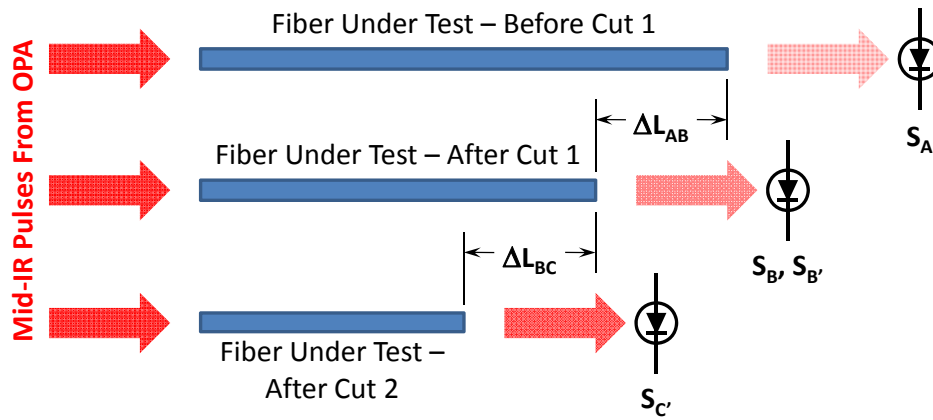
Figure 4.3 Simplified schematic of the typical measurement process for performing two cut-back measurements. The signals S_A, S_B, $S_{B'}$, and $S_{C'}$ are the ratio of the voltage amplitudes from the pulse transmitted through the fiber to that of the incident pulse. The primes indicate that the combination of neutral density filters at the fibers input may have changed from the combination used when the unprimed signals were measured.

The fiber loss, FL_{xy}, is computed using the expression,

$$FL_{xy} = -10 \cdot \log_{10}\left(\frac{S_x}{S_y}\right)\Big/\Delta L_{xy} \qquad 4.1$$

where S_x and S_y represent the measured signals, and ΔL_{xy} is the length of fiber that was cut between measuring the two signals. The so-called average fiber loss, $\langle FL \rangle$, is computed from the

average transmission after scaling the measured transmissions to a 1-m length of fiber, and is given in units of dB/m by,

$$\langle FL \rangle = -10 \cdot \log_{10}\left(10^{-FL_{xy}/10} + 10^{-FL_{yz}/10} + \cdots\right) + 10 \cdot \log_{10}(N) \qquad 4.2$$

where N is the total number of cut-back measurements performed. For most of the measurements presented here only two cut-backs were performed, simplifying the above expression to,

$$\langle FL \rangle = -10 \cdot \log_{10}\left(10^{-FL_{AB}/10} + 10^{-FL_{BC}/10}\right) + 10 \cdot \log_{10}(2) \qquad 4.3a$$

$$= -10 \cdot \log_{10}\left(\left(\frac{S_A}{S_B}\right)^{1/\Delta L_{AB}} + \left(\frac{S_{B'}}{S_{C'}}\right)^{1/\Delta L_{BC}}\right) + 10 \cdot \log_{10}(2) \qquad 4.3b$$

The measured fiber losses are plotted together with the average fiber loss for kagome-structured and hypocyloidal HC-PCFs with different pitches and core diameters in the following sections. Table 4.2 provides a summary of the HC-PCF fibers whose mid-IR loss characteristics were

Table 4.2 Summary of HC-PCFs received from the Gas-Phase Photonic Materials group at the University of Bath and used in mid-IR fiber loss measurements. All fibers listed were received September of 2011.

Part Number/Structure	Core Diameter (µm)	Pitch (µm)	Defect (# of missing cells)	# of rings in cladding	Loss at 1550 nm (dB/m)
110727-CFD-K7C3R-C11J11/Kagome	85 – 94	18.75	7	3	0.122
110708-CFD-K7C3R-C5J5/Kagome	87.5 – 92.5	20	7	3	0.237
110727-CFD-K7C3R-C3J16/Kagome	85 – 93.75	22.5	7	3	0.03
110903-CFD-K7C3R-C20J8/Kagome	112.5 – 137.5	31.25	7	3	0.267
110811-YYW1R-D1C6B2/Hypocycloid	58	32	1	1	–
110811-YYW1R-D1C6B1/Hypocycloid	64	42	1	1	4

studied. These fibers were generously provided to us by Dr. Fetah Benabid, head of the Gas-Phase Photonic Materials group at the University of Bath. All six fibers were received September of 2011.

4.2.1 7-Cell, 3-Ring, 18.75-µm Pitch Kagome-Structured HC-PCF

Figure 4.4a shows the cross section of fiber 110727-CFD-K7C3R-C11J11 viewed with an optical microscope. From this image three rings of kagome cladding structure resembling a star-of-David pattern can clearly be seen surrounding the hollow core region. The fiber's hollow core is created by leaving out the center and the six adjacent hexagonal unit cells from the kagome cladding structure during fabrication, leaving a 7-cell defect. The core diameter ranges from $\sim 85 - 93.75$ µm, and the outer diameter of the solid glass cladding is 300 µm. The pitch of the fiber is defined as the spacing between adjacent unit cells, and for this fiber is 18.75 µm. The measured near-IR loss spectrum of the fiber is shown in Fig. 4.4b, from which the loss in the wavelength region near 1.5 µm is seen to be below 122 dB/km.
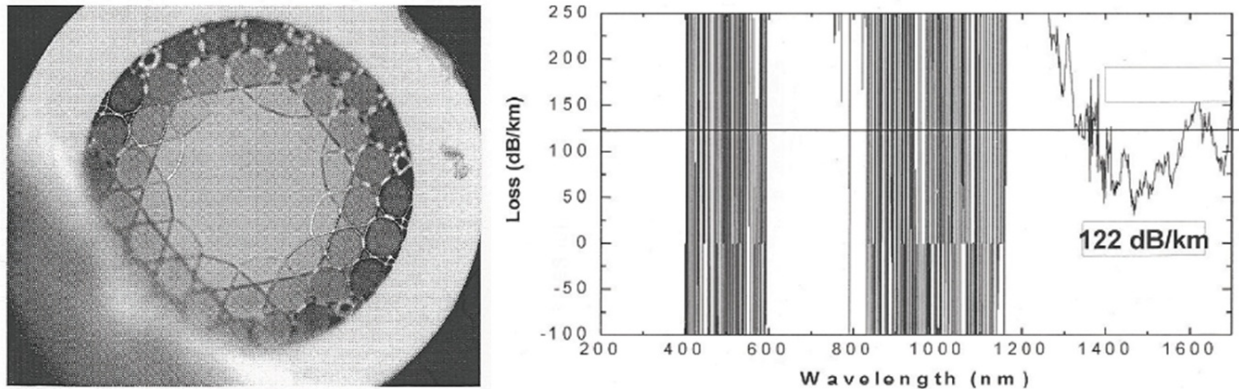
Figure 4.4 7-Cell, 3-Ring, 18.75-µm pitch kagome-structured HC-PCF (a) cross section and (b) near IR loss spectrum. Both the image and the loss spectrum were taken at the University of Bath by collaborators and are reproduced from Ref [52].

The fiber's measured loss spectrum in the mid-IR is shown in Fig. 4.5. Only one cut-back was performed for this particular fiber. The initial length of the fiber was ~ 2 m, and 47.6 ± 0.1 cm of fiber was cut. This was the first fiber characterized using the mid-IR fiber loss setup.

The fiber loss is ~ 2.5 dB/m near 2.6 μm and generally increases with the wavelength to a maximum loss of ~ 20 dB/m near 3.6 μm. The measured fiber loss is ~ 5 dB/m for wavelengths near 3.14 μm. This marks a ~ 15 dB/m reduction in the mid-IR loss compared to the fiber initially used in the gas-filled fiber laser setup, and so this 18.75-μm pitch fiber was placed in the laser setup with the expectation that lasing in this fiber would show improved performance over results from the higher-loss fiber first used. Laser results achieved using this fiber are described in detail in Chapter 6.

18.75-μm Pitch 7 Cell, 3 Ring Kagome Fiber Loss
Fiber ID: 110727-CFD-K7C3R-C11J11, Core: 85/93.75 μm
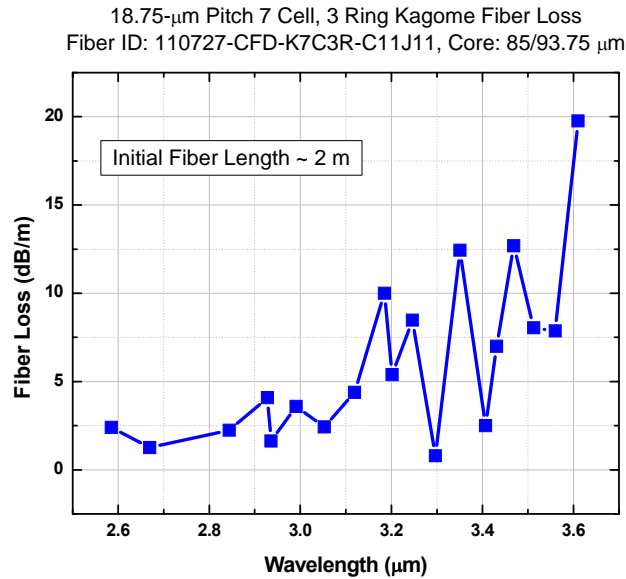
Figure 4.5 Mid-IR fiber loss from a 7-Cell, 3-Ring, 18.75-μm pitch kagome-structured HC-PCF. Only one cut-back was performed. The initial fiber length was ~ 2 m, and the length of fiber cut was 47.6 ± 0.1 cm. This image is reproduced from Ref [34].

4.2.2 7-Cell, 3-Ring, 20-μm Pitch Kagome-Structured HC-PCF

The cross section of fiber 110708-CFD-K7C3R-C5J5 viewed with an optical microscope is shown in Fig. 4.6a. Three rings of kagome-structured cladding surround this fiber's 7-cell defect hollow core, and the fiber pitch is 20 μm. The hollow core diameter ranges from ~ 87.5 – 92.5 μm, and the outer diameter of the solid glass cladding is again 300 μm. The measured near-IR loss spectrum of the fiber is shown in Fig. 4.6b. The fiber loss in the wavelength region near 1.5 μm is seen to be below 237 dB/km.
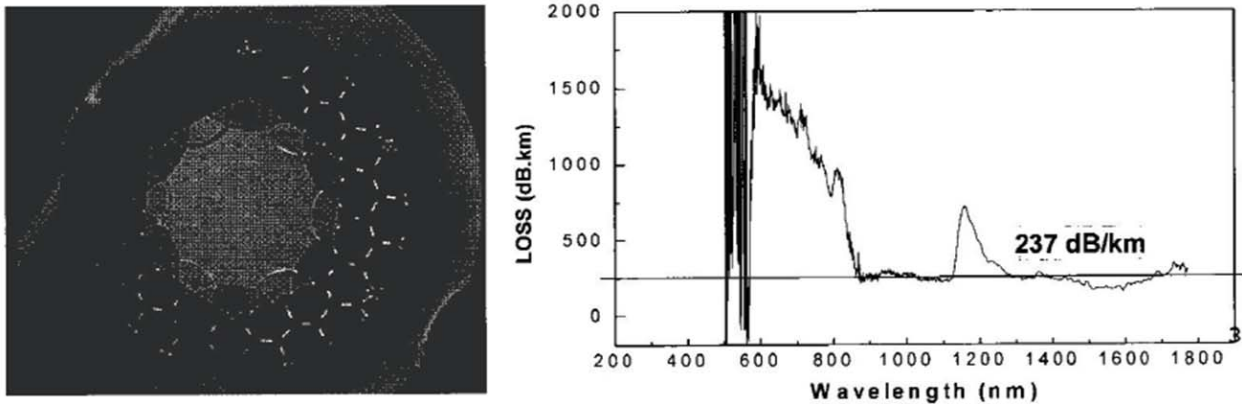
Figure 4.6 7-Cell, 3-Ring, 20-μm pitch kagome-structured HC-PCF (a) cross section and (b) near IR loss spectrum. Both the image and the loss spectrum were taken at the University of Bath by collaborators and are reproduced from Ref [52].

The fiber's measured loss spectrum in the mid-IR is shown in Fig. 4.7. Two cut-back measurements were performed. The red and blue data show the fiber losses measured from the individual cut-backs, while the green data shows the average fiber loss computed using Eq. 4.3b. The initial length of the fiber was ~ 10 m. The length of fiber cut during the first cut-back was 76.5 ± 0.1 cm, and the length of fiber cut during the second cut-back was 1.773 m ± 0.1 cm.

The fiber loss is ~ 1 dB/m near 2.6 μm and generally increases with the wavelength to a maximum loss below 10 dB/m near 3.6 μm. The measured fiber loss is below 3 dB/m for wavelengths between ~ 2.6 and 3.2 μm, marking a further improvement over the loss of the 18.75-μm pitch fiber near the mid-IR lasing wavelengths of interest. One of the cut-back measurements showed a negative fiber loss (gain), indicating more light was observed before the fiber was cut than after. This is clearly not indicative of the actual fiber loss, and while the source of the fluctuation is not known, it may be related to modal fluctuations in the unseeded OPA output, or fluctuations in the center wavelength from the OPA near spectral regions in the fiber with vastly different losses.

20.0-μm Pitch 7 Cell, 3 Ring Kagome Fiber Loss
Fiber ID: 110708-CFD-K7C3R-C5J5, Core: 87.5/92.5 μm
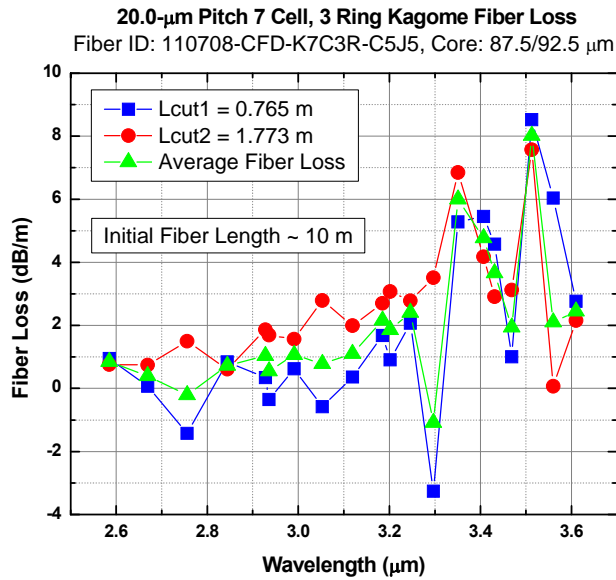
Figure 4.7 Mid-IR fiber loss from a 7-Cell, 3-Ring, 20-μm pitch kagome-structured HC-PCF. The fiber loss data shown in blue and red correspond to measurements from the individual cut-backs. The average fiber loss is shown in green. The initial fiber length was ~ 10 m, and the lengths of fiber cut were 76.5 ± 0.1 cm (blue data) and 1.773 m ± 0.1 cm (red data).

4.2.3 7-Cell, 3-Ring, 22.5-μm Pitch Kagome-Structured HC-PCF

Figure 4.8a shows an optical microscope image of the cross section of fiber 110727-CFD-K7C3R-C3J16. The fiber again has a kagome-structured cladding comprised of three concentric rings with a 7-cell defect hollow core. The fiber's pitch is 22.5 μm. The hollow core diameter ranges from ~ 85 – 93.75 μm, and the outer diameter of the solid glass cladding is 300 μm. The measured near-IR loss spectrum of the fiber is shown in Fig. 4.8b, from which the loss in the wavelength region near 1.5 μm is seen to be near 32 dB/km.
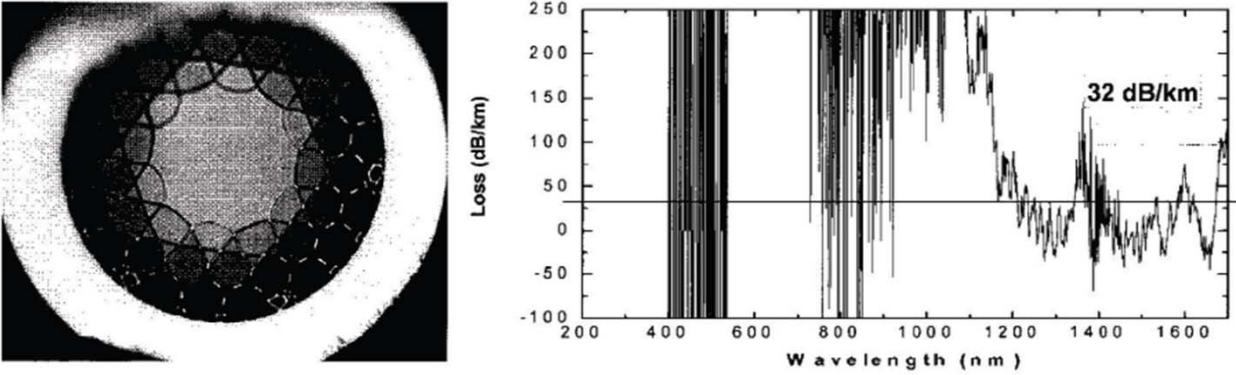
Figure 4.8 7-Cell, 3-Ring, 22.5-µm pitch kagome-structured HC-PCF (a) cross section and (b) near IR loss spectrum. Both the image and the loss spectrum were taken at the University of Bath by collaborators and are reproduced from Ref [52].

The fiber's measured loss spectrum in the mid-IR is shown in Fig. 4.9. Two cut-back measurements were performed. The blue and red data show the fiber losses measured from the individual cut-backs, while the green data shows the average fiber loss computed using Eq. 4.3b. The initial length of the fiber was ~ 10 m. The length of fiber cut during the first cut-back was 83.4 ± 0.1 cm, and the length of fiber cut during the second cut-back was 60.5 ± 0.1 cm.

The fiber loss is below 1 dB/m near 2.6 µm and increases to a loss of ~ 8 dB/m near 3.6 µm. The measured fiber loss is below 5 dB/m for wavelengths between ~ 3.0 and 3.2 µm. There is a large discrepancy in the measured losses at 3.36 µm, producing uncertainty in the average fiber loss reported here which is comparable with the reported loss value itself. The negative fiber loss measured occurs at a slightly longer wavelength than that of the discrepancy observed in the last fiber. It is interesting that both negative values were only seen in the first cut-back, but the source of the error is still not clear.

22.5-µm Pitch 7 Cell, 3 Ring Kagome Fiber Loss
Fiber ID: 110727-CFD-K7C3R-C3J16, Core: 85/93.75 µm
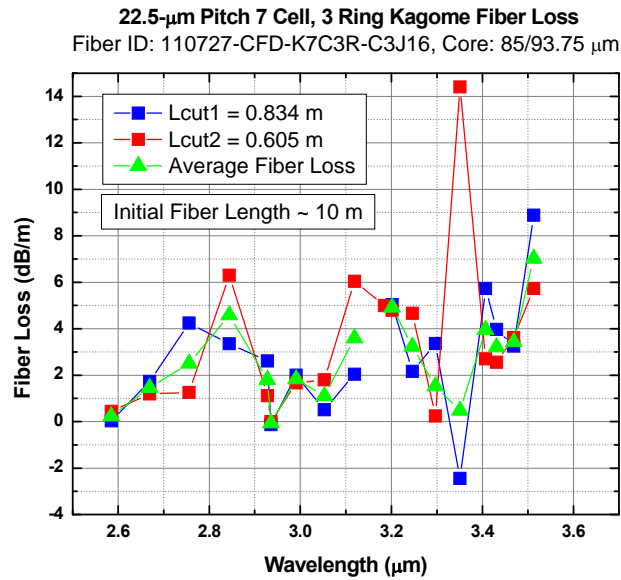
Figure 4.9 Mid-IR fiber loss from a 7-Cell, 3-Ring, 22.5-µm pitch kagome-structured HC-PCF. The fiber loss data shown in blue and red corresponding to measurements from the individual cut-backs. The average fiber loss is shown in green. The initial fiber length was ~ 10 m, and the lengths of fiber cut were 83.4 ± 0.1 cm (blue data) and 60.5 ± 0.1 cm (red data).

4.2.4 7-Cell, 3-Ring, 31.25-µm Pitch Kagome-Structured HC-PCF

Figure 4.10a shows the cross section of fiber 110803-CFD-K7C3R-C20J8 viewed with an optical microscope. This fiber too is made of a 3-ring kagome cladding structure with a 7-cell defect core. The pitch of this fiber is quite large at 31.25 µm. The fiber's hollow core diameter ranges from ~ 112.5 – 137.5 µm, and the outer diameter of the solid glass cladding is 400 µm. The measured near-IR loss spectrum of the fiber is shown in Fig. 4.10b, from which the loss in the wavelength region near 1.5 µm is seen to be near 267 dB/km.

44
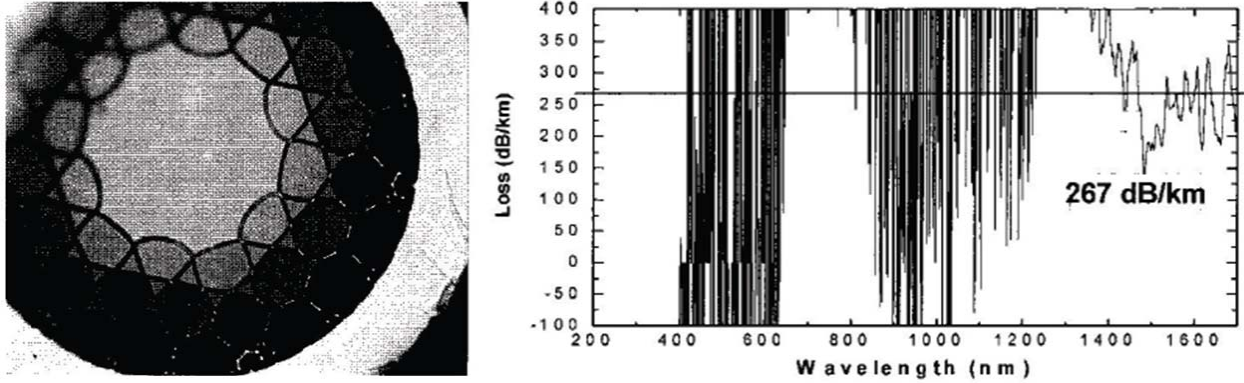
Figure 4.10 7-Cell, 3-Ring, 31.25-µm pitch kagome-structured HC-PCF (a) cross section and (b) near IR loss spectrum. Both the image and the loss spectrum were taken at the University of Bath by collaborators and are reproduced from Ref [52].

The fiber's measured loss spectrum in the mid-IR is shown in Fig. 4.11. Two cut-back measurements were performed. The blue and red data show the fiber losses measured from the individual cut-backs, while the green data shows the average fiber loss computed using Eq. 4.3b. The initial length of the fiber was ~ 10 m. The length of fiber cut during the first cut-back was 1.136 m ± 0.1 cm, and the length of fiber cut during the second cut-back was 46.1 ± 0.1 cm.

The fiber loss is ~ 5 dB/m near 2.6 µm and reaches to ~ 20 dB/m near 3.31 µm before dropping to ~ 10 dB/m near 3.6 µm. The measured fiber loss is between ~ 5 and 15 dB/m for wavelengths between ~ 3.1 and 3.14 µm. Several of the losses measured during the second cut-back are below zero. This is clearly not indicative of the actual fiber loss, and may be the result of coupling into different guided modes before the fiber was cut compared with after the fiber was cut. The modest loss of the fiber combined with its much larger core diameter make it less desirable for use in the gas-filled fiber laser than the lower loss, smaller diameter kagome-structured fibers tested, whose results are shown above.

45

31.25-μm Pitch 7 Cell, 3 Ring Kagome Fiber Loss
Fiber ID: 110903-CFD-K7C3R-C20J8, Core: 112.5/137.5 μm
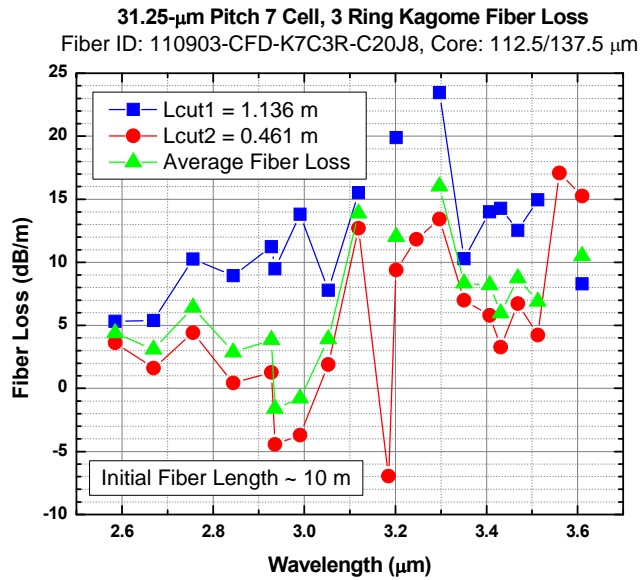
Figure 4.11 Mid-IR fiber loss from a 7-Cell, 3-Ring, 31.25-µm pitch kagome-structured HC-PCF. The fiber loss data shown in blue and red corresponding to measurements from the individual cut-backs. The average fiber loss is shown in green. The initial fiber length was ~ 10 m, and the lengths of fiber cut were 1.136 m ± 0.1 cm (blue data) and 46.1 ± 0.1 cm (red data).

The next fibers discussed are based on kagome-structured fibers with a unique hypocycloidal core-cladding boundary shape. This hypocycloidal core surround has been demonstrated to further decrease the fiber loss characteristics of kagome fibers while still permitting ultra-broad band guidance [53].

4.2.5 1-Cell, 1-Ring, 32-µm Pitch Hypocycloidal HC-PCF

Figure 4.12 shows the cross section of fiber 110701-YYW1R-D1C6B2 viewed with an optical microscope, where the hypocycloidal shape of the fused silica structure present at the core-cladding boundary can be seen quite clearly. The cladding is comprised of just one ring, and the core is a single-cell defect. The fiber's pitch is 32 μm. The hollow core is ~ 58 μm in diameter, and the outer diameter of the solid glass cladding is substantially smaller than that of the

46

previously characterized kagome-structured HC-PCFs, at just ~ 200 μm. The near-IR loss spectrum of this fiber was not measured.
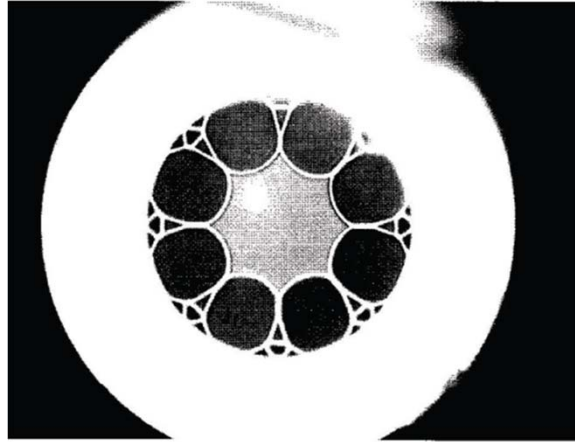
Figure 4.12 1-Cell, 1-Ring, 32-μm pitch hypocycloidal HC-PCF cross section. The optical microscope image was taken at the University of Bath by collaborators and is reproduced from Ref [52].

The fiber's measured loss spectrum in the mid-IR is shown in Fig. 4.13. Two cut-back measurements were performed. The blue and red data show the fiber losses measured from the individual cut-backs, while the green data shows the average fiber loss computed using Eq. 4.3b. The initial length of the fiber was ~ 3 m. The length of fiber cut during the first cut-back was 75.0 ± 0.1 cm, and the length of fiber cut during the second cut-back was 1.06 m ± 0.1 cm.

Unlike the kagome-structured fibers with non-hypocycloidal core surrounds, the fiber loss here is generally highest for shorter wavelengths (~ 17 dB/m near 2.6 μm) and decreases as the wavelength increases to ~ 5 dB/m near 3.6 μm. The average fiber loss in the wavelength region of interest between 3.0 and 3.2 μm is between ~ 10 and 3 dB/m. The core diameter of this hypocycloidal fiber is smaller, which makes it attractive for use in the gas-filled fiber laser as smaller mode areas produce higher intensities, all other things being equal. However, there are large disparities between the two cutback measurements over nearly the entire measurement region, at all but the longest wavelengths, making me wary of using this fiber for anything except further cut-back measurements.

32-μm Pitch 1 Cell, 1 Ring Hypocycloidal Kagome Fiber Loss
Fiber ID: 110811-YYW1R-D1C6B2, Core: 58 μm
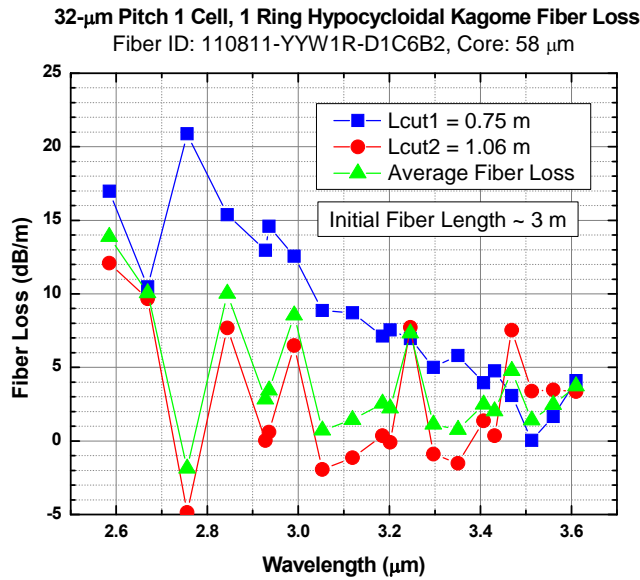
Figure 4.13 Mid-IR fiber loss from a 1-Cell, 1-Ring, 32-μm pitch hypocycloidal HC-PCF. The fiber loss data shown in blue and red correspond to measurements from the individual cut-backs. The average fiber loss is shown in green. The initial fiber length was ~ 3 m, and the lengths of fiber cut were 75.0 ± 0.1 cm (blue data) and 1.06 m ± 0.1 cm (red data).

4.2.6 1-Cell, 1-Ring, 42-μm Pitch Hypocycloidal HC-PCF

Figure 4.14a shows the cross section of fiber 110811-YYW1R-D1C6B1 viewed with an optical microscope. This fiber also has a 1-cell defect core with a 1-ring cladding, where the hypocycloidal shape of the fused silica structure present at the core-cladding boundary is again clearly visible. The fiber's pitch is 42 μm. The fiber's hollow core is ~ 64 μm in diameter, and the outer diameter of the solid glass cladding is about the same as for the smaller pitch kagome fibers at ~ 300 μm. The measured near-IR loss spectrum of the fiber is shown in Fig. 4.14b, from which the loss at wavelengths near 1.5 μm is seen to be ~ 5 dB/m. This is at least an order of magnitude higher than the losses from the kagome fibers.

The fiber's measured loss spectrum in the mid-IR is shown in Fig. 4.15. Two cut-back measurements were performed. The blue and red data show the fiber losses measured from the individual cut-backs, while the green data shows the average fiber loss computed using Eq. 4.3b.

The initial length of the fiber was ~ 5 m. The length of fiber cut during the first cut-back was 80.2 ± 0.1 cm, and the length of fiber cut during the second cut-back was 2.017 m ± 0.1 cm.
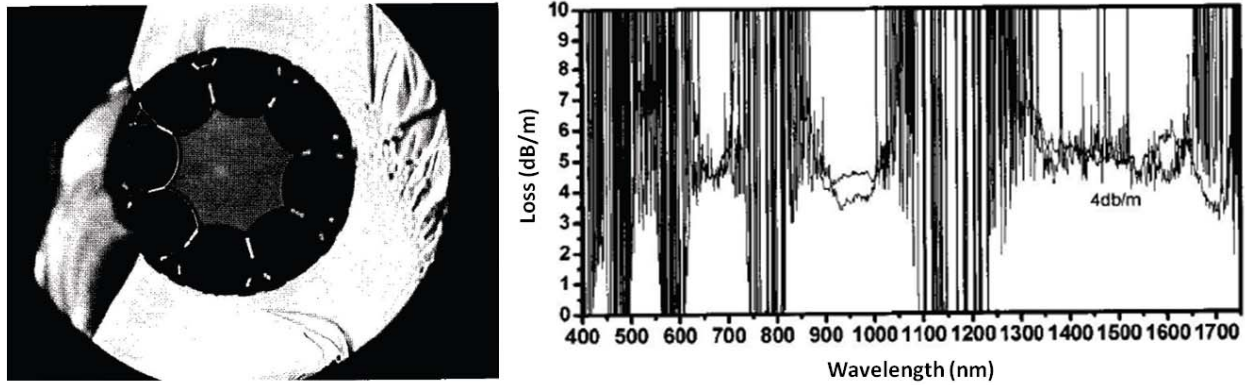
Figure 4.14 1-Cell, 1-Ring, 42-µm pitch hypocycloidal HC-PCF (a) cross section and (b) near IR loss spectrum. Both the optical microscope image and the loss spectrum were taken at the University of Bath by collaborators and are reproduced from Ref [52].

The average fiber loss is seen to be small (below 5 dB/m) and very flat across the entire wavelength region measured. There are large discrepancies at wavelengths below 3 µm, but the two cut-back measurements agree quite well from ~ 3.0 − 3.6 µm, which includes the wavelengths of interest for the C_2H_2 and HCN-filled fiber lasers. Because the loss near the laser wavelengths is only a few dB/m, this fiber will be used in the next round of gas-filled fiber laser measurements.

In addition to measuring the mid-IR fiber loss, initial measurements of the mid-IR fiber mode profile were made using equipment at the National Institute for Standards and Technology (NIST) in Boulder, Colorado. The measurement setup is shown in Fig. 4.16. CW mid-IR light at ~ 3.3 µm is generated by mixing ~ 250 mW of 1555 nm light with ~ 100 mW of 1053 nm light in a fiber-coupled ridge waveguide PPLN crystal. The output fiber from the device is a fluoride-doped fiber which provides reasonable low-loss guidance at mid-IR wavelengths. The mid-IR light is coupled from the fluoride-doped fiber to free space and then into the 42-µm pitch hypocycloidal fiber using uncoated CaF_2 lenses. The input side of the hypocycloidal fiber is positioned with a 5-axis stage for optimal coupling. The other end of the fiber is placed in front

of an IRC191 thermal camera which employs a liquid-nitrogen cooled, 20-μm pitch 640 x 512 pixel InSb focal plane array.
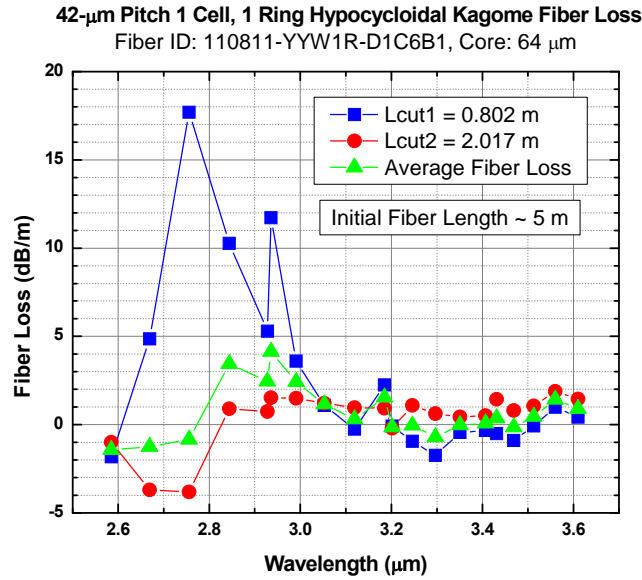
Figure 4.15 Mid-IR fiber loss from a 1-Cell, 1-Ring, 42-μm pitch hypocycloidal HC-PCF. The fiber loss data shown in blue and red corresponding to measurements from the individual cut-backs. The average fiber loss is shown in green. The initial fiber length was ~ 5 m, and the lengths of fiber cut were 80.2 ± 0.1 cm (blue data) and 2.017 m ± 0.1 cm (red data).

An image of the 3.3-μm wavelength mode profile from the 42-μm pitch hypocycloidal fiber is shown in Fig. 4.17. The image was taken by placing the fiber end as close to the camera's input window as possible, and is magnified some from the camera optics. The mode shows reasonably good azimuthal symmetry. More importantly, as the mid-IR coupling is changed by adjusting the fiber's end position via the 5-axis stage, the mode profile is not seen to change noticeably. This is a strong indication that the mid-IR guidance is fairly single mode. This near single mode guidance is highly desirable as it may help reduce fluctuations currently seen in the mid-IR pulse energy produced from the gas-filled fiber lasers.
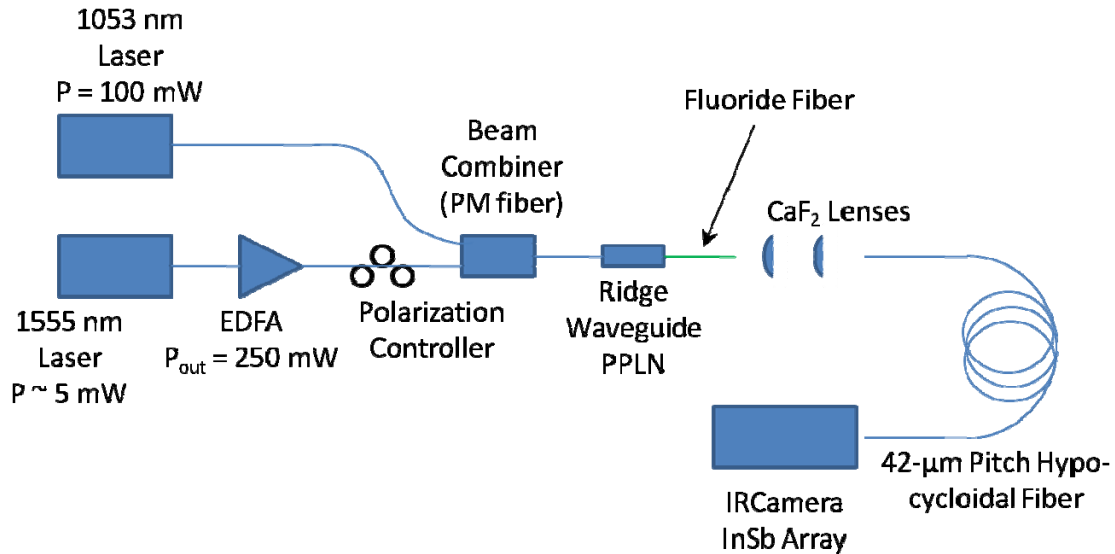
Figure 4.16 Setup used to observe mid-IR mode profile from a 42-µm pitch hypocycloidal HC-PCF. Light at 3.3 µm is generated by mixing 1555 nm and 1053 nm light in a fiber-coupled ridge waveguide PPLN crystal. The mid-IR output is coupled from the fluoride-doped output fiber to free space and then into the hypocycloidal fiber using CaF₂ optics. The mode from the hypocycloidal fiber is imaged directly from the fiber's end using an IRC191 thermal camera, employing a liquid-nitrogen cooled, 20-µm pitch 640 x 512 pixel InSb focal plane array.
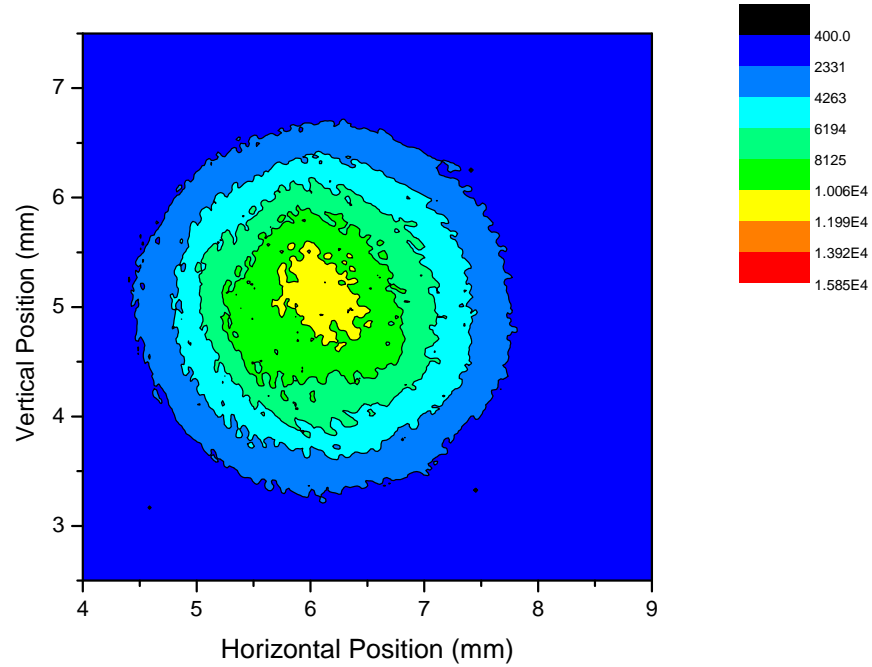
Figure 4.17 Mid-IR mode profile from a 42-µm pitch hypocycloidal HC-PCF. The shape of the profile is not seen to noticeably change when the coupling into the fiber is widely adjusted.

Chapter 5 - Lasers Based on Population Inversion from Gas-Filled Hollow Core Fibers: Initial Results

5.1 Introduction

The first demonstration of laser emissions from population inversion in a gas-filled HC-PCF took place in Dr. Wolfgang Rudolph's lab at the Univeristy of New Mexico in October of 2009. Following promising results from initial mid-IR fiber loss measurements we conducted in the same lab a month or so prior, it seemed we had the best chance for a successful demonstration if we combine the HC-PCF fiber setups and associated expertise we had at Kansas State Univeristy with the high power OPO pump source and OPGL expertise afforded by Dr. Rudolph's group. So I loaded up my Honda hatchback with our HC-PCF vacuum chamber setup, pressure gauges, various optics and photodetectors, and several hollow-core fibers and drove 12 hours and 700 miles from Manhattan, Kansas to Alberquerque, New Mexico. Results from the initial experiments performed during this and one subsequent trip are presented in Ref [33] and are discussed in detail in the following section.

5.2 First Demonstrations of C_2H_2 and HCN-Filled Fiber Lasers

The laser setup is shown in Fig 5.1. The heart of the laser is the 1.65-m long kagome-structure HC-PCF waveguide, which both contains the gas-phase gain medium and serves as the laser cavity by guiding only emissions that coincide with the guided mode(s) of the fiber, effectively providing the spectral and spatial feedback enabling coherent laser oscillation. Both ends of the kagome fiber are supported inside vacuum chambers within 1 cm of the vacuum windows, as shown in the Fig. 5.1 inset, allowing light to be coupled through the evacuated fiber. BK7 glass optics are used to couple ~ 1.5-μm wavelength pump light into the fiber. CaF_2 optics are used to couple light out of the fiber, so that both the transmitted pump and the generated mid-IR light can be transmitted, focused, and collimated with negligible material absorption. Polished germanium wafers are used to filter transmitted pump light from the mid-IR laser pulses exiting the fiber. Transmission curves for all three of these optical materials are shown in Fig. 5.2.
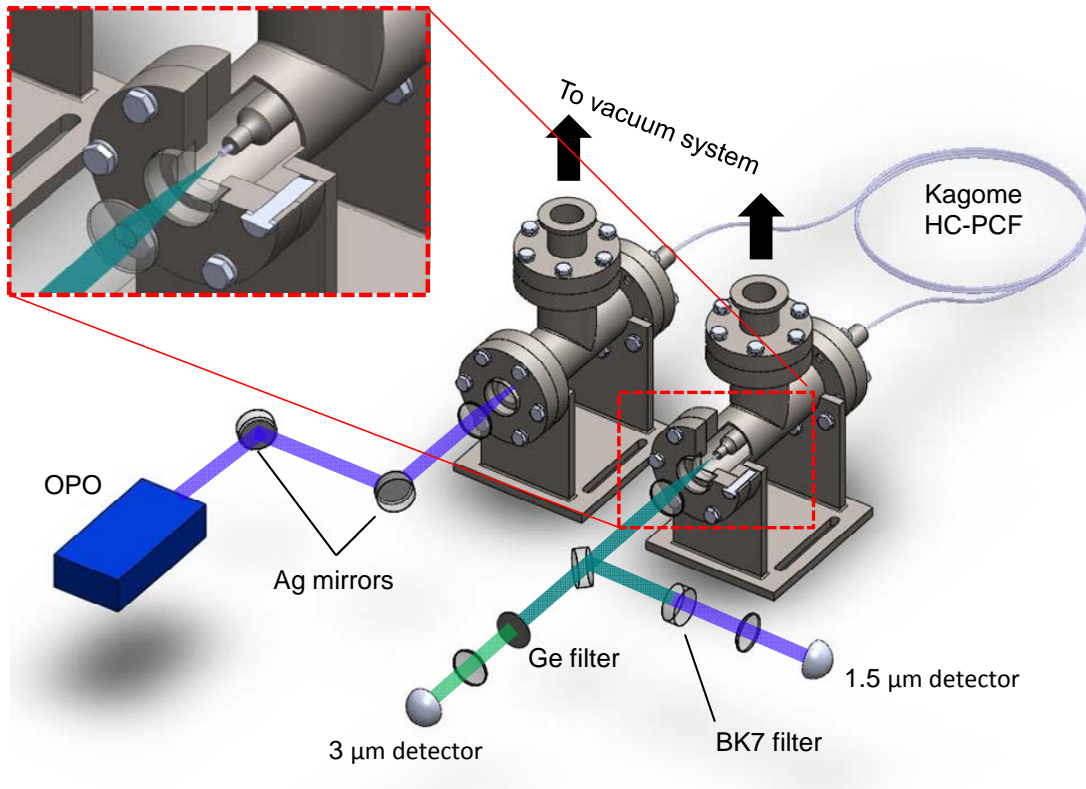
Figure 5.1 Experimental setup for OPO-pumped gas-filled hollow-core fiber laser. Pulses from an optical parametric oscillator (shown in blue) with center wavelengths of ~ 1.5 μm and 5-ns duration are coupled into a kagome-structured HC-PCF containing low pressure (< 20 torr) acetylene gas. Pump radiation excites overtone vibrations in the gas which relax to fundamental ro-vibrational states while undergoing stimulated emission, producing mid-IR wavelength laser pulses (shown in green). Unabsorbed pump light transmitted through the fiber is detected using a fast InGaAs detector. Laser energy is filtered from pump energy by a polished germanium wafer and detected by a fast, room-temperature HgCdTe photovoltaic detector. Inset: Close-up partial cutaway showing a fiber end suspended inside a vacuum chamber.
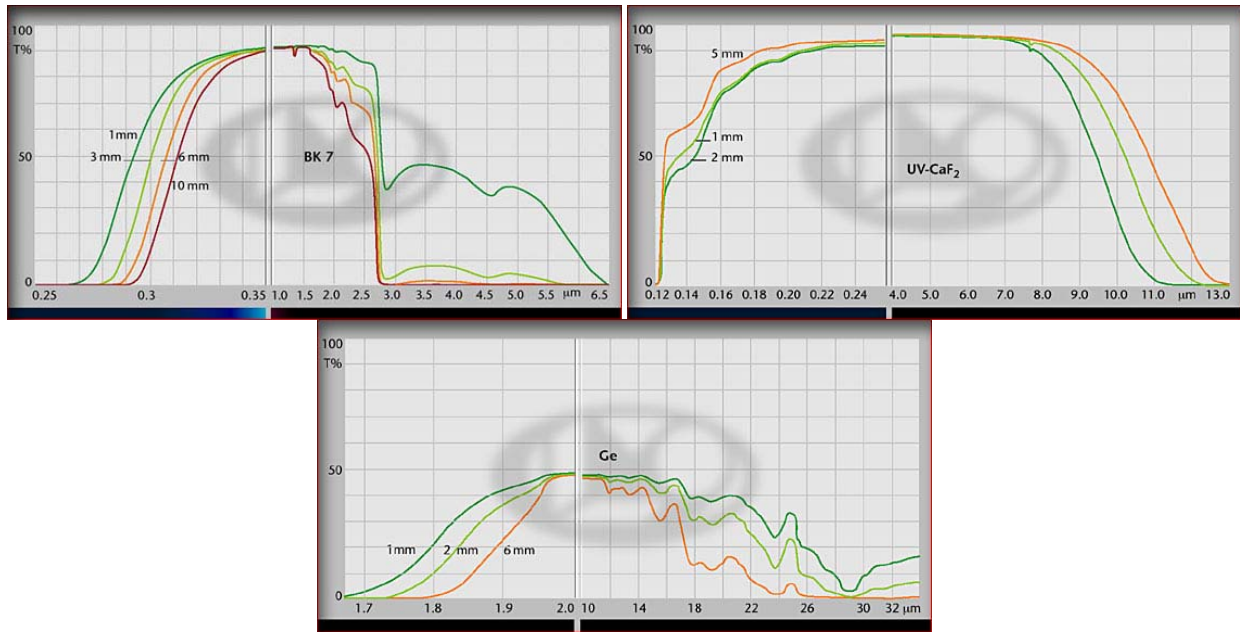
Figure 5.2 External transmission of (a) BK7 glass, (b) CaF₂, and (c) Germanium substrates of various thicknesses. The transmission values shown here include losses from Fresnel reflections from the surfaces of the polished substrates. Reproduced from Ref [54].

A fast InGaAs photodetector is used to observe pump pulses while a fast HgCdTe photodetector observes mid-IR laser pulses.

The kagome fiber used in the initial demonstration of the laser is the first to demonstrate multi-octave spanning guidance that includes the mid-IR. Its cross section and calculated guided modes are shown in Fig. 5.3a-c. The fiber is formed from high purity, low OH content (~ 0.1 ppm) fused silica using a stack and draw technique. Light out to ~ 3.4 μm is reasonably well guided in the fiber, even though fused silica exhibits strong absorption at wavelengths beyond ~ 3 μm, because the light that propagates is mostly confined to the hollow central core. A 3-ring cladding with a 23-μm pitch surrounds a single-cell defect core ~ 45 μm in diameter, with excellent guidance at the pump wavelength of 1.52 μm and weak guidance near the laser wavelengths in the mid-IR. Figure 5.3d shows the measured and calculated fiber loss spectrum and the calculated group velocity for this particular fiber. Standard cut-back measurements were performed to measure the wavelength dependent loss of the fiber. A broadband optical source and an optical spectrum analyzer were used at wavelengths below 1.75 μm. The data at 3.16 μm was taken using the long-wavelength idler output of an optical parametric oscillator (OPO)

coupled through the fiber and detected by a PbSe photodetector. The measured fiber loss is less than 0.5 dB/m near 1.5 µm and is 20 dB/m at 3.16 µm. More data points in the region beyond 1.75 µm can be taken but require a more stable OPO output mode and pulse energy while tuning the wavelength than was available. The calculated fiber loss is a result of the confinement loss of the fiber, which arises partially from the fact that the microstructured cladding region is finite in size, and partly from the intrinsic guidance mechanism of the fiber whereby there is a residual coupling between the cladding continuum modes and the guided core modes [30]. This results in a light leakage from core guided modes though the microstructured cladding into the outer bulk silica. The confinement loss was calculated by collaborators at the University of Bath using finite element analysis software from JCMwave which was also used to solve the fiber modes. The measured and calculated fiber losses are in good agreement, allowing fast and accurate numerical customization and optimization of fiber loss profiles in the future.
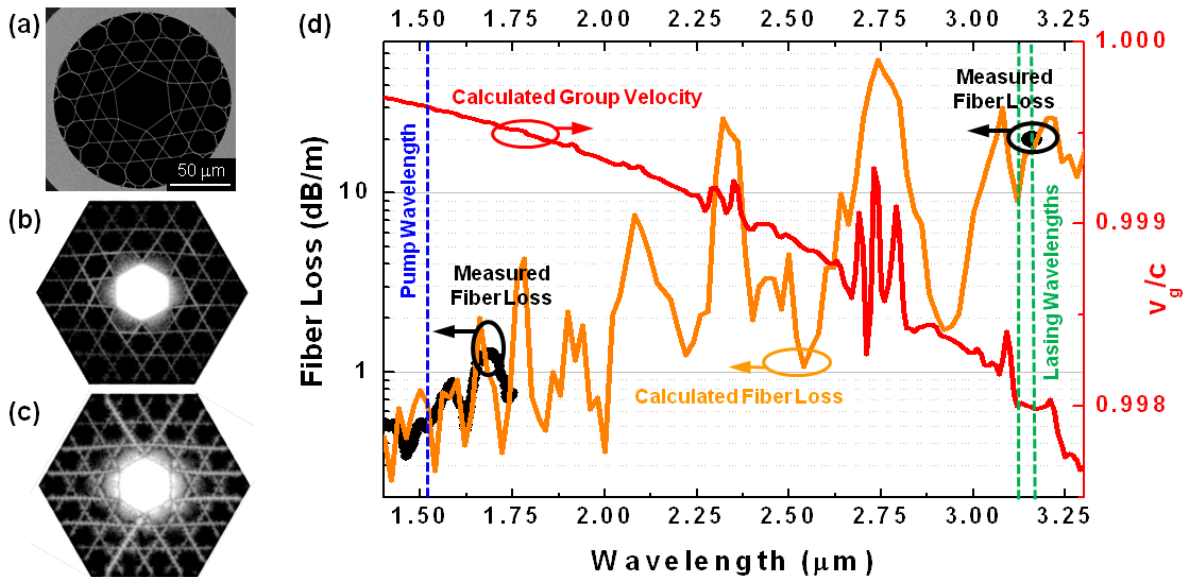
Figure 5.3 Kagome-structured HC-PCF fiber cross section, guided mode profiles, and loss spectrum and group velocity. (a) Scanning electron microscope image of the cross section of the fiber used in the experiment. The diameter of the hollow core varies from 42.4 – 48.3 µm. The fiber pitch is ~ 23 µm, and the typical strut thickness is ~ 0.4 µm. Calculated core mode profiles at (b) 1.52 µm and (c) 3.12 µm. (d) Wavelength dependence of the measured (black circles) and calculated (orange) fiber loss along with the calculated group velocity (red). Figure reproduced from Ref [33].

Filling the evacuated fiber with $^{12}C_2H_2$ gas to equilibrium pressures of several tens of torr takes only minutes owing to the relatively large core diameter of the fiber. Based on the relative dimensions of the fiber, this implies average flow rates of $\sim 10^{10}$ molecules/s. Use of a 19-cell defect fiber with core diameters of 50 – 70 μm would further decrease the filling times and allow even higher flow rates.

The laser is pumped using the signal wavelength from the same OPO used previously to measure the fiber loss in the mid-IR as described above. The OPO produces broadly tunable $\sim$ 1.5-μm wavelength pulses with spectral bandwidths of about 3.5 GHz, pulse durations of roughly 5 ns, and pulse energies up to $\sim$ 10 mW. The pump pulse energy incident on the fiber is kept below 100 μJ to avoid damage [55]. Filter wheels containing various neutral density filters permit up to 4 filters to be used simultaneously to control the pump pulse energy coupled into the fiber. The wavelength of these pulses is then tuned to resonance with the R(7), $v_1 + v_3$ ro-vibrational transition in $^{12}C_2H_2$, corresponding to a wavelength of 1521.06 nm [40]. For clarity, the normal modes of vibration for the acetylene molecule are shown in Fig. 2.2a. The v_1 vibrational mode is seen to correspond to the symmetric C–H stretch, while the v_3 vibrational mode corresponds to the anti-symmetric stretch. Transitions between the vibrational ground state and the $v_1 + v_3$ vibrational state are attractive candidates for laser pumping for several reasons. First, the spectroscopic properties of these transitions are well understood and have been measured very precisely by the scientific community [40]. Second, some of these transitions lie within the spectral window beyond $\sim$ 1.53 μm where readily available commercial laser sources and amplifiers based on gain from excited Er^{3+} ions like erbium-doped fiber lasers and amplifiers could be used, an attractive prospect for eventual commercialization of these devices. The R(7) transition in particular was chosen because it lies very near the maximum R-branch absorption as can be seen in Fig. 2.3, allowing for stronger absorption of the pump by the gas molecules as compared to transitions between most other rotational states.

A measured spectrum of the mid-IR laser output is shown in Fig. 5.4a together with an energy level diagram in Fig. 5.4b showing the relevant transitions for C_2H_2 gas molecules participating in the laser action. Pump pulses excite acetylene molecules from the $J = 7$ rotational state of the vibrational ground state to the $J = 8$ rotational state of the $v_1 + v_3$ vibrational manifold. Acetylene molecules can then leave this excited state via radiative

transitions to the v_1 vibrational state with corresponding emission wavelengths in the 3-μm region. Alternatively, molecules initially in the excited state may exchange energy nonradiatively through intermolecular collisions and collisions with the fiber wall, processes that can decrease the overall laser efficiency. The relative contribution of wall collisions is expected to be small at pressures above 2 torr, where the calculated mean free path of idealized hard-sphere gas molecules is < 20 μm.
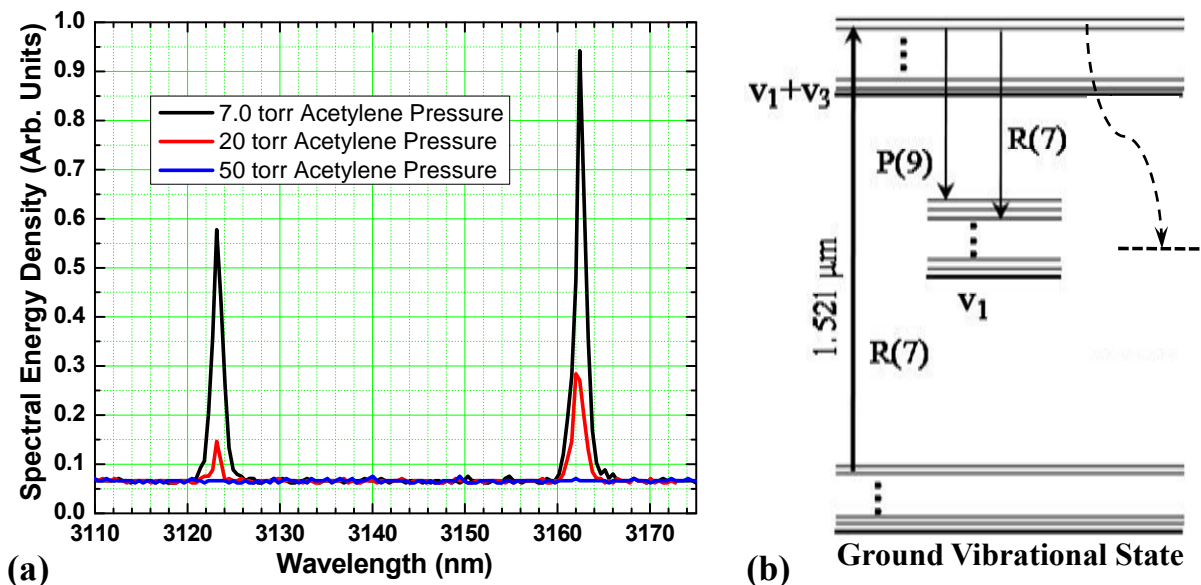
Figure 5.4 Spectrum and energy level diagram from the acetylene-filled HC-PCF laser. (a) The laser spectrum was taken at gas pressures of 7.0, 20, and 50 torr using a grating spectrometer with ~ 1 nm resolution. While the relative energy density of the spectral features changes with pressure, no spectral shifts or additional features are observed. The two peaks correspond to transitions from the $J = 8$, $v_1 + v_3$ excited state to the $J = 7$ and $J = 9$, v_1 state, corresponding to wavelengths of 3123.2 nm and 3162.4 nm, respectively. (b) An energy level diagram showing the pertinent ro-vibrational transitions in the acetylene molecules. The dotted line represents potentially unobserved relaxation pathways.

The laser spectrum was measured by focusing the collimated mid-IR beam from the laser onto the entrance slit of a computer controlled grating monochromater which used a liquid nitrogen cooled, cryogenic InSb photodetector. The spectral resolution of the monochromater was measured to be ~ 1 nm using the second diffraction order of the narrowband (~ 30 pm)

pump light. Just as in the free space acetylene laser [16], only two peaks are observed in the laser spectrum. These peaks fall at 3.123 μm and 3.162 μm and correspond to the R(7) and P(9) dipole allowed transitions ($\Delta J = \pm 1$) from the $J = 8$, $v_1 + v_3$ excited state to the $J = 7$ and $J = 9$ rotational states of the v_1 vibrational state, respectively. The absence of any other spectral peaks indicates insufficient time for molecules in the excited state to rotationally mix through intermolecular collisions before the onset of lasing and vibrational relaxation. Total removal rates from the upper pump level are measured to be $\sim 10^{-9}$ cm^{3}s^{-1} [56].

A measured far-field beam profile of the mid-IR laser output is shown in Fig. 5.5. The mid-IR laser output was collimated from the fiber's end, and the resulting power transmitted through a 750-μm diameter aperture was recorded as the aperture was scanned in the plane transverse to the beam. While the beam is not perfectly symmetric, it does look relatively clean with only one hotspot in addition to the central peak intensity region.
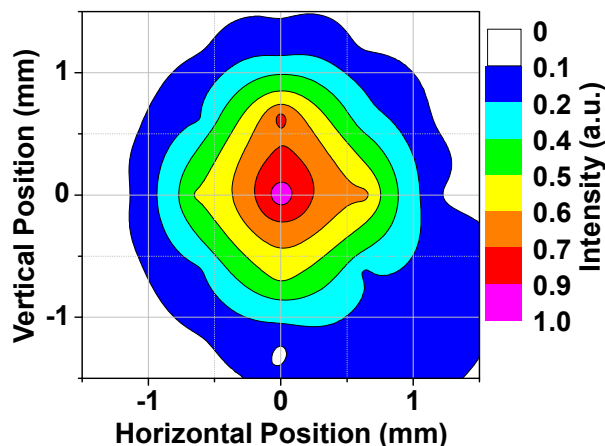
Figure 5.5 Far-field mid-IR laser beam profile. The profile is taken by measuring the optical power in the collimated mid-IR laser beam transmitted through a 750-μm diameter circular aperture as the aperture is scanned transverse to the beam. This data was taken by collaborators at the University of New Mexico. Figure reproduced from Ref [33].

Figure 5.6 shows maximum laser pulse energies (black) and pump-to-laser pulse timing delays (red) measured at various acetylene gas pressures for launched pump pulse energies of ~ 1 μJ. The maximum laser pulse energy is seen to increase with increasing gas pressure up to a maximum of ~ 6 nJ measured at an acetylene pressure of 7 torr. Further increasing the gas

pressure leads to a decrease in the total amount of laser pulse energy observed. This is likely a result of the pump pulse energy being too strongly absorbed before the end of the fiber, creating a smaller population inversion near the end of the fiber. While any population inversion will result in gain and not reabsorption, a decrease in the magnitude of the gain per unit length below the 20 dB/m fiber loss means that more light is escaping the guided fiber mode through leakage, scattering, and material absorption than is being produced through stimulated emission, reducing the total laser pulse energy emitted from the fiber's end.

A time delay is observed between the peak of the transmitted pump pulse and that of the generated mid-IR laser pulse, with the peak of the pump pulse always occurring before that of the laser pulse. A maximum peak-to-peak delay between the transmitted pump and laser pulses of ~ 5 ns is observed at the lowest measured acetylene pressure (~ 0.5 torr) where the pump can create the largest population inversion. As the gas pressure increases, the delay decrease and reaches a minimum delay of ~ 1 ns. Laser pulse durations are observed to be between ~ 3 and 5 ns (FWHM).

The lasing threshold occurs at about 200 nJ of coupled pump pulse energy and varies with pressure. The slope efficiency is only ~ 1% in comparison with about 10% from the free space acetylene laser [16]. The slope efficiency can be improved by reducing the fiber attenuation at the laser wavelength through optimization of the fiber length and pitch. Neglecting relaxation processes, the maximum possible slope efficiency for this 4-level laser is 33% and is a result of saturating the pump and both lasing transitions.

In the limit of lossless fiber and 33% efficiency the ultimate achievable pulse energies to expect from these lasers should be limited by the fiber damage threshold. Damage fluences for 8-ns pulses at 1064 nm on the order of 100 J/cm^2 were observed for the cladding in HC-PCFs [55], which roughly corresponds to the critical fluence of bulk fused silica. In contrast, a roughly 10 times higher fluence was demonstrated by the guided mode without causing catastrophic damage [55]. If we assume that the damage fluence scales as the square root of the pulse duration [55] and is rather wavelength independent we obtain an estimate for the maximum pump energy that can be coupled into our fiber on the order of 10 mJ, resulting in a maximum laser energy of a few millijoules. This energy limit can be increased through the use of larger core fibers, longer pulse durations, and more efficient lasing schemes.
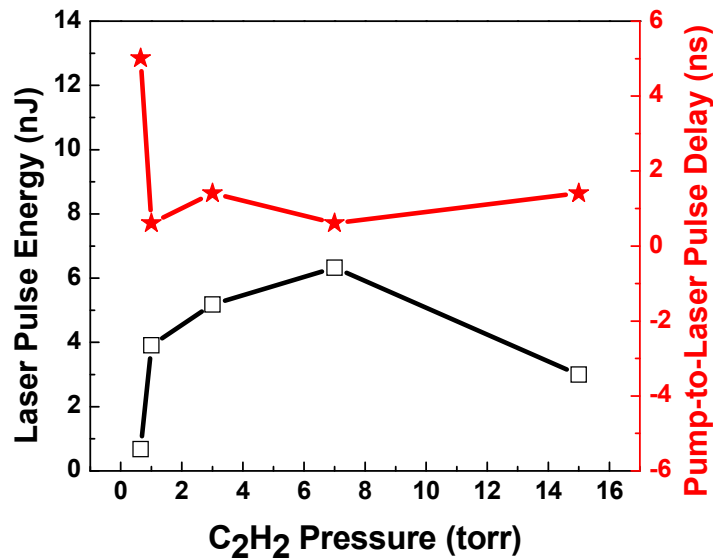
Figure 5.6 Measured dependence of maximum laser pulse energy (black) and pump-to-laser pulse delay (red) on gas pressure from a $^{12}C_2H_2$-filled 23-μm pitch kagome-structured HC-PCF. The maximum laser pulse energy increases with gas pressure until it peaks at ~ 6 nJ at 7 torr. The peak-to-peak delay between the transmitted pump pulse and the mid-IR laser pulse is seen to decrease from ~ 5 ns at ~ 0.5 torr to ~ 1 ns at higher pressures. The pump pulse energy launched into the 1.65 m long fiber was about 1 μJ.

Pumping the laser with a broadly tunable commercial OPO is a natural choice for the initial demonstration of the laser, since the OPO wavelength can be adjusted at the touch of a button, and pulse energies corresponding to fluences up to (and in excess of) the estimated damage threshold of the fiber can be reached. However, the mid-IR laser pulse energies produced by the OPO-pumped acetylene-filled hollow fiber show large shot-to-shot fluctuations at any given pump pulse energy. Furthermore, the spatial mode produced by the OPO in the ~ 1.5-μm wavelength region is observed to be asymmetric with several hot spots visible on an IR viewing card. Figure 5.7 shows a measurement of the OPO pump pulse energy transmitted through the kagome-structured HC-PCF as a function of pump pulse energy incident on the fiber for various acetylene pressures ranging from 0.0 torr (fully evacuated) up to 60 torr. As the pressure is increased the ratio of pump pulse energy exiting the fiber to that incident on the fiber is expected to decrease monotonically due to the increase in molecular absorption accompanying

the increase in the molecular number density. However, this ratio is observed to vary somewhat sporadically, increasing by up to a factor of 6 between successive pressure measurements from 0.0 to 1.0 torr, 5.0 to 7.0 torr, and 20 to 25 torr. These variations are thought to have been caused by changes in the fiber-to-source coupling. Changes in this coupling may be a result of fluctuations in the pump mode profile emitted from the OPO and/or by wavelength variations on the order of ~ 1 GHz causing the amount of energy absorbed by the gas to change and with it the pump transmission through the fiber.
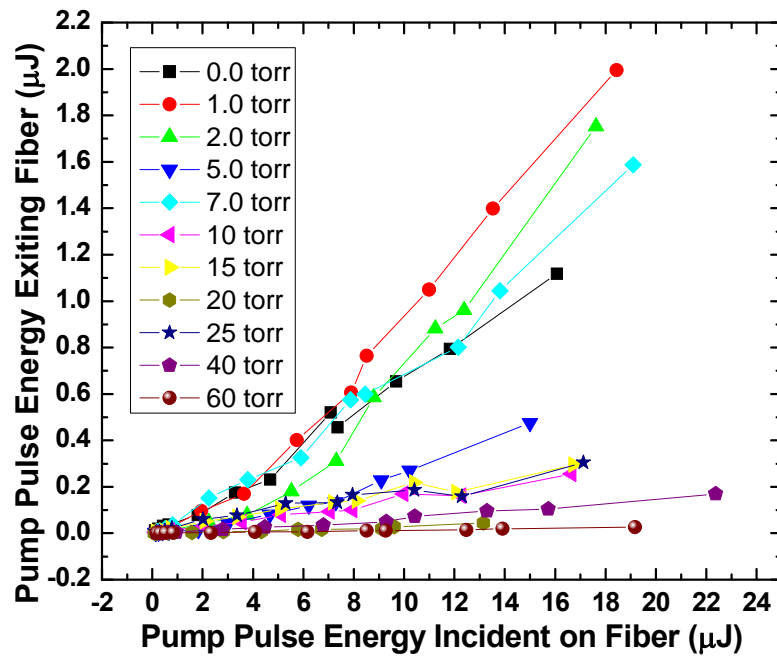
Figure 5.7 OPO pump pulse energy transmitted through the C_2H_2-filled 23-μm pitch kagome-structure HC-PCF as a function of incident pump pulse energy for various gas pressures. The ratio of incident to transmitted pump pulse energy is expected to decrease monotonically as the gas pressure is increased in the absence of changes in source-to-fiber coupling and center wavelength instabilities.

Switching the pump source from an OPO to an OPA offers a potential solution to these problems. By using a stable, narrow linewidth laser to provide signal light to seed the OPA, the OPA can be expected to provide stable, narrowband amplified signal pulses that can be used to

pump the gas-filled fiber laser. Furthermore, by using a laser with a single mode fiber output, one can ensure that the beam profile of the signal light to be amplified is near Gaussian, ensuring a more spatial stable and higher quality OPA mode profile.

The OPA constructed is discussed in detail in Section 3.2. A schematic of the OPA-pumped laser setup is shown in Fig. 5.8. The setup is generally the same as that which uses the OPO with a few improvements. Instead of inserting various neutral density filters into the pump beam to adjust the pump pulse energy, a variable attenuator constructed using wave plates and a
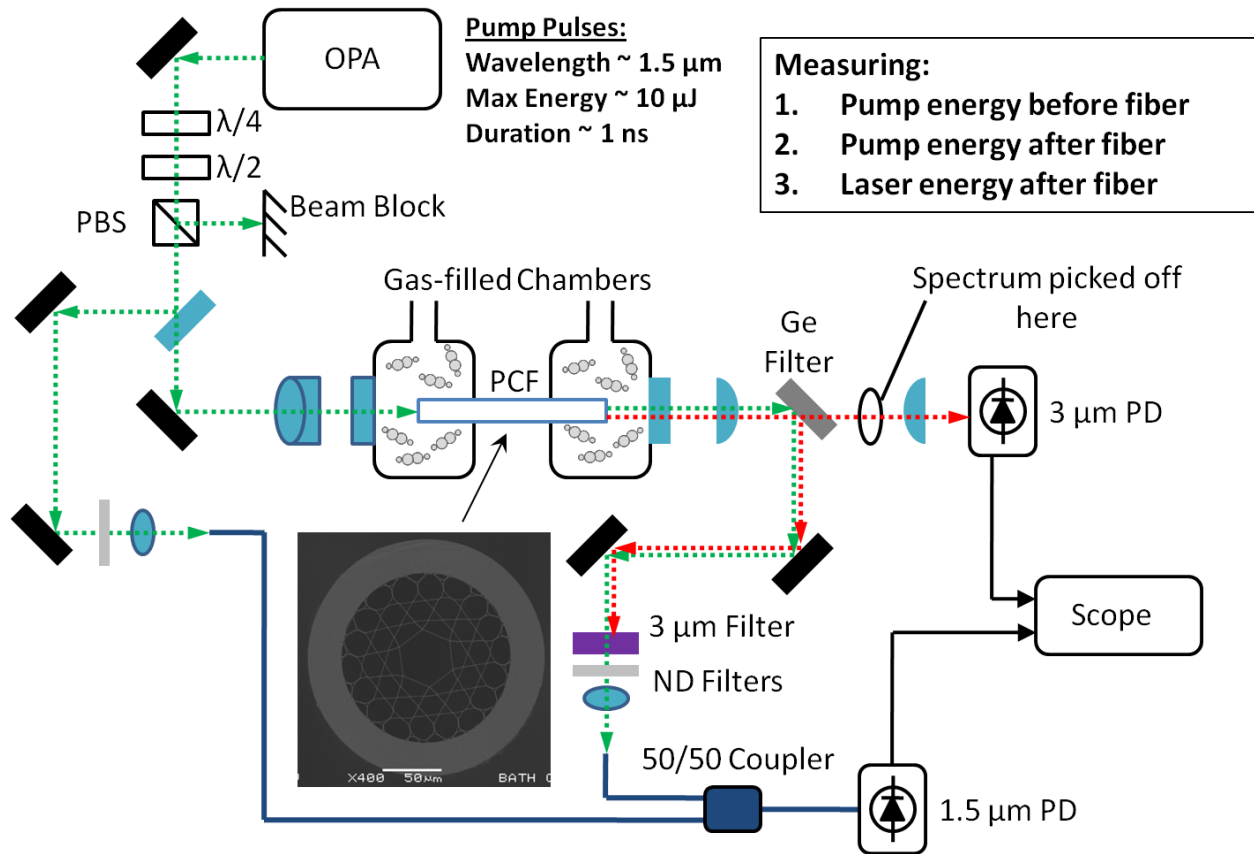
Figure 5.8 Gas-filled fiber laser setup using OPA as pump source. Gas is contained inside the HC-PCF. Pump pulses from an OPA are coupled into the fiber through one end while the generated mid-IR light and any unabsorbed pump light are coupled out of the opposite end of the fiber. Mid-IR light passes through a 2-mm thick, un-coated germanium filter at 45° incidence and is focused onto a HgCdTe detector. A large portion of the unabsorbed pump light is reflected from the angled germanium filter and sent to a fiber coupled, 25-GHz InGaAs photodetector.

polarized beam splitting cube is used to precisely and continuously adjust the pump pulse energy. Following the attenuator a BK7 wedged window is used to split a small fraction (~ 1%) of the pump pulse energy off from the main beam. This small fraction of the pump pulse energy is then further attenuated and coupled into an SMF patch cord. The majority of the pump light is coupled into a 33-cm long piece of gas-filled kagome-structured HC-PCF, whose ends are supported inside vacuum chambers, using anti-reflection coated BK7 optics. This kagome fiber is a shortened piece of the same 23-μm pitch fiber used in the OPO-pumped laser.

While the basic design of the vacuum chambers and fiber holders remain unchanged, some effort was made to shrink the total volume of the vacuum chamber system. This was done in order to minimize the total amount of gas required to fill the hollow-core fiber to any given gas pressure. While this is a generally desirable characteristic for any setup that requires consumables like molecular gases, our desire to use HCN in the setup and the difficulty of procuring HCN gas is the driving force for this design change.

The generated mid-IR laser light as well as the unabsorbed pump light are coupled out of the fiber and collimated using uncoated CaF_2 optics. The distance between the end of the fiber and the collimating lens is adjusted to optimize the collimation of the ~ 1.5-μm pump beam. This is much easier in practice than trying to collimate the all-but-invisible mid-IR beam. Furthermore, precise collimation of the transmitted pump light is more important as the unabsorbed pump light is partially reflected from an uncoated polished germanium filter angled ~ 45° to the incident beam, filtered, attenuated, and then coupled into an SMF patch cord. The quasi-collimated mid-IR beam is transmitted through the 2-mm thick, angled germanium filter and either focused onto an exposed 1-mm x 1-mm room temperature HgCdTe photodetector (Boston Electronics, P/N PVI-3.4) or focused into a grating monochrometer for spectral measurements of the laser output. The mid-IR output is never fiber coupled, and therefore the collimation of this beam is not so critical.

In order to use a single, fast, fiber-coupled photodetector, both the pump light split off from the main beam before the HC-PCF and the pump light transmitted through the HC-PCF are coupled into single mode fiber (SMF) patch cords. The two separate patch cords are connected to the input ports of a 50/50 fiber beam combiner. A single SMF patch cord is then connected from the combiner's output to the input of a fiber-coupled, 25-GHz InGaAs photodetector (New Focus, P/N 1414). This single detector is then used to detect both the pump pulse power incident

on the fiber as well as the pump pulse power transmitted through the fiber with sub-nanosecond rise times limited by the 4-GHz bandwidth of the CSA7404 digital oscilloscope. The free-space and fiber path lengths are such that the peak-to-peak separation of the incident pump pulse and the transmitted pump pulse is ~ 7 ns, which is more than enough separation to fully resolve each ~ 1-ns duration pulse profile from the one-channel oscilloscope trace. Figure 5.9 shows an oscilloscope trace of the 25-GHz photodetector signal taken off resonance.
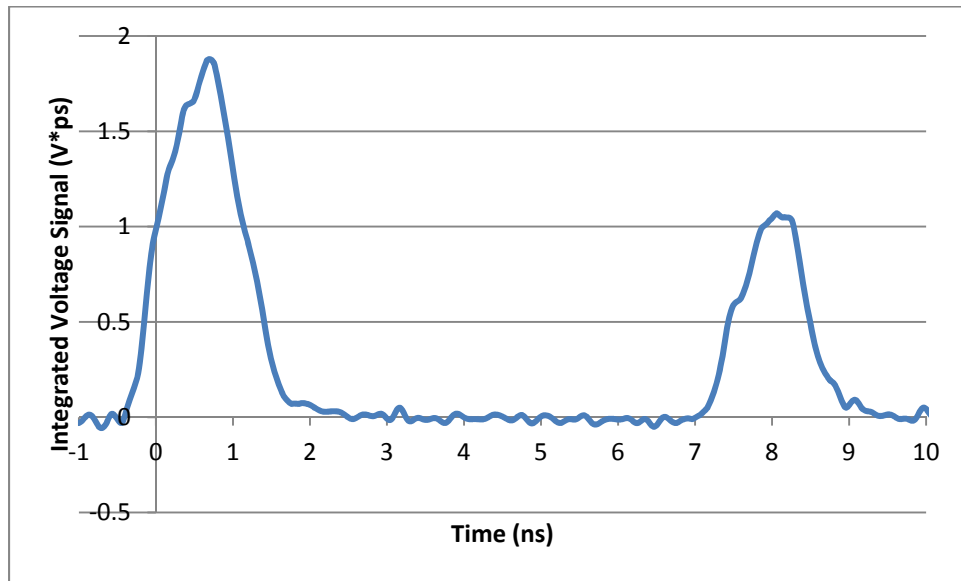
Figure 5.9 Single-shot oscilloscope trace showing non-resonant incident and transmitted pump pulse detected using a single 25-GHz InGaAs photodetector. A small fraction of the incident pump pulse is detected first, followed ~ 7 ns later by the pulse transmitted through the hollow-core kagome fiber. The pulses are seen to be ~ 1 ns in duration.

With this more stable OPA pump source, the pump wavelength can be maintained very precisely or tuned via the CW seed laser without concern that the spatial mode emitted by the OPA may change. This allows the pump pulse energy transmitted through the kagome fiber to be measured both at a wavelength resonant with the absorbing pump transition and at a wavelength widely (at least a few gigahertz) detuned from this transition. This is very useful, as a close approximation to the absorbed pump pulse energy can be calculated by subtracting the measured resonant pulse energy from the non-resonant pump pulse energy transmitted through the fiber. Computing the absorbed pump energy in this way is not exact as resonant pump light

65

that is absorbed after propagating only a short distance in the fiber experiences less fiber loss than light that is transmitted through the entire length of fiber. This makes the computed absorbed pump energy a little lower than the actual. An upper limit on the error can be estimated assuming that all the pump absorption happens at the very start of the fiber, and that the remaining transmitted light is just attenuated by the fiber loss. For a 1.65-m long fiber with 0.5 dB/m loss, the calculated absorbed pump energy would be 83% of the actual energy absorbed by the gas. This is an overestimation, and our collaborators have estimated that the discrepancy is only ~ 5% for the same fiber length and fiber loss assuming linear absorption of the pump.

5.2.1 Quantitative Study of Laser Optical Properties

Figure 5.10 shows a simplified schematic of the laser setup indicating the relative measurement locations for the detected voltage signals and pulse energies for the pump light (green arrows) and laser light (red arrows). The gray arrows correspond to transmission coefficients to account for losses due to Fresnel reflections incurred from various optical elements.
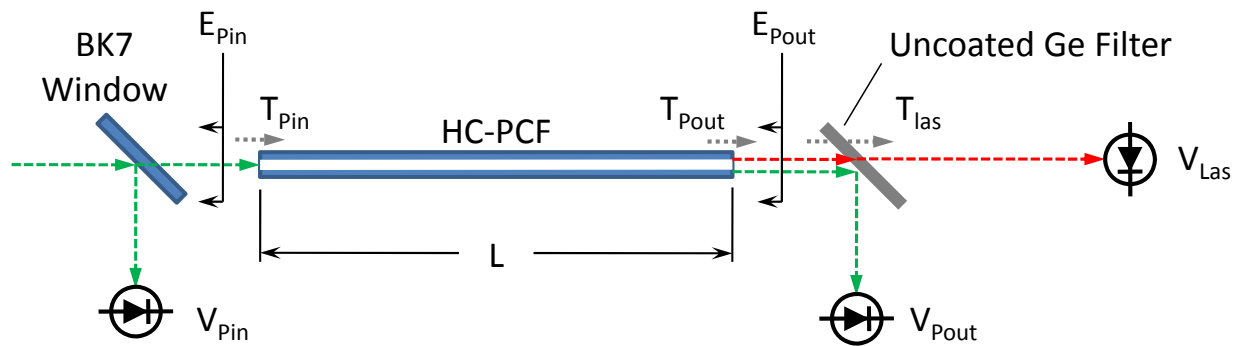
Figure 5.10 Simplified gas-filled fiber laser diagram showing where pulse energies and photodetector signals are measured. V_{Pin} and V_{Pout} are the photodetector signals measured for the incident and transmitted pump pulses, respectively, using a 25 GHz InGaAs photodetector. V_{Las} is the photodetector signal measured for the generated laser pulse using a HgCdTe photodetector. The energy measurements for both the incident and transmitted pump pulses are made using a pyroelectric energy sensor.

The physical quantities most useful in describing the laser behavior and performance are not the quantities that are directly measured. To convert the photodetector signals into pulse energies requires careful calibration and must account for numerous Fresnel reflections. What follows is a detailed discussion of the calibration process.

Fresnel reflections result from the boundary conditions imposed on the electric and magnetic field components at the interface of materials with different refractive indices. For the situation diagramed in Fig. 5.11, The power reflection coefficients for s-polarized light (electric field polarization parallel to the plane of the interface) and p-polarized light (electric field polarization parallel to the plane containing the propagating light) are given in terms of the angle, θ_i, between the incident propagation direction and the vector normal to the boundary plane by the equations [57],

$$R_s = \left[\frac{n_1 \cdot cos(\theta_i) - n_2 \sqrt{1 - \left(\frac{n_1}{n_2} \cdot sin(\theta_i)\right)^2}}{n_1 \cdot cos(\theta_i) + n_2 \sqrt{1 - \left(\frac{n_1}{n_2} \cdot sin(\theta_i)\right)^2}} \right]^2 \qquad 5.1$$

$$R_p = \left[\frac{-n_2 \cdot cos(\theta_i) + n_1 \sqrt{1 - \left(\frac{n_1}{n_2} \cdot sin(\theta_i)\right)^2}}{n_2 \cdot cos(\theta_i) + n_1 \sqrt{1 - \left(\frac{n_1}{n_2} \cdot sin(\theta_i)\right)^2}} \right]^2 \qquad 5.2$$

Using Eq. 5.1 and 5.2 the Fresnel power reflection coefficients for s-, p-, and unpolarized (average of s- and p-) light can be computed for air-CaF$_2$ and air-germanium interfaces, which can then be used to estimate the transmission (given by $T_{s/p/un} = 1 - R_{s/p/un}$ which represents the power transmission coefficient through one boundary of regions with non-identical refractive indices) through the various optical elements in the laser setup. The calculated reflection coefficients are shown in Fig. 5.12 as functions of the incident angle, θ_i, for wavelengths in the 3-μm region near the laser wavelengths (reflection coefficients for CaF$_2$ decrease by a few percent at the pump wavelength). Unless specified, all the calculated transmission coefficients

67
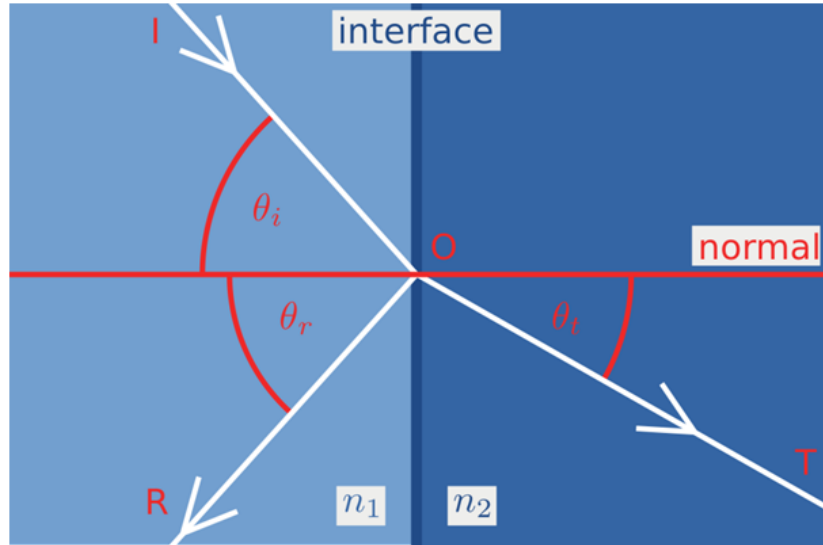
Figure 5.11 Diagram showing Fresnel reflection of light at interface of two materials having different indices of refraction. Reproduce from Ref [58].

assume un-polarized light. The wavelength-dependent indices of refraction are given by the Sellemeier equation found in reference [59].
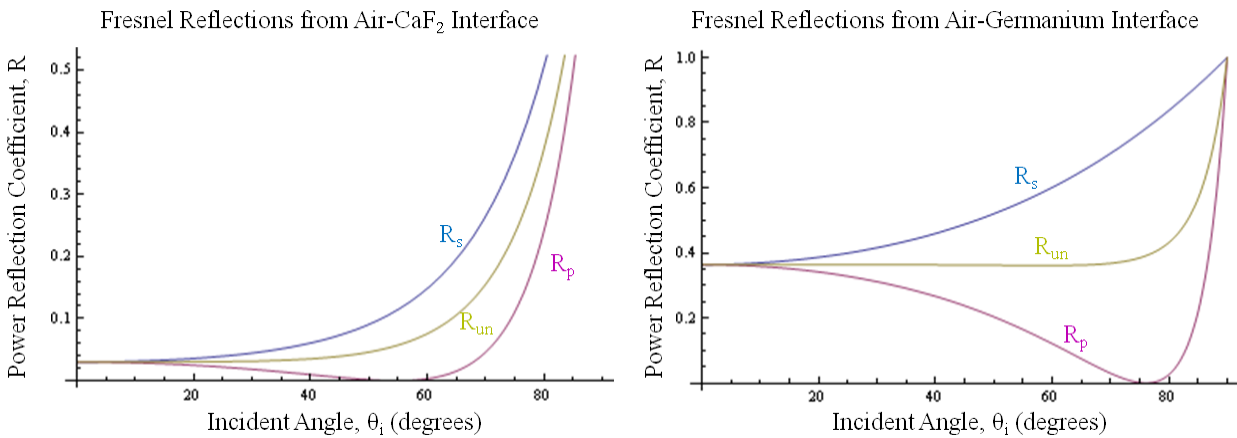
Figure 5.12 Polarization and angular dependence of Fresnel reflections from an air-CaF$_2$ (left) and air-germanium (right) interface.

Photodetector voltage signals can be used to compute pulse energy. This is best done by comparing the integrated photodetector signal to the reading from an energy meter over a range of pulse energies. The signals V_{Pin} and V_{Pout} labeled in Fig. 5.11 represent the integrated pump

pulse voltage signals (in units of V·ps) measured before and after the fiber respectively. V_{Las} is the integrated laser pulse signal measured after the germanium filter. All of the integrated voltage signals are calculated using the MATLAB code shown in Appendix E which computes the area under the voltage signal waveforms (like that shown in Fig. 5.9) read out from the LabVIEW-controlled oscilloscope.

The calibration of pulse energy from an integrated voltage signal is done using a pyroelectric energy meter. These integrated voltage signals are proportional to the incident pump, transmitted pump, and the mid-IR laser pulse energies. To calibrate the pump signals in terms of pulse energy, a pyroelectric energy sensor is used to measure the observed pulse energies at the locations shown before and after the fiber at pump wavelengths both resonant and non-resonant with the pump transition in the gas. This is performed at several different incident pump pulse energies for each gas pressure. The slope from a linear regression performed on the data gives the desired calibration factors. Using these calibration factors, measurements of the laser pulse energy as a function of pump pulse energy absorbed by the gas can be made while continuously varying the incident pump pulse energy via the variable attenuator after the OPA.

The initial mid-IR energy calibration of the HgCdTe photodetector was performed using idler pulses from the OPA with center wavelengths of 3478 nm. While this was convenient in that it did not require any tuning or reconfiguring of the OPA crystal position or temperature, the response of the particular HgCdTe detector used was measured to be about five-times stronger (units of V/W) at 3.5 μm as it was at the gas-filled fiber laser wavelengths near ~ 3.2 μm. A simple calibration procedure was used, and consisted of 1) measuring the transmission through several filters using the OPA idler, 2) measuring the energy of the mid-IR pulses emitted directly from the OPA with a pyroelectric sensor, and 3) placing the filters of known optical density between the OPA output and the HgCdTe photodetector and measuring the resulting integrated voltage signal. The filters were necessary to ensure that the photodetector was not saturated by the ~ 10-μJ energy mid-IR pulses. The ratio of the measured pulse energy to the integrated voltage signal from the detector multiplied by the filters' transmission coefficients gives the calibration factor (in units of nJ/(V·ps)). A similar calibration described in the next chapter is repeated using the actual acetylene laser output as the mid-IR source and gives the correct calibration factor. This later, more accurate calibration factor is used in the analysis of all OPA-pumped laser data presented in this thesis.

The laser pulse energy, E_{Las}, can then be computed in terms of the measured integrated voltage signal, V_{Las}, measured from the HgCdTe photodetector and is given by,

$$E_{Las}(V_{Las}) = (T_{Pout} \cdot T_{Las})^{-1} \cdot m_{Las} \cdot V_{Las} \qquad 5.3$$

where T_{Pout} accounts for the combined losses from Fresnel reflections of un-polarized light at the air-glass interfaces for the uncoated CaF_2 window and collimating lens and T_{Las} accounts for the combined losses from Fresnel reflections from un-polarized light at the air-material interfaces for the 2-mm thick uncoated germanium filter, and the CaF_2 lens used to focus the laser light onto the HgCdTe photodetector. m_{Las} is the voltage to energy calibration factor which is equal to the slope of the line fit to the measured pulse energy versus the integrated voltage signal measured by the laser photodetector, $i.e.$,

$$m_{Las} = \frac{\Delta E_{Las}}{\Delta V_{Las}}. \qquad 5.4$$

The pump pulse energy incident on the fiber on resonance is given by,

$$E_{Pin,ON}(V_{Pin,ON}) = (T_{Pin})^{-1} \cdot m_{Pin,ON} \cdot V_{Pin,ON} \qquad 5.5$$

where the subscript "ON" indicates that the quantities used are measured at a wavelength "on resonance" with the pump transition, and T_{Pin} accounts for the losses from the AR-coated BK7 window and focusing lens used to couple into the hollow fiber. The calibration factor, $m_{Pin,ON}$, is determined by performing a linear regression analysis of the average pump pulse energy and integrated voltage signal data measured before the fiber, and is given by,

$$m_{Pin,ON} = \frac{\Delta E_{Pin,ON}}{\Delta V_{Pin,ON}} \qquad 5.6$$

The calibration data is taken for several incident pump pulse energy increments, while on resonance with the pump transition. This analysis is illustrated in Fig. 5.13 which shows the

measured data with the fit line and calibration factor (slope of fit equation) both on and off resonance. A corresponding plot of the measured pump pulse energy just before the fiber on and off resonance is also shown in Fig. 5.13. From the plot of the measured pump pulse energy before the fiber off resonance versus the pump pulse energy measured before the fiber on
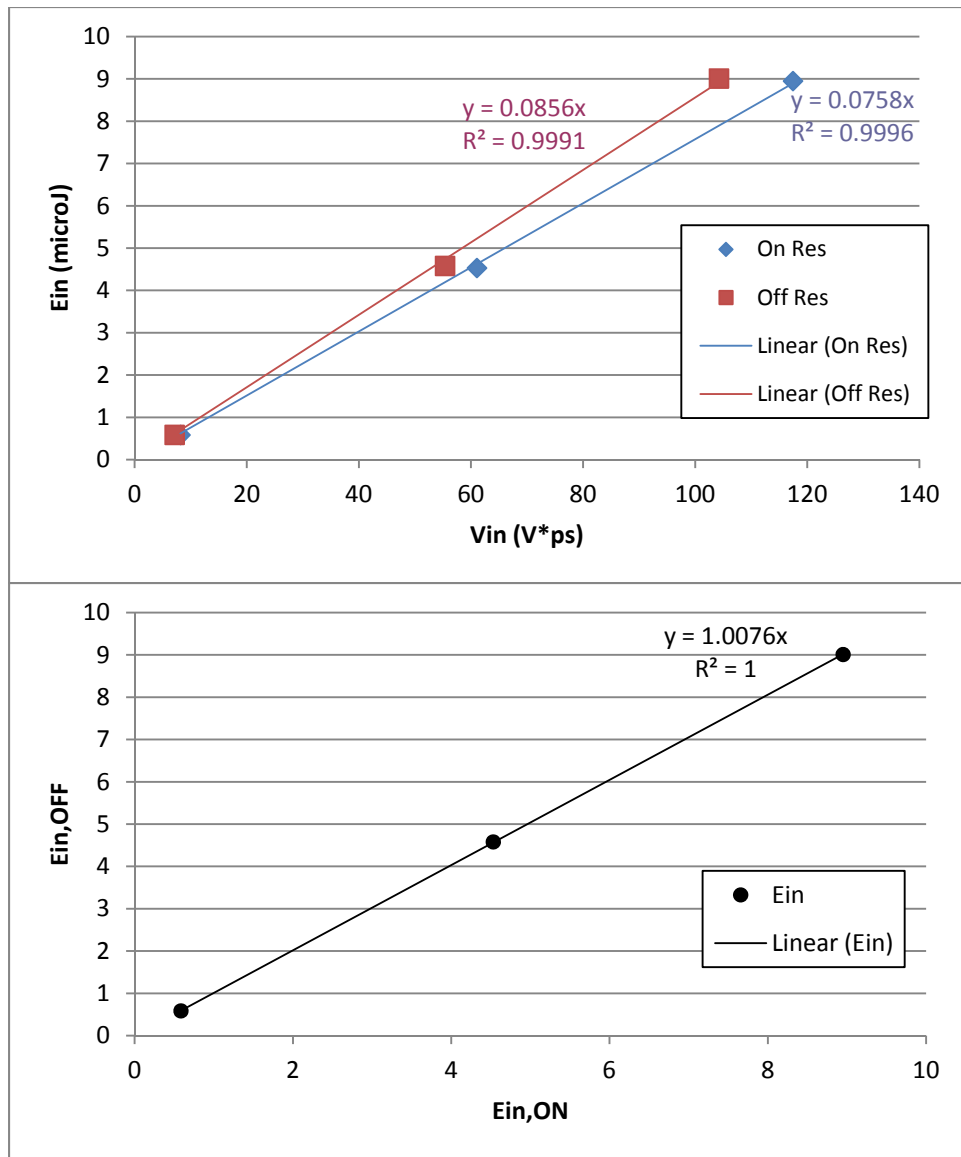
Figure 5.13 Data and linear fits of the pump pulse energy as a function of the integrated voltage signal recorded before the fiber both on (blue) and off (red) resonance, and plot showing measured pump pulse energy before the fiber on and off resonance. While the integrated voltage signal is seen to change by ~ 10% in moving from on resonance to off, this change is well quantified and can be accurately accounted for.

resonance it is clear that the pump pulse energy emitted from the OPA is quite stable when the output is repeatedly tuned over a ~ 2 GHz range, as shown by the slope of 1.0076 in the bottom plot in Fig. 5.13. The integrated voltage signal measured before the fiber is however seen to change by ~ 10% when tuning over the same range. This may be due to slight changes in optical fiber coupling or some wavelength-dependent transmission of the optical fiber components and/or filters after the position at which the energy meter is inserted. While this variation is not desirable, both the resonant and non-resonant data are linear, allowing accurate calibration factors to be calculated in each case.

To calibrate the pump pulse energy exiting the gas-filled fiber, the energy on resonance is measured just after the fiber. However, this measured energy necessarily has contributions from both the pump and laser light. Therefore, the pump pulse energy exiting the fiber on resonance is most precisely given by,

$$E_{Pout,ON}(V_{Pout,ON}, V_{Las}) = (T_{Pout})^{-1} \cdot m_{Pout,ON} \cdot V_{Pout,ON} - (T_{Las,2})^{-1} \cdot E_{Las}(V_{Las}) \quad 5.7$$

where, unlike $E_{Pout,OFF}$, the energy measured at the fiber output on resonance, $E_{Pout,ON}$, actually contains both the transmitted pump pulse energy and the emitted mid-IR laser pulse energy, and the last term in the expression subtracts this additional contribution from the laser pulse energy. Since $V_{Pout,ON}$ and V_{Las} are measured simultaneously for every pump pulse, this calculation could be done in theory. However, using the calibration factor, $m_{Pout,ON}$, given by,

$$m_{Pout,ON} = \frac{\Delta E_{Pout,ON}}{\Delta V_{Pout,ON}} \quad\quad\quad 5.8$$

is problematic because the contribution to $E_{Pout,ON}$ from the laser pulse energy is not expected to have a linear dependence in general, as the laser pulse energy will certainly saturate at high pump pulse energies because the absorbed pump energy saturates. In order to use the calibration factor mentioned above, the actual dependence of $E_{Pout,ON}$ on $V_{Pout,ON}$ should be measured over many small intervals and fit with an appropriate function that reflects the interplay of the

transmitted pump and generated laser pulse energy. This could be done but represents a very time intensive measurement.

Instead, a good approximation to the pump pulse energy exiting the fiber on resonance can be made using the measured off-resonance, pump-only pulse energy, $E_{Pout,OFF}$. This pulse energy is directly proportional to the integrated voltage signal recorded by the photodetector after the fiber as no mid-IR light is generated off resonance. Using this approximation the calculated pump pulse energy transmitted through the fiber on resonance is given by,

$$E_{Pout,ON}(V_{Pout,ON}) \cong (T_{Pout})^{-1} \cdot m_{Pout,OFF} \cdot V_{Pout,ON} , \qquad 5.9$$

where $m_{Pout,OFF}$ is given by,

$$m_{Pout,OFF} = \frac{\Delta E_{Pout,OFF}}{\Delta V_{Pout,OFF}}. \qquad 5.10$$

The behavior of E_{Pout} as a function of V_{Pout} at pump wavelengths both on and off resonance is shown in Fig. 5.14. The line fit to the off resonance data gives the calibration factor used in the analysis. Only two data points are shown for the on-resonance case because the pulse energy after the fiber corresponding to the lowest incident pump pulse energy was too low to be measured. A line with a non-zero y-intercept is fit to this data and serves to put an upper limit on the error incurred by using the off-resonant calibration factor with the on-resonant data. From the comparison of these two slopes, the error introduced is less than 9%.

By comparing this energy to the expected pump pulse energy transmitted through the fiber in the absence of any absorption by the gas, $E'_{Pout,ON}$, the total absorbed pump pulse energy can be calculated. The expected pump pulse energy transmitted through the fiber without absorption in terms of the integrated voltage signal from the incident pulse measured on resonance is given by,

$$E'_{Pout,ON}(V_{Pin,ON})$$
$$= (T_{Pout})^{-1} \cdot m_{Pout,OFF} \cdot \left(\frac{\Delta V_{Pout,OFF}}{\Delta V_{Pin,OFF}}\right) \cdot \left(\frac{\Delta V_{Pin,OFF}}{\Delta V_{Pin,ON}}\right) \cdot V_{Pin,ON} \qquad 5.11$$
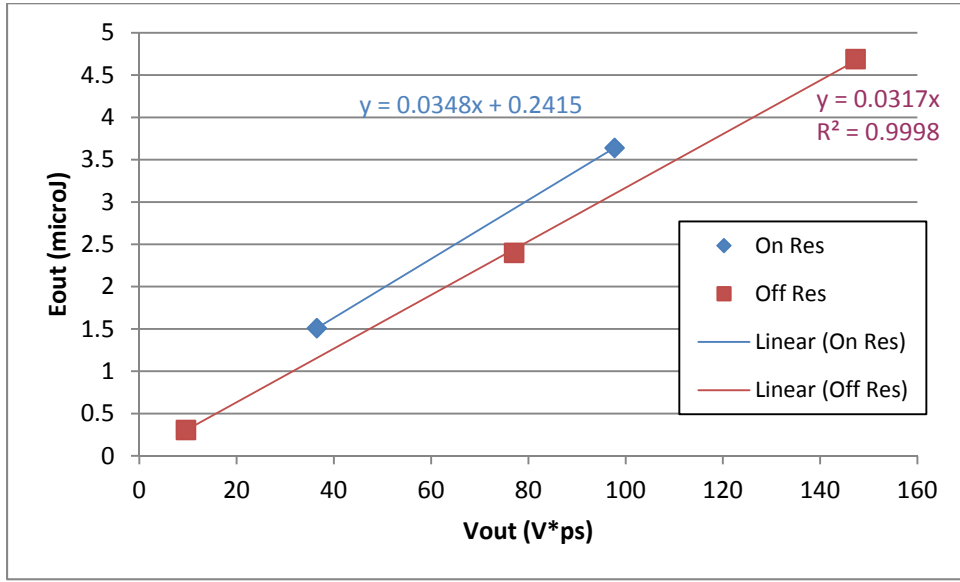
Figure 5.14 Total pulse energy measured after the fiber as a function of the integrated voltage signal from the transmitted pump pulse both on- (blue) and off- (red) resonance. The slope of the line fit through the off-resonance data gives the integrated voltage to energy calibration factor. Since the integrated voltage signal is only sensitive to the transmitted pump light, the on-resonance pulse energy after the fiber is observed to be higher than the off-resonance pulse energy due to the additional mid-IR laser pulse energy being measured. The slope of the on-resonance data provides an estimate of the upper limit to the error introduced by using the off-resonance calibration factor with the integrated voltage signals measured on-resonance after the fiber.

where the factor $\frac{\Delta V_{Pin,OFF}}{\Delta V_{Pin,ON}}$ accounts for the difference in the integrated voltage signal on and off resonance, and the factor $\frac{\Delta V_{Pout,OFF}}{\Delta V_{Pin,OFF}}$ is used to convert signals measured before the fiber to the values that would be expected after the fiber. Figure 5.15 shows a plot of $V_{Pin,OFF}$ as a function of $V_{Pin,ON}$. The slope of the line fit to this data is less than unity, indicating some wavelength-dependent fluctuation in the fiber coupled pump signal as evidenced by the discrepancy in the on and off resonance energy data shown in Fig. 5.13.
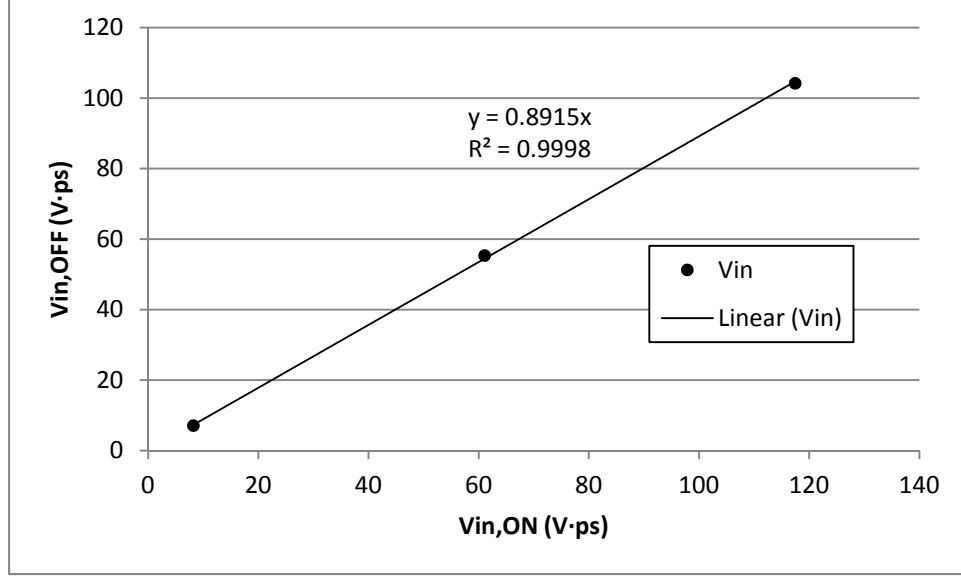
Figure 5.15 Plot of the integrated voltage signal measured before the fiber off-resonance versus that measured on-resonance. The slope of the fit line differs from unity indicating that the amount of signal observed by the photodetector varies over the ~ 2 GHz tuning range of the pump wavelength used to move between on and off resonance.

The total pump pulse energy absorbed by the gas on resonance, E_{abs}, can be calculated by subtracting the measured from the expected pump pulse energy transmitted through the fiber on resonance. The absorbed pump pulse energy is then given by,

$$E_{abs}(V_{Pin,ON}, V_{Pout,ON}) = E'_{Pout,ON}(V_{Pin,ON}) - E_{Pout,ON}(V_{Pout,ON})$$

$$\cong (T_{Pout})^{-1} \cdot m_{Pout,OFF} \cdot \left[\left(\frac{\Delta V_{Pout,OFF}}{\Delta V_{Pin,OFF}} \right) \cdot \left(\frac{\Delta V_{Pin,OFF}}{\Delta V_{Pin,ON}} \right) \cdot V_{Pin,ON} - V_{Pout,ON} \right] \qquad 5.12$$

This quantity is somewhat fundamental to our laser since it represents the amount of energy we are actually able to impart on the molecular system which is responsible for the production of the mid-IR laser light. For this reason the absorbed pump pulse energy is a natural metric for the laser system and will be used to examine quantities of interest including the laser pulse energy and pump-to-laser pulse delay. Recall that we may be underestimating the amount of absorbed pump pulse energy by ~ 5%, due to the 0.5 dB/m loss of the hollow-core fiber.

5.2.2 Experimental Results in Acetylene

A spectrum of the mid-IR laser output taken at an acetylene pressure of 111 torr is shown in Fig. 5.16a along with an energy level diagram in Fig. 5.16b showing the relevant transitions. The spectrum was taken using a computer controlled grating monochrometer and a room temperature PbSe photodetector (Thorlabs, P/N PDA20H). A maximum resolution of ~ 0.2 nm (FWHM) was determined by looking at the second diffraction order of the narrowband (~ 1 kHz), ~ 1.5-μm wavelength OPA seed laser, with entrance and exit slit widths of 50 μm. The spectral region from ~ 1.5 to 4.1 μm was examined, but just as in the case of the OPO-pumped laser, only two peaks are observed in the laser spectrum.

For the initial trials of the OPA-pumped laser, the gas was excited via the P(13) transition between the vibrational ground state and the $v_1 + v_3$ vibrational state at a wavelength of
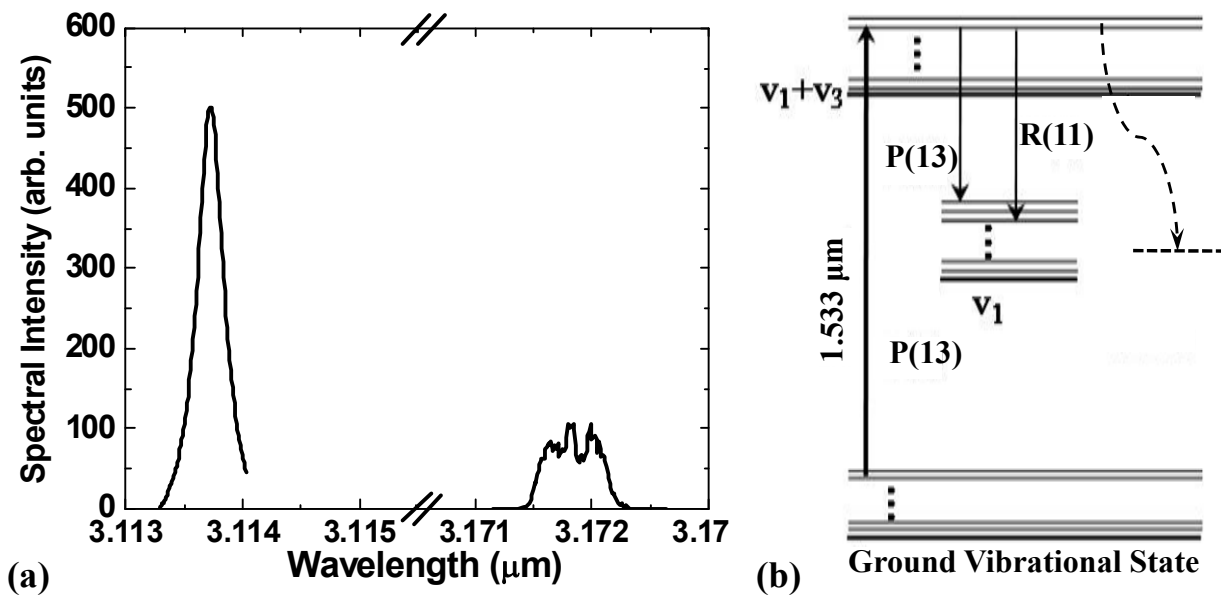
Figure 5.16 (a) OPA-pumped C_2H_2–filled fiber laser spectrum and (b) the molecular energy level diagram showing the relevant transitions. The laser was pumped on the P(13) transition between the vibrational ground state and the $v_1 + v_3$ vibrational state. Two peaks are observed in the laser spectrum, corresponding closely with the R(11) and P(13) transitions at 3114.6 and 3172.4 nm between the excited state and the v_1 vibrational state [37]. The monochrometer's entrance and exit slit widths were 150 μm. Figure adapted from Ref [60].

1532.83 nm. This was preferable to pumping the laser via the R(7) transition utilized in the OPO-pumped laser demonstration which would have required using a less powerful and less

The observed laser pulse energy as a function of pump pulse energy absorbed by the gas molecules contained within the 33-cm long piece of 23-µm pitch kagome-structured HC-PCF is shown in Fig. 5.17 for acetylene gas pressures ranging from ~ 15 to 75 torr. As a result of the much improved mode quality of the pump beam, more pump energy can be coupled into the fiber and absorbed by the gas than was possible with the OPO-pumped laser. Not surprisingly the maximum observed laser pulse energies are seen to exceed those observed from the 1.65-m long section of the same fiber used in the OPO-pumped laser. In general the data show that as the pressure increases the laser thresholds increase while the slope efficiencies (defined here as the slope of the data in the linear region) and the total optical-to-optical efficiencies decrease. These trends are summarized by the quantities tabulated in Table 5.1. Just as is seen from the OPO-pumped laser, the maximum laser pulse energy here is seen to increase as the pressure is increased until reaching maximum values at 37.0 – 56.1 torr, after which increasing the pressure begins to decrease the maximum laser pulse energy. Again, this is likely due to the fact that for a given fiber length and pump pulse energy available there is a maximum number of molecules that can be inverted to produce saturated gain down the entire length of the fiber. If more molecules are added (pressure increased), the gain will drop below the 20 dB/m loss before the end of the fiber, and less total laser pulse energy will be emitted.
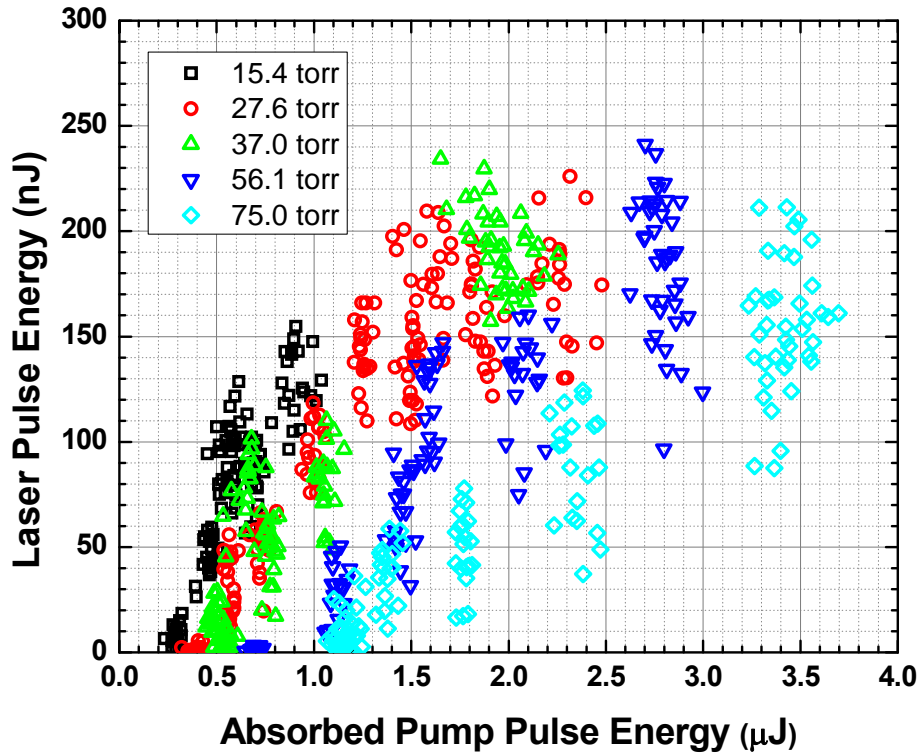
Figure 5.17 Mid-IR laser pulse energy versus absorbed pump pulse energy for various pressures of C_2H_2 gas contained within a 45-μm core diameter, 23-μm pitch kagome-structured HC-PCF. Plots showing each pressure individually are shown in Appendix C.

Table 5.1 Summary of laser threshold and efficiency values for various C_2H_2 gas pressures.

C_2H_2 Gas Pressure (torr)	Absorbed Pump Pulse Energy at Laser Threshold (μJ)	Maximum Optical-to-Optical Laser Efficiency (%)
15.4	0.26	17
27.6	0.35	12
37.0	0.39	12
56.1	0.71	7.6
75.0	1.1	4.8

Unfortunately, it is quite clear from the large scatter in the laser pulse energy data shown in Fig. 5.17 that pumping the laser with an OPA has not produced the shot-to-shot stability from the laser output as was hoped. One possible explanation comes from the fact that the hollow

fiber likely guides multiple transverse modes. Different transverse modes would likely experience slightly different fiber losses and different gain coefficients, the latter owing to varying degrees of overlap between different mid-IR modes and the transverse gain profile. Unfortunately, this idea is difficult to explore since to the best of my knowledge the mid-IR mode characteristics of these kagome-structured HC-PCFs have not yet been measured.

The observed peak-to-peak delay between the absorption-free transmitted pump pulse and the generated mid-IR laser pulse as a function of the laser pulse energy is shown in Fig. 5.18 for several acetylene pressures. The delays also show large scatter and range from zero for
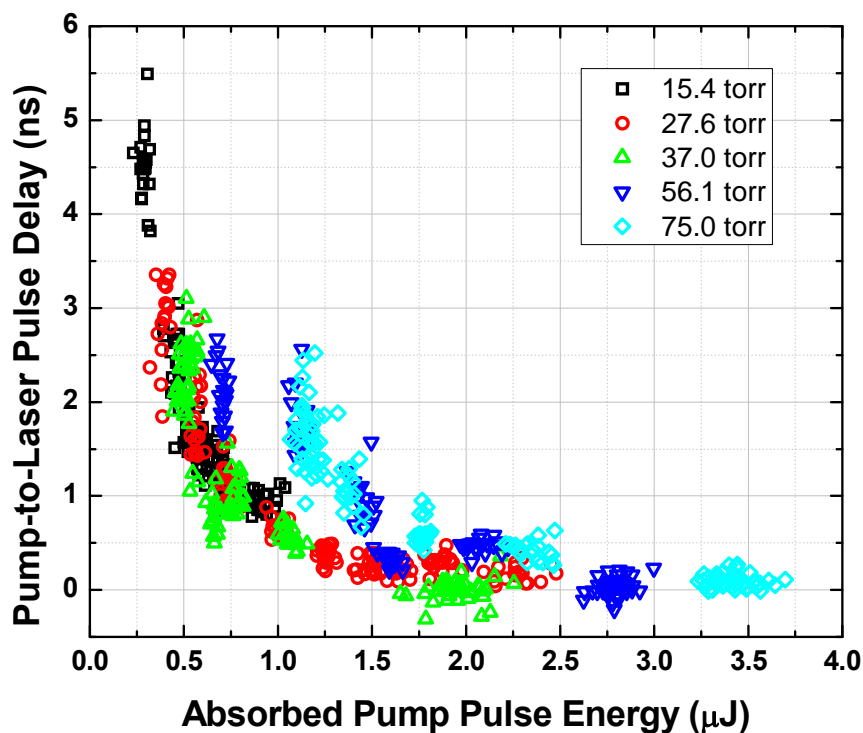
Figure 5.18 The observed peak-to-peak delay between the absorption-free transmitted pump pulse and the generated mid-IR laser pulse as a function of the laser pulse energy at various acetylene pressures. Plots showing each pressure individually are shown in Appendix C.

relatively high laser pulse energies to ~ 5.5 ns for the lowest laser pulse energies, near the lasing threshold, at an acetylene pressure of 15.4 torr. This is an interesting effect, and may indicate that near the lasing threshold, lasing cannot begin until almost all of the pump pulse energy is

absorbed. Thus the laser pulse begins to form near the very tail end of the pump pulse, producing large delays and low total laser pulse energies.

5.2.3 Experimental Results in HCN

HCN gas was also explored using the OPA-pumped laser setup. The driving force for exploring HCN is related to its potential for creating a small quantum defect laser that can be operate with ultrahigh optical-to-optical efficiencies (~ 99%) and has potential to create a strong coherent output from many mutually incoherent pump sources – ideas of particular interest for high power applications. These ideas are discussed in detail in Chapter 7. The current focus is the performance characteristics of HCN gas in the same pulsed laser configuration used to explore acetylene, shown in Fig 5.8.

All of the HCN gas used in the laser experiments was produced in-house at Kansas State University by Professor Chris Levy's research group. This was a necessity as buying more than a small (~ 100 mL) glass sample cell filled with ~ 10 torr of HCN was found to be all but impossible. The gas is synthesized in a single replacement reaction between the organic acid $CH_3(CH_2)_{16}CO_2H$ (stearic acid), which is solid at room temperature but has a low melting temperature, and KCN salt using the setup shown in Fig. 5.19. The reaction is carried out under vacuum using liquid nitrogen to freeze out the gas and moving it through the setup. The KCN salt and stearic acid are combined together in a flask which is then heated, melting the acid and producing HCN gas. The gas is then passed over phosphorous pentoxide (P_4O_{10}), an aggressive drying agent, and transferred to a 1.0 L stainless steel sample bottle.
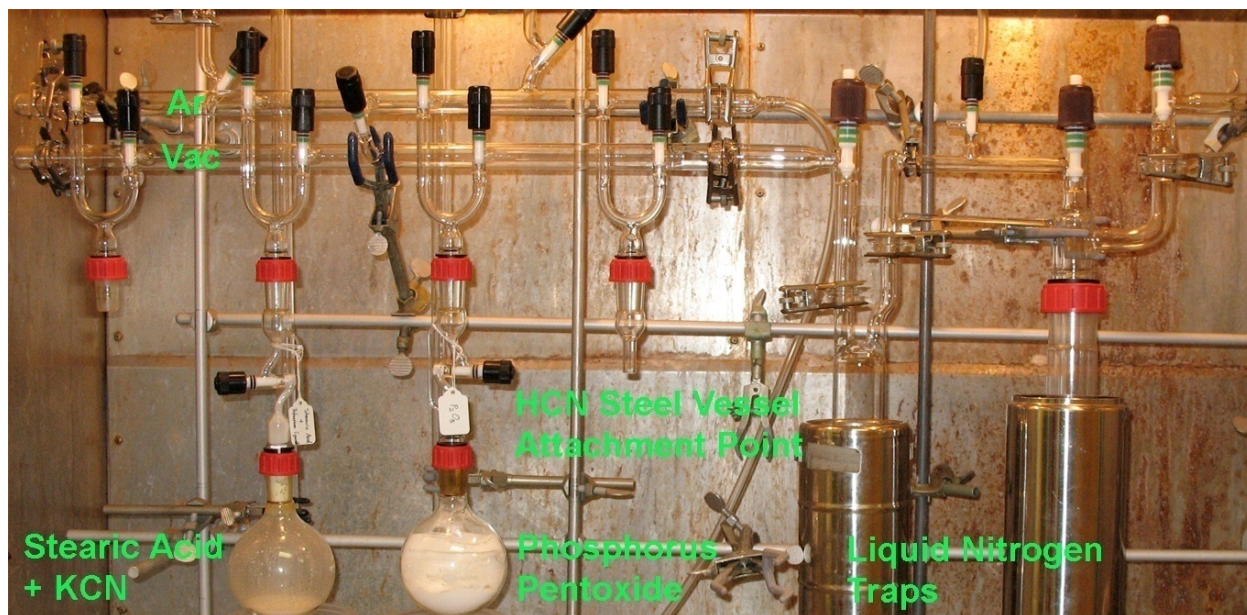
Figure 5.19 Setup for synthesis of HCN gas. The gas is produced by reacting melted stearic acid (CH$_3$(CH$_2$)$_{16}$CO$_2$H) and KCN salt. The HCN gas produced is dried using phosphorus pentoxide and frozen out into a stainless steel sample bottle using liquid nitrogen. Image provided by Professor Chris Levy.

The HCN laser was pumped via the P(10) transition between the $J = 10$, vibrational ground state and the $J = 9$, $2\nu_3$ vibrational state at a wavelength of 1541.27 nm [38]. For clarity the normal modes of vibration for the HCN molecule are shown in Fig. 2.2b [36]. The ν_3 vibrational mode is seen to correspond to the asymmetric C–H stretch. In order to seed the OPA at this longer wavelength the very stable, narrow linewidth fiber laser used with the acetylene laser was switched out for a less-stable, extended-cavity diode laser with a tuning range of 1505 – 1585 nm.

Like acetylene, HCN is linear, but unlike acetylene none of the normal modes of HCN are symmetric. This lack of symmetry may allow a more complete relaxation of the excited populations permitting more efficient lasing. However, we do not expect to see contributions to the laser pulse energy from transitions between the ν_3 states and the vibrational ground states because even though these transitions are allowed, the thermal populations in the $J = 7, 9,$ and 11 vibrational ground states at room temperature should be on the order of the total population initially in the $J = 10$ pump state. Thus no inversion should exist.

The observed laser spectrum is shown together with an energy level diagram for the HCN laser in Fig.5.20. The same computer controlled grating monochrometer used with the OPA-pumped acetylene laser was used here to measure the laser spectrum. The structure present on both of the spectral peaks is again most likely a result of the instability in the laser pulse energy. Just as in the case of the acetylene laser, two peaks are observed in the laser spectrum. These peaks closely correspond with the 3092.55-nm and 3146.81-nm wavelength R(8) and P(10) dipole allowed transitions ($\Delta J = \pm 1$) between the $J = 9$, $2v_3$ excited state and the $J = 8$ and $J = 10$, v_3 states [38].
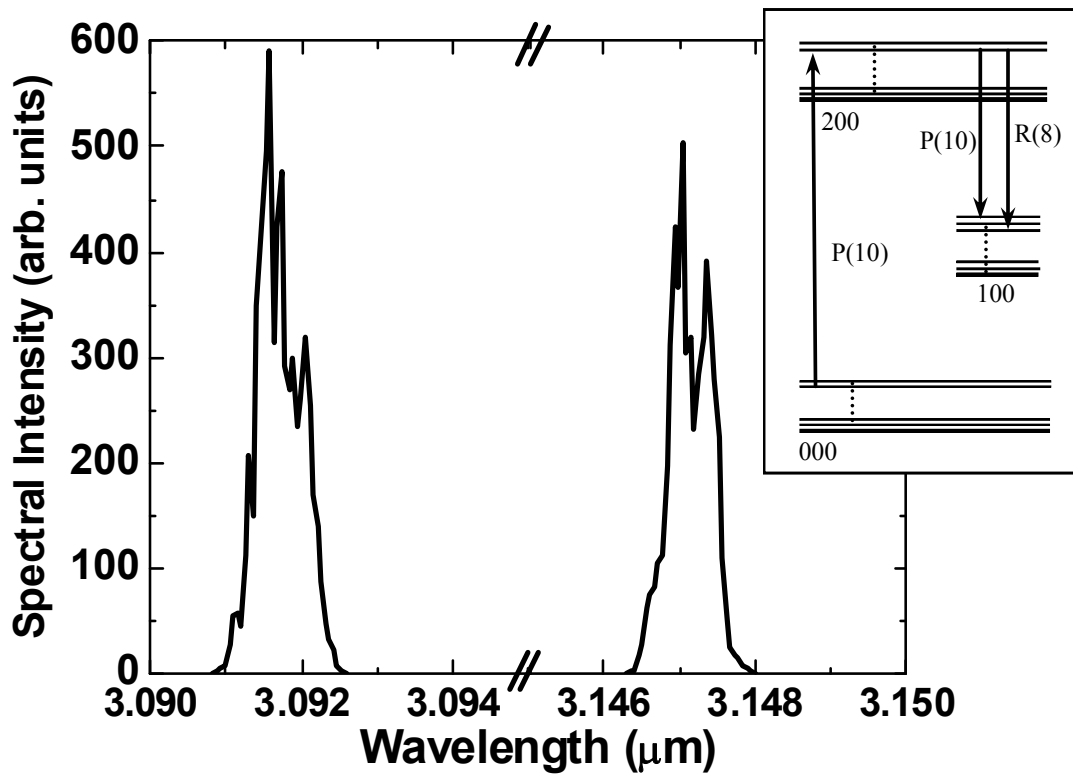
Figure 5.20 HCN-filled kagome-structured HC-PCF laser spectrum together with an energy level diagram showing relevant transitions. The laser was pumped via the P(10) transition between the vibrational ground state and the $2v_3$ vibrational state at a wavelength of 1541.27 nm [38]. The observed peaks correspond well with the R(8) and P(10) transitions from the excited state to the v_3 vibrational state at a wavelengths of 3092.55 and 3146.81 nm respectively [38]. Reproduced from Ref [60].

Figure 5.21 shows the mid-IR laser pulse energy, calculated using Eq. 5.8, as a function of the absorbed pump pulse energy taken at an HCN pressure of 19 torr. No other pressures are shown because lasing is only seen to occur at this single pressure. A summary of the measured laser threshold energy and efficiency are presented in Table 5.2. The maximum laser pulse energy emitted from the HCN laser is seen to be extremely week at ~ 7 nJ, which is roughly a factor of 20 times less than the maximum laser pulse energy observed at the lowest measured pressure from the acetylene-filled fiber in the same setup. The maximum observed optical-to-optical efficiency is also observed to be more than an order of magnitude less than is typical of the acetylene-filled fiber laser demonstrated using the very same fiber. This reduced laser performance may be due at least in part to the reduced performance of the OPA as compared to its performance when pumping the acetylene. This could of course be improved simply by procuring a CW seed laser similar to the tunable fiber laser used to seed the OPA near 1533 nm.
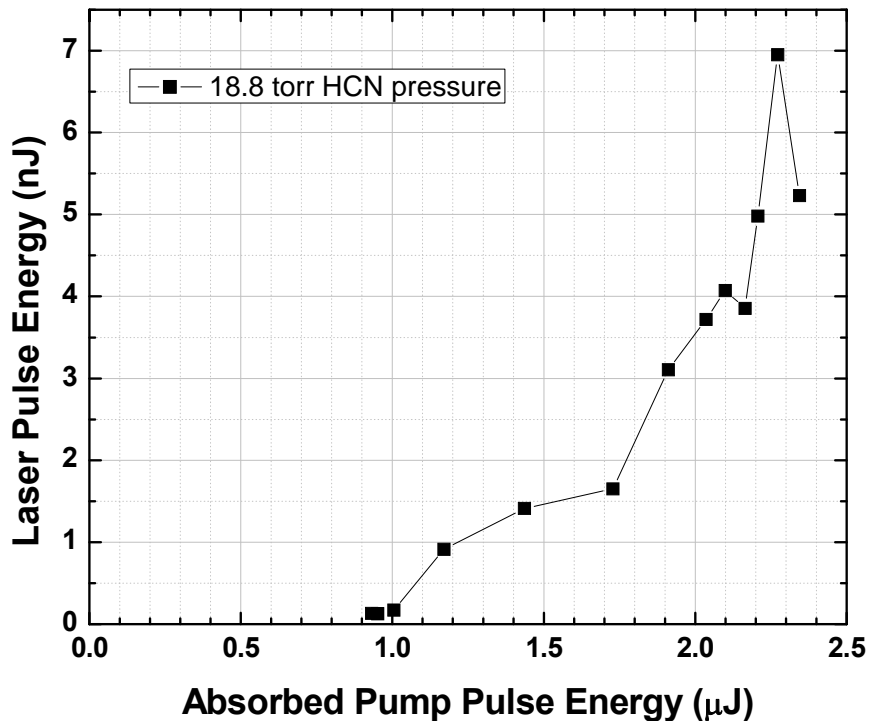
Figure 5.21 Laser pulse energy as a function of absorbed pump pulse energy for a 23-μm pitch kagome-structured HC-PCF filled with 18.8 torr of HCN gas. Increasing or decreasing the pressure by more than ~ 1 torr caused laser signal to drop below the detection threshold. Curve shown includes 3-point adjacent averaging of raw data points.

Table 5.2 Summary of laser threshold and efficiency values for HCN-filled HC-PCF laser.

HCN Gas Pressure (torr)	Absorbed Pump Pulse Energy at Laser Threshold (µJ)	Maximum Optical-to-Optical Laser Efficiency (%)
18.8	1.0	0.31

While both acetylene and HCN were demonstrated to produce mid-IR laser output from population inversions, it seems quite likely that the 20 dB/m fiber loss exhibited by the ~ 45-µm core diameter, 23-µm pitch kagome-structured HC-PCF is limiting the overall laser performance in terms of both the maximum pulse energy and the laser efficiency. Much time and effort was spent constructing a setup and performing mid-IR fiber loss measurements to find a fiber that exhibits lower loss at the mid-IR laser wavelengths. The setup and results from the mid-IR loss measurements performed on the various fibers produced by collaborators at the University of Bath are discussed in detail in Section 4.2. From those measurements several fibers with lower loss in the mid-IR have been identified, and results from one such fiber used in the gas-filled fiber laser setup showing improved performance in the case of both acetylene and HCN gas are the focus of Chapter 6.

5.3 Numerical Simulations of OPO-Pumped Laser Performance

A simple model is used by collaborators at the University of New Mexico to qualitatively predict the trends observed from the initial OPO-pumped laser experiment. The model system is comprised of only three states: a ground state, the pumped excited state, and a terminal excited state with no direct path for population to transfer to or from the ground state during our time scale of interest. The absorption cross-section for the pump transition is estimated as 7.7×10^{-18} cm^2 [61]. Since data for the stimulated emission cross-section for the lasing transition is not available, we assume that it is of the same order of magnitude as that for the $v_3 \rightarrow$ ground vibrational state transition, which is estimated to be $\sim 2.2 \times 10^{-16}$ cm^2 using the known Einstein A coefficient [61]. A Gaussian pump pulse 5-ns long and 2 GHz in bandwidth spectrally centered on resonance with the gas at a wavelength of 1.52 µm enters the fiber, creating a population

inversion. The laser pulse develops from spontaneous emission and co-propagates with the pump. The linear fiber losses at both the pump and laser wavelengths are accounted for.

The model predicts an optimum pressure where the maximum laser pulse energy is produced, like that experimentally observed in Fig. 5.6, which is a function of the fiber length and pump pulse energy. The optimum pressure essentially occurs when a given pump pulse energy creates just enough gain by the end of the fiber to balance the fiber loss. Any further increase in pressure causes additional pump absorption, resulting in a reduction of the gain to below the 20 dB/m fiber loss before the fiber's end. A smaller pressure dependent effect arises from broadening of the linewidth of the pump transition ($\sim$ 1 GHz at 7 torr [40]) at high pressures.

The measured and predicted laser pulse energies as a function of pump pulse energy are shown in Fig. 5.22a and b respectively for a 0.9-m long kagome-structured HC-PCF. The experimental and calculated data are in good qualitative agreement, showing exponential-like small signal gain followed by the onset of saturation as the pump pulse begins to saturate the gas absorption at the end of the fiber. Only relative comparisons between experiment and calculation can be made because the exact fiber-to-free space coupling efficiencies are not known. Cut-back measurements to determine the actual efficiencies are complicated by time-dependent fluctuations in the spatial mode and center frequency of pump pulses from the OPO.

Mid-IR laser output as a function of fiber length as predicted by the model is shown in Fig. 5.22c. When pumping at 6 μJ (solid curves), the first knee present in the laser pulse energy curve occurs when the saturated gain approximately equals the linear fiber loss for the laser radiation. The plateau in the output power persists while the pump is able to maintain (saturated) gain that equals the linear fiber loss for the laser radiation, ending when the depleted pump can no longer maintain sufficient population inversion. Figure 5.22d-f shows the evolution of pump (blue) and laser (green) pulse power calculated at different positions along the length of the fiber for a launched pump (gray) pulse energy of 6 μJ. Initially the laser pulse develops at the leading edge of the undepleted pump pulse (Fig. 5.22d). As the leading edge of the pump is absorbed and saturates the transition, the positive net gain window shifts towards later times during the pump pulse. As a result the laser pulse broadens and its center moves backwards (Fig. 5.22e). At long fiber lengths the pump is almost completely absorbed and the laser pulse energy begins to decrease as the pump can no longer sustain the inversion necessary to compensate the fiber

loss (Fig. 5.22f). Additionally, the temporal width of the laser pulse broadens as it propagates along the fiber and never exceeds the 5-ns duration of the launched pump pulse.
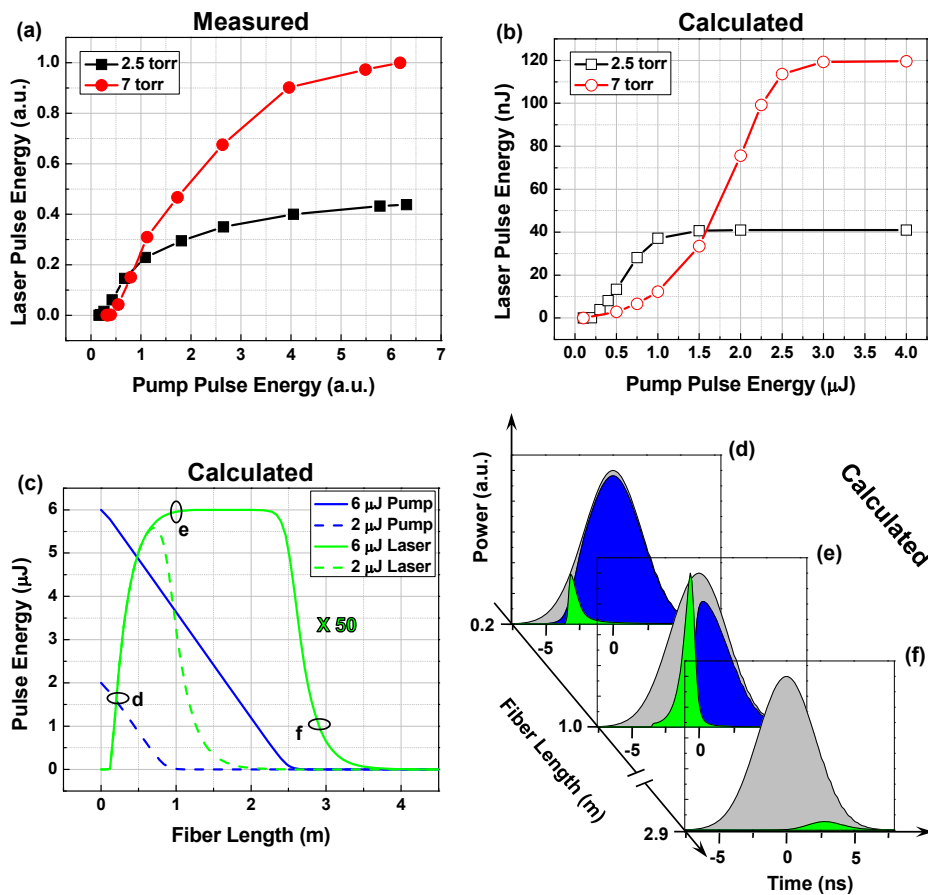
Figure 5.22 Experimental and calculated laser pulse energy dependence on pump energy and fiber length. Laser pulse energy (a) measured and (b) calculated for various levels of pump pulse energy coupled into a 0.9 m long fiber containing $^{12}C_2H_2$ at pressures of 2.5 and 7 torr. (c) The calculated laser (green curves) and pump (blue curves) pulse energies at different positions along the fiber length containing 7 torr of $^{12}C_2H_2$ gas for two different launched pump pulse energies; the laser energy is multiplied by a factor of 50. (d-f) The calculated temporal profiles of the laser (green), and transmitted pump (blue) pulses along with the launched pump (gray) pulse at several positions along the fiber, where the laser power is scaled up by a factor of 5.5. Figure reproduced from Ref [33].

86

Chapter 6 - Lasers Based on Population Inversion from Gas-Filled Hollow Core Fibers: High Efficiency

6.1 Introduction

While the 20 dB/m loss exhibited by the kagome-structured HC-PCF used in Chapter 5 was sufficiently low to demonstrate mid-IR lasing based on population inversion, it was expected that this relatively high fiber loss was limiting the ultimate laser pulse energies and efficiencies. Following these initial laser demonstrations new fibers where designed and fabricated by collaborators at the University of Bath. Some time was then spent to better characterize the mid-IR loss of these newly designed hollow-core fibers in hopes of developing a lower loss fiber for use in the laser, as is discussed in detail in Chapter 4. These efforts were rewarded with the discovery of a much lower loss fiber which has produced lasers with better performance than those initially demonstrated with the higher-loss fiber.

The loss profile of the particular kagome-structured HC-PCF used in the mid-IR laser work discussed in this chapter is shown in Fig. 6.1. The fiber's kagome cladding structure can
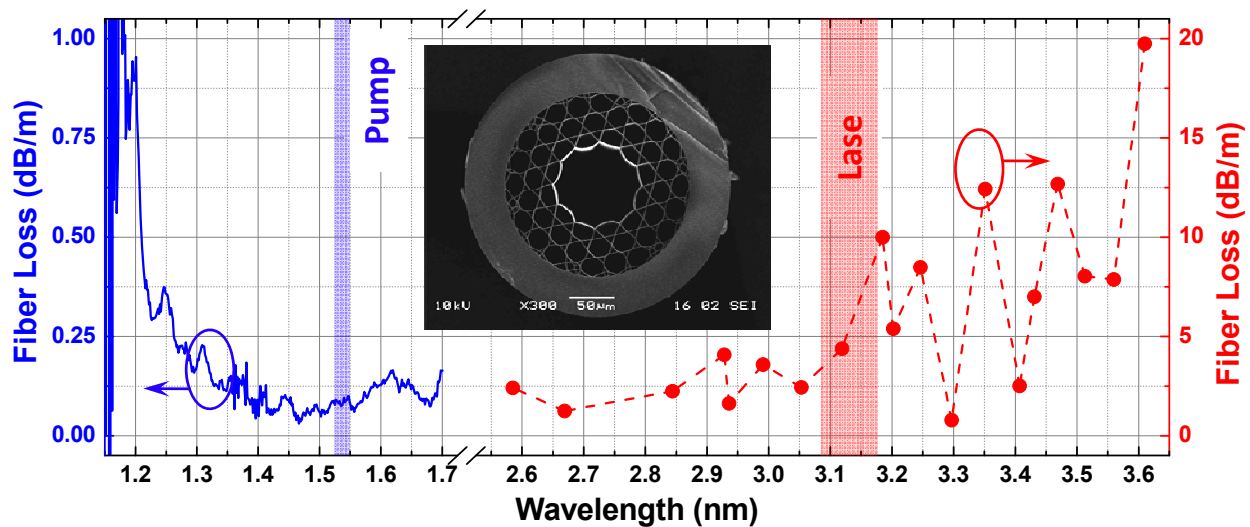
Figure 6.1 Measured loss spectrum of the kagome-structured HC-PCF used in the laser. The pump wavelengths are contained within the blue line near 1.5 μm, and the mid-IR laser wavelengths are contained within the red line just beyond 3 μm. Inset: SEM image of the fiber end. The fiber is seen to have a pitch of 18.75 μm and a core diameter of 85 – 94 μm. Figure adapted from ref [34].

be seen from the scanning electron microscope (SEM) image of the fiber cross section shown in the Fig. 6.1 inset. The fiber loss at 1.5 μm, in the region of the pump wavelengths, is seen to be ~ 0.1 dB/m, while the loss between 3.1 and 3.2 μm, near the laser wavelengths, is approximately 5 dB/m. This represents a more than thirty-fold (~ 15 dB/m) reduction in mid-IR fiber loss from the previous fiber used in the laser setup [62].

6.2 Experimental Setup

A schematic of the OPA-pumped C_2H_2 and HCN-filled HC-PCF laser setup is shown in Fig. 6.2. The setup is almost identical to that used with the previous fiber shown in Fig. 5.8, but now 45-cm or 1.46-m long sections of the lower-loss, 18.75-μm pitch kagome-structured HC-PCF are installed in the low volume vacuum chambers. With the exception of the new fiber, the setup is unchanged up to the point where the uncoated polished germanium filter was previously used to split off a portion of the pump light that is transmitted through the hollow fiber. The uncoated germanium filter angled at ~ 45° to the incident beam is removed and replaced with an uncoated CaF_2 window. An AR-coated polished germanium filter is then placed at normal incidence to the pump and mid-IR laser beams after the angled CaF_2 window to filter the pump from the generated mid-IR light. This filter transmits more of the generated mid-IR light to the HgCdTe detector than the uncoated filter, improving the system sensitivity by more than a factor of 2.

Using the angled CaF_2 window reduces the amount of reflected pump light by almost a factor of 10, owing to the much reduced refractive index of CaF_2 compared to germanium (1.43 [59] compared to 4.35 [63] at 1.5 μm, respectively). This factor of 10 reduction in the reflected pump pulse energy can easily be compensated for by adjusting the neutral density filter values to remove 10 dB of optical attenuation before coupling the transmitted pump light into the SMF patch cord. The filter previously used to remove mid-IR light from the transmitted pump light just prior to coupling the pump light into the SMF patch cord is also removed, as no contribution from the mid-IR pulses is observed at the 25-GHz InGaAs photodetector.

While it was used in the initial OPA-pumped laser setup as a precautionary measure, this filter is expected to be unnecessary for several reasons. First, the ~ 2-mm thick AR-coated aspheric lens will be more reflective and have higher material absorption at mid-IR wavelengths than at the 1.5-μm pump wavelength where the lens's transmission is optimal. Second, coupling

into the fiber's ~ 10-μm diameter guided mode is extremely sensitive to the exact spatial alignment of the lens to the fiber's end. While some coupling is observed to be maintained in switching between near and mid-IR wavelengths while coupling into the large-core kagome fibers, an order of magnitude or more drop in the coupling efficiency is typically observed. This effect is expected to be even more pronounced when using a fiber like SMF that has a much smaller core diameter. Third, light coupled into the fiber must travel several meters to reach the
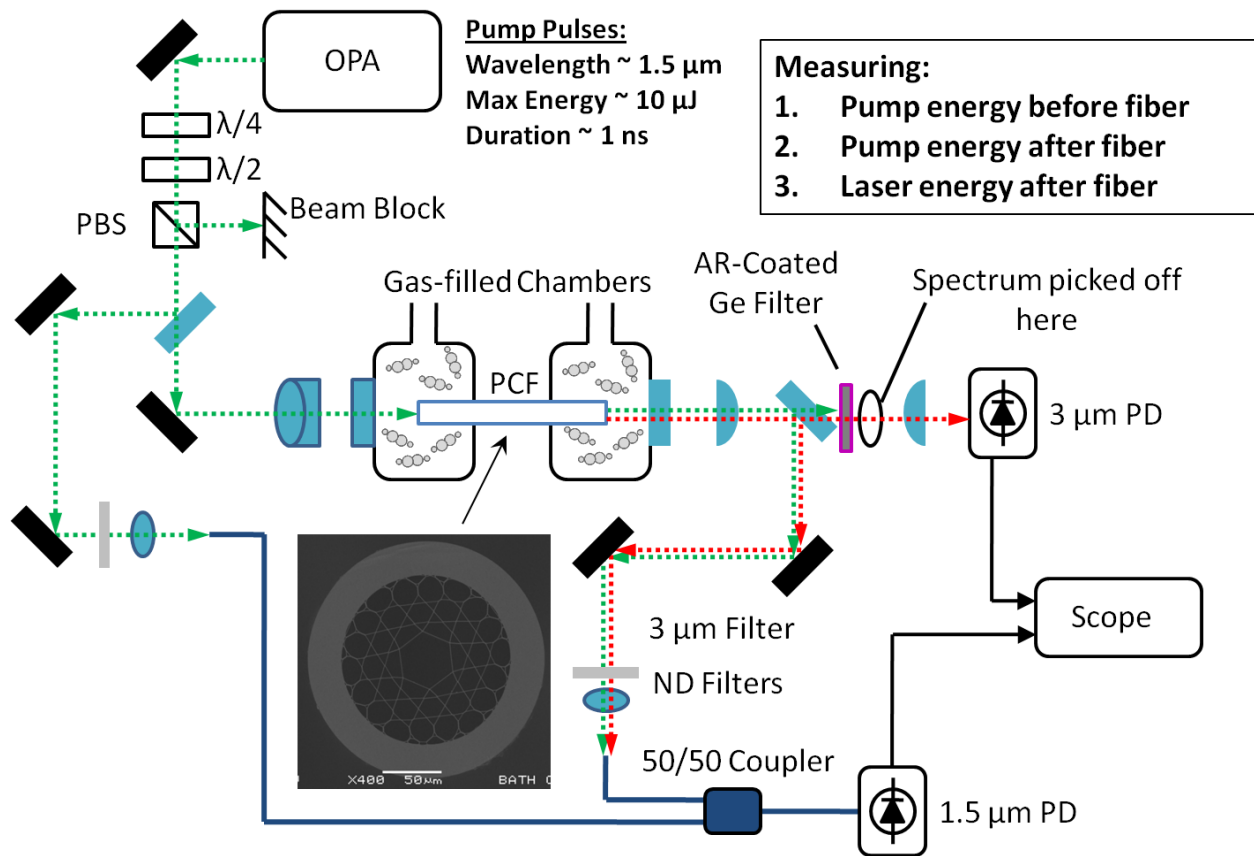
Figure 6.2 Efficient gas-filled HC-PCF laser setup. C_2H_2 or HCN gas is contained inside the HC-PCF. Pump pulses from an OPA are coupled into the fiber through one end while the generated mid-IR light and any unabsorbed pump light are coupled out of the opposite end of the fiber. Mid-IR light passes through a 2-mm thick, AR-coated germanium filter at normal incidence and is focused onto a HgCdTe detector. A fraction of the unabsorbed pump light is picked off from the main beam using an angled CaF_2 window and sent to a fiber coupled, 25-GHz InGaAs photodetector.

photodetector, and SMF is fabricated from fused silica which exhibits large material absorption for wavelengths beyond ~ 3 μm. Lastly, even if mid-IR light were to make it to InGaAs photodiode, the response of the detector is several orders of magnitude below the response near 1.5 μm.

In addition to improving the detection efficiency of the laser system at mid-IR wavelengths, the AR-coated germanium filter at normal incidence is expected to be much less susceptible to polarization effects than the uncoated filter angled 45° to the incident light, which may be responsible for instabilities in the laser pulse energy like those observed in Fig. 5.17.

For the uncoated, angled germanium filter, the total power transmitted through the filter (two air-germanium boundaries) for s- and p-polarized light can be calculated by accounting for the Fresnel reflections using Eqs. 5.1 and 5.2, respectively. Using the index of refraction of germanium near 3.2 μm equal to 4.05 [63] and an angle of 45° between the filter's normal and the incident light, the percentage of power transmitted through the filter is 26% for s-polarized light and 58% for p-polarized light. Fluctuations between these two transmission extremes would produce fluctuations in the measured laser pulse energy on the order of 50% of the maximum value, which is on par with what is observed in the initial laser data shown in Fig. 5.17.

The same analysis performed for the uncoated CaF_2 window at the same 45° angle and having an index of refraction equal to 1.42 [59] at wavelengths near 3.2 μm gives expected variations on the order of 10% of the maximum pulse energy, which would be a noticeable improvement over the previous pulse energy fluctuations. Fluctuations due to shot-to-shot variations in the polarization of the mid-IR light could further be reduced by adjusting the setup so that the CaF_2 window could be put at near normal incidence to the incident pump light. This is clear from the angular dependence of the Fresnel reflections shown in Fig. 5.12, where the reflection coefficients for s- and p-polarized light are seen to converge when the angle, θ_i, between the propagation direction of the incident light and the vector normal to the plane containing the index of refraction boundary is zero (boundary is perpendicular to the propagation direction of the light).

The transmission of the AR-coated germanium filter was measured directly using narrow bandwidth, mid-IR idler pulses from the CW-seeded OPA, having a center wavelength of 3478 nm. The pulse energy from the OPA was measured using a pyroelectric energy sensor both

90

with and without the filter in the beam path at normal incidence to the beam. The data corresponding to this process is shown in Fig. 6.3a. The ratio of the pulse energy observed with the filter to that observed without the filter present gives the filter's transmission, which from the average of the "With Filter" region (shown in red) and the "Without Filter" regions (shown in green), is equal to 96%.

(a)

(b)
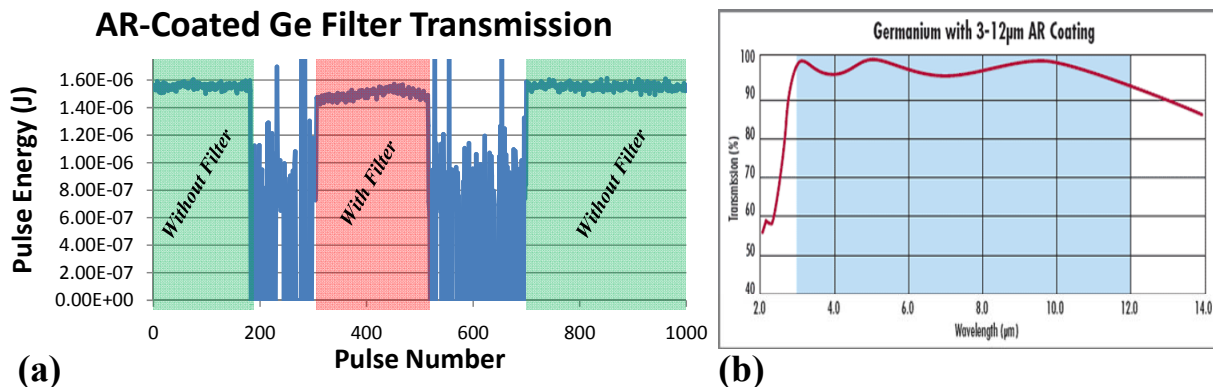
Figure 6.3 The measured transmission data of the AR-coated germanium filter and the typical transmission of the filter from the manufacturer. (a) The measured 3478-nm wavelength pulse energy emitted from the OPA without the filter present is shown in the green regions while the pulse energy measured with the filter present is shown in the red region. (b) The typical transmission through the filter is seen to be ~ 96% to 99% in the region between 3.0 and 3.5 µm. A typical transmission curve for an AR-coated filter of this type is reproduced from ref [64].

Figure 6.3b shows the AR-coated filters typical transmission curve, provided by the manufacturer. The measured value of 96% near 3.5 µm is in good agreement with the typical value. From this curve it is also apparent that the filter's transmission should only be different by a few percent at the actual laser wavelengths near 3.2 µm.

The HgCdTe photodetector is also recalibrated for the mid-IR laser pulse energy using actual mid-IR output from the acetylene-filled fiber laser. This is made possible by the laser's much improved performance owing to the lower-loss fiber, and from the much reduced Fresnel losses at the mid-IR wavelengths achieved by employing the AR-coated germanium filter. Pulse energies recorded using a pyroelectic sensor placed just in front of the photodetector are

compared to the integrated voltage signals measured from the photodetector after removing the pyroelectic sensor for a few different incident pump pulse energies. The calibration curve for the HgCdTe photodetector is shown in Fig. 6.4. The y-intercept of the fit line is set equal to zero, since both the laser pulse energy and the integrated voltage signal should tend to zero as the laser pulse energy drops, as the backgrounds of these signals have been subtracted off, leaving them devoid of offsets.
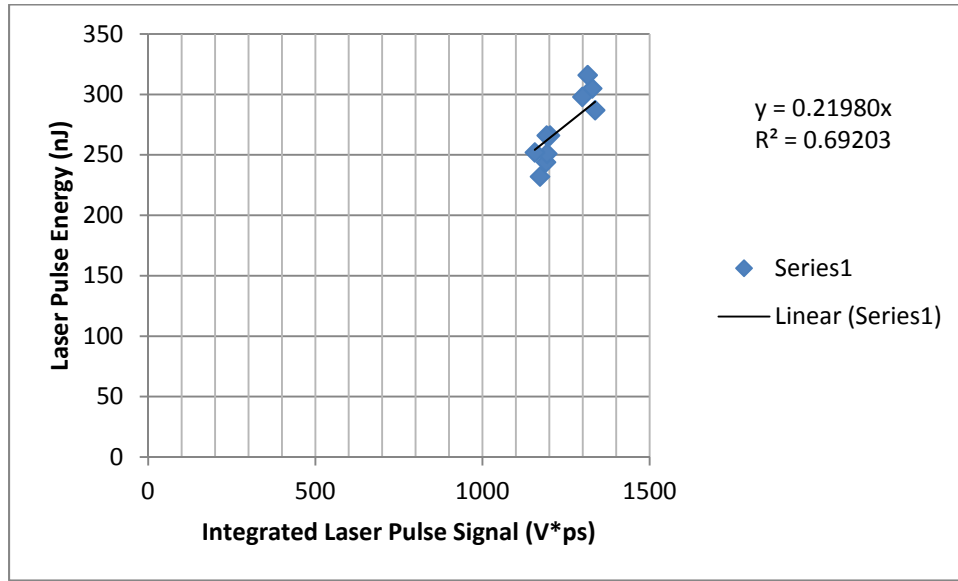
Figure 6.4 Energy calibration curve for the room-temperature HgCdTe photodetector measured using P(13)-pumped C₂H₂-filled 1.46-m long kagome HC-PCF laser output.

6.3 Experimental Results: Acetylene

Just as was done in Chapter 5 using the 23-µm pitch fiber, acetylene gas inside of a 1.46-m long piece of the new, 18.75-µm pitch kagome fiber is pumped at a wavelength of 1532.8 nm corresponding to the P(13) overtone transition between the vibrational ground state and the $v_1 + v_3$ vibration state. The pump pulse excites a fraction of the population from the $J = 13$ ground state to the $J = 12$ excited state. This very quickly creates a population inversion between the pumped state and both the dipole allowed $J = 11$ and $J = 13$, v_1 states, since the thermal population of the v_1 states at room temperature is negligible. Since there is no dipole allowed transition from the v_1 states directly to the ground vibrational state, we expect that once the

intensity of stimulated emission is sufficient to equalize the populations between the pumped state and the v_1 states, the laser action will stop, and no additional transitions will be observed.

The measured spectra of the mid-IR laser pulses taken at various acetylene pressures together with an energy level diagram illustrating the relevant transitions are shown in Fig. 6.5a and b, respectively. Spectra were taken using the same computer-controlled grating monochrometer used to take the OPA-pumped laser spectra shown in Chapter 5, with a spectral resolution of ~ 0.2 nm for 50 μm entrance and exit slit widths. The measured peak wavelengths match well with the expected R(11) and P(13) transitions between the $J = 12$, $v_1 + v_3$ excited state and the $J = 11$ and $J = 13$, v_1 terminal laser state, at wavelengths of 3114.6 and 3172.4 nm respectively. The total relative energy of the laser pulses which is proportional to the area under the spectral curves is seen to reach a maximum at a pressure of 20 torr. Just as is the case for the acetylene laser in the higher-loss kagome fiber, the R-branch transition is seen to always be favored by a factor of ~ 2 − 5. The relative contribution to the laser energy from the two transitions involved is not seen to be grossly pressure dependent.
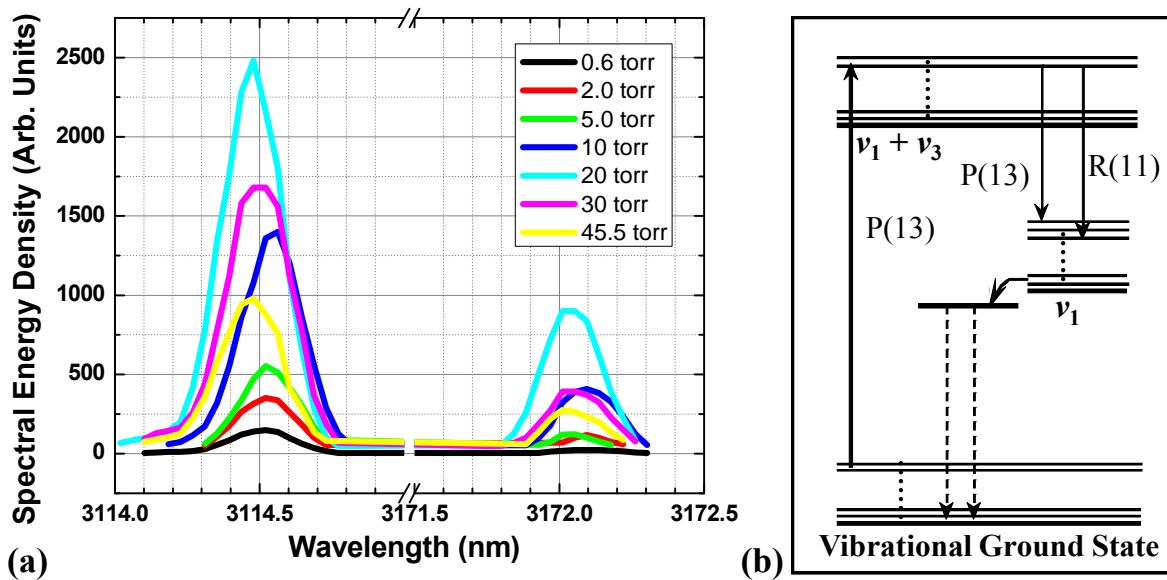
Figure 6.5 (a) Measured spectra of the mid-IR laser output taken at different acetylene pressures and (b) an energy level diagram showing the relevant ro-vibrational transitions. While the total laser pulse energy which is proportional to the total area under the curve is seen to reach a maximum at a pressure of 20 torr, the distribution of energy between the two spectral components is not seen to change much. Figure adapted from ref [34].

The measured mid-IR laser pulse energy as a function of absorbed pump pulse energy is shown in Fig. 6.6 for various acetylene pressures. Both the slope efficiency and the total optical-to-optical efficiency of the laser, defined as the ratio of the laser pulse energy to the absorbed pump pulse energy, are seen to reach maximums at a pressure of 2.0 torr, where a maximum total efficiency of ~ 31% is observed at ~ 1.0 μJ of absorbed pump pulse energy. Additionally, the laser threshold energy, defined as the amount of pump pulse energy absorbed by the gas at the onset of lasing, is seen to be ~ 0.25 μJ. The laser threshold energy and the maximum total efficiency observed at each pressure are summarized in Table 6.1. As the gas pressure is increased from 2.0 torr, laser threshold energy increases while the slope efficiency and the maximum total efficiency are generally seen to decrease. The data at 20 torr are the exception to
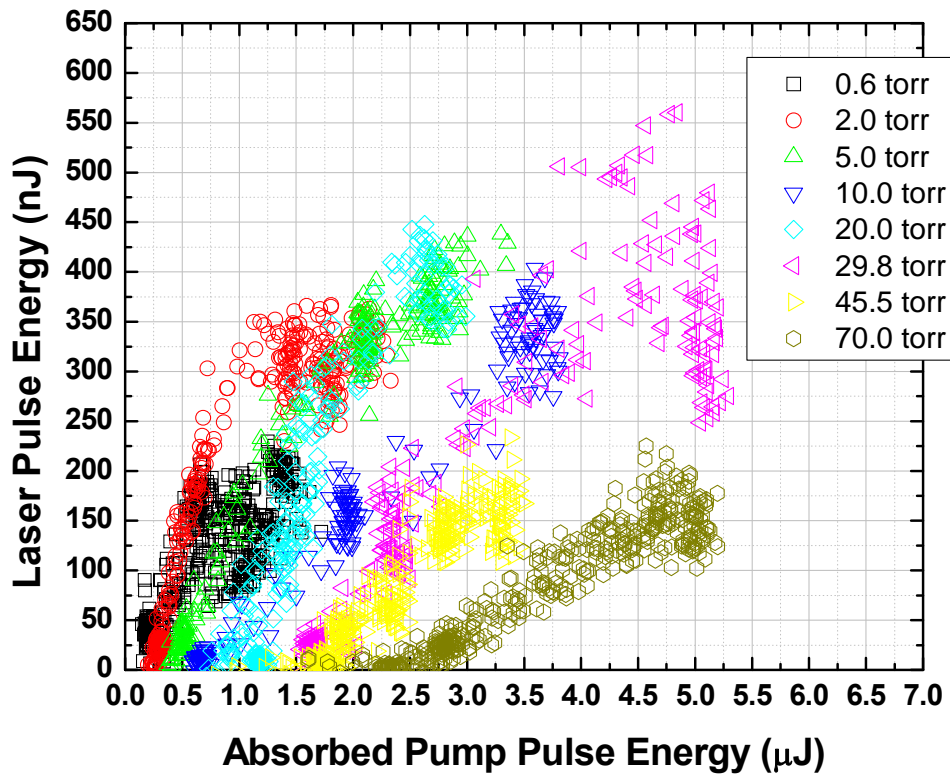
Figure 6.6 Plot of the measured mid-IR laser pulse energy as a function of absorbed pump pulse energy for a 1.46-m long, 18.75-μm pitch kagome-structured HC-PCF filled with various pressures of C₂H₂ gas. Plots of each pressure individually are shown in Appendix C. Reproduced from ref [34].

Table 6.1 Summary of laser threshold and efficiency values for various C$_2$H$_2$ gas pressures.

C$_2$H$_2$ Gas Pressure (torr)	Absorbed Pump Pulse Energy at Laser Threshold (µJ)	Maximum Optical-to-Optical Laser Efficiency (%)
0.6	0.055	24
2.0	0.25	31
5.0	0.40	17
10.0	0.60	10
20.0	1.0	16
29.8	1.5	9.9
45.5	1.6	5.3
70.0	2.4	3.4

this and are suspect. More data should be taken at this pressure to either confirm or dispel the seemingly anomalous characteristics present in this preliminary data.

An interesting feature of the low pressure data, 5.0 torr and below, is the saturation-type behavior occurring at high absorbed pump pulse energies. Saturation behavior like this would be expected if the laser pulse energy were plotted as a function of the incident (or transmitted) pump pulse energy, since there is a critical amount of energy that can be absorbed by the gas corresponding to complete inversion, after which any additional light is simply transmitted through the gas. However, Fig 6.6 shows the laser pulse energy as a function of absorbed pump pulse energy, where the laser pulse energy is expected to simply increase until the critical energy corresponding to complete inversion is reached. The saturation behavior would seem to indicate the onset of an additional process like excited state pump absorption that may remove population from the pumped state at high pump intensities, causing additional energy to be absorbed by the gas without creating additional mid-IR laser output.

The amount of absorbed pump energy necessary to reach saturation can be estimated using the initial and the saturated, steady-state ro-vibrational state populations for a four-level system. Assume that the system is comprised of a ground state, an excited state, and two terminal laser levels in between which only couple only to the excited state (not to the ground state). Before the pump pulse enters the gas, the overwhelming majority of the molecular population

occupies the vibrational ground state and is thermally distributed according to the Boltzmann distribution given by Eq. 2.10.

The total number of molecules in the $J = 13$ state, $N(J = 13)$, is equal to the total number of molecules contained within the fiber laser system, N_{tot}, multiplied by the fraction of molecules in the $J = 13$ rotational state alone. At thermal equilibrium, the probability of finding an acetylene molecule in the $J = 13$, vibrational ground state, $P(J = 13)$, can be computed from Eq. 2.10 and is equal to 0.082. Under saturation conditions, the populations in all states will be equal. Under saturation conditions at steady-state the ground state population for this four level system will then approach $N(J = 13)/4$. (as the ground state population is shared evenly between all four states)

The total pulse energy absorbed by the gas to reach saturation, $E_{abs,sat}$, is related to the total number of photons absorbed by the gas by,

$$E_{abs,sat} = n_{p,abs} \cdot \frac{hc}{\lambda_p}$$

6.1

where h is Plank's constant, c is the speed of light in vacuum, λ_p is the wavelength of the pump photons, and $n_{p,abs}$ is the total number of photons absorbed by the gas which is given by,

$$n_{p,abs} = \left[N(J = 13) - \frac{1}{4} N(J = 13) \right] = \frac{3}{4} N(J = 13) = \frac{3}{4} P(J = 13) \cdot N_{tot}$$

6.2

The total number of molecules in the system, N_{tot}, can be computed using the ideal gas law as,

$$N_{tot} = \frac{p \cdot V}{k_B T} = \frac{p \cdot \frac{\pi}{4} d_f^2}{k_B T}$$

6.3

where p is the gas pressure, d_f is the mode field diameter of the pump beam, k_B is the Boltzmann constant, and T is the temperature of the gas (room temperature in this case). Combining Eq. 6.1 − 6.3 gives the following expression for the absorbed pump energy at the point of optical saturation,

$$E_{abs,sat} = \frac{3}{4}P(J = 13) \cdot \frac{p \cdot \frac{\pi}{4}d_f^2}{k_B T} \cdot \frac{hc}{\lambda_p}$$ 6.4

Assuming a mode field diameter of 50 μm, Table 6.2 shows the calculated saturation energies at pressures corresponding to those where the data shown in Fig. 6.6 was taken. For acetylene pressures of 5.0 torr and below, absorbed pump pulse energies equal to those necessary to saturate the gas contained inside the fiber can be reached, and at these pressures the calculated absorbed pulse energies are seen to coincide fairly well with the apparent onset of saturation indicated by a plateau in laser pulse energy.

Table 6.2 Summary of the calculated absorbed pump pulse energies required to saturate the C$_2$H$_2$ gas at various gas pressures.

C$_2$H$_2$ Gas Pressure (torr)	Pump Pulse Energy Absorbed at Saturation (μJ)
0.6	0.3
2.0	1.0
5.0	2.6
10.0	5.1
20.0	10.3
29.9	15.4
45.5	23.7
70.0	36.0

The observed peak-to-peak delay between the generated mid-IR laser pulse and the absorption-free transmitted pump pulse as a function of the absorbed pump pulse energy is shown in Fig. 6.7 for various acetylene pressures. The delays are seen to range from near zero to beyond 30 ns, more than 5 times the maximum delays observed from the higher-loss fiber. Generally, for high absorbed pulse energies the delay seems to be quite small, indicating that the laser pulse power continues to grow until just after the peak of the pump pulse. For lower absorbed pump pulse energies, the laser power peak arrives later relative to the absorption-free

pump pulse, likely indicating that for low energy pump pulses more time is needed for the molecules to absorb enough energy to produce the maximum population inversion and thus the maximum laser power. Striation in the delays for the lowest pressure data arises from the fact that multiple peaks can be seen in the temporal profile of the laser pulse, and the relative height of these peaks changes from pulse to pulse.
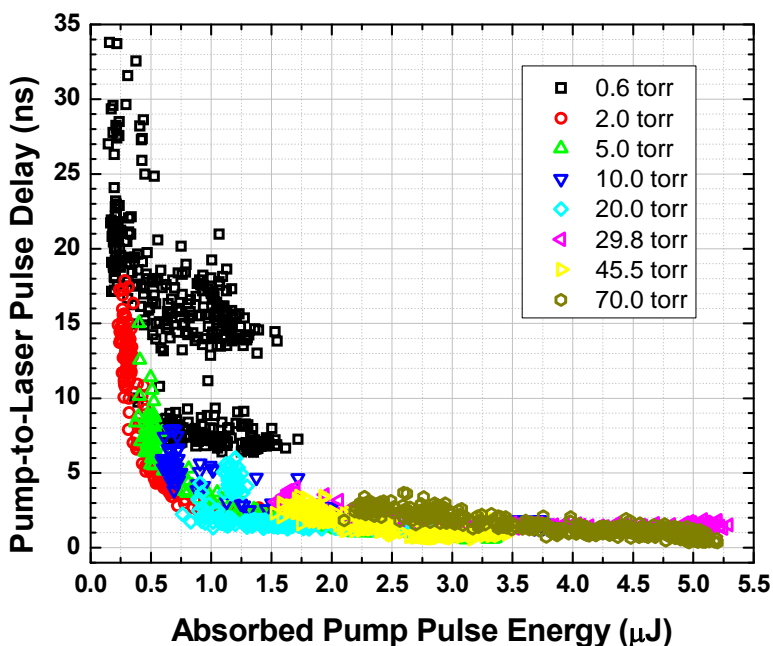
Figure 6.7 The observed peak-to-peak delay between the generated mid-IR laser pulse and the absorption-free transmitted pump pulse as a function of the absorbed pump pulse energy at various acetylene pressures. The striation in the delays at low absorbed pump energies and low pressure is due to multiple peak in the laser pulse. Plots of each pressure individually are shown in Appendix C. Figure adapted from Ref [34].

A comparison of the OPA-pumped acetylene laser results obtained using the lower-loss 18.75-μm pitch kagome HC-PCF to those initially obtained using the higher-loss 23-μm pitch fiber clearly shows that better laser performance is achieved by using lower-loss fiber. The loss per unit length of the lower-loss fiber is ~ 5 dB/m at the mid-IR laser wavelengths, between 3.1 and 3.2 μm. This translates into a total loss of more than 7 dB for light traveling the entire 1.46-m length of the fiber. To explore what effect this total fiber loss might have on the laser's performance, the ends of a shorter, 45-cm long piece of the same 18.75-μm pitch kagome fiber

were installed in the vacuum chambers. The total mid-IR loss from the shortened piece is ~ 2.3 dB.

The short fiber was filled with acetylene gas to an optimum pressure of 30 torr which was determined by maximizing the laser pulse energy observed from the fiber while using the maximum pump pulse energy available from the OPA. The laser was pumped using the same P(13) transition between the vibrational ground state and the $v_1 + v_3$ overtone state used with the 1.46-m long fiber. The spectrum of the laser, taken using the same computer-controlled grating monochromer used to observe the output from the 1.46-m long fiber, is shown in Fig. 6.8. Just like the spectrum shown in Fig. 6.5a from the 1.46-m long acetylene-filled fiber, the spectrum from the 45-cm long fiber shows two spectral peaks corresponding to the expected R(11) and P(13) transitions between the $J = 12$, $v_1 + v_3$ excited state and the $J = 11$ and $J = 13$, v_1 terminal laser state, at wavelengths of 3114.6 and 3172.4 nm respectively.

One striking difference between this spectrum and all the spectra taken using the longer kagome fiber is that here the longer wavelength P-branch transition is now favored over the shorter wavelength R-branch transition by about the same factor that the R-branch is favored
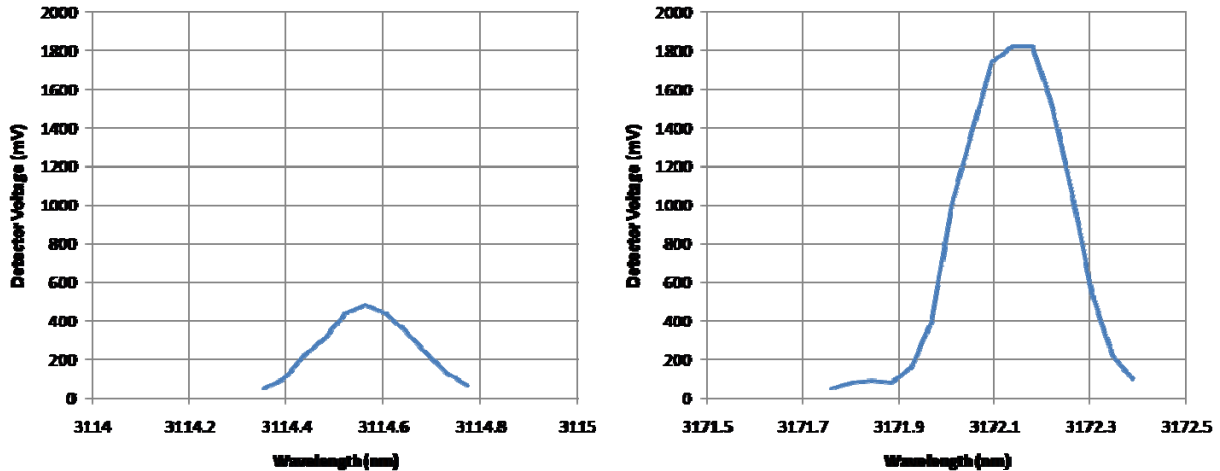
Figure 6.8 Measured spectrum of the acetylene-filled 45-cm long kagome-structured HC-PCF laser output taken at a pressure of 30 torr. Two spectral peaks are observed, corresponding to the R(11) and P(13) transitions between the $v_1 + v_3$ excited state and the v_1 terminal laser state, at wavelengths of 3114.6 and 3172.4 nm respectively. Unlike the spectra taken from the 1.46-m long acetylene-filled fiber, the longer wavelength P-branch transition is seen to be favored here over the shorter wavelength R-branch transition.

over the P-branch in the 1.46-m long fiber. The P-branch is typically favored in conventional gas lasers, and results from the J-dependence of the number of available states, proportional to $2J + 1$, which dictates that rotational levels with higher J values have more states available. However, we have not ruled out that the change in the relative spectral contributions is an artifact of the spectrometer.

The laser pulse energy was measured and characterized as a function of the absorbed pump pulse energy and is shown in Fig. 6.9. The absorbed pump pulse energy required to reach the lasing threshold and the maximum optical-to-optical efficiency are determined from the plot and are tabulated in Table 6.3. Compared to the 30 torr data taken in the 1.46-m long fiber, the laser threshold is slightly higher while the observed maximum efficiency from the 45-cm fiber is nearly identical. Even the shapes of the plotted data look nearly identical. This leads one to reason that the total fiber loss likely plays no role in the laser behavior in the pump energy, fiber
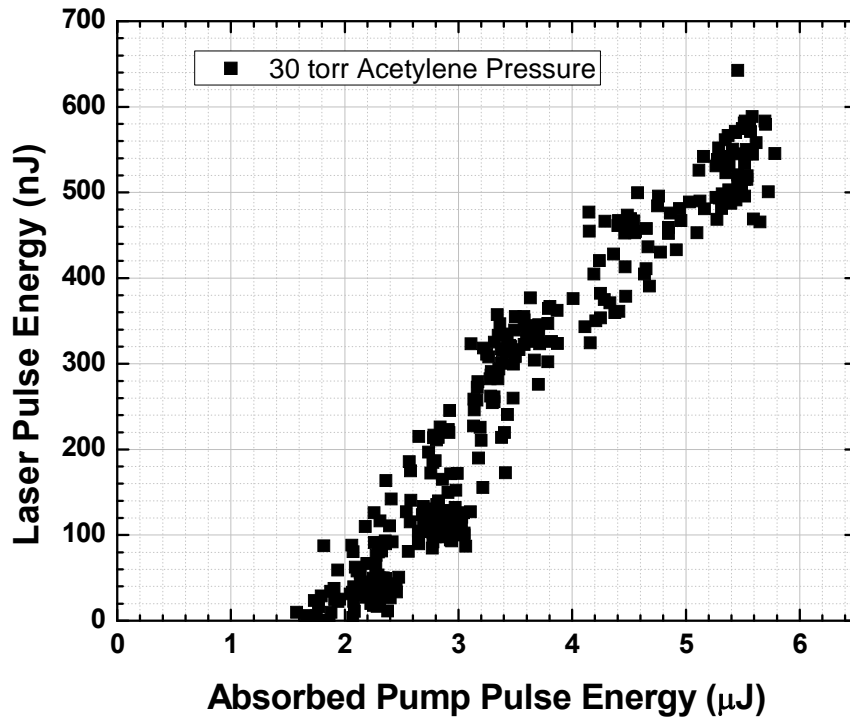
Figure 6.9 Laser pulse energy as a function of absorbed pump pulse energy for the 45-cm long, 18.75-μm pitch kagome-structured HC-PCF filled with 30 torr of C₂H₂ gas. The shape of the data is seen to very closely mimic that observed under the same conditions in the 1.46-m long fiber of the same pitch.

Table 6.3 Summary of laser threshold and efficiency values for 45-cm long, C_2H_2-filled HC-PCF laser.

C_2H_2 Gas Pressure (torr)	Absorbed Pump Pulse Energy at Laser Threshold (μJ)	Maximum Optical-to-Optical Laser Efficiency (%)
30	2.0	9.8

length, and pressure regimes explored, and the primary factor responsible for the laser performance is the fiber's loss per unit length.

The relative time delay between when the peak of the pump pulse would arrive at the HgCdTe photodetector in the absence of any absorption by the gas, and when the peak of the laser pulse does arrive at the HgCdTe photodetector was observed and is shown in Fig. 6.10. The data shows the same general trend as is observed in Fig. 6.7 from the 1.46-m long fiber. The delay is nearly zero for relatively high absorbed pump pulse energies and increases as the absorbed pump pulse decreases toward the laser threshold energy. Comparing the data sets taken
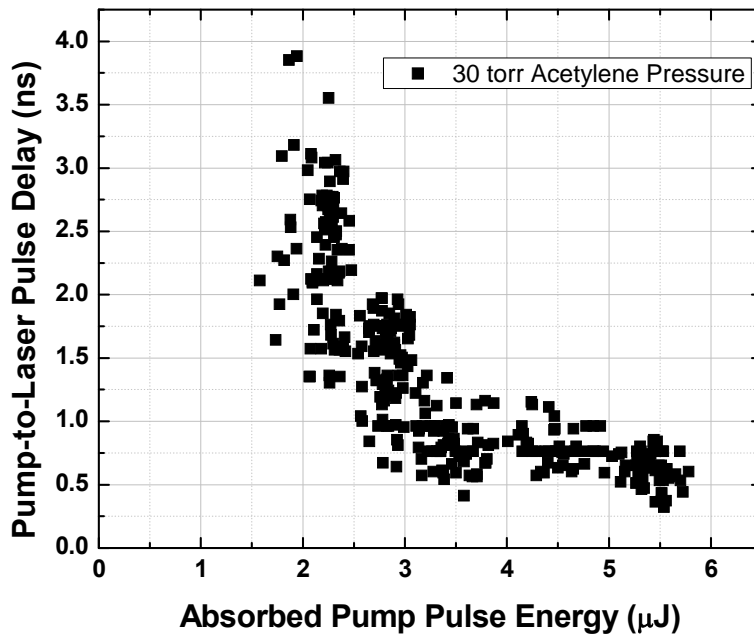
Figure 6.10 Relative timing between the expected pump pulse peak and the observed peak of the laser pulse measured on the HgCdTe photodetector.

at 30 torr, the data from both fiber lengths again very nearly coincides, further indicating that the fiber length, and total fiber loss is not a critical parameter limiting performance under the present operating conditions of our acetylene-filled fiber laser systems.

6.4 Experimental Results: HCN

HCN gas inside of a 45-cm long piece of the lower-loss, 18.75-μm pitch kagome fiber is pumped at a wavelength of 1541.3 nm corresponding to the P(10) overtone transition between the vibrational ground state and the $2v_3$ vibration state, just was done in Chapter 5 using the 23-μm pitch kagome fiber. The pump pulse excites population from the $J = 10$ ground state to the $J = 9$ excited state, creating a population inversion between the pumped state and both the dipole allowed $J = 8$ and $J = 10$, v_3 states. The measured spectrum of the mid-IR laser output from the HCN laser is shown in Fig. 6.11a, while an energy level diagram with the relevant transitions is shown in Fig. 6.8b. Similar to the acetylene laser demonstrated in the 45-cm long fiber, the HCN laser spectrum indicates that the longer wavelength P-branch transition is favored over the shorter wavelength R-branch transition.

(a) **(b)**
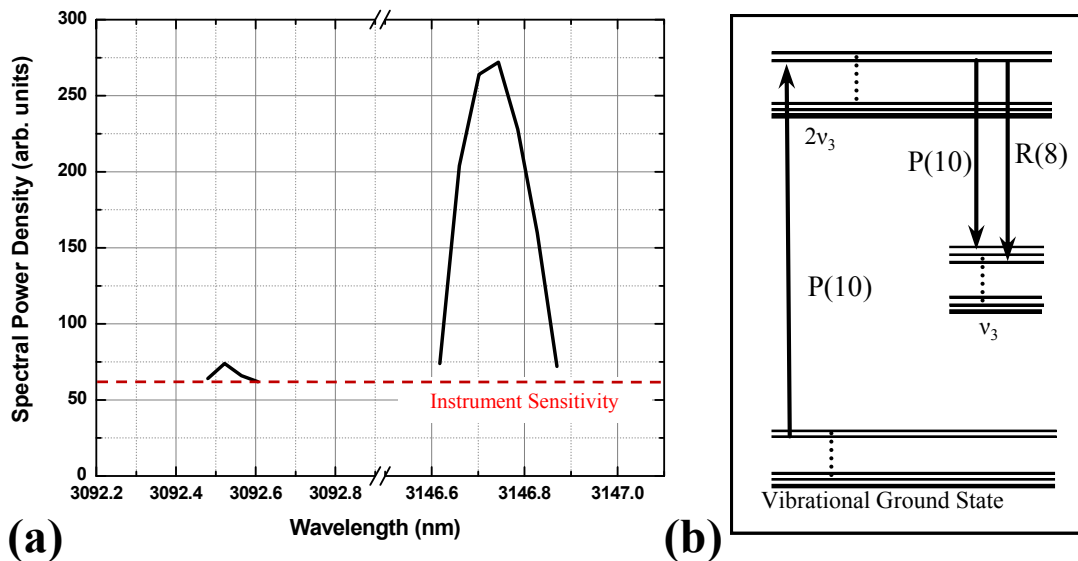
Figure 6.11 (a) Spectrum of the mid-IR laser pulses created in a 45-cm long kagome-structured HC-PCF filled with 11.6 torr of HCN gas. The horizontal dashed red line indicates the limitation imposed by the instrument's sensitivity. (b) An energy level diagram showing the relevant ro-vibrational transitions. Adapted from Ref [34].

Figure 6.12 shows the maximum observed laser pulse energy as a function of absorbed pump pulse energy for various pressures of HCN gas contained within the 45-cm long hollow-core fiber. It is preferable to measure the laser pulse energy at multiple absorbed pump pulse energies between the laser threshold value and the maximum achievable absorbed pump pulse energy. However, due to seemingly random fluctuations in the OPA output pulse energy at the time data was taken, only laser pulse energy data corresponding to the maximum amount of incident (and thus absorbed) pump pulse energy was recorded.
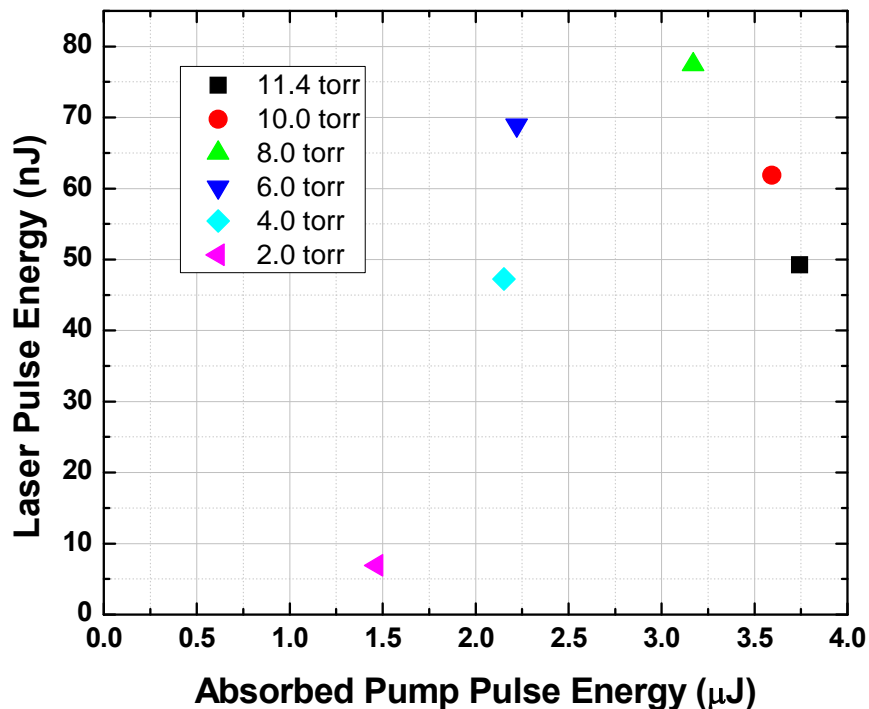
Figure 6.12 Maximum laser pulse energy as a function of absorbed pump pulse energy for various pressures of HCN gas contained within a 45-cm long kagome-structured HC-PCF. Reproduced from Ref [34].

The maximum laser pulse energy observed is ~ 77 nJ and occurs at an HCN pressure of 8.0 torr. This is about a factor 10 higher than the maximum laser pulse energy observed from the HCN-filled higher-loss 23-μm pitch kagome fiber, and only about a factor of 10 lower than the maximum laser pulse energy produced by the acetylene laser in the same fiber. The maximum observed laser efficiency is ~ 3% at a pressure of 6 torr. Since only the maximum laser pulse

103

energies were recorded and the laser pulse energies from the acetylene filled fibers have been seen to saturate at relatively high absorbed pump pulse energies, it should not be assumed that the laser efficiency corresponding to the maximum observed laser pulse energy is the maximum optical-to-optical laser efficiency at any particular pressure. However, computing the laser efficiency using the absorbed pump pulse energy corresponding to the maximum laser pulse energies measured will provide a lower limit to the actual maximum laser efficiency at each pressure. Table 6.4 summarizes the measured maximum laser pulse energies and the corresponding optical-to-optical efficiencies.

Table 6.4 Summary of the maximum laser pulse energies and the corresponding laser efficiencies for 45-cm long, HCN-filled HC-PCF laser.

C_2H_2 Gas Pressure (torr)	Maximum Observed Laser Pulse Energy (nJ)	Optical-to-Optical Laser Efficiency (%)
2.0	6.9	0.5
4.0	47	2.2
6.0	69	3.1
8.0	77	2.4
10.0	62	1.7
11.4	49	1.3

By looking at the changes in performance of the OPA-pumped acetylene and HCN-filled fiber lasers when using fibers with different mid-IR loss characteristics and different lengths and core diameters, several conclusions can be drawn.

First, the efficiency of both the acetylene and the HCN lasers are seen to increase in switching from the higher-loss 23-μm pitch fiber, to the lower-loss 18.75-μm pitch fiber. This is expected as lower fiber loss essentially allows increased interaction lengths between mid-IR photons and the inverted molecules that provide them gain.

While the loss per unit length is reduced by a factor of ~ 30 in switching to the 18.75-pitch fiber, the core diameter is increased by a factor of 2. This reduces the fluence of the light propagating in the fiber by a factor of ~ 4. The reduced fluence is most likely responsible for the

increase in the threshold energies. For example, the threshold energy at 30 torr is seen to increase from ~ 0.35 µJ in the higher-loss fiber to ~ 1.5 – 2.0 µJ in the in the lower-loss fiber.

Changing the length of the low loss fiber is not seen to have much impact on the laser performance. While the energy distribution in the spectrum shifted from favoring the shorter wavelength R-branch transition to favoring the longer wavelength P-branch transition, neither the laser threshold energy nor the maximum optical-to-optical efficiency of the acetylene laser were seen to change appreciably when the length of the lower-loss, 18.75-µm pitch fiber was decreased from 1.46 m to 45 cm.

6.5 Numerical Simulations of OPA-Pumped Laser

Simulations of the expected laser output from the acetylene-filled hollow-core fiber laser were carried out using simple rate equations to describe the coupled molecular populations and pump and laser intensities along the length of the fiber. To begin, we assume a simple four-level system. State $|1\rangle$ represents the $J = 13$, vibrational ground state. State $|2\rangle$ represents the $J = 12$, $v_1 + v_3$ excited state. States $|3\rangle$ and $|4\rangle$ represent the $J = 11$ and $J = 13$, v_1 terminal laser states. The laser states are assumed to only couple to the excited state, forbidding population to transfer directly to the ground state. This condition seems appropriate, as above threshold the laser process happens almost instantaneously with the pump, not allowing much time for the populations to rotationally or vibrationaly relax. The energy level diagram is shown in Fig. 6.13.
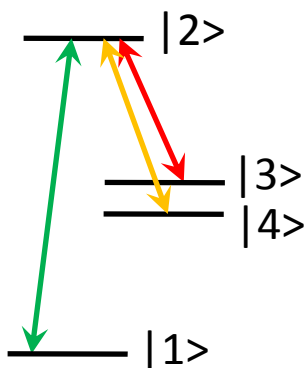
Figure 6.13 Four-level energy level diagram used to model gas-filled hollow-core fiber laser. State $|1\rangle$ is the ground state. State $|2\rangle$ is the pumped excited state. States $|3\rangle$ and $|4\rangle$ represent the two terminal laser states, which do not couple directly to the ground state.

The fiber total fiber length is divided up into small sections of length dz, ~ 1-cm long or less. Similarly, the pump pulse is assumed to have a Gaussian temporal profile and is divided into time segments, $dt = dz/c$, where c is the speed of light. This situation is illustrated in Fig. x, where the pump pulse is shown in green and the generated laser pulse is shown in red. The pump pulse is then propagated through the fiber through successive fiber segments in time intervals equal to dt.
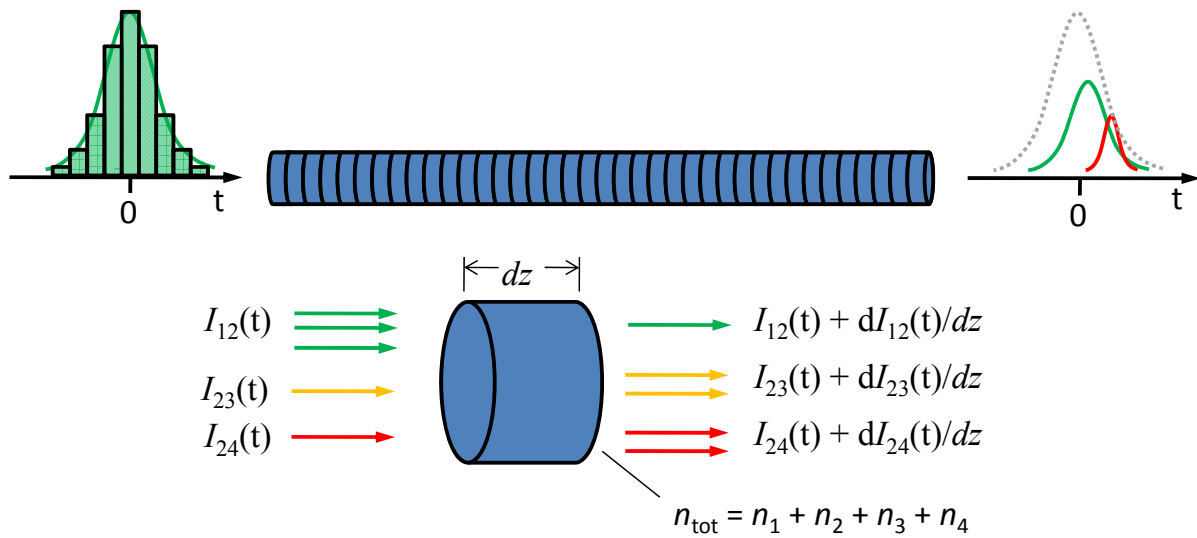
Figure 6.14 Geometry used to model four-level gas-filled hollow-core fiber laser system. The fiber is divided into small segments, each of length dz, equal to ~ 1 cm or less. The Gaussian pump pulse is divided into time incremenets of $dt = dz/c$, where c is the speed of light. The pump pulse is then stepped through the individual fiber segments in time increments steps of dt.

The time rate of change in the number density of molecules in the lower state n_1 (in units of molecules·m^{-3}) is given by [65],

$$\frac{dn_1}{dt} = w_{21}^{spont} + w_{21}^{stim} - w_{12}^{stim} \qquad 6.5$$

where the quantities w_{ij} represent the rates of spontaneous and stimulated transitions from the state i to the state j (in units of molecules·m^{-3}s^{-1}). The transition rates are given by [23],

$$w_{21}^{spont}(t) = A_{21}n_2(t)$$ 6.6

$$w_{21}^{stim}(t) = \frac{\sigma_{21}}{h\nu_{12}}n_2 I_{12}(t)$$ 6.7

$$w_{12}^{stim}(t) = \frac{\sigma_{12}}{h\nu_{12}}n_1 I_{12}(t)$$ 6.8

where A_{21} is the Einstein coefficient representing the spontaneous transition rate, h is Planck's constant, σ_{12} and σ_{21} are the stimulated transition cross sections for the pump light (in units of m^2), and ν_{12} and I_{12} are the frequency and intensity of the stimulating light, respectively. The frequency dependent cross sections for stimulated transitions are related to the Einstein A_{21} coefficients by [66],

$$\sigma_{12}(\nu) = \frac{\lambda^2 A_{21}}{8\pi}\frac{g_2}{g_1}S(\nu)$$ 6.9

$$\sigma_{21}(\nu) = \frac{\lambda^2 A_{21}}{8\pi}S(\nu)$$ 6.10

where g_1 and g_2 are the degeneracy factors of the for population in the states 1 and 2 and $S(\nu)$ is the line shape function for the transition, defined such that,

$$\int_0^\infty S(\nu)\,d\nu = 1$$ 6.11

The spectral overlap of the lineshape of the molecular transition with the bandwidth of pump light can be used to determine how much energy should be absorbed by the molecules when optically pumping. This allows us to predict how the absorbed pump energy should change in the presence of transition broadening effects such as pressure broadening. If the degeneracy

factors are similar (as they are for the case of ro-vibrational levels for all but the lowest J values), the same cross section can be used to describe both absorption and emission, *i.e.* $\sigma_{12}(\nu) \sim \sigma_{21}(\nu)$. Combining Eqs. 2.12 – 2.15 gives the expression,

$$\frac{dn_1}{dt} = A_{21}n_2(t) + \frac{\sigma_{12}}{h\nu_{12}}\big(n_2(t) - n_1(t)\big)I_{12}(t) \tag{6.12}$$

In a similar manner the rate equations for states $|3\rangle$ and $|4\rangle$ can be written as,

$$\frac{dn_3}{dt} = A_{23}n_2(t) + \frac{\sigma_{23}}{h\nu_{23}}\big(n_2(t) - n_3(t)\big)I_{23}(t) \tag{6.13}$$

$$\frac{dn_4}{dt} = A_{24}n_2(t) + \frac{\sigma_{24}}{h\nu_{24}}\big(n_2(t) - n_4(t)\big)I_{24}(t) \tag{6.14}$$

where the cross sections σ_{23} and σ_{24} are taken to be equal to each other. As neither cross sections nor the Einstein A coefficients measured for transitions from the $\nu_1 + \nu_3$ excited state to the ν_1 laser states excited could be found, the Einstein A coefficient from the ν_3 state to the vibrational ground state is used, as this rate should be similar for these similar transitions. As the total molecular number density in the system is constant, the rate equation for state $|2\rangle$ can be calculated from the other rates using,

$$\frac{dn_2}{dt} = -\frac{dn_1}{dt} - \frac{dn_3}{dt} - \frac{dn_4}{dt} \tag{6.15}$$

Similarly, the change in intensities as the light traverses a fiber segment dz depends on the population densities in the upper and lower states according to [23],

$$\frac{dI_{12}}{dz} = A_{21}n_2(t)\Omega h\nu_{21} + \sigma_{12}\big(n_2(t) - n_1(t)\big)I_{12} \tag{6.16}$$

$$\frac{dI_{23}}{dz} = A_{23}n_2(t)\Omega h\nu_{23} + \sigma_{12}\big(n_2(t) - n_3(t)\big)I_{23} \qquad\qquad 6.17$$

$$\frac{dI_{24}}{dz} = A_{24}n_2(t)\Omega h\nu_{24} + \sigma_{12}\big(n_2(t) - n_4(t)\big)I_{24} \qquad\qquad 6.18$$

where Ω is a factor used to account for the fact that only a fraction of the spontaneously emitted light will be in the direction of the incident light, and only this fraction will then contribute to the propagating intensities. For calculations involving the gas-filled hollow-core fiber laser, the factor Ω will be set equal to the fractional solid angle subtended by the guided mode of the fiber, giving $\Omega \sim 0.0001$.

Equations 6.12 – 6.18 above represent coupled equations between the populations of the various energy levels and the pump and laser intensities. Given the initial energy level population densities and the temporal character of the pump intensity are known, these equations can be numerically integrated in time along the fiber to calculate the expected laser intensity at the end of the fiber.

These equations are numerically integrated using the MATLAB code shown in Appendix D, assuming a 1-ns duration pump pulse tuned to resonance with the pump transition at 1533 nm. The fiber length is taken to be 1.46 m, and the fiber loss is equal to 0.1 dB/m at the pump wavelength and 5 dB/m at the laser wavelengths. The guided modes of the pump and laser light in the fiber are assumed to have flat-top profiles with diameters of 50 μm.

Fig. 6.15 shows the calculated laser pulse energy versus the absorbed pump pulse energy for acetylene pressures of 2, 5, and 30 torr. The model predicts most of the same overall trends that are seen in the experimental data shown in Fig. 6.6. For example, the slope efficiency of the laser in both cases is seen to decrease with increasing pressure. Similarly, the threshold absorbed pump pulse energy is generally seen to increase with increasing pressure for both the calculated and measured data. Even the maximum observed laser pulse energies agree to within a factor of two.

However, one striking difference can be seen. The overall shapes of the calculated curves always curve upwards, while the experimental data usually turn over. Furthermore, at the lowest pressures, the experimental data shows what looks like saturation, with the laser pulse energy remaining relatively unchanged as the gas continues to absorb energy. The calculated

109

data never show anything of the sort. This saturation effect may indicate that additional, more complex physics exists in the real system than what this simple model is accounting for, such as the excited state pump absorption mentioned earlier. Collaborators at the University of New Mexico have looked at the effect of excited state pump absorption in this acetylene system and have seen that it can produce the saturation-like behavior observed experimentally.
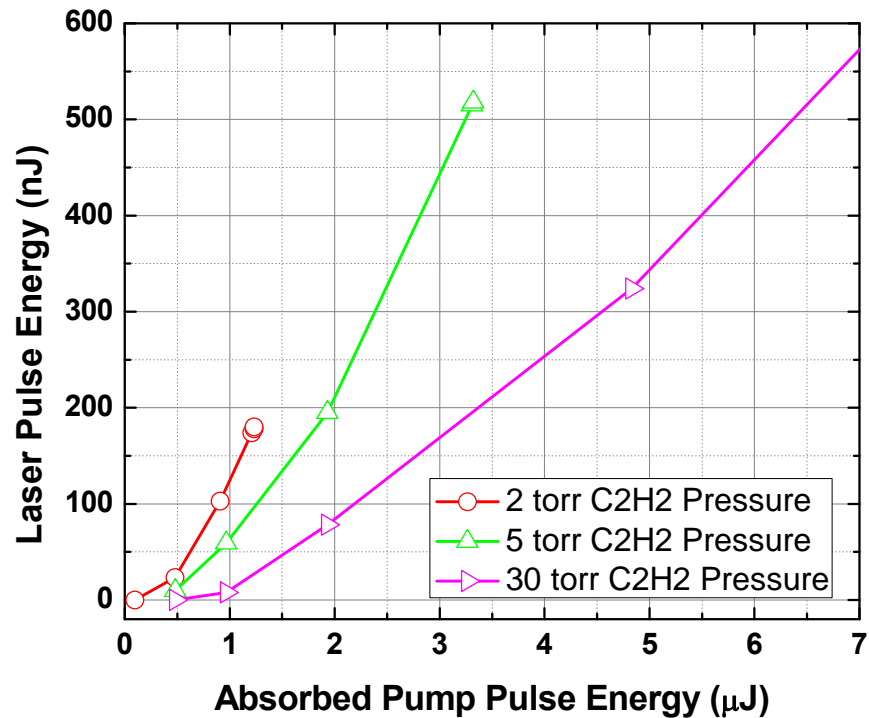
Figure 6.15 Calculated laser pulse energy as a function of absorbed pump pulse energy for a 1.46-m long fiber filled with various pressures of acetylene gas. The linear fiber loss is equal to 0.1 dB/m at the pump wavelength and 5 dB/m at the mid-IR laser wavelengths.

Chapter 7 - Continuous Wave Small Quantum Defect Lasers

7.1 Introduction

While Chapters 5 and 6 have focused on generating mid-IR light from population inversions in molecular gas-filled hollow-core fibers, the same laser architecture has the potential to create lasers that operate with a small quantum defect, whose pump and laser wavelengths differ by only ~ 1%. Such a laser system has the potential to be up to ~ 99% efficient, where the only power lost is a result of the small photon energy difference between the pump and laser light (the quantum defect). Lasers like this offer a means to generate coherence, where multiple, mutually incoherent pump sources are used to pump the laser and produce a single, strong coherent output. A devise like this would be extraordinary for applications requiring high powers and good beam quality, long sought-after characteristics that are currently being pursued using techniques like coherent beam combining [67].

The idea of coherence generation is illustrated by the energy level diagram shown in Fig. 7.1. The pump sources, indicated by the upward-pointing blue arrows, are used to excite populations between slightly different rotational states within the same vibrational states. If the excited vibrational state lifetime is long compared to the rotational mixing time, the rotational state populations thermalize through intermolecular collisions, creating rotational state populations that follow the Boltzmann distribution given by Eq. 2.10, with similar total numbers of molecules in both the ground and excited vibrational states. If enough molecules are pumped to the excited state, population inversions on one or more ro-vibrational transitions can be achieved [68]. These inversions permit lasing, indicated by the downward-pointing green arrows, at wavelengths longer than those corresponding to the pumps. If single frequency output is desired, it may be necessary to tune the spectrum of the laser gain using wavelength-dependent feedback, perhaps by employing dichroic optics or a dispersive element like a grating or prism.
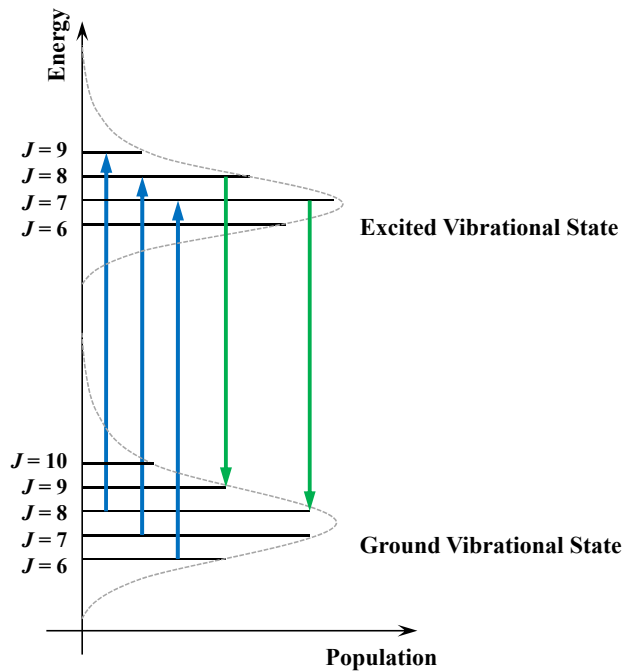
Figure 7.1 Energy level diagram illustrating the process of coherence generation with a small quantum defect laser. Pump transitions are indicated by the blue arrows pointing upwards while the laser transitions are indicated by the green arrows pointing downward and only occur between dipole-allowed transitions where population inversions exist. The rotational state population in each vibrational state follows a Boltzmann distribution (indicated by the gray dashed lines) owing to fast thermalization from collisions between molecules in the various rotational levels.

Calculations performed by collaborators at the University of New Mexico have shown that a CW, small quantum defect laser should be possible using small core diameter (~ 10 μm), low loss (~ 0.02 dB/m) gas-filled HC-PCFs. Furthermore, the fiber will likely need to be placed within a resonator having moderate finesse (round trip loss ~ 10% or less) at the laser wavelength to reduce the pump powers required to reach the laser threshold to on the order of several watts. Generating several watts of tunable narrow linewidth power in the 1.5-μm wavelength region is nontrivial, but can be done with specially designed high-power double clad fiber amplifiers.

7.2 High Power 1.5-µm Wavelength Continuous Wave Pump Source

Nearly single mode, multi-watt level powers in the 1.5-µm wavelength region can be achieved using erbium/ytterbium co-doped, double clad fiber amplifiers. A schematic illustrating the architecture of the high-power double clad amplifying fiber is shown in Fig. 7.2. A high index single mode core is surrounded by a lower index cladding region, which in turn is surrounded by a lower index polymer buffer that acts as a second, outer cladding. While this looks similar to a typical step index fiber with one cladding layer surrounded by a buffer, double clad fibers are called such because multimode pump light is purposely injected into both the inner core and cladding regions and is confined to propagate in modes contained within the inner cladding. Furthermore, unlike typical step index fibers the inner cladding cross section is typically not round, often having a polygonal cross section which keeps the pump light from propagating in modes that have poor overlap with the doped core region.
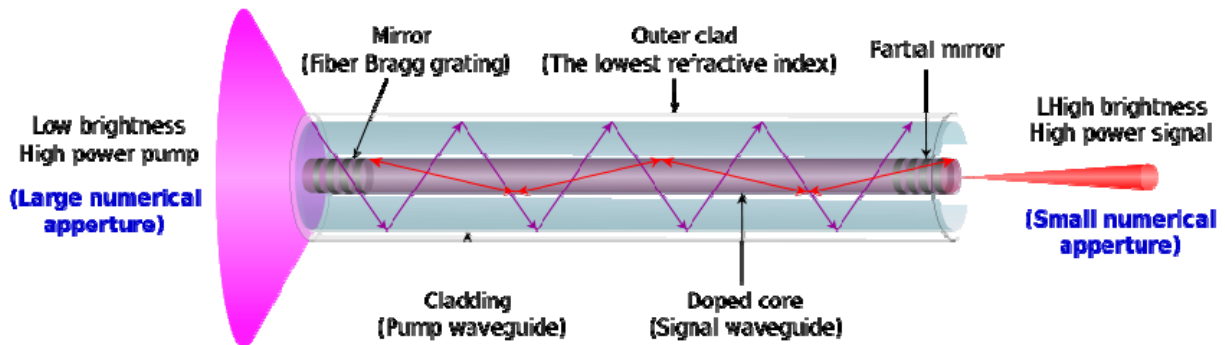
Figure 7.2 Diagram illustrating the use of a doped double clad fiber in a cladding pumped high-power laser architecture. A high-power, low brightness pump is coupled into the un-doped inner cladding of the fiber. This pump light overlaps the doped single mode core region, allowing amplification of light propagating in the guided mode. Bragg reflectors are not present in the fibers used for amplification only. Image reproduced from Ref [69].

The low-power signal light that is to be amplified is coupled into the doped single mode core at one end of the fiber. Pump light is coupled into the inner cladding through one or both ends of the fiber to excite electronic transitions in the dopant ions within the fiber's single mode core and provide gain at the signal wavelengths. Typically, high-power low-brightness multimode pump diodes are used, where brightness (or more precisely, radiance) is defined as

the power emitted per unit area per unit solid angle (units of $W \cdot m^{-2} \cdot sr^{-1}$). Low-brightness diodes are preferred as the diodes' cost scales with brightness. However, high-power low-brightness diodes tend to emit into large solid angles. It is precisely this situation that double clad gain fibers where developed for. The cladding of typical Er/Yb co-doped double clad fibers has a high numerical aperture (> 0.45) which allows the pump light to be coupled into the fiber with high efficiency. Only a small portion of the pump mode spatially overlaps the doped single mode core of the fiber, allowing efficient pumping of the core region without causing the extremely high intensities associated with damaging thermal and nonlinear effects [35] that would occur if the fiber were core pumped.

The amplified signal light is confined to propagate through the fiber in the single mode core region, which can be doped with a variety of transition metals, such as erbium (Er), ytterbium (Yb), or Thulium (Tm). Of course the spectral regions corresponding to the pump and amplified signal wavelengths are completely dependent on the particular dopant used in the fiber. The fiber used in the amplifier for the small quantum defect laser trials is doped with a combination of Er and Yb. A simplified energy level diagram illustrating the pump and amplification scheme for the Er/Yb co-doped double clad fiber is shown in Fig. 7.3. Both Er^{3+} and Yb^{3+} have absorption peaks near 980 nm. However, the absorption cross section for Yb^{3+} is much larger at 980 nm and covers a broad range from $\sim 800 - 1100$ nm [70]. Therefore, the fiber is primarily pumped via the $^2F_{7/2} \rightarrow {}^2F_{5/2}$ transition in the trivalent Yb ion. Excited Yb ions located near Er ions in the glass fiber can then relax back to the electronic ground state while resonantly exciting electrons in Er^{3+} via the $^4I_{15/2} \rightarrow {}^4I_{11/2}$ transition [70], allowing the Er ions to be efficiently pumped and effectively increasing their absorption cross sections. Population in the $^4I_{11/2}$ electronic state then quickly relaxes to the $^4I_{13/2}$, where it can then make stimulated transitions back to the $^4I_{15/2}$ ground state while amplifying signal light in the 1.5-µm wavelength region.
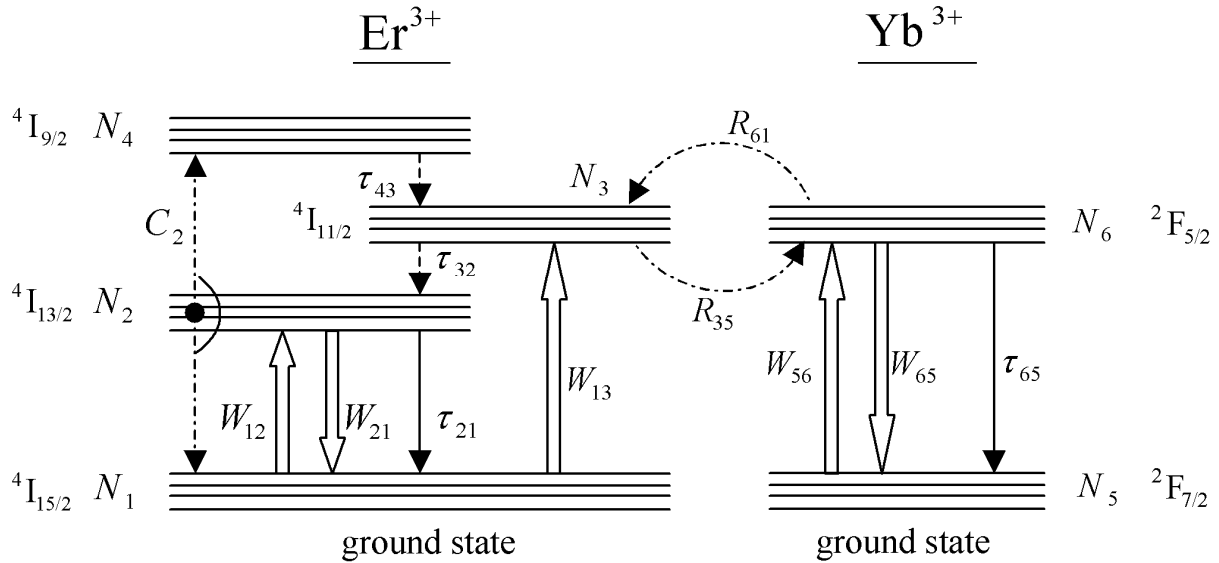
Figure 7.3 Electronic energy level diagram for the coupled Er³⁺ and Yb³⁺ ions used in the co-doped double clad fiber. The amplifier system is pumped via the ²F₇/₂ → ²F₅/₂ transition in Yb³⁺ at wavelengths of 800 – 1100 nm. Population relaxation between these same two states causes a resonant excitation from the ⁴I₁₅/₂ state to the ⁴I₁₁/₂ state in nearby Er³⁺ ions. Population then quickly relaxes from the ⁴I₁₁/₂ state to the ⁴I₁₃/₂ state, where stimulated transitions back to the ⁴I₁₅/₂ ground state amplify the signal wavelength in the 1.5-μm region. This image is reproduced from Ref [70].

A block diagram of the Er/Yb co-doped double clad fiber amplifier constructed by Precision Photonics Corporation and used in the initial small quantum defect laser trials is shown in Fig. 7.4. The amplifier consists of two stages, a low-power preamplifier stage and a high-power power amplifier stage. The preamplifier stage uses standard single clad Er-doped fiber to boost the signal power from the seed laser from the milliwatt level up to hundreds of miliwatts. This is done so that the power amplifier stage is properly seeded. The input power to the high-power stage must be sufficiently high during high-power operation so that the signal light is preferentially amplified instead of the amplified spontaneous emission (ASE) produced in the high-power stage itself. If the ASE power is allowed to overwhelm the seed power, the high-power stage may self-lase. Self-lasing can produce large spikes in power which can lead to

damaging nonlinear effects including fiber-fuse effects in which the core region along the entire length of fiber can become pitted and ruined.
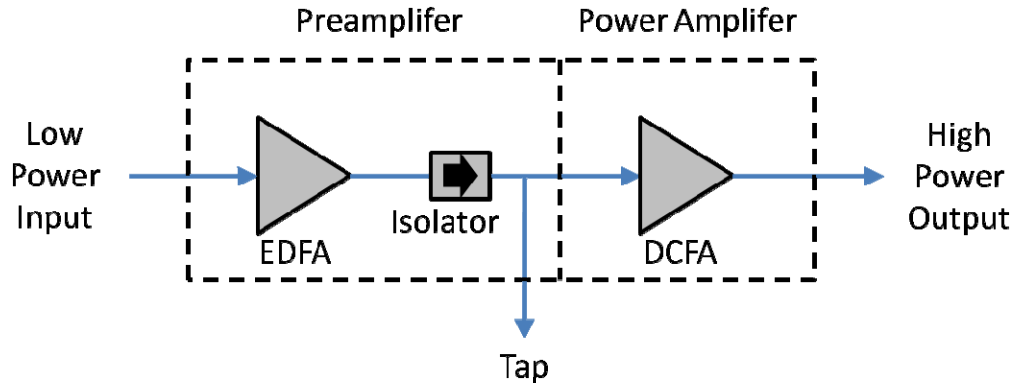
Figure 7.4 Block diagram of the Er/Yb co-doped double clad fiber amplifier built by Precision Photonics Corporation for use pumping a small quantum defect laser in the 1.5-µm wavelength region. The amplifier has a low-power preamplifier stage and a high-power power amplifier stage capable of producing a maximum output power of 2 W.

After passing through an optical isolator and a fiber coupler with a few-percent tap for preamplifier diagnostics, the preamplifier output enters the power amplifier stage. This stage consists of a section of near single-mode Er/Yb co-doped double clad fiber. The fiber is pumped using ~ 900-nm wavelength multimode pump diodes capable of delivering a total power of many tens of watts. Due to the high powers involved, many of the components have to have some heat sinking for thermal management.

7.3 Gas-Filled Fiber Laser Resonator Designs for Small Quantum Defect Lasing

7.3.1 Introduction

In addition to a high-power CW pump source, a successful demonstration of small quantum defect lasing from a gas-filled HC-PCF will likely require the fiber be placed inside a resonator at the laser wavelengths, as more feedback will be needed than can be provided by the guided

mode of the fiber alone. Several different resonator designs have been investigated, including designs based on polarization optics and dichroic optics.

Polarization optics can be used to allow pump light having a well defined polarization to be coupled through cavity optics that are then highly reflective for the orthogonal polarization. This scheme is particularly convenient as the pump and laser light will only differ by ~ 10 nm near 1530 nm. While dichroic optics could be used to reflect the laser wavelengths while transmitting the pump wavelengths, optics that transition from near fully transmissive to near fully reflective over just a 1% change in wavelength are not typical and are difficult and expensive to custom manufacture. On the other hand, using polarization to separate pump and lasing wavelengths which differ by 1% is no problem.

Several different cavities utilizing polarization optics were examined, while only one cavity was developed which utilizes dichroic optics. In all cases the gas is contained in a commercial photonic band gap fiber (PBGF) from Crystal Fibre. The fiber has a hollow-core diameter of 10 μm, a mode field diameter of 9 μm (1/e^2) at 1550 nm, and a numerical aperture of ~ 0.20 [71]. Figure 7.5 shows the fiber's cross section together with the fiber's attenuation (shown in black) and D-parameter (shown in red) in the 1.5-μm wavelength region. This fiber was chosen for its small core diameter and very low attenuation (< 20 dB/km near 1550 nm), to help maximize the pump and laser intensities in the gas, reducing the power required to reach the lasing threshold.
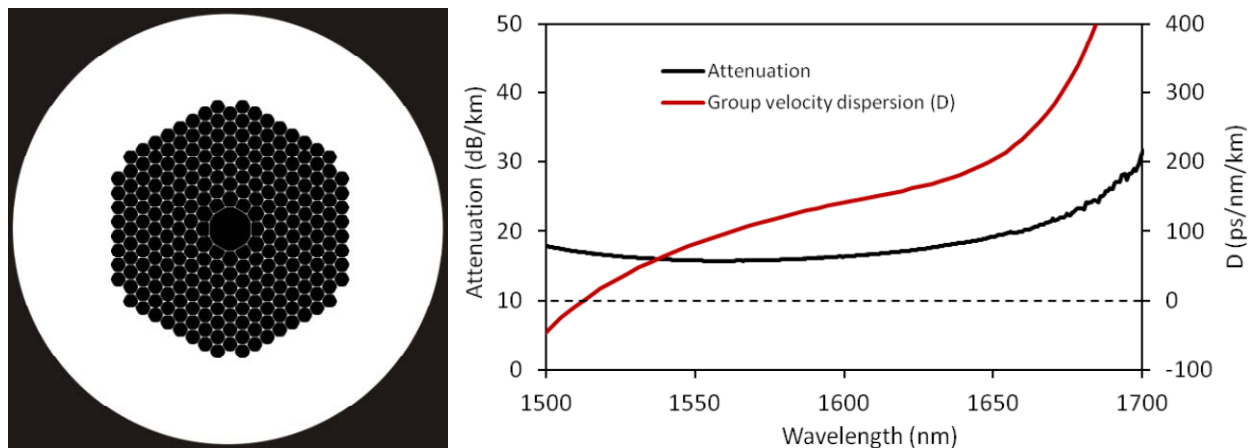
Figure 7.5 An SEM image of the cross section (left image) and a plot (right image) of the attenuation (black curve) and D-parameter (red curve) for the 10-μm core diameter PBGF from Crystal Fibre. Figures reproduced from Ref [71].

7.3.2 Gas-Filled Fiber Laser Resonators Based on Polarization Optics

The first cavity design investigated is shown in Fig. 7.6 and is by far the simplest to construct and to align. One end of PBGF is spliced to an SMF patch cord, allowing pump and laser light to easily be coupled in and out of the fiber. The patch cord is then connected to the combined output port of fiber-based polarizing beam combiner.   One of the polarized inputs to the combiner is connected to a gold-coated fiber mirror, while the orthogonally polarized input is connected to the output from a commercial, 300 mW (maximum output) erbium doped fiber amplifier (EDFA), which is used as the pump source since the Er/Yb co-doped double clad fiber amplifier was not available at the time. The other end of the PBGF is held in a vacuum chamber
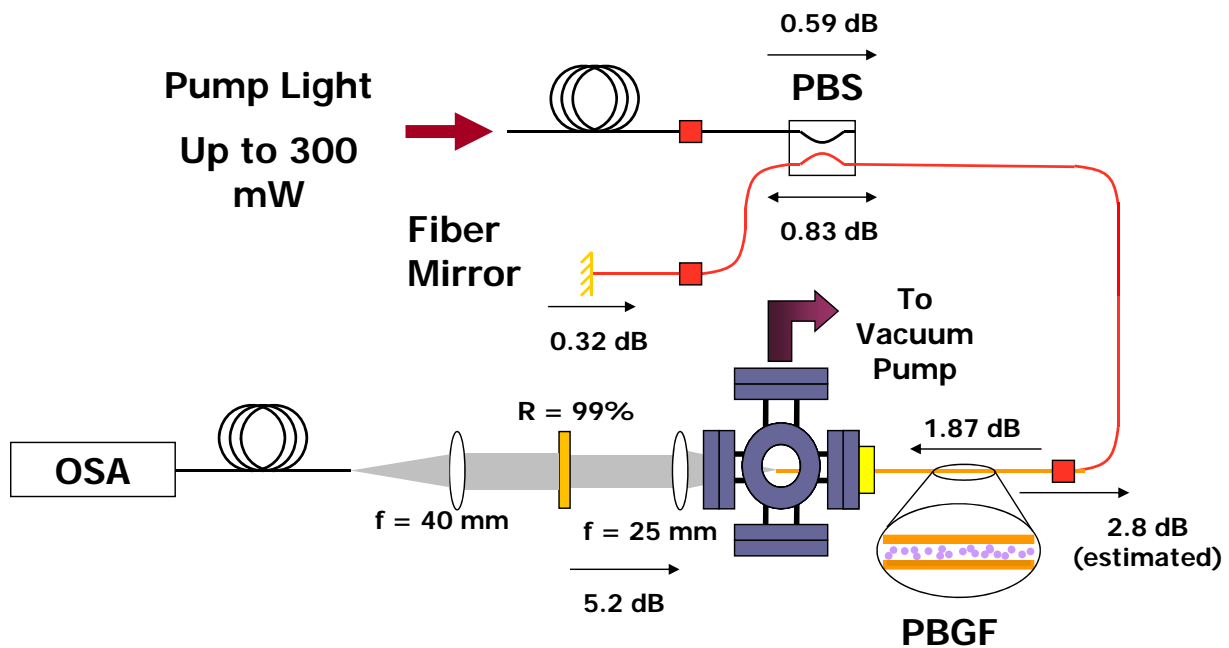
Figure 7.6 Initial setup for C$_2$H$_2$-filled PBGF small quantum defect laser using a polarized cavity. Acetylene gas is contained in the 10-µm diameter hollow core of a ~ 1.5-m long PBGF.   The laser cavity is formed by the gold-coated fiber mirror connected to the polarizing beam combiner and the 99% reflective, plano dielectric mirror which functions as the laser output coupler. Pump light is polarized orthogonal to the polarization that the cavity supports and is coupled into the cavity through the polarizing beam combiner. The losses through various components are labeled in the figure.

similar to those used in the pulsed mid-IR laser experiments, which permits gas to diffuse in and fill the fiber's hollow core region. The fiber's end is held near an AR-coated BK7 window to allow the pump and any laser light to be coupled in and out of the PBGF. Light is collimated from the PBGF using an AR-coated achromatic doublet lens. The collimated beam is incident on a dielectric mirror, which retroreflects 99% of the incident light back toward the collimating lens and the PBGF, and transmits the remaining 1%. The transmitted light is then coupled into SMF and sent to an optical spectrum analyzer (OSA) to look for spectral components not belonging to the pump, indicating lasing.

The EDFA used to pump the laser is seeded using a ~ 20 mW, narrow linewidth fiber laser tuned to resonance with the P(13) transition between the vibrational ground state and the $v_1 + v_3$ vibrational state, at a wavelength of 1533 nm. Estimates from collaborators at the University of New Mexico showed that pumping on an R-branch transition and lasing on a P-branch transition would likely have lower pump power thresholds than pumping and lasing on P-branch transitions alone. However, the gain from EDFAs in general is seen to decrease rapidly at wavelengths below about 1532 nm. Therefore, to avoid running the EDFA with a signal wavelength that could not be amplified (a situation where self-lasing can occur), it was deemed best to pump at a wavelength longer than 1532 nm somewhere within the P-branch.

The PBGF was filled with a variety of C_2H_2 gas pressures ranging from a few tens of millitorr to a few torr. However, no additional spectral components where ever seen using this setup, indicating that we were not able to reach the lasing threshold in the gas-filled fiber. This likely results from some combination of too little pump power being present in the gas and there being too little feedback at the laser wavelength. This second point seems quite likely from the loss values through the various optical components labeled on the diagram in Fig. 7.6. From these values the total round trip loss is more than 10 dB, or greater than 90%. The largest losses in the system are from the PBGF-to-SMF splice and from the free space-to-fiber recoupling. The splice loss results from a mismatch in the mode field diameters between the two fibers, and it is nonreciprocal because of the multimode nature of the PBGF [72]. The high loss incurred during recoupling of the retroreflected light was quite perplexing and inspired a reexamination of how light might be more efficiently coupled in and out of the PBGF.

119

Up to this point, light had been coupled in and out of all of the HC-PCFs using either spherical or achromatic doublet lenses. While these types of lenses are used quite successfully in other PBGF setups within our lab, they were not seen to function with the high coupling efficiencies required for intracavity use when used in the retroreflection configuration required for a laser cavity. A quantitative study was done of the recoupling efficiency for the retroreflection configuration using a combination of SMF and PBGF fibers and a spherical lens in conjunction with a plano dielectric retroreflector as well as a concave dielectric retroreflector alone. Both mirrors are 99% reflective at wavelengths near 1550 nm.

The setup used to measure the recoupling loss is shown for the lens-plano mirror system in Fig. 7.7a and for the concave mirror system in Fig. 7.7b. Light at 1533 nm is injected into port 1 of a fiber circulator, where it is transmitted to port 2. The fiber from port 2 is connected to either a single SMF patch cord or to a SMF patch cord which is spliced to a ~ 1-m long section of PBGF. Light propagates out of port 2, through the fiber and is emitted into free space at the end of the SMF patch cord or the PBGF. From the end of the fibers, the light is either collimated with a 25-mm focal length spherical lens and retroreflected with a plano/plano mirror (Fig. 7.7a) or simply retroreflected without collimation from a 25-mm radius of curvature plano/concave mirror (Fig. 7.7b). Following retroreflection, the light is recoupled into the fiber and transmitted back into port 2 of the fiber circulator where it is transmitted to port 3 which is connected to a large area germanium photodetector for measurement.
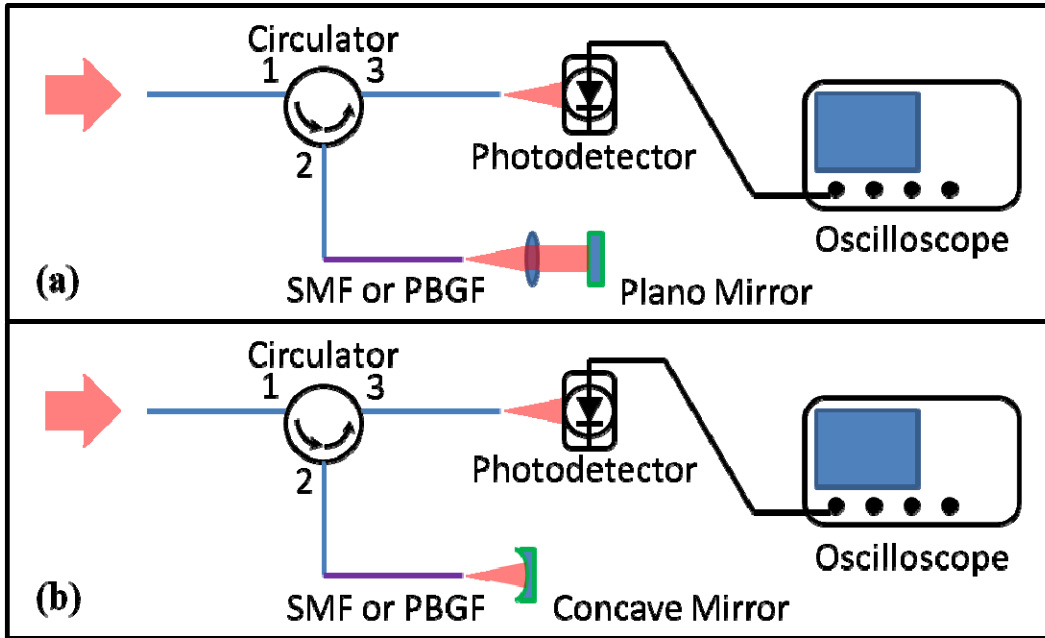
Figure 7.7 Setup for fiber-to-free space recoupling loss measurements using SMF and PBGF fibers in conjunction with (a) a 25-mm focal length spherical lens and plano mirror or (b) a 25-mm radius of curvature concave mirror alone. Light at 1533 nm is injected into SMF or PBGF via ports 1 and 2 of the circulator shown. Retroreflected light is recoupled and sent back to port 2 of the circulator where it is transmitted to port 3 and detected using a large area Ge photodetector.

Table 7.1 summarizes the results of the observed recoupling losses after optimizing the free space optics in all cases. The highest recoupling losses when using either the lens and plano mirror or the concave mirror alone were achieved using PBGF. This is not terribly surprising as the PBGF is known to guide multiple modes that may exhibit different divergence angles. What is somewhat surprising is that when the plano/concave mirror alone was used, the recoupling loss was very low for both fibers, at somewhere in the range of 0 – 4%. The vast improvement over the lens-mirror configuration likely has to do with the fact that lens produces aberrations that prevent the beam from being perfectly collimated, thus reducing the recoupling efficiency after retroreflection. This effect seems to be made even worse if one is trying to couple multiple transverse modes as is likely the case with the PBGF. Armed with the knowledge gained from these measurements, new cavity designs were sought to reduce the free space-to-fiber recoupling losses by using curved mirrors whenever possible.

Table 7.1 Summary of results from fiber-to-free space recoupling loss measurements using SMF and PBGF fibers in conjunction with a 25-mm focal length spherical lens and plano/plano mirror or a 25-mm radius of curvature plano/concave mirror alone.

Fiber Type	Minimum Recoupling Loss from Lens-Plano/Plano Mirror	Minimum Recoupling loss from Plano/Concave Mirror
SMF	$\sim 15\%$	$0 - 4\%$
PBGF	$\sim 70\%$	$0 - 4\%$

The second cavity design for a gas-filled PBGF small quantum defect laser based on polarization is shown in Fig. 7.8. In contrast to the initial setup shown in Fig. 7.6, no high loss splice between SMF and PBGF exists here. The cavity is formed by two dielectric mirrors that are 99% reflective at wavelengths near 1550 nm. The mirror on the right is plano/concave with a 25-mm radius of curvature and is used to retroreflect both the pump and any generated laser light in the 1550-nm wavelength region with efficiencies up to > 96% (from Table 7.1). The mirror on the left is plano/plano and is used as the output coupler, where light transmitted through this mirror can be sent to an OSA for spectral measurements as was done in the initial setup. Pump light is coupled into the cavity using the polarizing beam splitter. This beam splitter is optimized to transmit s-polarized light and reflect p-polarized light. The pump and any generated laser light are coupled in and out of the left side of the fiber using an AR-coated achromatic doublet lens.

Just as in the initial trial, the laser is pumped using 1533-nm wavelength light from a narrow linewidth fiber laser, tuned to resonance with the P(13) transition between the vibrational ground state and the $v_1 + v_3$ vibrational state. This light is amplified to ~ 2 W using the Er/Yb co-doped double clad fiber amplifier discussed in section 7.2.
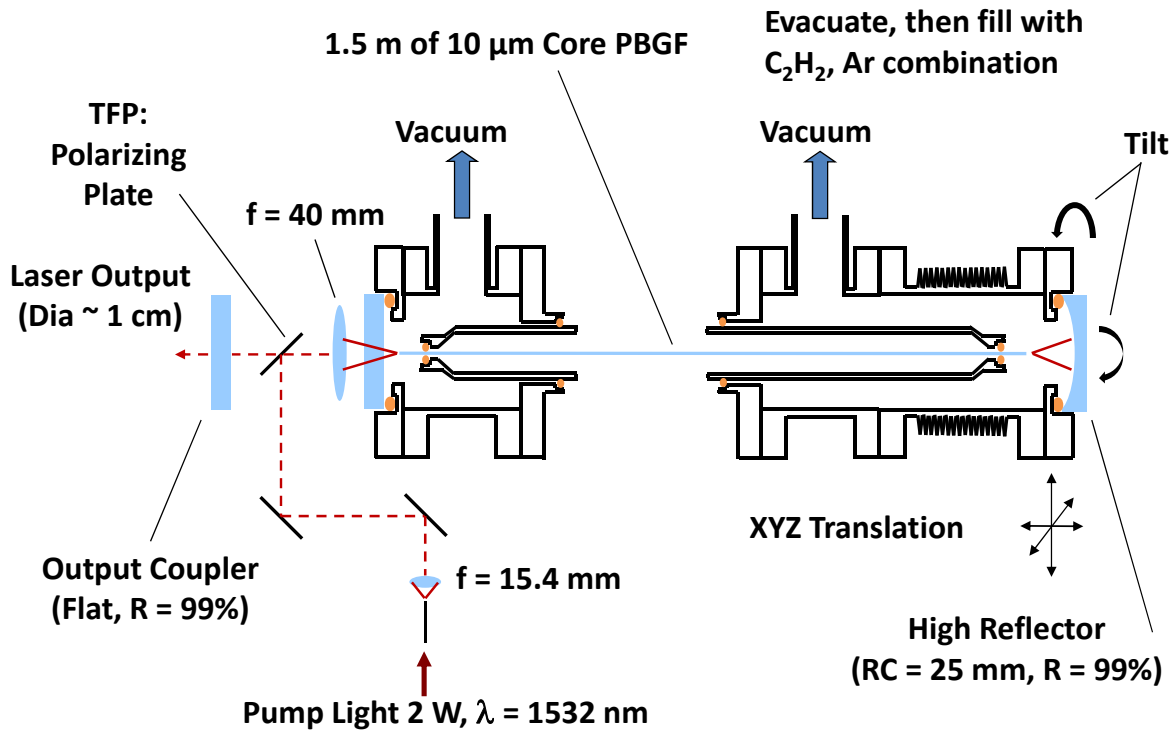
Figure 7.8 Setup for C₂H₂-filled PBGF small quantum defect laser based on a polarized cavity employing a free space plate polarizing beam splitter and a curved mirror. The vacuum chambers and fiber holders are shown in cross section. The orange circles indicate the cross sections of the O-rings used to form a gas-tight seal against various components. The rib structure on the right vacuum chamber indicates a bellows which allows the curved mirror to be tilted and translated during alignment to the hollow fiber's end.

Lasing with this system was only briefly attempted, and did not show any indications of success. Even with the near perfect coupling achieved from the curved mirror, the round trip cavity loss for this laser configuration is ~ 85%. Again, the largest loss in the cavity comes from the lens-to-fiber coupling, and this loss seems to only be exacerbated by the polarizing plate placed between the lens and the output coupler. One potential solution is to use curved mirrors at both ends of the fiber, and place the polarizing plate between one of the curved mirrors and the fiber's end. This configuration would be challenging to construct and align as the polarizing plate would be completely contained inside one of the vacuum chambers, requiring the chamber to be fit with mechanical feedthroughs for alignment control and an additional window in order to couple the pump light into the PBGF from the beam splitter. Furthermore, the polarizing

beam splitter requires a collimated beam to function properly, so the splitter must be positioned after any collimating optics. An off-axis parabolic mirror may have offered a reasonable alternative to a collimating lens, but was overlooked at the time. Seemingly at the limit of what can be accomplished using resonators based on polarization multiplexing, a move was made toward cavities based on dichroic optics.

7.3.3 Gas-Filled Fiber Laser Resonators Based on Dichroic Optics

Instead of using polarization to distinguish different wavelengths of light, we can employ dichroic optics, which reflect and transmit differently at different wavelengths, to make the wavelength distinction directly. Dichroic optics typically rely on multilayer, multi-thickness thin-film dielectric coatings of materials with alternating high and low indices of refraction. These optics are usually designed using sophisticated computer software which can analyze the wavelength-dependent interference created by alternating dielectric layers with complex thickness variations and wavelength-dependent indices of refraction and material absorption. One very nice feature of dichroic optics is that they can be made to work reliably on curved surfaces (although extremely short radii of curvature still pose a significant challenge). A low loss cavity can therefore be constructed using a curved dichroic mirror at one end of the PBGF together with a standard curved dielectric mirror at the opposite end of the fiber.

The sharp dichroic mirrors required for pumping and lasing between the ground vibrational state and the $v_1 + v_3$ vibrational state in C_2H_2 or the ground vibrational state and the $2v_3$ vibrational state in HCN require transitioning from 99% transmissive to 99% reflective over just a 10-nm change in wavelength at ~ 1535 nm. A variety of mirrors have been constructed by Precision Photonics Corporation which meet this specification, with center wavelengths ranging from about 1532 – 1540 nm. These mirrors were only completed in the past few months, and as such have not yet been tried in any laser setup.

Prior to the very recent production success of these plano/plano sharp dichroics, no appropriate dichroic optics existed for use in the gas-filled PBGF small quantum defect lasers we are interested in investigating in the 1.5-μm wavelength region. However, there is some evidence that acetylene might be pumped from the ground to the $v_1 + v_3$ vibrational state and made to lase between the $v_1 + v_3$ and the v_4 vibrational states. As indicated in Fig. 2.2, the v_4

vibrational state corresponds to the symmetric C–H bending mode. The relative energy of this bending mode compared to the symmetric and anti-symmetric C–H stretching modes is seen from Table 2.1 to be only 608 cm^{-1} compared to 3397 cm^{-1} and 3317 cm^{-1}, respectively. This puts the emission wavelengths corresponding to transitions between the $v_1 + v_3$ and the v_4 vibrational states near 1650 nm, which is still a relatively small quantum defect allowing CW efficiencies of > 90%. Curved dichroic mirrors that exhibit high transmission at wavelengths near 1533 nm and high reflection at wavelengths from 1600 – 1700 nm are relatively easy to produce, so these mirrors were fabricated for use in an acetylene-filled PBGF laser setup employing curved cavity mirrors at both ends of the fiber. The spectral transmission of the mirrors was measured using a supercontinuum source and an OSA. The transmission measured through one of the plano dichroic mirrors is shown in Fig. 7.9.
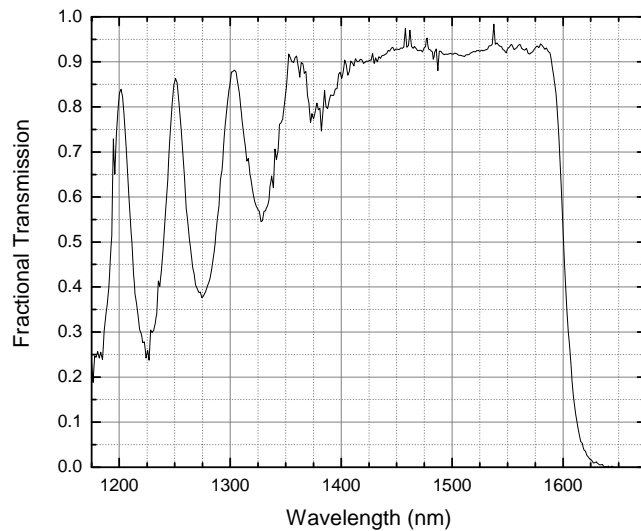
Figure 7.9 Measured transmission spectrum of 1650-nm plano dichroic mirror for use in C$_2$H$_2$-filled PBGF small quantum defect laser cavity. The transmission was measured using a supercontinuum source and OSA, by comparing the spectrum of the source recorded with and without the dichroic mirror present.

One potential problem with this lasing scheme is that the vibrational relaxation rate from the v_4 state back to the ground state is thought to be relatively slow, causing a potential bottle neck for the lasing populations. One way to circumvent this bottle neck is to use a pulsed pump,

allowing sufficient time for the population in the v_4 vibrational state empty between successive excitations of population to the excited state.

The OPA was not yet constructed at the time this laser system was being investigated, but it would be interesting to insert the 10-μm core diameter PBGF into the single-pass laser setup used in the mid-IR laser investigations presented in Chapters 5 and 6, as the PBGF likely has much higher loss at the mid-IR wavelengths where lasing was seen previously. This high mid-IR loss would likely prevent the mid-IR lasing seen before and may preferentially allow lasing at wavelengths near 1650-nm where the fiber loss is likely many orders of magnitude lower.

A straightforward solution to generating 1533-nm wavelength pump pulses of adjustable duration is to pulse the 1533-nm wavelength signal input to the Er/Yb co-doped double clad amplifier. The setup for this is shown in Fig. 7.11. The 1533-nm wavelength signal light is effectively switched on and off using a fiber-coupled acousto-optic modulator (AOM). This modulator essentially consists of a tellurium dioxide (TeO_2) crystal and a piezoelectric transducer. The transducer applies an oscillatory force (at a frequency of 200 MHz) to one side of the crystal in a direction transverse to the propagation direction of light through the crystal. This in turn creates a pressure wave inside of the crystal which causes a periodic modulation in the index of refraction. The modulated index of refraction of the crystal acts like a diffraction grating, effectively redirecting the light from its incident path at a specific angle from the crystal. Only the redirected light is coupled into the output fiber, and thus the AOM acts like a switch, only transmitting light when the transducer is vibrating. The speed at which the light can be switched on or off is determined by the size of the optical beam and the propagation speed of the acoustical wave in the crystal. The particular AOM used has a rise time of ~ 10 ns. Switching is performed by providing a TTL voltage pulse to the AOM. The time duration of the voltage pulse is equal to the time duration of the optical pulse produced by the AOM.

The high-power optical amplifier always produces the same average output power, but by switching the signal laser on and off we can effectively control whether the majority of the output power is generated at the signal wavelength or at other wavelengths. To avoid running the amplifier without any input (a scenario that can produce self lasing and catastrophic damage in the amplifier as discussed in section 7.2) the amplifier is always seeded with some amount of protection light, which is spectrally well separated from the 1533-nm wavelength pump light. The protection light used had a wavelength of 1545 nm. The optical power level of the

126

protection light was set so that its spectral power density measured on the OSA was ~ 10 dBm/nm higher than the highest spectral power density observed in the amplifier's ASE spectrum.
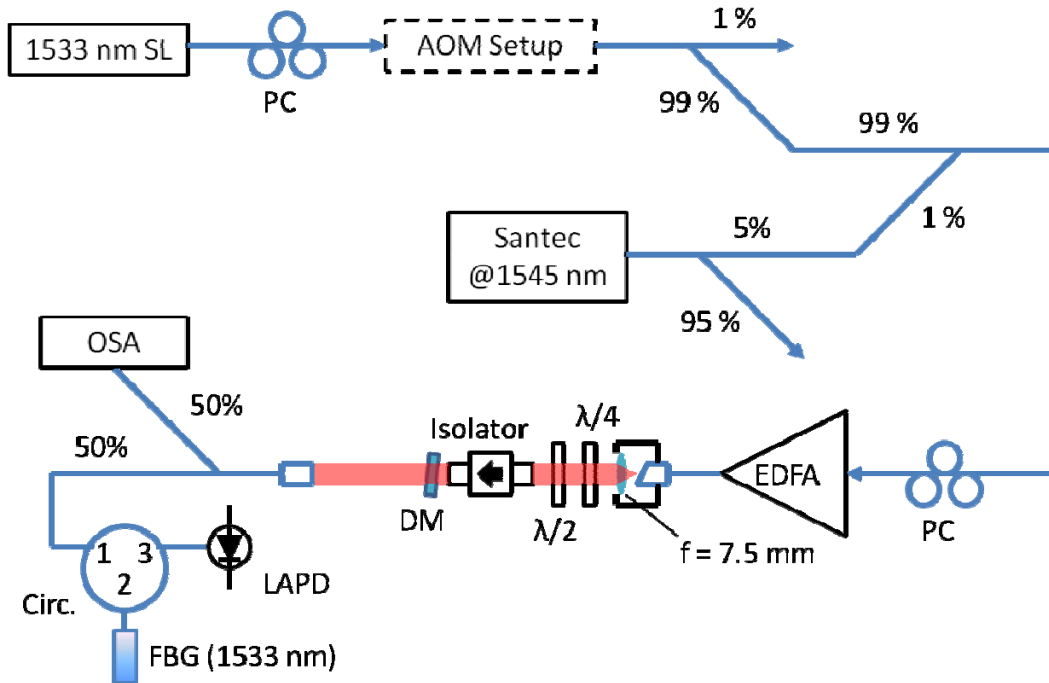
Figure 7.10 Optical setup used to pulse the Er/Yb co-doped double clad fiber amplifier's 1533-nm wavelength output. The CW pump light at 1533 nm is sent through a fiber coupled AOM used to form the pulse. The pump light is combined together with low power 1545-nm wavelength protection light and sent to the amplifier's input. High power 1533-nm pulses are generated at the amplifier's output as shown in Fig. 7.12.

A majority of the pump light (99%) is combined together with 1% of the protection light using a 99/1 fiber coupler. The combined output is connected to the input of the Er/Yb co-doped double clad fiber amplifier. When the amplifier is run in this way without pulsing the input pump light, ~ 90% of the amplifier's output power lies at the 1533-nm pump wavelength. The remaining 10% of the output power is spread between the protection light at 1545 nm and the ASE. Interestingly, if the pump light input is pulsed, the peak power of the amplified pump light output is seen to increase above the CW level by almost a factor of 10 as shown in Fig. 7.12. While this gain spiking phenomenon is undesirable for applications like signal amplification for

optical communications, it is a welcome side effect here as it provides a slight increase in the pump power that can be delivered to the gas-filled fiber laser system.
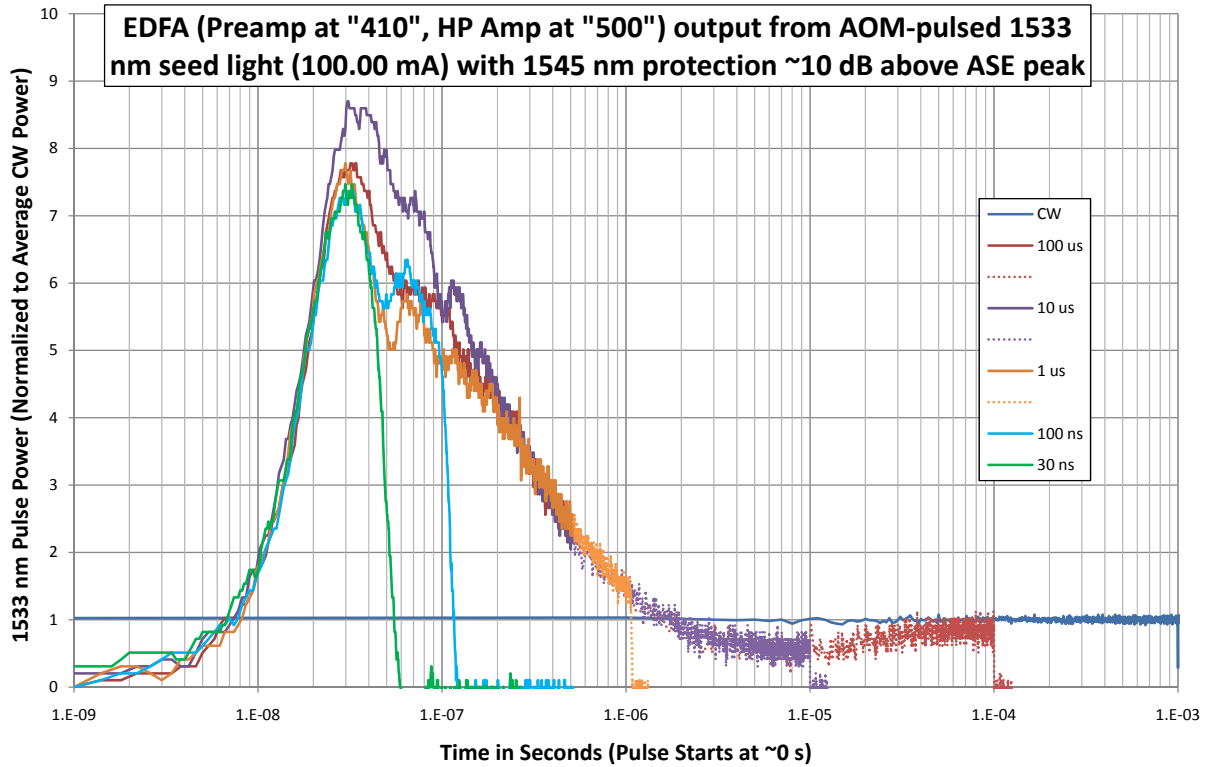
Figure 7.11 Temporal profiles of the high-power pump light after the amplifier's output for various pulse durations input to the amplifier. The power is normalized to that measured from the amplifier using CW pump light at the input (the maximum CW power from the amplifier is ~ 1.8 W at 1533 nm). The pulse repetition rate is 1 kHz and the pump pulse durations range from 30 ns to 100 μs. The peak power is seen to spike to almost 10 times the CW power. The exponential tail from this spiking leads to FWHM pulse widths of ~ 200 ns.

The dual-curved mirror cavity configuration to be used with this pulsed pump source is shown in Fig. 7.13. The collimated free space pump pulses from the high-power amplifier are sent through half and quarter wave plates to optimize transmission through a high-power isolator. This isolator protects the amplifier from any reflections of the pump light from the laser setup, which could otherwise provide unwanted feedback to the amplifier. From the isolator the high-

power pump pulses are coupled into the curved mirror-PBGF resonator through the 25-mm radius of curvature dichroic mirror using a ~ 40-mm focal length achromatic doublet lens. Approximately 1% of the pump light and any circulating laser light are transmitted through the 25-mm radius of curvature dielectric mirror at the opposite end of the PBGF and collimated using another achromatic doublet lens. Following collimation, a plano/plano dichroic mirror is used to filter any laser light from the pump light. The pump light is transmitted through the dichroic mirror, coupled into SMF, and sent to a Ge (for high sensitivity) or InGaAs photodetector for observation. Any light at wavelengths longer than ~ 1600 nm is reflected from the flat dichroic mirror and coupled into SMF using two additional flat dichroic mirrors to further attenuate light at the pump wavelengths. This SMF fiber is then connected to another Ge photodetector for detection of laser light.

This laser cavity should be very low loss, since the primary loss comes from the curved mirror-to-PBGF recoupling which can be as low as 0 – 4%. This low-loss cavity configuration comes at a steep price, as alignment of the cavity for lasing at 1650 nm is quite a challenge. Three separate laser sources having wavelengths near 1300, 1533, and 1600 nm are used during various phases of the alignment procedure. The main difficulty comes in ensuring that both the dichroic mirror (high reflector) and the 99% reflective dielectric mirror (output coupler) are simultaneously aligned to retroreflect the lasing light back into the fiber. 1300-nm wavelength light is used to initially align the high reflector to the end of the PBGF because it passes through the output coupler with only ~ 20% reflection loss. Similarly, 1600-nm wavelength light is used to align the output coupler because it passes through the high reflector with only ~ 50% reflection loss.

The alignment procedure begins with aligning the high reflector to the end of the PBGF. Rough alignment is performed using a 1300-nm wavelength fiber-coupled laser diode. This diode is connected to the SMF patch cord normally connected to the Ge or InGaAs photodetector used to observe pump light. The collimated 1300-nm wavelength light is then sent through the dichroic mirror used to filter the laser light from the pump and coupled through the output coupler into the PBGF. The dichroic mirrors reflect ~ 85% of the light at 1300 nm, so once the curved dichroic mirror is aligned to the end of the PBGF, the light is transmitted back through the fiber and the output coupler and is mostly reflected from the plano dichroic mirror used to

separate the pump and laser light. The light is then detected after this reflection using a large
area Ge photodetector.

      With the curved dichroic cavity mirror aligned, the next step is to align the curved output
coupler to the other end of the PBGF. This is done using the 1533-nm wavelength pump light.
Pump light from the amplifier is coupled into the PBGF by adjusting the achromatic doublet lens
position and the pump beam steering, while being careful not to disturb the dichroic mirror-to-
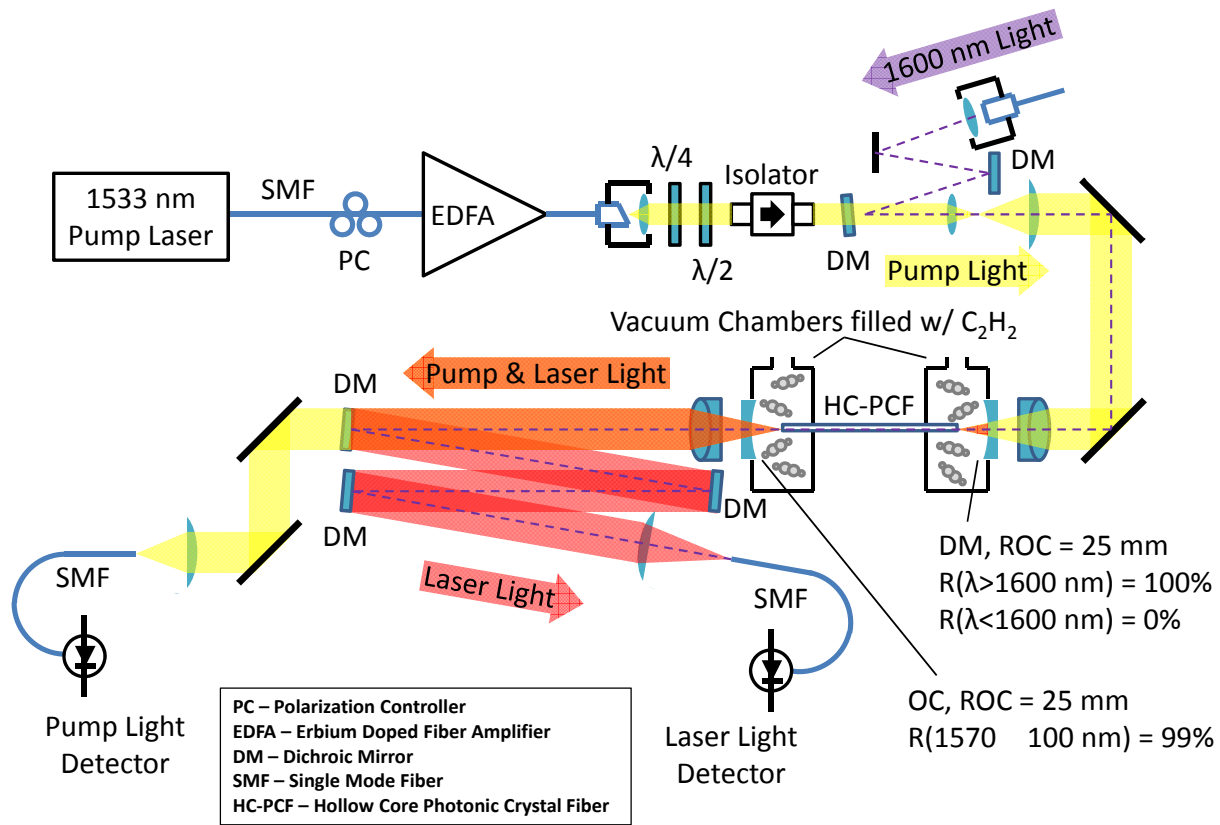
**Figure 7.12 Low loss setup for C_2H_2-filled PBGF small quantum defect laser based on
dichroic optics. The cavity consists of two curved mirrors with radii of curvature equal to
25 mm. One of the curved cavity mirrors is dichroic, allowing 1.5-μm wavelength pump
light to be transmitted while reflecting light at wavelengths longer than ~ 1600 nm. A flat
dichroic mirror (which is otherwise identical to the curved cavity mirror) is used to
separate the pump and lasing wavelengths. Two additional flat dichroic mirrors are used
to further filter the lasing light before coupling it into SMF for detection.**

PBGF alignment. With the pump light coupled into the PBGF, the output coupler position is optimized until the maximum reflection is observed. The reflected light is transmitted back to the free-space isolator where it is dumped out the rejection port (preventing it from reentering the amplifier) and detected using a large area Ge photodetector.

Finally, the laser light detection path is aligned using 1600-nm wavelength light. The light is coupled along the path of the pump light using the dichroic mirror placed just after the free-space isolator. The 1600-nm wavelength light is then coupled into the PBGF through the dichroic mirror with a ~ 50% reflection loss. Approximately 1% of the light is then coupled through the output coupler and collimated. The light is then ~ 50% reflected off the flat dichroic mirror used to filter the laser from the pump light. The beam steering into the SMF along with the position of the lens just before the SMF are optimized to give the maximum voltage from the laser light detector. If the cavity is well aligned, the signal on this detector shows interference when the positions of any of the cavity optics or the fiber ends are perturbed. Tweaking the cavity mirror alignment to maximize this interference signal provides the fine control needed to reach optimal cavity alignment.

The cavity alignment is very sensitive to the position of the fiber relative to the cavity mirrors. If the ends of the PBGF extend too far from the vacuum seal on the fiber holder, the cavity alignment will drift as the pump power incident on the fiber increases, because the hollow fiber heats and deflects with time. Therefore, short (~1 mm) bare fiber lengths protrude from the fiber holder in order to mitigate these thermal effects, and those caused by mechanical vibrations. Filling the vacuum chambers with gas also causes some misalignment of the cavity, and so the cavity alignment must be reoptimized using the 1600-nm wavelength light whenever the gas pressure in the vacuum chambers is changed.

While lasing in this system was attempted using acetylene gas pressures of up to ~ 100 torr, no lasing was ever demonstrated with this system. Because of the alignment challenges, issues with the double-clad amplifier, and the desire to attempt mid-IR lasing in a single-pass configuration (which was known to have a much higher chance for success), the experimental trials to demonstrate small quantum defect lasing from gas-filled HC-PCFs were put on hold.

Chapter 8 - Summary and Outlook

Realization of the first gas fiber laser based on population inversion holds great promise for coherence generation applications as well as for engineering high power, portable and robust, all fiber mid-IR sources in the future. Using this architecture, one may effectively engineer gas-filled fiber laser sources at numerous wavelengths difficult to obtain with other technologies by both carefully selecting the gas and designing the optical fiber. The gas must absorb at wavelengths where inexpensive, high-power pump sources exist, and lase at the wavelength or wavelengths of interest. The fiber should be highly transmissive at both the pump and laser frequencies while suppressing lasing on unwanted transitions. Sealing the fiber permits an all-fiber device, facilitating easy integration into optical systems.

While the performance of solid core fiber lasers at high powers can be limited by the onset of nonlinear processes such as Brillouin and Raman scattering [35], gas-filled HC-PCF lasers can be expected to surpass these limits and have higher thresholds for damage, because no glass or other host material is present in the high intensity region (within the gas-filled fiber core) of the propagating modes. Phase-locking multiple gas-filled fiber lasers together might then be used directly to achieve higher ultimate powers than can be realized from a similar solid-core system.

These higher damage thresholds may be capitalized on by employing a small quantum defect lasing scheme [73], in which the pump and laser wavelengths differ by as little as 1%, to generate coherence between multiple incoherent pump sources. This may be accomplished using a molecular gas which can be optically pumped simultaneously via different ro-vibrational transitions and forced to lase on a single transition. Small quantum defect lasing will require fast rotational mixing and repopulation of the ground state, which may favor asymmetric molecules or require buffer gases for tailored energy transfer. Owing to the needed thermalization between rotational states, small quantum defect lasing should allow CW laser operation which is paramount for use in many potential applications.

Many interesting effects, including long (~ 30 ns) laser-to-pump pulse delays and pressure dependent spectral contributions to the mid-IR laser pulses have been observed from these gas filled fiber lasers, which require further study to more fully characterize and understand. Mid-IR laser efficiencies as high as ~ 20% have now been observed from acetylene-

filled kagome-structured HC-PCF. Since gas-filled HC-PCF lasers have such great potential as mid-IR sources for a multitude of applications, further experiments aimed at understanding the behavior and dependencies of these lasers is paramount to further improving laser performance.

While overall this project has been quite successful with the initial demonstrations and basic characterizations of mid-IR emissions from gas-filled hollow-core fiber lasers, much work remains to refine the precision of current measurements as well as to examine measure other fundamental quantities related to performance of this new laser architecture. Work is ongoing with collaborators at the University of Bath to continue to develop better HC-PCFs, with the specific goals of improving the current mid-IR fiber loss, and pushing this low loss region to longer wavelengths within the mid-IR and beyond, opening the door to exploring additional gases like CO and CO_2.

Large (10 – 50%) pulse-to-pulse fluctuations in the mid-IR laser pulse energy generated by the laser can be seen, while the source remains a mystery. The laser setup was changed to minimize the effect that fluctuations in the mid-IR laser polarization would have on the measured pulse energies, but this seemed to have no effect on the laser pulse energy scatter. A more exotic explanation relies on the fact that the large core fiber is likely multimode. If this is the case, perhaps more than one guided mid-IR fiber mode exists with sufficiently high gain to support lasing. The observed fluctuations in the shot-to-shot laser pulse energy then could be related to the fluctuations in the constituent guided mid-IR modes, which may produce different net gains depending on how the pulse energy couples between the various modes as the light propagates. While verification of such a hypothesis nearly impossible in the current large core fiber, the nearly single-mode mode profile from one of the 42-μm pitch hypocycloidal fiber received recently from collaborators at the University of Bath may offer a means to help rule out the idea that multiple competing mid-IR modes are responsible for fluctuations in the laser pulse energy. This fiber is currently being installed in the laser setup where testing will soon begin.

In addition to improving the measurements already being done, there are several more measurements that should be considered. From the initial findings our University of New Mexico collaborators, it seems that the polarization of the pump and mid-IR laser light are correlated. Determination of the exact relative pump and laser polarizations is complicated by the wavelength-dependent polarization rotation generally induced by non-polarization maintaining optical fiber. However, a measurement to determine if a polarization correlation

exists would be reasonably simple to duplicate in our lab with the appropriate polarizers. One reason a polarization correlation might exist may have to do with the absorbing and emitting vibrational transitions both having dipole moments that oscillate along the internuclear axis, and too little time for the molecule to change orientations before the onset of lasing.

Another interesting measurement would be to examine the temporal coherence of the generated mid-IR pulses. The temporal coherence can be measured using a Michelson interferometer where the path length between the two arms is varied. The difficulty with this is the ~ 1-ns duration of the pulses which corresponds to a length of ~ 30 cm in air. This measurement could be done at various pump pulse energies to see if the temporal coherence changes near threshold where the pump field is weaker and it takes more time to build sufficient population inversion to reach the onset of lasing.

While considerable effort was put into demonstrating a CW small quantum defect laser with no success, this remains one of the most interesting and promising areas to continue investigating. We now have in our possession the sharp dichroic mirrors described in Chapter 7 which should allow a low loss cavity to be constructed which is ~ 99% reflective at wavelengths near 1547 nm while exhibiting high transmission at wavelengths near 1536 nm. These wavelengths correspond to ro-vibrational transitions in $H^{13}CN$ which was produced for us by Dr. Chris Levy in the Chemistry Department at Kansas State University. The only piece of infrastructure missing is a 40-W Er/Yb co-doped double clad fiber amplifier, which should arrive in the coming months. Using the new low loss cavity together with the high power pump, we should be able to exceed the necessary pump power thresholds estimated by collaborators at the University of New Mexico by more than a factor of two.

References

1. Kong, M., Z. Luo, and W. J. Fan, *Inspection of Car's Emission Using Infrared Spectrum Technique.* Journal of Physics: Conference Series, 2006. **42**: p. 1186-1189.
2. German, K.R., *Optimization of $F_A(II)$ and $F_B(II)$ Color-Center Lasers.* Journal of the Optical Society of America B-Optical Physics, 1986. **3**(1): p. 149-157.
3. Chen, W.D., et al., *Continuous-wave mid-infrared laser sources based on difference frequency generation.* Comptes Rendus Physique, 2007. **8**(10): p. 1129-1150.
4. Martienssen, W., ed. *Group VIII, Volume 1: Laser Physics and Applications. Subvolume B: Laser Systems. Part 2*. Springer-Verlag, Berlin, Heidelberg, New York 2008.
5. Tacke, M., *Lead-salt lasers.* Philosophical Transactions of the Royal Society of London Series A-Mathematical Physical and Engineering Sciences, 2001. **359**(1780): p. 547-566.
6. Razeghi, M., *Recent Advance in Semiconductor Mid-Infrared Lasers Emitting at 3-12 μm.* Opto-Electronics Review, 1999. **7**(1): p. 29-58.
7. Faist, J., et al., *Quantum Cascade Laser.* Science, 1994. **264**(5158): p. 553-556.
8. Daylight Solutions. *Product description*. cited 2012; Available from: http://www.daylightsolutions.com/products/.
9. Colombelli, R., et al., *Quantum cascade surface-emitting photonic crystal laser.* Science, 2003. **302**(5649): p. 1374-1377.
10. Curl, R.F., et al., *Quantum cascade lasers in chemical physics.* Chemical Physiscs Letters, 2010. **487**(1-3): p. 1-18.
11. Phua, P.B., et al., *High-efficiency mid-infrared $ZnGeP_2$ optical parametric oscillator in a multimode-pumped tandem optical parametric oscillator.* Applied Optics, 1999. **38**(3): p. 563-565.
12. Shi, W. and Ding, Y.J., *Coherent radiation in the range of 15-28 μm in a cadmium-selenide crystal.* Optics Communications, 2002. **207**(1-6): p. 273-277.
13. McCord, J.E., et al., *Experimental investigation of an optically pumped mid-infrared carbon monoxide laser.* IEEE Journal of Quantum Electronics, 1999. **35**(11): p. 1602-1612.
14. McCord, J.E., et al., *Frequency-tunable optically pumped carbon monoxide laser.* IEEE Journal of Quantum Electronics, 2000. **36**(9): p. 1041-1052.
15. Miller, H.C., D.T. Radzykewycz, and G. Hager, *An optically pumped midinfrared HBr laser.* IEEE Journal of Quantum Electronics, 1994. **30**(10): p. 2395-2400.
16. Nampoothiri, A.V.V., et al., *Molecular C_2H_2 and HCN lasers pumped by an optical parametric oscillator in the 1.5-μm band.* Optics Express, 2010. **18**(3): p. 1946-1951.
17. Chang, T.Y. and T.J. Bridges, *Laser action at 452, 496, and 541 μm in optically pumped CH_3F.* Optical Communications, 1970. **1**(9): p. 423-426.
18. Chang, T.Y. and O.R. Wood, *An optically pumped CO_2 laser.* IEEE Journal of Quantum Electronics, 1972. **8**(6): p. 598.
19. Schlossberg, H.R. and H.R. Fetterman, *Optically pumped vibrational transition laser in OCS.* Applied Physics Letters, 1975. **26**(6): p. 316-318.
20. Ehrenreich, T., et al., *Diode pumped cesium laser.* Electronics Letters, 2005. **41**(7): p. 415-416.
21. Krupke, W.F., et al., *Resonance transition 795-nm rubidium laser.* Optics Letters, 2003. **28**(23): p. 2336-2338.

22.   Zhdanov, B.V., T. Ehrenreich, and R.J. Knize, *Highly efficient optically pumped cesium vapor laser.* Optics Communications, 2006. **260**(2): p. 696-698.

23.   Kletecka, C.S., et al., *Cascade lasing of molecular HBr in the four micron region pumped by a Nd : YAG laser.* IEEE Journal of Quantum Electronics, 2004. **40**(10): p. 1471-1477.

24.   Cregan, R.F., et al., *Single-mode photonic band gap guidance of light in air.* Science, 1999. **285**(5433): p. 1537-1539.

25.   Benabid, F., et al., *Stimulated Raman scattering in hydrogen-filled hollow-core photonic crystal fiber.* Science, 2002. **298**(5592): p. 399-402.

26.   Roberts, P.J., et al., *Ultimate low loss of hollow-core photonic crystal fibres.* Optics Express, 2005. **13**(1): p. 236-244.

27.   Benabid, F., et al., *Compact, stable and efficient all-fibre gas cells using hollow-core photonic crystal fibres.* Nature, 2005. **434**(7032): p. 488-491.

28.   Bhagwat, A.R. and A.L. Gaeta, *Nonlinear optics in hollow-core photonic bandgap fibers.* Optics Express, 2008. **16**(7): p. 5035-5047.

29.   Benabid, F., et al., *Ultrahigh efficiency laser wavelength conversion in a gas-filled hollow core photonic crystal fiber by pure stimulated rotational Raman scattering in molecular hydrogen.* Physical Review Letters, 2004. **93**(12): p. 123903.

30.   Couny, F., et al., *Generation and photonic guidance of multi-octave optical-frequency combs.* Science, 2007. **318**(5853): p. 1118-1121.

31.   Corwin, K.L., et al., *Gas Filled Hollow Fiber Laser Based on Population Inversion.* Provisional Patent, filed January 21, 2010.

32.   Couny, F., F. Benabid, and P.S. Light, *Large-pitch kagome-structured hollow-core photonic crystal fiber.* Optics Letters, 2006. **31**(24): p. 3574-3576.

33.   Jones, A.M., et al., *Mid-infrared gas filled photonic crystal fiber laser based on population inversion.* Optics Express, 2011. **19**(3): p. 2309-2316.

34.   Jones, A. M., et al., *Characterization of mid-infrared emissions from C_2H_2, CO, CO_2, and HCN-filled hollow fiber lasers.* in *Photonics West.* 2012: SPIE.

35.   Dawson, J.W., et al., *Analysis of the scalability of diffraction-limited fiber lasers and amplifiers to high average power.* Optics Express, 2008. **16**(17): p. 13240-13266.

36.   Herzberg, G. and J.W.T. Spinks, *Molecular spectra and molecular structure.* Prentice-Hall physics series. 1939, New York: Prentice-Hall. 3 v.

37.   Herman, M., et al., *Vibrational spectroscopic database on acetylene, (X)over-tilde (1)Sigma(+)(g) ((C2H2)-C-12, (C2D2)-C-12, and (C2H2)-C-13).* Journal of Physical and Chemical Reference Data, 2003. **32**(3): p. 921-1361.

38.   Maki, A., et al., *Infrared transitions of (HCN)-C-12-N-14 and (HCN)-C-12-N-15 between 500 and 10000 cm(-1).* Journal of Molecular Spectroscopy, 1996. **180**(2): p. 323-336.

39.   Griffiths, D.J., *Introduction to Quantum Mechanics*, ed. E. Fahlgren. 2005, Upper Saddle River: Pearson Prentice Hall.

40.   Swann, W.C. and S.L. Gilbert, *Pressure-induced shift and broadening of 1510-1540-nm acetylene wavelength calibration lines.* Journal of the Optical Society of America B, 2000. **17**(7): p. 1263-1270.

41.   McQuarrie, D.A., *Statistical Mechanics.* 2000, Sausalito: University Science Books.

42.   Boyd, R.W., *Nonlinear optics.* 2nd ed. 2003, San Diego, CA: Academic Press.

43.   Siegman, A.E., *Lasers.* 1986, Sausalito, CA: University Science Books.

44.	Paul, O., et al., *Temperature-dependent Sellmeier equation in the MIR for the extraordinary refractive index of 5% MgO doped congruent LiNbO₃.* Applied Physics B-Lasers and Optics, 2007. **86**(1): p. 111-115.

45.	Kim, Y.S. and R.T. Smith, *Thermal Expansion of Lithium Tantalate and Lithium Niobate Single Crystals.* Journal of Applied Physics, 1969. **40**(11): p. 4637-4641.

46.	Sutherland, R.L., *Handbook of Nonlinear Optics*. Second ed. 2003, New York: Marcel Dekker, Inc.

47.	Benabid, F., *Hollow-core photonic bandgap fibre: new light guidance for new science and technology.* Philosophical Transactions of the Royal Society A-Mathematical Physical and Engineering Sciences, 2006. **364**(1849): p. 3439-3462.

48.	Shephard, J.D., et al., *Single-mode mid-IR guidance in a hollow-core photonic crystal fiber.* Optics Express, 2005. **13**(18): p. 7139-7144.

49.	Light, P.S., et al., *Double photonic bandgap hollow-core photonic crystal fiber.* Optics Express, 2009. **17**(18): p. 16238-16243.

50.	Neumann, J.v. and E. Wigner, *Uber merkwurdige diskrete Eigenworte.* Physik Z, 1929. **30**(465).

51.	Wang, Y.Y., et al., *Low loss broadband transmission in hypocycloid-core Kagome hollow-core photonic crystal fiber.* Optics Letters. **36**(5): p. 669-671.

52.	Benabid, F., *Fiber Datasheet*, Personal communication to K.L. Corwin, September 2011.

53.	Wang, Y., et al. *Low Loss Broadband Transmission in Optimized Coreshape Kagome Hollow-core PCF*. in *Conference on Lasers and Electro-Optics/International Quantum Electronics Conference*. 2010: Optical Society of America.

54.	Laseroptik. cited 2012; Available from: http://www.laseroptik.de/index.php?Substrates:Transmission_Curves.

55.	Shephard, J.D., et al., *High energy nanosecond laser pulses delivered single-mode through hollow-core PBG fibers.* Optics Express, 2004. **12**(4): p. 717-723.

56.	Heaven, M.C., J. Han, and K. Freel. *Rotational and vibrational energy transfer from the first overtone stretch of acetylene*. in *International Symposium on Molecular Spectroscopy*. 2010. Ohio State University.

57.	Griffiths, D.J., *Introduction to Electrodynamics*. Third ed. 1999, Upper Saddle River: Prentice-Hall, Inc.

58.	Wikipedia. *Ray diagram for Fresnel reflection*. cited 2012; Available from: http://en.wikipedia.org/wiki/Fresnel_equations.

59.	Malitson, I.H., *A Redetermination of Some Optical Properties of Calcium Fluoride.* Applied Optics, 1963. **2**(11): p. 1103-1107.

60.	Jones, A.M., et al., *Mid-IR Fiber Lasers Based on Molecular Gas-filled Hollow-Core Photonic Crystal Fiber*, in *Conference on Lasers and Electro-Optics/International Quantum Electronics Conference*. 2011: Baltimore, MD.

61.	HITRAN. http://cfa-www.harvard.edu/HITRAN/.

62.	Jones, A.M., et al., *Mid-infrared gas filled photonic crystal fiber laser based on population inversion.* Optics Express. **19**(3): p. 2309-2316.

63.	Adachi, S., *Model Dielectric-Constants of Si and Ge.* Physical Review B, 1988. **38**(18): p. 12966-12976.

64.	Edmund Optics, *Transmission curve for AR-coated germanium window*. cited 2012; Available from: http://www.edmundoptics.com/products/displayproduct.cfm?productid=2685.

65. Demtroder, W., *Laser Spectroscopy*. Third ed. 2003, New York: Springer-Verlag Berlin Heidelberg.

66. Hilborn, R.C., *Einstein Coefficients, Cross-Sections, F Values, Dipole-Moments, and All That.* American Journal of Physics, 1982. **50**(11): p. 982-986.

67. Fan, T.Y., *Laser beam combining for high-power, high-radiance sources.* IEEE Journal of Selected Topics in Quantum Electronics, 2005. **11**(3): p. 567-577.

68. Skribano.N, M.S. Feld, and I.P. Herman, *Laser oscillation and anisotropic gain in the 1 → 0 vibrational band of optically pumped HF gas.* Applied Physics Letters, 1972. **21**(10): p. 466-470.

69. Wikipeida. *Double cald fiber laser architecture*. cited 2012; Available from: http://upload.wikimedia.org/wikipedia/commons/thumb/c/cd/Fl.svg/900px-Fl.svg.png.

70. Yahel, E. and A.A. Hardy, *Modeling and optimization of short Er^{3+}-Yb^{3+} codoped fiber lasers.* IEEE Journal of Quantum Electronics, 2003. **39**(11): p. 1444-1451.

71. NKT Photonics. *HC-1550-02 photonic band gap fiber datasheet*. cited 2012; Available from: http://www.nktphotonics.com/files/files/HC-1550-02-111221.pdf.

72. Thapa, R., et al., *Arc fusion splicing of hollow-core photonic bandgap fibers for gas-filled fiber cells.* Optics Express, 2006. **14**(21): p. 9576-9583.

73. Ratanavis, A., N. Campbell, and W. Rudolph, *Feasibility study of optically pumped molecular lasers with small quantum defect.* Optical Communications, 2010. **283**(6): p. 1075-1080.

Publications

Patents:

1. "A Gas Filled Hollow Fiber Laser Based on Population Inversion," K. L. Corwin, A. M. Jones, R. Kadel, A. V. V. Nampoothiri, A. Ratanavis, W. Rudolph, and B. R. Washburn, Provisional Patent, Submitted to the US Patent Office January 21, 2010.

Peer-Reviewed Publications and Conference Submissions:

1. W. Rudolph et. al., (Invited) ,Optical Materials Express (In Preparation).

2. A. M. Jones, A. V. V. Nampoothiri, A. Ratanavis, R. Kadel, N. V. Wheeler, F. Couny, F. Benabid, W. Rudolph, B. R. Washburn, and K. L. Corwin, "C_2H_2 Gas Laser Inside Hollow-Core Photonic Crystal Fiber Based on Population Inversion," paper CTuU1, Conf. on Lasers and Electro-Optics (CLEO), May 2010, San Jose, CA.

3. A. M. Jones, C. Fourcade-Dutin, C. Mao, B. Baumgart, A. V. V. Nampoothiri, N. Campbell, Y. Y. Wang, F. Benabid, W. Rudolph, B. R. Washburn, and K. L. Corwin, "Characterization of mid-infrared emissions from C_2H_2, CO, CO_2, and HCN-filled hollow fiber lasers," Photonics West, January 2012, San Fransico, CA.

4. A. M. Jones, R. Kadel, W. Hageman, K. L. Corwin, B. R. Washburn, A. V. V. Nampoothiri, T. Fiedler, W. Rudolph, N. V. Wheeler, F. Couny, F. Benabid, "Mid-IR Fiber Lasers Based on Molecular Gas-filled Hollow-Core Photonic Crystal Fiber," paper CThD1, Conference on Lasers and Electro Optics (CLEO), May 2011, Baltimore, MD.

5. A. M. Jones, A. V. V. Nampoothiri, A. Ratanavis, T. Fiedler, N. V. Wheeler, F. Couny, R. Kadel, F. Benabid, B. R. Washburn, K. L. Corwin, and W. Rudolph, "Mid-infrared gas filled photonic crystal fiber laser based on population inversion," Opt. Express 19, 2309-2316 (2011).

6. A. M. Jones, A. V. V. Nampoothiri, A. Ratanavis, R. Kadel, N. V. Wheeler, F. Couny, F. Benabid, W. Rudolph, B. R. Washburn, and K. L. Corwin, "C_2H_2 Gas Laser Inside Hollow-Core Photonic Crystal Fiber Based on Population Inversion," paper CTuU1, Conf. on Lasers and Electro-Optics (CLEO), May 2010, San Jose, CA.

7. A. V. V. Nampoothiri, A. Jones , A. Ratanavis, K. Corwin, B. R. Washburn, W. Rudolph, "Laser emission from a gas (acetylene) filled hollow fiber", Post-Deadline Photonics West, January 2010, San Francisco, CA.

Appendix A – Mathematica Code to Calculate Temperature-Dependent Quasi-Phase-Matched Signal and Idler Wavelengths in MgO:PPLN

■ Constants

```
a1 = 5.319725;
a2 = 0.09147285;
a3 = 0.3165008;
a4 = 100.2028;
a5 = 11.37639;
a6 = 0.01497046;
b1 = 4.753469 * 10^-7;
b2 = 3.310965 * 10^-8;
b3 = 2.760513 * 10^-5;
α = 1.53 * 10^-5; (* units of K^-1 *)
β = 5.3 * 10^-9; (* units of K^-2 *)
```

■ Adjustable parameters

```
Λ0 = 31.5 * 10^-6; (* Poling period in m *)
λ3 = 1063.81 * 10^-9; (* Pump wavelength in m. Measured to be 1063.81 +- 0.05 nm using OSA. *)
```

■ Define functions

```
f[tempC] := (tempC - 24.5) * (tempC + 570.82);
Λ[tempC] := Λ0 * (1 + α * (tempC - 19) + β * (tempC - 19)^2);

For[λ1 = 1834 * 10^-9, λ1 ≤ 2127.6 * 10^-9, λ1 += 0.2 * 10^-9,

  λ2 = 1 / (1/λ3 - 1/λ1);

  temp =
  NSolve[
    {1/Λ[tempC] == 1/λ3 Sqrt[(a1 + b1 * f[tempC] + (a2 + b2 * f[tempC])/((λ3 * 10^6)^2 - a3^2) + (a4 + b3 * f[tempC])/((λ3 * 10^6)^2 - a5^2) - a6 * (λ3 * 10^6)^2)] -
      1/λ2 Sqrt[(a1 + b1 * f[tempC] + (a2 + b2 * f[tempC])/((λ2 * 10^6)^2 - a3^2) + (a4 + b3 * f[tempC])/((λ2 * 10^6)^2 - a5^2) - a6 * (λ2 * 10^6)^2)] -
      1/λ1 Sqrt[(a1 + b1 * f[tempC] + (a2 + b2 * f[tempC])/((λ1 * 10^6)^2 - a3^2) + (a4 + b3 * f[tempC])/((λ1 * 10^6)^2 - a5^2) - a6 * (λ1 * 10^6)^2)]}, {tempC}];

  If[temp[[4, 1, 2]] ≥ 20 && temp[[4, 1, 2]] ≤ 200,
    Print[temp[[4, 1, 2]], ",", λ1 * 10^9 // N, ",", λ2 * 10^9 // N]
    (*Print[temp[[4,1,2]]//N];*)
    (*Print[λ1*10^6//N];*)
    (*Print[λ2*10^6//N];*)
  ];
];
```

Appendix B – Optical Parametric Amplifier Simulation Code

■ **Constants**

```
ε0 = 8.854 * 10^-12 (* units of F/m *);
c = 299 792 458 (* units of m/s *);
deff = d33 = 27 * 10^-12 (* m/V *);
```

■ **Initial powers**

```
p10 = 0.300 (* Signal power in W *);
p20 = 0 (* Diff. frequency power in W *);
et30 = 10 / 30 * 10^-3; τ30 = 24 * 10^-9;

p30 = Sqrt[Log[16]/π] et30 / τ30 // N (* Peak pump power in W (assuming Gaussian pulse with "et30" J pulse energy and "τ30" s FWHM duration) *)
```

13 047.7

■ **Area of beam inside crystal (assuming no divergence)**

```
beamDiameter = 0.0025 * 40 / 150 // N (* units of m *)
beamArea = π * beamDiameter^2 / 4; (* units of m^2 *)
```

0.000666667

■ **Define functions**

```
λ1 = 1532 * 10^-9;
λ3 = 1064 * 10^-9;
λ2 = (1/λ3 - 1/λ1)^-1 // N
tempC = 130; (* Crystal temp in degrees centigrade *)
f = (tempC - 24.5) * (tempC + 570.82);

n1 = Sqrt[(5.319725 + 4.753469 * 10^-7 * f + (0.09147285 + 3.310965 * 10^-8 * f)/((λ1 * 10^6)^2 - (0.3165008)^2) + (100.2028 + 2.760513 * 10^-5 * f)/((λ1 * 10^6)^2 - (11.37639)^2) - 0.01497046 * (λ1 * 10^6)^2)];

n2 = Sqrt[(5.319725 + 4.753469 * 10^-7 * f + (0.09147285 + 3.310965 * 10^-8 * f)/((λ2 * 10^6)^2 - (0.3165008)^2) + (100.2028 + 2.760513 * 10^-5 * f)/((λ2 * 10^6)^2 - (11.37639)^2) - 0.01497046 * (λ2 * 10^6)^2)];

n3 = Sqrt[(5.319725 + 4.753469 * 10^-7 * f + (0.09147285 + 3.310965 * 10^-8 * f)/((λ3 * 10^6)^2 - (0.3165008)^2) + (100.2028 + 2.760513 * 10^-5 * f)/((λ3 * 10^6)^2 - (11.37639)^2) - 0.01497046 * (λ3 * 10^6)^2)];

ω1 = 2 π * c/λ1; k1 = n1 * ω1/c;
ω2 = 2 π * c/λ2; k2 = n2 * ω2/c;
ω3 = 2 π * c/λ3; k3 = n3 * ω3/c;
```

3.48301×10^{-6}

■ **Length of nonlinear crystal**

```
l = 0.050 (* units of m *);
Λ = 2 π / (k3 - k1 - k2) // N (* poling period of crystal in m *) (* Try to add temperture dependence to this *)
m = 1 (* m is order of phase matching *);
dQ = deff * (2/(m * π)) * Sin[(m * π)/2];
```

0.000030003

■ **Define arrays and calculate field amplitudes**

```
Δz = 0.000001; (k3 - k1 - k2) * Δz / (2 π) // N (* For amplitudes to have accurate phase dependence (k3-k1-k2)Δz/(2π) << 1 *)
Array[zCrystal, Round[l / Δz + 1], 0]; zCrystal[0] = 0;
Array[p1, Round[l / Δz + 1], 0]; p1[0] = p10;
Array[p2, Round[l / Δz + 1], 0]; p2[0] = p20;
Array[p3, Round[l / Δz + 1], 0]; p3[0] = p30;
```

0.03333

```mathematica
Array[a1, Round[l / Δz + 1], 0]; a1[0] = Sqrt[ (p10 / beamArea) / (2 * n1 * ϵ0 * c) ] ;

Array[a2, Round[l / Δz + 1], 0]; a2[0] = Sqrt[ (p20 / beamArea) / (2 * n2 * ϵ0 * c) ] ;

Array[a3, Round[l / Δz + 1], 0];

a3[0] = Sqrt[ (p30 / beamArea) / (2 * n3 * ϵ0 * c) ] ;

p1max = p2max = p3max = zmax = 0;

For[z = Δz, z ≤ 1, z += Δz,
 {
  zCrystal[Round[z / Δz]] = z;
  a1[Round[z / Δz]] = a1[Round[z / Δz - 1]] + (2 i * ω1 * dQ * Sign[Sin[2 π * ((z - Δz) / Λ)]]) / (n1 * c) * a3[Round[z / Δz - 1]] * Conjugate[a2[Round[z / Δz - 1]]] *
     Δz * e^(i*(k3-k1-k2)*(z-Δz));
  a2[Round[z / Δz]] = a2[Round[z / Δz - 1]] + (2 i * ω2 * dQ * Sign[Sin[2 π * ((z - Δz) / Λ)]]) / (n2 * c) * a3[Round[z / Δz - 1]] * Conjugate[a1[Round[z / Δz - 1]]] *
     Δz * e^(i*(k3-k1-k2)*(z-Δz));
  a3[Round[z / Δz]] = a3[Round[z / Δz - 1]] + (2 i * ω3 * dQ * Sign[Sin[2 π * ((z - Δz) / Λ)]]) / (n3 * c) * a1[Round[z / Δz - 1]] * a2[Round[z / Δz - 1]] * Δz * e^(-i*(k3-k1-k2)*(z-Δz));
  p1[Round[z / Δz]] = 2 * n1 * ϵ0 * c * (Abs[a1[Round[z / Δz]]])^2 * beamArea;
  p2[Round[z / Δz]] = 2 * n2 * ϵ0 * c * (Abs[a2[Round[z / Δz]]])^2 * beamArea;
  p3[Round[z / Δz]] = 2 * n3 * ϵ0 * c * (Abs[a3[Round[z / Δz]]])^2 * beamArea;
  If[p1[Round[z / Δz]] > p1max,
   {
    p1max = p1[Round[z / Δz]] // N;
    p2max = p2[Round[z / Δz]] // N;
    p3max = p3[Round[z / Δz]] // N;
    zmax = z // N;
   }
  ];
 };
]

Print["P_sig,max = ", p1max * 10^3, " mW"];
Print["E_sig,max = ", p1max * τ30 * 10^6, " μJ"];
Print["E_idler,max = ", p2max * τ30 * 10^6, " μJ"];
Print["E_pump,max = ", p3max * τ30 * 10^6, " μJ"];
Print["z_max = ", zmax * 10^3, " mm"];
Print["η_sig = ", p1max / p30 * 100, "%"];
```

P_sig,max = 12 627.5 mW

E_sig,max = 0.30306 μJ

E_idler,max = 0.130135 μJ

E_pump,max = 312.72 μJ

z_max = 49.999 mm

η_sig = 0.0967792%

```mathematica
(*
Show[ListPlot[Array[p1,Round[l/Δz+1]],PlotRange→{-.05*p30,1.05*p30},Frame->True,FrameLabel->{"z_crystal (μm)","Peak power (W)"}],
 ListPlot[Array[p2,Round[l/Δz+1]]],ListPlot[Array[p3,Round[l/Δz+1]]]]
*)

(*
Show[ListLogPlot[Array[p1,Round[l/Δz+1]],PlotRange→{0.0001,1.2*p30},Frame->True,FrameLabel->{"z_crystal (μm)","Peak power (W)"}],
 ListLogPlot[Array[p2,Round[l/Δz+1]]],ListLogPlot[Array[p3,Round[l/Δz+1]]]]
*)

(*
table1=Table[{zCrystal[i],p1[i],p2[i],p3[i]},{i,0,Round[l/Δz]}];
Export["C:\\Documents and Settings\\Admin\\Desktop\\OPA Calculations\\Exported Data Files\\Data1.csv",table1]
*)
```

Appendix C – Single-Pressure Data Plots

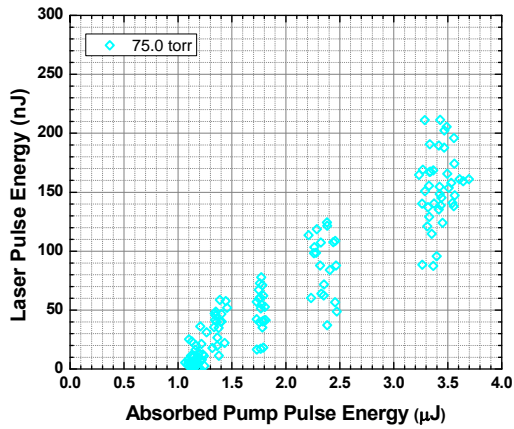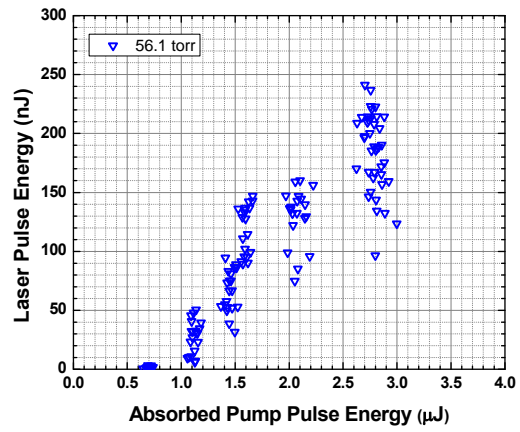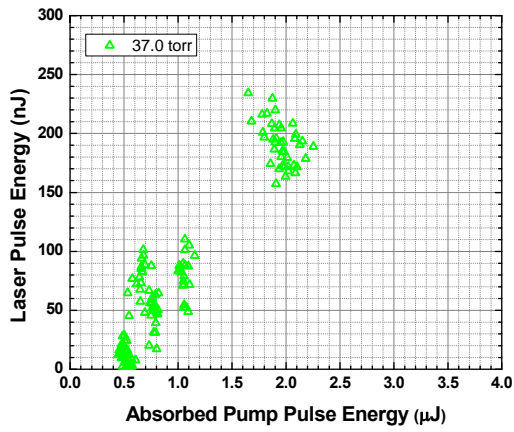Figure 5.17 data sets are shown separately in the plots below.
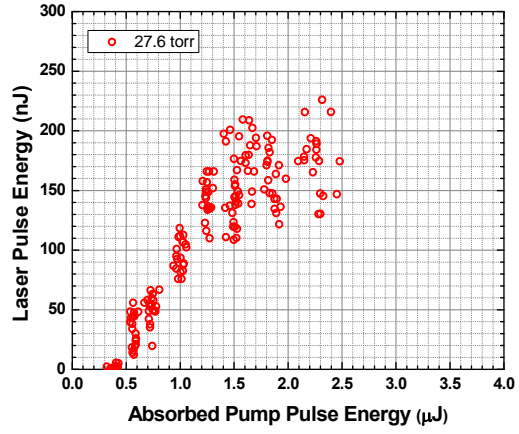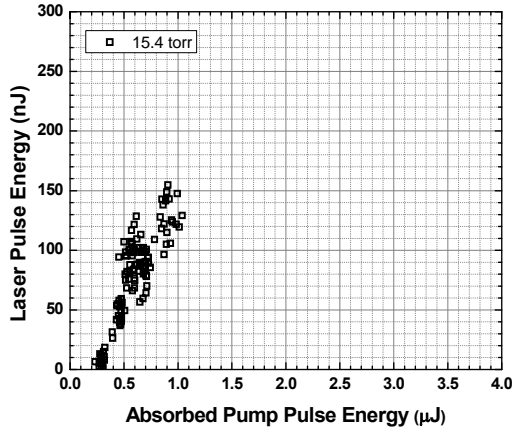
Figure 5.18 data sets are shown separately in the plots below.
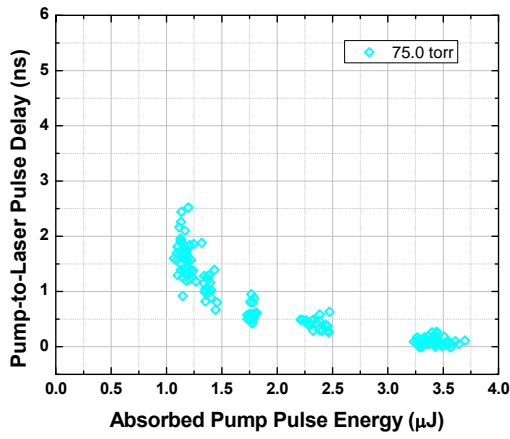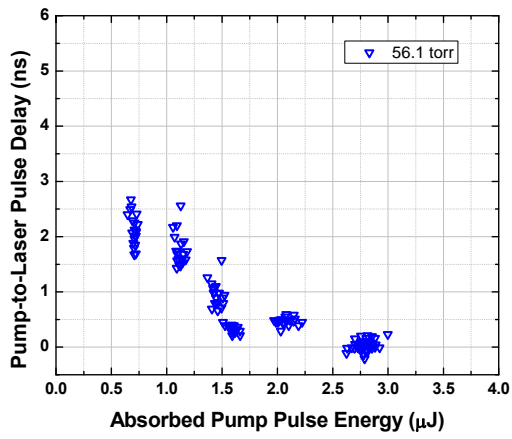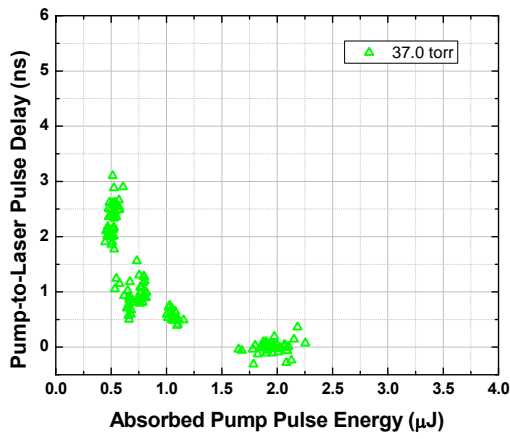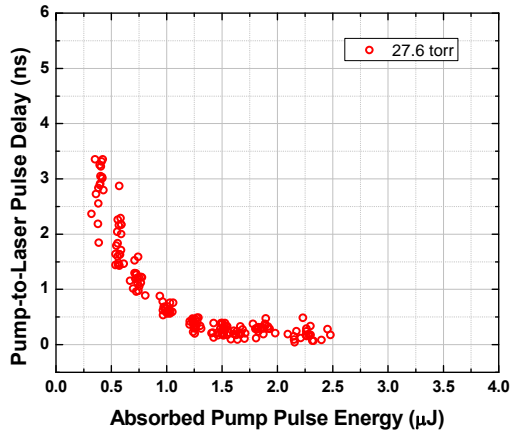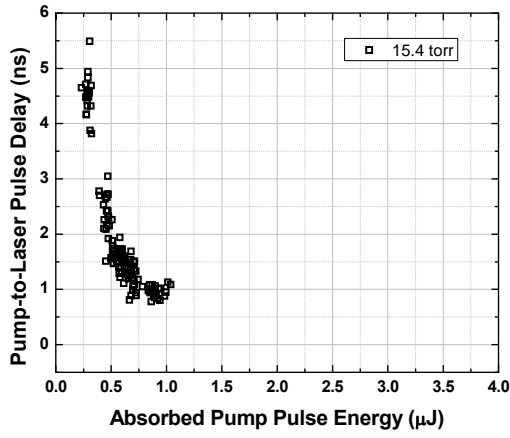
Figure 6.6 data sets are shown separately in the plots below.
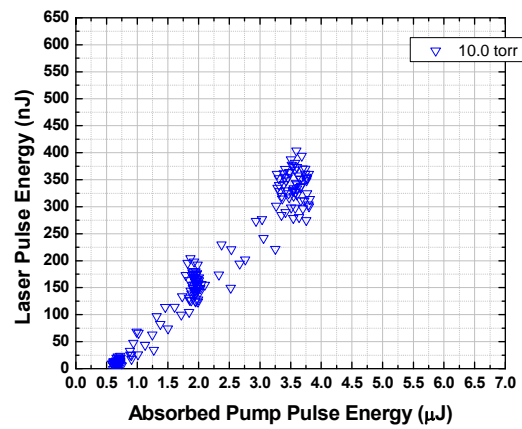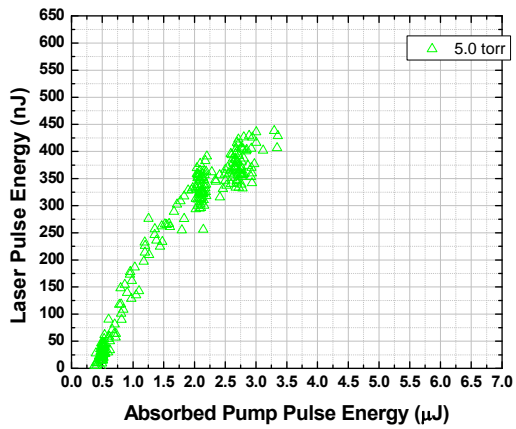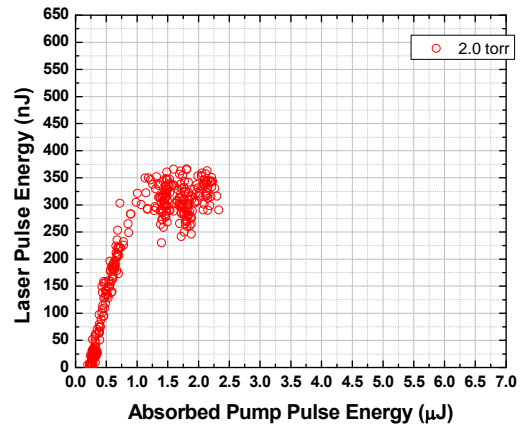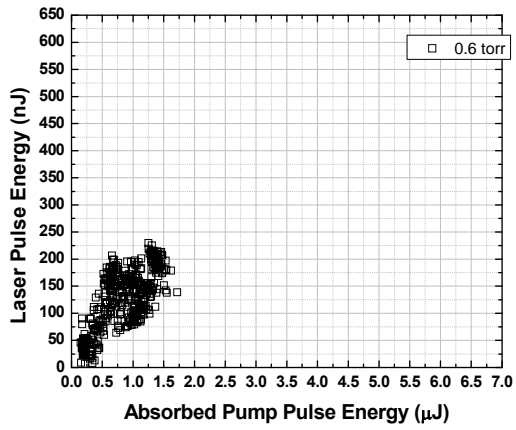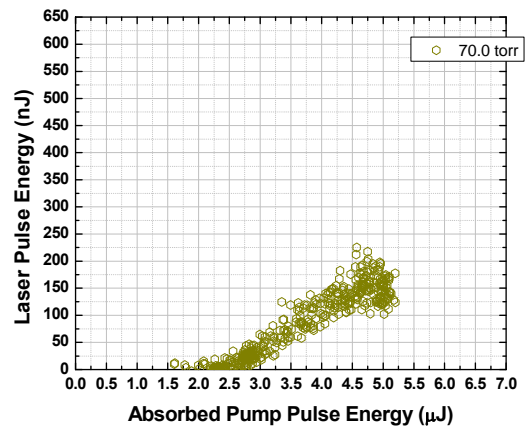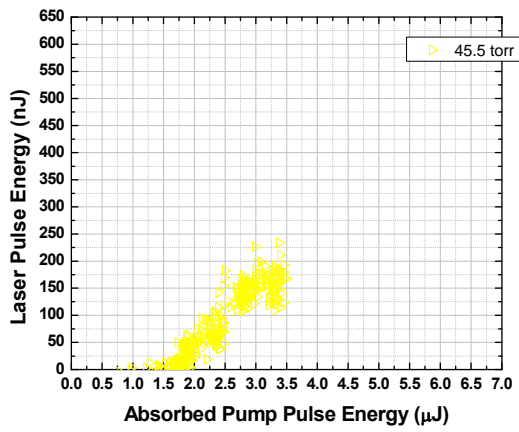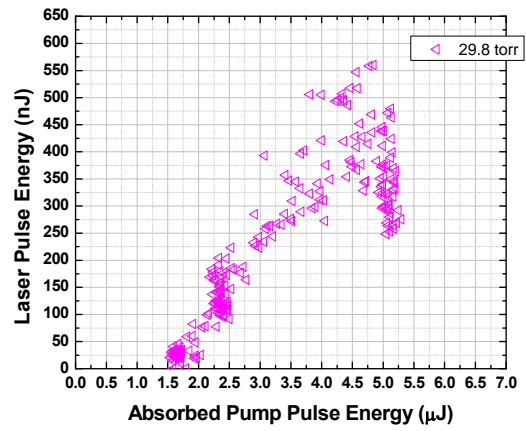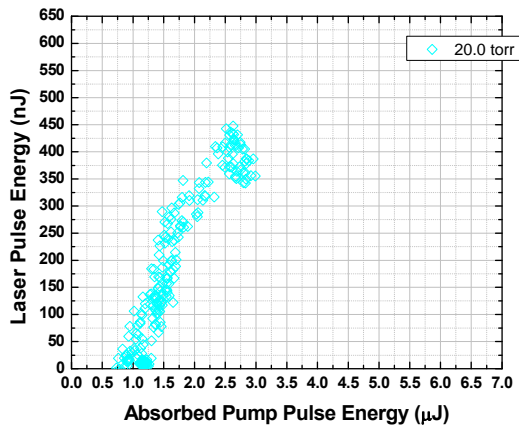
Figure 6.7 data sets are shown separately in the plots below.
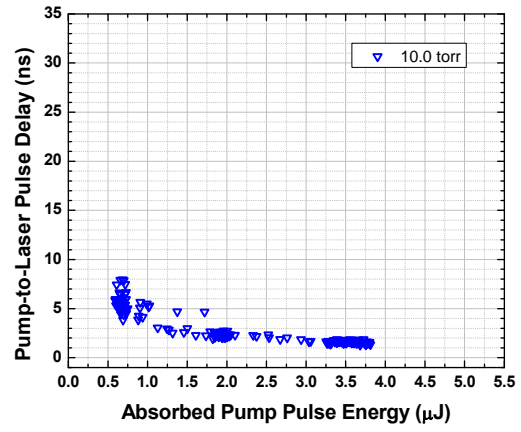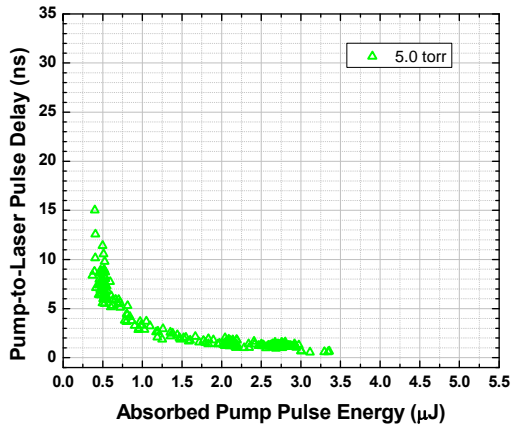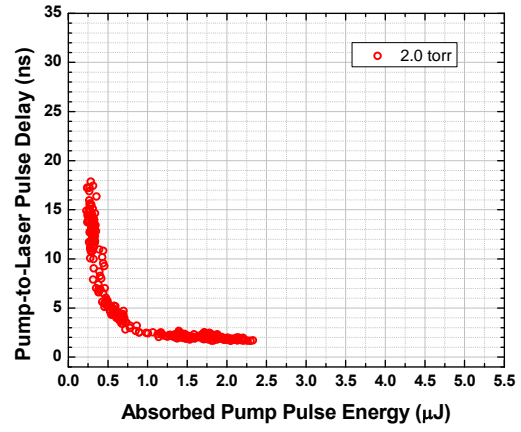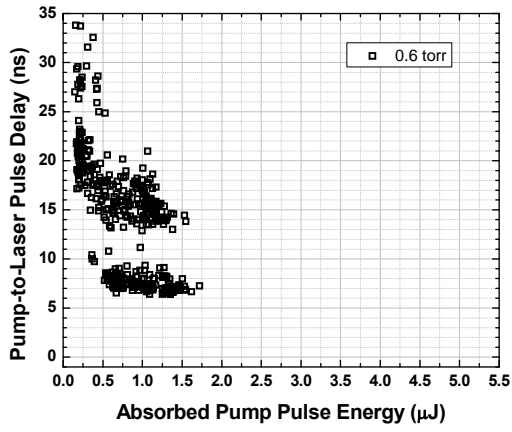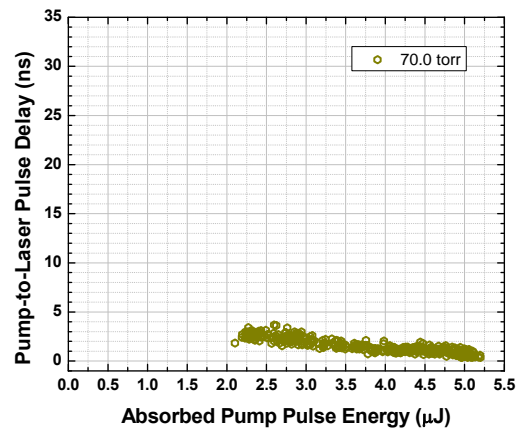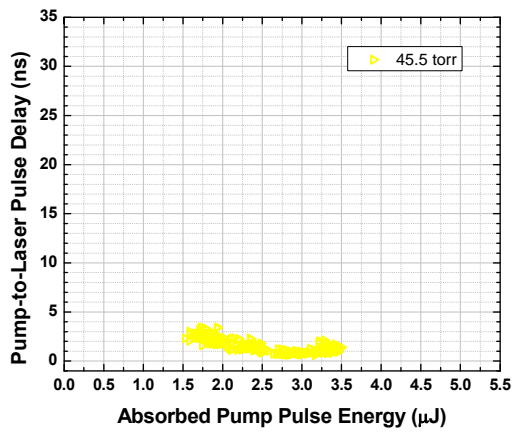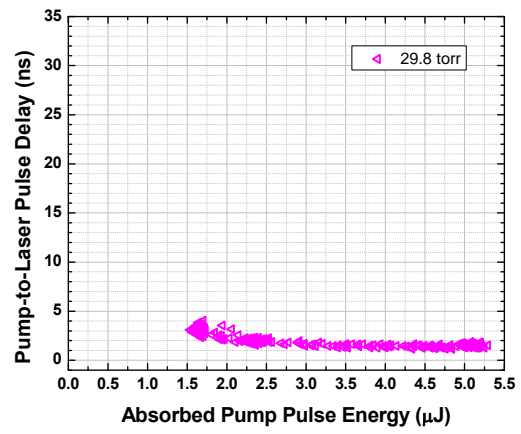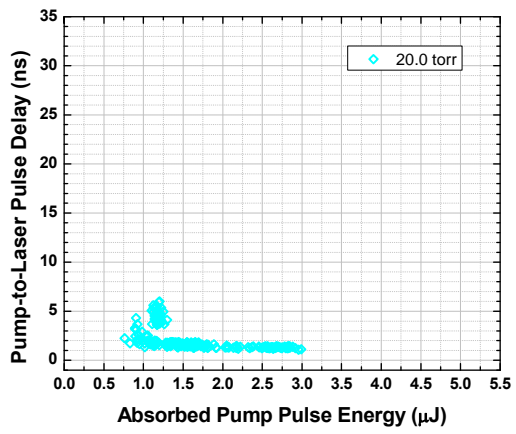
Appendix D – Pulsed Gas-Filled Hollow-Core Fiber Laser Simulation Code

```
%{
    This program models the C2H2 gas fiber laser behavior and calculates
and plots the teporal profile of (1) the incident and (2) transmitted pump
pulse energy and (3) the emitted ~ 3 micron laser pulse energy relative to
the input pump pulse where t = 0 is defined to occur at the peak of the
incident pump pulse intensity.
%}
%-------------------------------------------------------------------------
%   Universal constants

h = 6.626068*10^-34;    % J*s, Planck's constant
c = 2.99792458*10^8;    % m/s, speed of light
kb = 1.3806503*10^-23;  % J/K, Boltzmann constant
R = 8.314472;           % J/(K*mol), universal gas constant


%-------------------------------------------------------------------------
%   Fiber properties

fiberradius = 25*10^-6;   % m, fiber radius
el = 1.46;              % m, length of fiber
lsP = 0.0230259;              % 1/m, exponential loss coefficient for pump
                % corresponding to 0.1 dB/m loss (0.023 =
                % -Ln[10^-(0.75/10)])
lsL = 1.151;                % 1/m, exponential loss coefficient for laser
                % corresponding to 5 dB/m loss (1.151 =
                % -Ln[10^-(5/10)])
NA = 0.05;              % unitless, numerical aperture of fiber
omega = 0.0001; %1/2*(1-cos(asin(NA)));  % unitless, fraction of solid angle
                % subtended by the guided fiber mode


%-------------------------------------------------------------------------
%   temperature and pressure of gas inside fiber

T = 300;            % K, gas temperature
P = 30;             % torr, gas pressure


%-------------------------------------------------------------------------
%   C-12 C2H2 gas properties

MC2H2 = 26.015*10^-3;   % kg/mol, molar mass of C2H2
krPerP = 2.898*10^7;    % 1/(s*torr), rotational relaxation rate
kr = P*krPerP;          % 1/s, rotational relaxation rate
```

```matlab
tr = 1/kr;             % s, rotational relaxation time
vcPerP = 6*10^6;       % Hz/torr, HWHM collisional broadening
deltavc = vcPerP*P;    % Hz, HWHM collisional broadening
Nt = P*133.322/(kb*T); % molecules/m^3, total molecular number density

Np = 0.08*Nt;          % molecules/m^3, approx. number density in J = 7 of
                       %   vibrational ground state
   % REPLACE THIS EXPRESSION WITH ACTUAL J-DEPENDENT EQUATION FOR
GROUND
   % STATE VIBRATIONAL POPULATION IN THERMAL EQUILIBRIUM


%-------------------------------------------------------------------------
%   PUMP LIGHT AND TRANSITION CHARACTERISTICS

lambdap = 1.533*10^-6;   % m, pump wavelength
Vpump = 1*10^9;          % Hz, pump spectral width
pumpenergy = 20*10^-6;   % J, pump energy
tp = 1*10^-9;            % s, pump pulse duration
Ap = 5;                  % 1/s, A-coefficient: pump

nup = c/lambdap;         % Hz, pump frequency

deltavdp = 2/lambdap*sqrt(2*log(2)*R*T/MC2H2);
   % Hz, FWHM pump Doppler broadening from eq. 7.72b, "Atoms, Molecules,
   %   and Photons", Demtroder.

Vpwidth = 0.5346*2*deltavc+sqrt((0.2166*(2*deltavc)^2)+deltavdp^2);
   % Hz, FWHM Voigt pump linewidth

if (Vpwidth - Vpump < 0)
   spectralfactor = 1;
else
   spectralfactor = 1;
end;
   % Compares spectral overlap between pump laser and Doppler + collision
   %   braodened pump transition to determine fraction of pump laser
   %   energy absorbed

pumpenergy = pumpenergy*spectralfactor;
   % J, pump energy scaled by linewidth overlap (Vpwidth >= Vpump, overlap
   %   = 1)

IP0 = pumpenergy/(pi*fiberradius^2)*1/tp*sqrt(4*log(2)/pi);
   % W/cm^2, peak initial pump intensity

bp = sqrt(4*log(2))*deltavc/deltavdp;
```

% b coefficient for pump light from eq 3.12.5, "Laser Physics", Milonni
%   & Eberly

Sp = sqrt(4*log(2)/pi)*1/deltavdp*exp(bp^2)*erfc(bp);
   % s, Voigt pump profile

sigmap = lambdap^2*Ap/(8*pi)*Sp;
   % m^2, pump stimulated emission cross section

S12 = sigmap*2/(h*nup); % WHY THE FACTOR OF 2?
   % m^2/J, pump stimulated emission cross section per energy?

%---
%   Laser light and transition characteristics (same calculations as for
%   pump)

lambdaL = 3.16*10^-6;   % m, laser wavelength
laserenergy0 = 0*10^-25; % initial laser energy (from quantum noise)
Al = 13;   % 1/s, A-coefficient: laser

nuL = c/lambdaL;   % Hz, laser frequency
IL0 = laserenergy0/(pi*fiberradius^2)*1/tp*sqrt(4*log(2)/pi);
   % W/cm^2, peak initial laser intensity (from quantum noise? - why not
   %   one photon per mode?)

deltavdL = 2/lambdaL*sqrt(2*log(2)*R*T/MC2H2);
   % Hz, FWHM laser Doppler broadening

VLwidth = 0.5346*2*deltavc+sqrt((0.2166*(2*deltavc)^2)+deltavdL^2);
   % Hz, Voigt laser linewidth (FWHM)

bL = sqrt(4*log(2))*deltavc/deltavdL;
   % b coefficient for laser light from eq 3.12.5, Laser, Milonni & Eberly

SL = sqrt(4*log(2)/pi)*1/deltavdL*exp(bL^2)*erfc(bL);
   % s, Voigt laser profile

sigmaL = lambdaL^2*Al/(8*pi)*SL;
   % m^2, laser stimulated emission cross section

S23 = sigmaL*2/(h*nuL);
   % m^2/J, laser stimulated emission cross section per energy?

%---
%   Create temporal profiles of incident pump pulse and inital laser pulse
%   (intial laser pulse represents quantum noise?)

```
T0 = -1.5*tp;          % s, start of time window
TE = 3.5*tp;           % s, end of time window
NT = 5001;             % NT-1 is the number of time slices
Dt = (TE-T0)/(NT-1);   % s, Incremental time step

for i = 1:NT
   % Create 1-D array of time values
   t(i) = T0+(i-1)*Dt;

   % Create 1-D array of incident pump intesity at each time value
   IP(i) = IP0*exp(-4*log(2)*(t(i)/tp)^2);
   IPin(i) = IP(i);

   % Create 1-D array of incident laser intesity at each time value
   IL(i) = IL0*exp(-4*log(2)*(t(i)/tp)^2);   % SET "IL0" = 0
   IL2(i) = IL0;
end;

M = 5000;       % number of fiber slices
dz = el/M;      % m, length of each fiber slice
lossP = dz*lsP; % loss per slice at pump wavelength
lossL = dz*lsL; % loss per slice at laser wavelengths


%--------------------------------------------------------------------------
%   Propagate initial pump pulse through fiber in space and time

% THIS LOOP STEPS THROUGH EACH "dz" SEGMENT OF FIBER
for i = 1:M
   n1(i) = Np;
   n2(i) = 0;
   n3(i) = 0;
   n4(i) = 0;
   IP = IP*exp(-lossP);
      % Attenuates all time elements of pump intesity array by the loss
      %   associated with propogating a distance "dz" in the fiber
   IL = IL*exp(-lossL);
   IL2 = IL2*exp(-lossL);
      % Attenuates all time elements of laser intesity array by the loss
      %   associated with propogating a distance "dz" in the fiber

   % THIS LOOP STEPS THROUGH EACH "Dt" TIME STEP AT A GIVEN FIBER
POSITION
   for j = 1:NT
      deltaIP(j) = sigmap*(n2(i)-n1(i))*IP(j)*dz + Ap*n2(i)*h*nup*omega*dz;
      deltaIL(j) = sigmaL*(n2(i)-n3(i))*IL(j)*dz + Al*n2(i)*h*nuL*omega*dz;
```

```
        deltaIL2(j) = sigmaL*(n2(i)-n4(i))*IL2(j)*dz + Al*n2(i)*h*nuL*omega*dz;

        deltan1 = Ap*n2(i)*Dt + sigmap/(h*nup)*(n2(i)-n1(i))*IP(j)*Dt;
        deltan3 = Al*n2(i)*Dt + sigmaL/(h*nuL)*(n2(i)-n3(i))*IL(j)*Dt;
        deltan4 = Al*n2(i)*Dt + sigmaL/(h*nuL)*(n2(i)-n4(i))*IL2(j)*Dt;
        deltan2 = -deltan1 - deltan3 - deltan4;

        IP(j) = IP(j) + deltaIP(j);
        IL(j) = IL(j) + deltaIL(j);
        IL2(j) = IL2(j) + deltaIL2(j);

        n1(i) = n1(i) + deltan1;
        n2(i) = n2(i) + deltan2;
        n3(i) = n3(i) + deltan3;
        n4(i) = n4(i) + deltan4;
    end;
end;

PowerPin = IPin*pi*fiberradius^2;
PowerP = IP*pi*fiberradius^2;
PowerL = IL*pi*fiberradius^2 + IL2*pi*fiberradius^2;

EnergyPin = Dt*pi*fiberradius^2*sum(IPin(1:NT)) % J, input pump energy
EnergyP = Dt*pi*fiberradius^2*sum(IP(1:NT))     % J, output pump energy
EnergyPabs = EnergyPin*exp(-lsP*el)-EnergyP    % J, absorbed pump energy
EnergyL = Dt*pi*fiberradius^2*sum(IL(1:NT)) + Dt*pi*fiberradius^2*sum(IL2(1:NT))     % J,
laser energy

plot(t(1:NT),PowerPin(1:NT)/max(PowerPin(1:NT)),'g',t(1:NT),PowerP(1:NT)/max(PowerPin(1
:NT)),'b',t(1:NT),PowerL(1:NT)/max(PowerPin(1:NT)),'r');
%plot(t(1:NT),PowerPin(1:NT),'r',t(1:NT),PowerP(1:NT),'g',t(1:NT),PowerL(1:NT),'b');
```

Appendix E – MATLAB Program to Process Oscilloscope Data

```
%------------------------------------------------------------------------
% INPUT FILE AND FILE ANALYSIS PARAMETERS

gasName = 'C2H2';          % Used in file name as saved by scope
gasPressure = '30.0 torr';  % Used in file name as saved by scope

% File path where data file is located and where results file is created
filePath = 'D:\Measurements and Data\_Gas-Filled Fiber Laser Data\C2H2\2011-11-21 18.75um
pitch kagome - 45-cm length\';
resultsFileName = ['Results\',gasName,'_',gasPressure,'_Energy and Timing Corrected
Results.xls'];

numOfEs = 3;              % Number of pump pulse energy settings where data were taken
numOfFilesPerE = 50;      % Number of files taken at each energy setting
DelayLPinOffset = -27.52000040888; % Delay in nanoseconds on scope between peak of 1.5
micron pulse detected at fast HgCdTe detector and peak of incident pump pulse detected at 25
GHz, 1.5 micron detector
DelayPoutPinOffset = 8.31800011112; % Delay in nanoseconds on scope between peak of 1.5
micron pulse detected at fast HgCdTe detector and peak of pump pulse transmitted through fiber
and detected at 25 GHz, 1.5 micron detector

i1a = 2601; % Ch1 'pump in' analysis starting point
i1b = 3600; % Ch1 'pump in' analysis ending point

i1c = 3601; % Ch1 'pump out' analysis starting point
i1d = 4600; % Ch1 'pump out' analysis ending point

j1a = 1;   % Ch1 background analysis starting point
j1b = 2600; % Ch1 background analysis ending point
```

i2a = 1; % Ch2 'laser' analysis starting point

i2b = 3500; % Ch2 'laser' analysis ending point

j2a = 3501; % Ch2 background analysis starting point

j2b = 5000; % Ch2 background analysis ending point

%--

% CREATE TABLE OF CALIBRATION, CONVERSION, AND COMPONENT
TRANSMISSION

% VALUES AT BOTTON OF MIDDLE COLUMN OF Excel SPREADSHEET

% Fractional transmission through optics between where pump pulse energy is measured before
fiber and the start of the fiber

ToptPumpIn = '0.99';   % Transmission from ThorLabs Ag mirror at 45 deg and through 2 AR-
coated BK7 optics (from literature on website)

% Fractional transmission through optics between where pump pulse energy is measured after
fiber and the end of the fiber

ToptPumpOut = '0.8821';   % Transmission through 1 CaF2 window and 1 CaF2 lens
(calculated)

% Fractional transmission through optics between HgCdTe laser pulse detector and the start of
the fiber

ToptLasOut = '=0.7700*0.9481*0.1333'; % Transmission through AR-coated GE filter
(measured @ 3.5 microns) and 4 CaF2 optics, one at 45 deg (calculated), and one ND=1.0 filter

% Fractional transmission through fiber at pump wavelength

TfiberPump = '=10^(-0.1*1.460/10)'; % Loss of 7 cell, 3 ring, 18.75 micron pitch kagome at
1.53 microns is <= 0.1 dB/m (from plot of fiber loss sent with fiber).

% HgCdTe detector calibration used to convert V*ps to nJ

ElasLaser = '0.04136'; % Calibration performed using OPA at wavelength of 3.5 microns

% Factor used to convert from V*ps to microJ

EinONPumpInOn =

['=LINEST(K3:K',num2str(2+numOfEs),',C',num2str(6+numOfEs*numOfFilesPerE),':C',num2st

r(5+numOfEs*(1+numOfFilesPerE)),',0,0)'];

% Factor used to convert from V*ps to microJ

EoutONPumpOutOn =

['=LINEST(L3:L',num2str(2+numOfEs),',D',num2str(6+numOfEs*numOfFilesPerE),':D',num2st

r(5+numOfEs*(1+numOfFilesPerE)),',0,0)'];

% Factor used to convert from V*ps to microJ

EoutOFFPumpOutOFF =

['=LINEST(N3:N',num2str(2+numOfEs),',G',num2str(6+numOfEs*numOfFilesPerE),':G',num2s

tr(5+numOfEs*(1+numOfFilesPerE)),',0,0)'];

% Write column labels and parameter values to results file below table structure for measured
energy values

dataOut =

{'ToptPumpIn',ToptPumpIn;'ToptPumpOut',ToptPumpOut;'ToptLasOut',ToptLasOut;'TfiberPum

p',TfiberPump;'Elas/Laser (nJ/(V*ps))',ElasLaser;'EinON/PumpInON

(microJ/(V*ps))',EinONPumpInOn;'EoutON/PumpOutON

(microJ/(V*ps))',EoutONPumpOutOn;'EoutOFF/PumpOutOFF

(microJ/(V*ps))',EoutOFFPumpOutOFF};

xlswrite([filePath,resultsFileName],dataOut,1,['J',num2str(5+2*numOfEs)]);

%--

% COMPUTE INTEGRATED PUMP AND LASER PULSE DATA (UNITS OF V*ps) FROM
FILES

% WRITEN BY SCOPE AND COLLECTED VIA LabVIEW

% Write column labels to results file
dataOut = {'','','ON RES','ON RES','ON RES','OFF RES','OFF RES','OFF RES';'E','File','PumpIn (V*ps)','PumpOut (V*ps)','Laser (V*ps)','PumpIn (V*ps)','PumpOut (V*ps)','Laser (V*ps)'};
xlswrite([filePath,resultsFileName],dataOut,1,'A1');

for ei = 1:1:numOfEs   % Loop through all energies
    for fi = 1:1:numOfFilesPerE % Loop through all files

        %--
        % ON RESONANCE DATA

        % Read in ch1 data files
        fid = fopen([filePath,'Data\',gasName,'_',gasPressure,'_on res_E ',num2str(sprintf('%04d',ei)),'_',num2str(sprintf('%04d',fi)),'_CH1.csv'],'r');
        ch1DataOn = textscan(fid,'%q %f %q %f %f','delimiter',',');   % Import data
        fclose(fid);   % Close file

        % Read in ch2 data files
        fid = fopen([filePath,'Data\',gasName,'_',gasPressure,'_on res_E ',num2str(sprintf('%04d',ei)),'_',num2str(sprintf('%04d',fi)),'_CH2.csv'],'r');
        ch2DataOn = textscan(fid,'%q %f %q %f %f','delimiter',',');   % Import data
        fclose(fid);   % Close file

        % Create variable and arrays
        ch1TimeStepOn = ch1DataOn{2}(2,1)*10^12;   % Units of ps   %disp(timeStep);
        ch1TimeOn = ch1DataOn{4};   %disp(time(:));
        ch1VoltOn = ch1DataOn{5};   %disp(volt(:));
        ch2TimeStepOn = ch2DataOn{2}(2,1)*10^12;   % Units of ps   %disp(timeStep);
        ch2TimeOn = ch2DataOn{4};   %disp(time(:));

158

```
        ch2VoltOn = ch2DataOn{5};                          %disp(volt(:));


        % Analyze data
        v1BackgroundOn = 0;   % Initialize integrated voltage to 0 V*ps
        for j = j1a:1:j1b
            v1BackgroundOn = v1BackgroundOn + ch1VoltOn(j);   % Sum Ch1 voltage between j1a
and j1b
        end
        vPeakPumpInOn(ei,fi) = v1BackgroundOn/(j1b-j1a+1); % Calculate average voltage to
determine peak voltage timing
        vPeakPumpOutOn(ei,fi) = vPeakPumpInOn(ei,fi);
        v1BackgroundOn = v1BackgroundOn*ch1TimeStepOn/(j1b-j1a+1);  % Units of V*ps/pt
        tPeakPumpInOn(ei,fi) = 0;
        tPeakPumpOutOn(ei,fi) = 0;
        tPeakLaser(ei,fi) = 0;


        v1abOn = 0;   % Initialize integrated voltage to 0 V*ps
        for i = i1a:1:i1b
            v1abOn = v1abOn + ch1VoltOn(i);   % Sum Ch1 voltage between i1a and i1b
            if ch1VoltOn(i) > vPeakPumpInOn(ei,fi)
                vPeakPumpInOn(ei,fi) = ch1VoltOn(i);   % Record peak voltage value
                tPeakPumpInOn(ei,fi) = ch1TimeOn(i);   % Records time corresponding to first (b/c of
">" sign) maximum in "Pump In" voltage
            end
        end
        vIntPumpInOn = v1abOn*ch1TimeStepOn-v1BackgroundOn*(i1b-i1a+1);  % Units of
V*ps


        v1cdOn = 0;   % Initialize integrated voltage to 0 V*ps
        for i = i1c:1:i1d
            v1cdOn = v1cdOn + ch1VoltOn(i);   % Sum Ch1 voltage between i1c and i1d
```

```
        if ch1VoltOn(i) > vPeakPumpOutOn(ei,fi)
            vPeakPumpOutOn(ei,fi) = ch1VoltOn(i);  % Record peak voltage value
            tPeakPumpOutOn(ei,fi) = ch1TimeOn(i);  % Records time corresponding to first (b/c
of ">" sign) maximum in "Pump In" voltage
        end
    end
    vIntPumpOutOn = v1cdOn*ch1TimeStepOn-v1BackgroundOn*(i1d-i1c+1); % Units of
V*ps


    v2BackgroundOn = 0;   % Initialize integrated voltage to 0 V*ps
    for j = j2a:1:j2b
        v2BackgroundOn = v2BackgroundOn + ch2VoltOn(j);   % Sum Ch1 voltage between j1a
and j1b
    end
    vPeakLaser(ei,fi) = v2BackgroundOn/(j2b-j2a+1);    % Calculate average voltage to
determine peak voltage timing
    v2BackgroundOn = v2BackgroundOn*ch2TimeStepOn/(j2b-j2a+1);  % Units of V*ps/pt


    v2abOn = 0;   % Initialize integrated voltage to 0 V*ps
    for i = i2a:1:i2b
        v2abOn = v2abOn + ch2VoltOn(i);   % Sum Ch2 voltage between i2a and i2b
        if ch2VoltOn(i) > vPeakLaser(ei,fi)
            vPeakLaser(ei,fi) = ch2VoltOn(i);  % Record peak voltage value
            tPeakLaser(ei,fi) = ch2TimeOn(i);  % Records time corresponding to first (b/c of ">"
sign) maximum in "Pump In" voltage
        end
    end
    vIntLaserOn = v2abOn*ch2TimeStepOn-v2BackgroundOn*(i2b-i2a+1);   % Units of V*ps


    %-----------------------------------------------------------------
    % OFF RESONANCE DATA
```

```matlab
    % Read in ch1 data files
    fid = fopen([filePath,'Data\',gasName,'_',gasPressure,'_off res_E
',num2str(sprintf('%04d',ei)),'_',num2str(sprintf('%04d',fi)),'_CH1.csv'],'r');
    ch1DataOff = textscan(fid,'%q %f %q %f %f','delimiter',',');   % Import data
    fclose(fid);    % Close file

    % Read in ch2 data files
    fid = fopen([filePath,'Data\',gasName,'_',gasPressure,'_off res_E
',num2str(sprintf('%04d',ei)),'_',num2str(sprintf('%04d',fi)),'_CH2.csv'],'r');
    ch2DataOff = textscan(fid,'%q %f %q %f %f','delimiter',',');   % Import data
    fclose(fid);    % Close file

    % Create variable and arrays
    ch1TimeStepOff = ch1DataOff{2}(2,1)*10^12;  % Units of ps   %disp(timeStep);
    ch1TimeOff = ch1DataOff{4};                      %disp(time(:));
    ch1VoltOff = ch1DataOff{5};                      %disp(volt(:));
    ch2TimeStepOff = ch2DataOff{2}(2,1)*10^12;  % Units of ps   %disp(timeStep);
    ch2TimeOff = ch2DataOff{4};                      %disp(time(:));
    ch2VoltOff = ch2DataOff{5};                      %disp(volt(:));

    % Calculate integrated pulse data (Units of V*ps)
    v1BackgroundOff = 0;   % Initialize integrated voltage to 0 V*ps
    for j = j1a:1:j1b
        v1BackgroundOff = v1BackgroundOff + ch1VoltOff(j);   % Sum Ch1 voltage between
j1a and j1b
    end
    v1BackgroundOff = v1BackgroundOff*ch1TimeStepOff/(j1b-j1a+1);  % Units of V*ps/pt

    v1abOff = 0;   % Initialize integrated voltage to 0 V*ps
    for i = i1a:1:i1b
```

```
        v1abOff = v1abOff + ch1VoltOff(i);   % Sum Ch1 voltage between i1a and i1b
    end
    vIntPumpInOff = v1abOff*ch1TimeStepOff-v1BackgroundOff*(i1b-i1a+1);  % Units of
V*ps


    v1cdOff = 0;   % Initialize integrated voltage to 0 V*ps
    for i = i1c:1:i1d
        v1cdOff = v1cdOff + ch1VoltOff(i);   % Sum Ch1 voltage between i1c and i1d
    end
    vIntPumpOutOff = v1cdOff*ch1TimeStepOff-v1BackgroundOff*(i1d-i1c+1); % Units of
V*ps


    v2BackgroundOff = 0;   % Initialize integrated voltage to 0 V*ps
    for j = j2a:1:j2b
        v2BackgroundOff = v2BackgroundOff + ch2VoltOff(j);   % Sum Ch1 voltage between
j1a and j1b
    end
    v2BackgroundOff = v2BackgroundOff*ch2TimeStepOff/(j2b-j2a+1);  % Units of V*ps/pt


    v2abOff = 0;   % Initialize integrated voltage to 0 V*ps
    for i = i2a:1:i2b
        v2abOff = v2abOff + ch2VoltOff(i);   % Sum Ch2 voltage between i2a and i2b
    end
    vIntLaserOff = v2abOff*ch2TimeStepOff-v2BackgroundOff*(i2b-i2a+1);   % Units of
V*ps


    % Write integrated pulse data to Excel file
    curRowNum = num2str(2+fi+(ei-1)*numOfFilesPerE);    % current row number being
written to in output file
```

```
    dataOut =
{ei,fi,vIntPumpInOn,vIntPumpOutOn,vIntLaserOn,vIntPumpInOff,vIntPumpOutOff,vIntLaserO
ff}; % Store values to be written
    xlswrite([filePath,resultsFileName],dataOut,1,['A',curRowNum]);
    %-----------------------------------------------------------------
  end
end


%--------------------------------------------------------------------------
% CREATE TABLE OF AVERAGED VALUES BELOW LEFT COLUMN OF DATA IN
Excel
% SPREADSHEET

% Write column labels to results file
dataOut = {'','','ON RES','ON RES','ON RES','OFF RES','OFF RES','OFF RES';'E','','Avg
PumpIn (V*ps)','Avg PumpOut (V*ps)','Avg Laser (V*ps)','Avg PumpIn (V*ps)','Avg PumpOut
(V*ps)','Avg Laser (V*ps)'};
xlswrite([filePath,resultsFileName],dataOut,1,['A',num2str(4+numOfEs*numOfFilesPerE)]);


for ei = 1:1:numOfEs    % Loop through all energies

   % Write formulas for averaging to variables
   avgPumpInON = ['=AVERAGE(C',num2str(3+(ei-
1)*numOfFilesPerE),':C',num2str(2+ei*numOfFilesPerE)];
   avgPumpOutON = ['=AVERAGE(D',num2str(3+(ei-
1)*numOfFilesPerE),':D',num2str(2+ei*numOfFilesPerE)];
   avgLaserON = ['=AVERAGE(E',num2str(3+(ei-
1)*numOfFilesPerE),':E',num2str(2+ei*numOfFilesPerE)];
   avgPumpInOFF = ['=AVERAGE(F',num2str(3+(ei-
1)*numOfFilesPerE),':F',num2str(2+ei*numOfFilesPerE)];
```

163

```
   avgPumpOutOFF = ['=AVERAGE(G',num2str(3+(ei-
1)*numOfFilesPerE),':G',num2str(2+ei*numOfFilesPerE)];
   avgLaserOFF = ['=AVERAGE(H',num2str(3+(ei-
1)*numOfFilesPerE),':H',num2str(2+ei*numOfFilesPerE)];


   % Write label (1,2,3,...) and average value (averaged over all files for that "E"
   curRowNum = num2str(5+numOfEs*numOfFilesPerE+ei);  % current row number being
written to in output file
   dataOut =
{num2str(ei),'',avgPumpInON,avgPumpOutON,avgLaserON,avgPumpInOFF,avgPumpOutOFF,
avgLaserOFF};
   xlswrite([filePath,resultsFileName],dataOut,1,['A',curRowNum]);
end

dataOut = {'','','Std Dev (V*ps)','Std Dev (V*ps)','Std Dev (V*ps)','Std Dev (V*ps)','Std Dev
(V*ps)','Std Dev (V*ps)'};
xlswrite([filePath,resultsFileName],dataOut,1,['A',num2str(6+numOfEs*(1+numOfFilesPerE))]);

for ei = 1:1:numOfEs    % Loop through all energies

   % Write formulas for averaging to variables
   stDevPumpInON = ['=STDEV(C',num2str(3+(ei-
1)*numOfFilesPerE),':C',num2str(2+ei*numOfFilesPerE)];
   stDevPumpOutON = ['=STDEV(D',num2str(3+(ei-
1)*numOfFilesPerE),':D',num2str(2+ei*numOfFilesPerE)];
   stDevLaserON = ['=STDEV(E',num2str(3+(ei-
1)*numOfFilesPerE),':E',num2str(2+ei*numOfFilesPerE)];
   stDevPumpInOFF = ['=STDEV(F',num2str(3+(ei-
1)*numOfFilesPerE),':F',num2str(2+ei*numOfFilesPerE)];
   stDevPumpOutOFF = ['=STDEV(G',num2str(3+(ei-
1)*numOfFilesPerE),':G',num2str(2+ei*numOfFilesPerE)];
```

```matlab
    stDevLaserOFF = ['=STDEV(H',num2str(3+(ei-
1)*numOfFilesPerE),':H',num2str(2+ei*numOfFilesPerE)];


    % Write label (1,2,3,...) and average value (averaged over all files for that "E"
    curRowNum = num2str(6+numOfEs*(1+numOfFilesPerE)+ei);  % current row number being
written to in output file
    dataOut =
{num2str(ei),'',stDevPumpInON,stDevPumpOutON,stDevLaserON,stDevPumpInOFF,stDevPu
mpOutOFF,stDevLaserOFF};
    xlswrite([filePath,resultsFileName],dataOut,1,['A',curRowNum]);
end


%--------------------------------------------------------------------------
% CREATE TABLE STRUCTURE AT TOP MIDDLE OF Excel SPREADSHEET WHERE
VALUES
% FOR MEASURED INCIDENT AND TRANSMITTED PUMP PULSE ENERGIES CAN BE
ENTERED.
% THE Excel FILE MUST BE OPENNED AFTER RUNNING THIS PROGRAM TO INPUT
VALUES
% FOR THE MEASURED PULSE ENERGIES BEFORE AND AFTER THE FIBER, ON AND
OFF
% RESONANCE

% Write column labels to results file
dataOut = {'','ON RES','ON RES','OFF RES','OFF RES';'E','Avg Ein (microJ)','Avg Eout
(microJ)','Avg Ein (microJ)','Avg Eout (microJ)'};
xlswrite([filePath,resultsFileName],dataOut,1,'J1');


for ei = 1:1:numOfEs    % Loop through all energies

    % Write label (1,2,3,...) for energy measurement
```

```
    curRowNum = num2str(2+ei);  % current row number being written to in output file
    xlswrite([filePath,resultsFileName],num2str(ei),1,['J',curRowNum]);
end

dataOut = {'','Std Dev (microJ)','Std Dev (microJ)','Std Dev (microJ)','Std Dev (microJ)'};
xlswrite([filePath,resultsFileName],dataOut,1,['J',num2str(3+numOfEs)]);

for ei = 1:1:numOfEs    % Loop through all energies

    % Write label (1,2,3,...) for energy measurement
    curRowNum = num2str(3+numOfEs+ei);  % current row number being written to in output
file
    xlswrite([filePath,resultsFileName],num2str(ei),1,['J',curRowNum]);
end

%---------------------------------------------------------------------------
% WRITE FORMULAS TO Excel FILE THAT ARE USED TO ANALYZE AND
TRANSFORM THE
% INTEGRATED VOLTAGE DATA INTO CALIBRATED ENERGY DATA

% Write column labels to results file
dataOut = {'','w/o Absorption','w/ Absorption','','','','','';'Ein (microJ)','Eout (microJ)','Eout
(microJ)','Eabs (microJ)','Elaunched (microJ)','Elaser (nJ)','Peak-to-Peak Delay (ns), Laser-
Pin','Peak-to-Peak Delay (ns), Laser-Pout'};
xlswrite([filePath,resultsFileName],dataOut,1,'P1');

for ei = 1:1:numOfEs    % Loop through all energies
    for fi = 1:1:numOfFilesPerE % Loop through all files

        curRowNum = num2str(2+fi+(ei-1)*numOfFilesPerE);    % current row number being
written to in output file
```

```
    % Write formulas used to calculate calibrated energy data to variables
    Ein = ['=C',curRowNum,'*$K$',num2str(5+2*numOfEs),'*$K$',num2str(10+2*numOfEs)];
    EoutWOAbs =
['=G',curRowNum,'*C',curRowNum,'/F',curRowNum,'*$K$',num2str(12+2*numOfEs),'*(1/$K$'
,num2str(6+2*numOfEs),')'];
    EoutWAbs =
['=D',curRowNum,'*$K$',num2str(11+2*numOfEs),'*(1/$K$',num2str(6+2*numOfEs),')'];
    Eabs = ['=Q',curRowNum,'-R',curRowNum];
    Elaunched = ['=Q',curRowNum,'*(1/$K$',num2str(8+2*numOfEs),')'];
    Elaser =
['=E',curRowNum,'*$K$',num2str(9+2*numOfEs),'*(1/$K$',num2str(7+2*numOfEs),')'];
    DelayLPin = (tPeakLaser(ei,fi) - tPeakPumpInOn(ei,fi))*10^9 - DelayLPinOffset;
    DelayLPout = (tPeakPumpOutOn(ei,fi) - tPeakPumpInOn(ei,fi))*10^9 -
DelayPoutPinOffset;

    % Write formulas to create calibrated energy data to file
    dataOut = {Ein,EoutWOAbs,EoutWAbs,Eabs,Elaunched,Elaser,DelayLPin,DelayLPout};
    xlswrite([filePath,resultsFileName],dataOut,1,['P',curRowNum]);
  end
end
```